

University of Windsor

Scholarship at UWindor

Electronic Theses and Dissertations

Theses, Dissertations, and Major Papers

Winter 2013

Ion Nitriding of Ti-10V-2Fe-3Al Alloy for Aerospace Applications

Jin Qian

University of Windsor

Follow this and additional works at: <https://scholar.uwindsor.ca/etd>

Recommended Citation

Qian, Jin, "Ion Nitriding of Ti-10V-2Fe-3Al Alloy for Aerospace Applications" (2013). *Electronic Theses and Dissertations*. 5039.

<https://scholar.uwindsor.ca/etd/5039>

This online database contains the full-text of PhD dissertations and Masters' theses of University of Windsor students from 1954 forward. These documents are made available for personal study and research purposes only, in accordance with the Canadian Copyright Act and the Creative Commons license—CC BY-NC-ND (Attribution, Non-Commercial, No Derivative Works). Under this license, works must always be attributed to the copyright holder (original author), cannot be used for any commercial purposes, and may not be altered. Any other use would require the permission of the copyright holder. Students may inquire about withdrawing their dissertation and/or thesis from this database. For additional inquiries, please contact the repository administrator via email (scholarship@uwindsor.ca) or by telephone at 519-253-3000ext. 3208.

Ion Nitriding of Ti-10V-2Fe-3Al Alloy for Aerospace Applications

by

Jin Qian

A Thesis
Submitted to the Faculty of Graduate Studies
through Engineering Materials
in Partial Fulfillment of the Requirements for
the Degree of Master of Applied Science at the
University of Windsor

Windsor, Ontario, Canada

2013

©2013 Jin Qian

Ion Nitriding of Ti-10V-2Fe-3Al Alloy for Aerospace Applications

by

Jin Qian

APPROVED BY:

S.H. Eichhorn, Outside Program Reader
Department of Chemistry and Biochemistry

R.J. Bowers, Program Reader
Department of Mechanical, Automotive, and Materials Engineering

A. Edrisy, Advisor
Department of Mechanical, Automotive, and Materials Engineering

Oct. 16th 2013

DECLARATION OF CO-AUTHORSHIP/ PREVIOUS PUBLICATION

I hereby certify that this research incorporates material that is the result of a joint research undertaken in collaboration with Exactatherm Ltd. and K. Farokhzadeh from Department of Mechanical, Automotive, and Materials Engineering at University of Windsor under the supervision of Dr. A. Edrisy. The research collaboration is covered in Chapter 3, 4, and 5 of the thesis.

I am aware of the University of Windsor Senate Policy on Authorship and I certify that I have properly acknowledged the contributions of other researchers to my thesis, and have obtained permission from each of the co-authors to include the above materials in my thesis.

I certify that, with the above qualification, this thesis, and the research to which it refers, is the product of my own work.

This thesis includes one original paper that has been submitted for publication in peer reviewed journals, as follows:

- J. Qian, K. Farokhzadeh, A. Edrisy, Ion Nitriding of a Near- β Titanium Alloy: Microstructure and Mechanical Properties, Surface and Coatings Technology, 2013.

I certify that I have obtained permission from the copyright owners to include the above published materials in my thesis. I certify that the above material describes work completed during my registration as a graduate student at the University of Windsor.

I certify that, to the best of my knowledge, my thesis does not infringe upon anyone's copyright nor violate any proprietary rights and that any ideas, techniques, quotations, or any other material from the work of other people included in my thesis,

published or otherwise, are fully acknowledged in accordance with the standard referencing practices. Furthermore, to the extent that I have included copyrighted material that surpasses the bounds of fair dealing within the meaning of the Canada Copyright Act, I certify that I have obtained permission from the copyright owners to include such materials in my thesis.

I declare that this is a true copy of my thesis, including any final revisions, as approved by my thesis committee and the Graduate Studies office, and that this thesis has not been submitted for a higher degree to any other University or Institution.

ABSTRACT

In this study, a low-temperature ion nitriding treatment has been developed with the aim of improving the sliding behaviour of Ti-10V-2Fe-3Al, without adverse effects on its strength and ductility. The optimized nitriding treatment was carried out at a temperature of 600°C for 8 hours in a pressure dilute nitriding atmosphere of 67 Pa and 2.9 vol.% N₂. The microstructural analysis indicated that the ion nitriding treatment led to the formation of a 0.5 µm thick compound layer. The microhardness measurements revealed the formation of an approximately 35 µm thick nitrogen diffusion zone beneath the compound layer. The tensile test results showed improvements in the tensile and yield strengths of the alloy with a minor decrease in the elongation. The load bearing capacity and friction properties of the nitrided surfaces under sliding were investigated by microscratch tests. It was found that the coefficient of friction values were reduced and the surfaces exhibited an excellent load bearing capacity.

DEDICATION

I dedicate this thesis to my loving parents for their unconditional love, support, and encouragement.

I also dedicate my thesis work to my advisor Dr. Afsaneh Edrisy. She is my respected advisor for my academic career.

ACKNOWLEDGEMENTS

I would never have been able to finish my dissertation without the guidance of my advisor and my committee members, help from collaborators, and support from my group members.

I would like to express my deepest gratitude to my advisor, Dr. A. Edrisy, for her excellent guidance, patience, and providing me with an excellent atmosphere for doing research; for letting me experience the research of titanium alloys in the field and practical issues beyond the textbooks, patiently corrected my writing and financially supported my research.

I would like to thank my committee members, Dr. R. Bowers and Dr. S.H. Eichhorn, for their help and comments in improving my research experiments. I would like to thank Graham Pigott and Peter Lidster, who as our collaborator members were always willing to help and give their best performance for treating samples. It would have been a long period without their kind support. Many thanks to K. Farokhzadeh and other colleagues in the laboratory of Dr. Edrisy for guiding me test procedures and helping me using all the instruments. My research would not have been possible without their helps.

TABLE OF CONTENTS

DECLARATION OF CO-AUTHORSHIP/ PREVIOUS PUBLICATION	III
ABSTRACT.....	V
DEDICATION.....	VI
ACKNOWLEDGEMENTS.....	VII
LIST OF TABLES.....	XV
LIST OF FIGURES	XVII
LIST OF APPENDICES.....	XXXI
LIST OF ABBREVIATIONS, SYMBOLS.....	XXXII
CHAPTER 1 INTRODUCTION.....	1
1.1 Overview.....	1
1.2 Motivation.....	1
1.3 Research objective	3
1.4 Organization of the thesis	4
CHAPTER 2 REVIEW OF LITERATURE.....	7
2.1 Overview.....	7
2.2 Titanium & titanium alloys.....	7
2.3 Beta titanium alloys	8
2.3.1 β titanium alloys microstructures.....	12
2.3.1.1 Annealed microstructures	12
2.3.1.2 Processed microstructures.....	13

2.3.1.3 Through-transus processed microstructures	14
2.3.1.4 Bi-modal microstructures.....	15
2.3.1.5 Thermomechanical processing microstructures.....	16
2.3.2 Properties of β titanium alloys	16
2.3.2.1 Mechanical properties	16
2.3.2.2 Fatigue behaviour.....	22
2.3.2.2.1 Fatigue strength enhancement: Mechanical surface treatments.....	28
2.3.2.3 Wear and friction properties	29
2.4 Surface treatment for β titanium alloys.....	34
2.4.1 Thermomechanical processes	34
2.4.1.1 Nitriding technologies.....	34
2.4.1.2 Plasma nitriding of titanium alloys	36
2.4.1.2.1 Nitriding temperature and time	36
2.4.1.2.2 Nitriding pressure.....	38
2.4.2 Other surface treatments	39
2.5 Nitriding effect on the titanium alloys	41
2.5.1 Nitriding effect on the near β Ti-10V-2Fe-3Al alloys	42
2.5.1.1 Microstructure after nitriding.....	42
2.5.1.2 Mechanical properties after nitriding.....	46
2.5.1.2.1 Tensile properties.....	46
2.5.1.2.2 Fracture toughness	47
2.5.1.2.3 Hardness.....	47
2.5.1.3 Fatigue.....	48

2.5.1.4 Wear and friction	50
CHAPTER 3 MATERIALS AND EXPERIMENTAL METHODS	66
3.1 Overview.....	66
3.2 Materials	67
3.3 Ion nitriding of Ti-10V-2Fe-3Al.....	67
3.3.1 Sample preparation	67
3.3.2 Ion nitriding process	68
3.3.3 Surface analysis of ion nitrided samples.....	70
3.3.3.1 Surface morphology.....	70
3.3.3.2 Compositional analysis by the X-ray diffraction method.....	70
3.3.4 Cross-sectional microstructure analysis.....	71
3.3.4.1 Cross-sectional sample preparation	71
3.3.4.2 Scanning electron microscopy analysis	71
3.3.4.3 Transmission electron microscopy and focused ion beam techniques	72
3.3.4.4 Micro-indentation hardness measurements.....	73
3.4 Wear testing	74
3.4.1 Ball-on-disk wear testing process	74
3.4.2 Scanning electron microscopy analysis of worn materials	75
3.4.3 Subsurface analysis of worn Ti-10V-2Fe-3Al.....	75
3.5 Micro-scratch testing	76
3.6 Tensile testing	76
3.6.1 Tensile sample preparation	76
3.6.2 Tensile testing process	77

3.7 Fatigue testing.....	78
3.7.1 Fatigue sample preparation.....	78
3.7.2 Fatigue testing process.....	79
CHAPTER 4 EXPERIMENTAL RESULTS	88
4.1 Overview.....	88
4.2 Characterization of Ti-10V-2Fe-3Al as-received.....	88
4.2.1 Microstructure evaluation on Ti-10V-2Fe-3Al.....	88
4.3 Ion nitriding of Ti-10V-2Fe-3Al.....	89
4.3.1 Effect of pre-treatment methods on surface roughness and cross-sectional microstructure	90
4.3.1.1 Surface roughness	91
4.3.1.2 Cross-sectional microstructure, depth of diffusion zone and compound layer thickness.....	91
4.3.1.3 Micro-indentation hardness profile.....	91
4.3.2 Effect of nitriding temperatures on surface roughness and cross-sectional microstructures.....	92
4.3.2.1 Surface roughness	92
4.3.2.2 Cross-sectional microstructure, depth of diffusion zone and compound layer thickness.....	93
4.3.2.3 Micro-indentation hardness profile.....	93
4.3.3 Effect of nitriding time on surface roughness and cross-sectional microstructure	93
4.3.3.1 Surface roughness	94

4.3.3.2 Cross-sectional microstructure, depth of diffusion zone and compound layer thickness.....	94
4.3.3.3 Micro-indentation hardness profile.....	95
4.3.4 Effect of nitriding pressure on surface roughness and cross-sectional microstructure	95
4.3.4.1 Surface roughness	96
4.3.4.2 Cross-sectional microstructure, depth of diffusion zone and compound layer thickness.....	96
4.3.4.3 Micro-indentation hardness profile.....	96
4.3.5 Effect of nitriding time on surface roughness and cross-sectional microstructure of samples pre-treated with prolonged gas sputtering	97
4.3.5.1 Surface roughness	97
4.3.5.2 Cross-sectional microstructure, depth of diffusion zone and compound layer thickness.....	98
4.3.5.3 Micro-hardness profile.....	98
4.3.6 Optimized ion nitriding conditions for Ti-10V-2Fe-3Al.....	98
4.3.6.1 Surface characterizations (WYKO, SEM, XRD)	99
4.3.6.2 Cross-sectional microstructure analysis (SEM, TEM, FIB)	100
4.3.6.3 Microhardness profile	101
4.4 Microscratch analysis.....	102
4.5 Wear behaviour of Ti-10V-2Fe-3Al.....	103
4.5.1 Wear behaviour of Ti-10V-2Fe-3Al as-received.....	103
4.5.2 Wear behaviour of ion nitrided Ti-10V-2Fe-3Al.....	106

4.6 Tensile properties of Ti-10V-2Fe-3Al	107
4.6.1 Tensile properties of Ti-10V-2Fe-3Al as-received.....	107
4.6.2 Tensile properties of ion nitrided Ti-10V-2Fe-3Al	109
4.7 Fatigue properties of Ti-10V-2Fe-3Al.....	110
4.7.1 Fatigue properties of Ti-10V-2Fe-3Al as-received.....	110
4.7.2 Fatigue properties of ion nitrided Ti-10V-2Fe-3Al	112
 CHAPTER 5 DISCUSSIONS.....	 178
5.1 Ion nitriding of Ti-10V-2Fe-3Al.....	178
5.1.1 Effect of nitriding parameters on surface morphology and cross-sectional microstructure	178
5.1.2 Microstructure analysis of ion nitrided Ti-10V-2Fe-3Al.....	180
5.1.3 Microscratch behaviour of ion nitrided Ti-10V-2Fe-3Al	183
5.2 Wear behaviour of Ti-10V-2Fe-3Al.....	185
5.3 Tensile properties of Ti-10V-2Fe-3Al.....	189
5.4 Fatigue properties of Ti-10V-2Fe-3Al.....	190
 CHAPTER 6 CONCLUSIONS AND RECOMMENDATIONS	 196
6.1 Overview.....	196
6.1.1 Effect of ion nitriding on the microstructure	196
6.1.2 Scratch resistance of ion nitrided Ti-10V-2Fe-3Al	197
6.1.3 Wear behaviour of ion nitrided Ti-10V-2Fe-3Al.....	198
6.1.4 Tensile and fatigue properties before and after ion nitriding.....	199
6.2 Recommendations for future research	200

REFERENCES	201
APPENDICES	212
VITA AUCTORIS	218

LIST OF TABLES

Chapter 2

Table 2.1 List of important β phase titanium alloys	11
Table 2.2 List of Materials Properties of Ti-10V-2Fe-3Al (ST at 760°C + Aged at 385°C) and Ti-6Al-4V ELI	18
Table 2.3 Effect of grain size on fracture toughness of Ti-10V-2Fe-3Al	19
Table 2.4 Wear classifications and mechanisms	30

Chapter 3

Table 3.1 Chemical analysis of Ti-10V-2Fe-3Al alloy	67
Table 3.2 List of metallographic preparation parameters of Ti-10V-2Fe-3Al coupons [73]	68
Table 3.3 List of ion nitriding treatment parameters for Ti-10V-2Fe-3Al.....	69
Table 3.4 Characteristics of AISI 52100 steel counterface [79]	75
Table 3.5 Dimension of tensile test samples according to ASTM E8 [80]	77
Table 3.6 Dimension of fatigue test samples according to ASTM E466-07 [81]	79

Chapter 4

Table 4.1 List of ion nitriding parameters for Ti-10V-2Fe-3Al with different pre-treatment measures.....	90
Table 4.2 List of ion nitriding parameters for Ti-10V-2Fe-3Al with different nitriding temperature	92
Table 4.3 List of ion nitriding parameters for Ti-10V-2Fe-3Al with different nitriding durations.....	94

Table 4.4 List of ion nitriding parameters for Ti-10V-2Fe-3Al with different nitriding pressures.....	95
Table 4.5 List of ion nitriding parameters for Ti-10V-2Fe-3Al with different nitriding duration	97
Table 4.6 Treatment conditions, compound layer thicknesses and diffusion zone depths.	99
Table 4.7 List of tensile properties for Ti-10V-2Fe-3Al and Ti-6Al-4V [5,86,87]	108
Table 4.8 Comparison of tensile properties between untreated and ion nitrided Ti-10V-2Fe-3Al	109

LIST OF FIGURES

Chapter 1

Figure 1.1 This figure shows the methodology used for this research study 6

Chapter 2

Figure 2.1 β isomorphous phase diagram of titanium alloys 51

Figure 2.2 Pseudo-binary phase diagram of titanium and α stabilizer element 51

Figure 2.3 Processing route for β annealed microstructure of heavily stabilized β titanium alloys 52

Figure 2.4 Processing route for β processed microstructures of β titanium alloys (schematically) 52

Figure 2.5 Ti-6264 microstructure showing the α layers along the β grain boundaries are partially discontinuous. 53

Figure 2.6 Processing route for through-transus processed microstructures of β titanium alloys 53

Figure 2.7 Time/temperature control of through-transus deformation (schematically) 54

Figure 2.8 Processing route for bi-modal microstructures of β titanium alloys (schematically) 54

Figure 2.9 Processing, heat treatment, and microstructure of β -titanium alloys in (a) class A, (b) class B, and (c) class C. 55

Figure 2.10 The classification of the fatigue behaviour of β -titanium alloys. 56

Figure 2.11 The dual S-N fatigue behavior in low volume fraction α_p microstructure 56

Figure 2.12 The two-stage S-N fatigue behavior in high volume fraction α_p microstructure 57

Figure 2.13 Residual stress field in Ti-10V-2Fe-3Al alloy	57
Figure 2.14 S-N curves for ground and shot peened Ti-10V-2Fe-3Al	58
Figure 2.15 The tribological process in a contact between two surfaces includes mechanical and tribochemical changes as well as material transfer	58
Figure 2.16 Tribological contact mechanisms: (a) macromechanical, (b) material transfer, (c) micromechanical, (d) tribochemical, and (e) nanomechanical contact	59
Figure 2.17 Typical light photographs of wear surfaces of Ti-4.5Al-3V-2Mo-2Fe alloy (a) disk and (b) pin, and SEM micrographs of wear surfaces of (c) disk and (d) pin of Ti-4.5Al-3V-2Mo-2Fe annealed at 1083K.	60
Figure 2.18 Dependence of the thickness of the diffusion zone h_d after ion nitriding of titanium VT10 (1) and alloy VT8 (2) at 900°C for 3 h on the nitrogen pressure p.	60
Figure 2.19 Microstructure of Ti-10V-2Fe-3Al alloy before nitriding	61
Figure 2.20 Microstructure of Ti-10V-2Fe-3Al alloy after nitriding at 900°C for 4 hours	61
Figure 2.21 Microstructure of the cross-section of Ti-10V-2Fe-3Al alloy after gas nitriding at 750°C for 1h, 3h, and 5 h.	62
Figure 2.22 Microstructure of Ti 10V-2Fe-3Al after gas nitriding at 950C and 1050C for 1, 3, and 5h.....	63
Figure 2.23 Ti-N phase diagram.....	64
Figure 2.24 Microhardness profile of Ti 10-2-3 alloy after gas nitriding at (a) 750C and (b) 850C.....	65
 Chapter 3	
Figure 3.1 Thermo Jarrell Ash IRIS Advantage optical emission spectrometer	81
Figure 3.2 Schematic presentation of Ti-10V-2Fe-3Al coupons	81

Figure 3.3 Treatment set-up showing the titanium samples are located in a titanium cage [83].....	82
Figure 3.4 Effective NT1100 offers all the advantages of industry-standard WYKO optical profiling, including the full Wyko Vision® analytical software package [74].	82
Figure 3.5 Scanning electron microscopy used in research objective from Great Lakes Institute for Environmental Research at University of Windsor	83
Figure 3.6 The user interface of EDS coupled with SEM.....	83
Figure 3.7 (a) BSI from deposition of a 1 micron thick tungsten layer to preserve the surface of nitrided Ti-10V-2Fe-3Al during milling, (b) BSI of ion milling of the sample on one side of subsurface region, and (c) BSI from ion milling of the sample on both sides of subsurface region.....	84
Figure 3.8 (a) BSI of the manipulator approaches the sample until they touch and then attached to the sample by sputtering a small W layer, (b) BSI of lifted sample from base materials by a manipulator, and (c) BSI shows the sample is taken to the grid by the manipulator and attached to the grid with W layer deposition.	84
Figure 3.9 Illustration of loading/ unloading curves during microhardness measurement	84
Figure 3.10 Schematic presentation of ball-on-disc wear test apparatus	85
Figure 3.11 Schematic presentation and real image shown of a tensile test sample	85
Figure 3.12 Real image shown of (a) the tensile test sample, and (b) fatigue test sample which have been ion nitrided according to optimized nitriding condition selected from Section 3.5.....	86
Figure 3.13 Uni-axial tensile testing on Ti-10V-2Fe-3Al using MTS Criterion Model 43 tensile testing machine with loading rate of 0.5 mm/min.	86

Figure 3.14 Schematic presentation and real image shown of a fatigue test sample 87

Figure 3.15 Bending rotation fatigue tests ($R = -1$) are performed on untreated Ti-10V-2Fe-3Al using R.R. Moore type fatigue machine at the 50 Hz in room temperature. 87

Chapter 4

Figure 4.1 Secondary electron SEM image (SI) showing top surface microstructure of untreated Ti-10V-2Fe-3Al alloy at various magnification (a) 1000X, (b) 5000X, (c) 10000X, and (d) 20000X 115

Figure 4.2 Secondary electron SEM image (SI) showing cross-sectional microstructure of untreated Ti-10V-2Fe-3Al alloy at various magnification (a) 1000X, (b) 5000X, (c) 10000X, and (d) 20000X. 116

Figure 4.3 Phase composition analysis using “Omnimet 8.9[®]” software showing β phase percentage constituents in untreated alloy. 117

Figure 4.4 Optical 3D profile from surface topography of Ti-10V-2Fe-3Al with pre-treatment method of chemical activation, gas activation, and elongated gas activation 118

Figure 4.5 Variation of surface roughness with nitriding pressure on ion nitrided Ti-10V-2Fe-3Al 119

Figure 4.6 Secondary electron SEM image (SI) showing the cross-sectional microstructure of nitrided Ti-10V-2Fe-3Al pre-treated with (a) chemical pickling, (b) gas sputtering, and (c) prolonged gas sputtering..... 120

Figure 4.7 Variation of depth of diffusion zone and thickness of compound layer with pre-treatment measures..... 121

Figure 4.8 Micro-indentation hardness depth profiles of Ti-10V-2Fe-3Al nitrided at 600C with various pre-treatment measures 121

Figure 4.9 Optical 3D profile from surface topography of Ti-10V-2Fe-3Al untreated, nitrided at 600°C and 800°C	122
Figure 4.10 Variation of surface roughness with nitriding temperature	123
Figure 4.11 Secondary electron SEM image (SI) showing the cross-sectional microstructure of Ti-10V-2Fe-3Al nitrided at (a) 600°C and (b) 800°C.....	123
Figure 4.12 Variation of depth of diffusion zone and thickness of compound layer with nitriding temperature.....	124
Figure 4.13 Micro-indentation hardness depth profiles of Ti-10V-2Fe-3Al nitrided at 600°C & 800°C.....	124
Figure 4.14 Optical 3D profile from surface topography of Ti-10V-2Fe-3Al untreated, nitrided at 8 hours and 24 hours.....	125
Figure 4.15 Variation of surface roughness with nitriding time	126
Figure 4.16 Secondary electron SEM image (SI) showing the cross-sectional microstructure of Ti-10V-2Fe-3Al nitrided at (a) 8 hours and (b) 24 hours.	126
Figure 4.17 Variation of depth of diffusion zone and thickness of compound layer with nitriding time.....	127
Figure 4.18 Micro-indentation hardness depth profiles of Ti-10V-2Fe-3Al nitrided for 8 & 24 hours.....	127
Figure 4.19 Optical 3D profile from surface topography of Ti-10V-2Fe-3Al untreated, nitrided at 600°C and 800°C.....	128
Figure 4.20 Variation of surface roughness with nitriding pressure	129
Figure 4.21 Secondary electron SEM image (SI) showing the cross-sectional microstructure of Ti-10V-2Fe-3Al nitrided at (a) 67 Pa and (b) 520 Pa.	129

Figure 4.22 Variation of depth of diffusion zone and thickness of compound layer with nitriding pressure	130
Figure 4.23 Micro-indentation hardness depth profiles of Ti-10V-2Fe-3Al nitrided under 67 & 520 Pa	130
Figure 4.24 Optical 3D profiles from surface topography of Ti-10V-2Fe-3Al untreated, nitrided at 8 hours, and 24 hours.....	131
Figure 4.25 Variation of surface roughness with nitriding time	132
Figure 4.26 Secondary electron SEM image (SI) showing the cross-sectional microstructure of Ti-10V-2Fe-3Al nitrided at (a) 8 hours and (b) 24 hours with prolonged gas sputtering pre-treatment.....	132
Figure 4.27 Variation of depth of the diffusion zone and thickness of the compound layer with nitriding duration.	133
Figure 4.28 Microhardness depth profiles of Ti-10V-2Fe-3Al nitrided for 8 & 24 hours	133
Figure 4.29 Back scatter electron SEM image (BSI) from surface morphology of Ti-10V-2Fe-3Al after ion nitriding (tilt angle: 54°).	134
Figure 4.30 Optical 3D profile from surface topography of Ti-10V-2Fe-3Al after ion nitriding.....	134
Figure 4.31 X-ray diffraction pattern of nitrided Ti-10V-2Fe-3Al showing Ti ₂ N as the major phase.	134
Figure 4.32 SEM micrograph from cross-sectional structure of nitrided Ti-10V-2Fe-3Al surface showing a thin compound layer deposited on the diffused region.	135
Figure 4.33 BSI shows milled sample is thinned with 300 pA, 150 pA and 40 pA ion beam sizes respectively and reached electron transparent (< 100 nm thick).....	135

Figure 4.34 BSI from subsurface region of nitrided Ti-10V-2Fe-3Al	136
Figure 4.35 A typical cross-sectional dark field transmission electron micrograph (DF-TEM) of overview cross-section on nitrided Ti-10V-2Fe-3Al sample with corresponding CBED patterns taken from α and β phase.....	136
Figure 4.36 A typical cross-sectional bright field transmission electron micrograph (BF-TEM) showing the compound layer morphology and corresponding CBED patterns taken from different layers labeled as b, c, and d.....	137
Figure 4.37 (a) Dark field TEM image (DF-TEM) from subsurface region of nitrided Ti-10V-2Fe-3Al, and (b) its corresponding element distribution map.....	138
Figure 4.38 (a) A cross-sectional bright field TEM image (BF-TEM) from an area located at approximately 3 μm below the nitride grains, (b) A typical diffraction pattern corresponding to α -Ti from the location marked as “a” in Figure 4.68-a. (c) A typical diffraction pattern corresponding to β -Ti from the location marked as “b” in Figure 4.68-a.....	139
Figure 4.39 Microhardness-depth profile of nitrided Ti-10V-2Fe-3Al showing the significant hardening of diffusion zone resulted from nitrogen interstitials diffusion effect.	140
Figure 4.40 Each cracking event (angular/ tensile/ transverse crack) during scratch test has an acoustic emission output whose magnitude is proportional to the area of crack generated it. Testing conditions: applied load: 0-20 N; loading rate: 10 N/min, and lateral sliding speed: 1 mm/min.....	140
Figure 4.41 SEM micrographs showing (a) scratch path of progressive increasing load test and corresponding cracking event showing in (b) to (d); (b) from the first micro-crack	

observed area, (c) tensile cracks observed near the area of 10N load applied, and (d) semi-circular cracks existed near the area of 20N applied.	141
Figure 4.42 Coefficient of friction versus scratch distance for untreated and ion-nitrided Ti-10V-2Fe-3Al at (a) 5N, (b) 10N, and (c) 20N.	142
Figure 4.43 Variation of coefficient of friction with applied load for untreated and ion-nitrided Ti-10V-2Fe-3Al at (a) 5N, (b) 10N, and (c) 20N.....	143
Figure 4.44 Secondary electron SEM micrograph (SEI) from scratch path where 17.2 N of load applied showing coating delaminated. (a) Overall progressively loading scratch path, (b) a higher magnification of the path where delamination observed, and (c) coating delamination existed near the edge of scratch path.	144
Figure 4.45 Secondary electron SEM micrograph (SEI) from scratch path of constant loading of 20N showing coating delaminates near the edge of the path.	145
Figure 4.46 Secondary electron SEM micrograph (SEI) from scratch path of constant loading of 10N showing tensile cracks distributed (b) in the middle and (c) near the edge of the path.	146
Figure 4.47 Variation of wear rate with applied normal load for Ti-10V-2Fe-3Al and ELI Ti-6Al-4V [83].....	146
Figure 4.48 Average steady-state COF for different loading conditions for Ti-10V-2Fe-3Al and ELI Ti-6Al-4V [83].....	146
Figure 4.49 Variation of COF with sliding distance during wear tests at (a) 0.8N and (b) 5N.....	147
Figure 4.50 Three-dimensional surface profiles from wear tracks at (a) 0.8N and (b) 5N.	147

Figure 4.51 Two-dimensional profiles illustrating depth and width of the wear tracks at (a) 0.8N and (b) 5N.	147
Figure 4.52 (a) BSE micrographs from (a) wear track morphology after wear test at 0.8N (tilted at 52°), (b) ploughing marks covered with fine debris particles and (c) fractured plateau surrounded by fine debris particles. The sliding direction is marked “SD”.....	148
Figure 4.53 SE micrographs from wear debris particles generated during wear test at 0.8N. (a) compacted plates, (b) fine equiaxed particles and (c) metallic belt-like particles.....	148
Figure 4.54(a) BSE micrographs from the location of FIB milling on the 0.8N wear track on the Ti-10V-2Fe-3Al test coupon after ion milling (tilt angle: 52°), (b) Cross-sectional BSE micrograph from the MML and subsurface plastic deformation.....	149
Figure 4.55 SE micrographs from (a) wear scar on the steel counterface ball after wear test at 0.8N and (b) transferred material from Ti-10V-2Fe-3Al surface to the counterface.	150
Figure 4.56 (a) BSE micrographs from (a) wear track morphology after wear test at 5N (tilted at 52°), (b) ploughing marks with some plastic deformation and (c) parallel cracks on a plateau and small platelets spalled off from the plateau. The sliding direction is marked “SD”.....	151
Figure 4.57 SE micrographs from wear debris particles generated during wear test at 5N. (a) platelets with layered morphology, corresponding EDS spectrum indicates presence of Ti, Al, V, O and Fe in the platelets (b) fine particles, also containing the same elements as platelets only with higher oxygen content.	152
Figure 4.58 (a) BSE micrographs from the location of FIB milling on the 5N wear track on the Ti-10V-2Fe -3Al wear track (tilt angle: 52°), (b) Cross-sectional BSE micrograph from the MML and subsurface plastic deformation.	153

Figure 4.59 BSE micrograph and corresponding EDS mapping from an iron-rich layer within the MML layer on 5N wear track.	154
Figure 4.60 SE micrographs from (a) wear scar on the steel counterface ball after wear test at 5N and (b) the wear scar consisted of transferred material (MML), abraded grooves and platelets that have spalled off.	154
Figure 4.61 Variation of wear rate with applied normal load for untreated and ion nitrided Ti-10V-2Fe-3Al	155
Figure 4.62 Average steady-state COF for different loading conditions for untreated and ion nitrided Ti-10V-2Fe-3Al.....	155
Figure 4.63 Variation of COF with sliding distance during wear tests at 2N	156
Figure 4.64 Variation of COF with sliding distance during wear tests at 3.5N	156
Figure 4.65 Plot of stress-strain curves for each tensile test sample	157
Figure 4.66 Comparison of tensile properties between Ti-10V-2Fe-3Al alloys and Ti-6Al-4V	157
Figure 4.67 Back-scattered electron image (BSI) from Ti-10V-2Fe-3Al tensile specimens with local macro-cracks near fracture surface.	158
Figure 4.68 Scanning electron fractographs showing (a) tensile fracture surface of Ti-10V-2Fe-3Al, (b) micro-voids and dimples in the dimple rupture region, (c) coalescence of microscopic voids surrounded by shallow dimples in overload region; and (d) crack formation in overload region.	160
Figure 4.69 Secondary electron images (SEI) from etched Ti-10V-2Fe-3Al tensile specimen surface near fracture region showing microstructure change	161

Figure 4.70 Plot of stress-strain curves for each of untreated and ion nitrided tensile test sample	162
Figure 4.71 Comparison of tensile properties of untreated and ion nitrided Ti-10V-2Fe-3Al.....	162
Figure 4.72 Secondary electron SEM images (SEI) showing fractured surface of (a) untreated and (b) ion nitrided alloys. The area fraction of ductile fractured region to overall fractured region for untreated alloy and ion nitrided alloy is 39% and 43%, respectively.	163
Figure 4.73 Secondary electron SEM image (SEI) showing near surface area from fractured surface of untreated Ti-10V-2Fe-3Al. Enclosed area is the location where higher magnification images are taken. (b) Secondary electron SEM image (SEI) showing sheared region containing dimples with average size of $12.3 \mu\text{m}^2$	164
Figure 4.74 Secondary electron SEM image (SEI) illustrating a diffusion zone underneath compound layer observed from fractured surface of nitrided alloy. Enclosed area is the location where higher magnification images are taken. (b) Secondary electron SEM image (SEI) showing compound layer and diffusion zone.	165
Figure 4.75 Comparison of S-N curves of Ti-10V-2Fe-3Al and Ti-6Al-4V in rotating beam loading (R=-1) [89,90]	166
Figure 4.76 Secondary electron image (SEI) shows fatigue crack initiation at various magnifications for Ti-10V-2Fe-3Al fractured at maximum stress level of 797 MPa.....	166
Figure 4.77 Secondary electron image (SEI) shows fatigue crack initiation at various magnifications for Ti-10V-2Fe-3Al fractured at maximum stress level of 827 MPa.....	167

Figure 4.78 Secondary electron image (SEI) shows primary fatigue crack initiation at various magnifications for Ti-10V-2Fe-3Al fractured at maximum stress level of 887 MPa.	167
Figure 4.79 Secondary electron image (SEI) shows secondary fatigue crack initiation at various magnifications for Ti-10V-2Fe-3Al fractured at maximum stress level of 887 MPa.	168
Figure 4.80 Secondary electron image (SEI) shows fatigue crack propagation at various magnifications for Ti-10V-2Fe-3Al fractured at maximum stress level of 797 MPa.....	169
Figure 4.81 Secondary electron image (SEI) shows the region of fatigue crack propagation at various magnifications for Ti-10V-2Fe-3Al fractured at maximum stress level of 827 MPa.	170
Figure 4.82 Secondary electron image (SEI) shows fatigue crack propagation at various magnifications for Ti-10V-2Fe-3Al fractured at maximum stress level of 887 MPa.....	171
Figure 4.83 Secondary electron image (SEI) shows ductile overload fracture (dimples) at different magnifications for Ti-10V-2Fe-3Al fractured at maximum stress level of 797 MPa.	172
Figure 4.84 Comparison of S-N curves for untreated and ion nitrided Ti-10V-2Fe-3Al.	173
Figure 4.85 Comparison of fatigue test results obtained in this investigation with those found in the literature [56,70,91]. The fatigue limit has increased by approximately 10% compared to those treated at 700C.....	173
Figure 4.86 Secondary electron SEM image (SEI) showing (a) cross-sectional fracture surfaces of the nitrided sample broken at 544 MPa, (b) a close observation of crack initiation region showing the compound layer and diffusion zone. A crack is initiated	

underneath the compound layer reveals the surface crack initiation, (c) β grains consists of α grains in crack propagation zone, and (d) different orientation of grain morphologies..... 175

Figure 4.87 Secondary electron SEM image (SEI) showing (a) cross-sectional fracture surfaces of the nitrided sample broken at 744 MPa, (b) a close observation of crack initiation region showing the compound layer and diffusion zone. Several cracks are initiated underneath the compound layer reveals the surface crack initiation, (c) β grains consists of α grains in crack propagation zone, and (d) different orientation of grain morphologies..... 177

Chapter 5

Figure 5.1 Secondary electron SEM image (SEI) showing chipping on the micro-scratch path of the sample nitrided at 600C, 24 hours, 67 Pa under constant loading of 20 N... 193

Figure 5.2 Schematic presentations of the ion nitrided Ti-10V-2Fe-3Al microstructure consisting of a thin compound layer and thick diffusion zone. 193

Figure 5.3 (a) A bright field TEM image (BF-TEM) showing a high magnification view of the ion nitrided Ti-10V-2Fe-3Al microstructure at location “B” in Figure 5. The locations where several convergent beam electron diffraction (CBED) patterns were taken are marked in the image. (b) A typical diffraction pattern confirming the formation of Ti_2N ($P4_2$ -mm) grains in the surface vicinity. (c) A typical diffraction pattern confirming formation of V_2N ($P-31m$) grains at grain boundaries in the near surface region. (d) A typical diffraction pattern from an α -Ti grain underneath the compound layer. 194

Figure 5.4 Back-scattered electron (BSE) SEM image from the flat area of wear track on Ti-10V-2Fe-3Al coupon after wear test at 5N. Magnification: (a) 500X, and (b) 4000X.

..... 195

LIST OF APPENDICES

Appendix 1: List of parameters for calculation of flash and bulk temperature during wear tests [125,135].....	212
Appendix 2: List of electropolishing parameters from Literatures [136]	214

LIST OF ABBREVIATIONS, SYMBOLS

Abbreviations

ASTM	American Society for Testing and Materials
b.c.c	body-centered cubic
BSE	backscattered electron
CBED	convergent beam electron diffraction
CL	compound layer
COF	coefficient of friction
DZ	diffusion zone
EDM	electrical discharge machine
EDS	energy dispersive spectroscopy
EELS	electron energy loss spectroscopy
f.c.c.	face centered cubic
FIB	focused ion beam
h.c.p	hexagonal compact packed
HR-TEM	high resolution transmission electron microscopy
MML	mechanically mixed layer
SE	secondary electron
SEM	scanning electron microscopy
STEM	scanning transmission electron microscopy
TEM	transmission electron microscopy
UTS	ultimate tensile strength
XRD	X-ray diffraction

Symbols

a	thermal diffusivity of metal
A	real/true area of contact
A_n	nominal area of contact
d	separation distance
d	grain size diameter
E	elastic modulus
F	applied force
F_f	frictional force
H_v	indentation hardness (Vickers)
H_o	bulk hardness at room temperature (Vickers)
h_o	outlet film thickness
K	thermal conductivity
l_b	linear diffusion distance for bulk heating
l_r	linear diffusion distance for flash heating
N	normal load
p	normal stress
P	normal load
r	radius
R	radius of sphere
R_a	average roughness
R_q	root-mean-squared roughness
s	sliding distance

T_b	average bulk hardness
t_c	critical thickness
T_f	flashing temperature
T_m	melting temperature
T_o	initial temperature
T^*	equivalent temperature
U	velocity
ν	Poisson's ratio
V	sliding velocity
W	rate of sliding wear
w	volume loss
W_i	wear rate
Z	asperity height
Z^*	thickness of oxide layer
ε	strain
η	viscosity
μ	coefficient of friction
ρ	materials density
σ_y	yield stress
τ	shear stress

CHAPTER 1

INTRODUCTION

1.1 Overview

This research study focuses on the ion nitriding of near β Ti-10V-2Fe-3Al to enhance the sliding behaviour while maintaining the mechanical properties. This chapter presents background information related to this research, as well as the overall objective and organization of the thesis.

1.2 Motivation

Titanium alloys are composed of different chemical elements balanced with titanium. Titanium alloys are well-known for properties such as good corrosion/oxidation resistance, which allows them to be used as automobile and motorcycle components. Their superior strength-to-weight ratio enables engineers to use them in aerospace applications such as aircraft engine blades, frame structures and landing gears. Good biocompatibility allows dentists and doctors to use the alloys for dental and orthopedic implants. They also possess high durability, which allows manufacturers to decorate them with various colors to produce jewelry and sports equipment.

Titanium alloys derive many of their properties from the allotropic transformations that occur at around 880°C from the low-temperature hexagonal close packed (hcp) α phase to the high temperature, body-centered cubic (bcc) β phase. The ability to manipulate their properties depends on the effect of alloying elements on the stability of each phase. The physical and mechanical behaviour of these alloys can be manipulated by varying these two phases both individually, as well as in a variety of microstructural permutations and combinations.

There are three types of alloying elements: α stabilizing, β isomorphous stabilizing, and β eutectoid stabilizing. The α stabilizers such as Al, O and N are more soluble in the α phase and raise the β transus temperature. For $\alpha + \beta$ alloys, 4-6% isomorphous β stabilizers such as Mo, V and W are added to allow the retention of β phase at room temperature after quenching. For β alloys, the eutectoid β stabilizers such as Fe, Cr and Cu are sufficiently added in sufficient quantities to retain a fully β structure after quenching.

Therefore titanium alloys can be classified into three main groups. Single-phase α alloys are used extensively in applications that are not demanding in terms of strength but focus more on the attractive corrosion resistance. Alternatively, two-phase $\alpha + \beta$ alloys offer a range of combinations of strength, toughness, and high temperature properties that make them attractive in a wide range of applications. Single-phase β alloys satisfy diverse requirements involving very high strength with the adequate toughness and fatigue resistance required in aerospace applications.

Ti-10V-2Fe-3Al is a high-strength near- β titanium alloy invented by Timet in the 1970s. It mainly consists of β stabilizers of 2 wt% Fe and 10 wt% V, and a solid solution strengthener of 3 wt% Al in the master Ti alloy. The alloy has a β transus temperature of $795 \pm 5^\circ\text{C}$, with a higher percentage of β phase in the $\alpha + \beta$ microstructure. The use of β titanium alloy Ti-10V-2Fe-3Al has been limited due to its poor tribological behaviour, such as galling, scuffing, ploughing, cracking, and high coefficient of friction. Various surface engineering methods have been employed to improve the tribological behaviour of titanium alloys. Surface treatments, include coating deposition techniques, such as thermal spray coatings, diamond-like carbon (DLC) coatings, electroplating and

electroless plating; as well as thermochemical treatments, such as anodizing, salt bath hardening, laser-assisted treatments, PVD/CVD, thermal oxidation, and ion implantation. These surface treatments, however, cause unacceptable changes in mechanical properties, such as decreases in fracture toughness and fatigue strength due to the promotion of grain growth in the substrate, the formation of a brittle α -case layer, and poor coating/substrate bonding.

However, plasma nitriding, a low-temperature heating process that diffuses nitrogen onto the surface of titanium to create a hardened layer, is the most efficient of the known methods of surface impregnation of titanium alloys. It is cost-effective for mass production. Additionally, the ion nitriding process produces homogeneous, uniform coatings that are sufficiently supported by the substrate; and the process is feasible at low temperatures.

Plasma nitriding has been introduced for titanium alloys in the aerospace and automotive sectors to improve their wear resistance for components subjected to sliding, such as flap tracks. However, the challenge is to prevent the deterioration of their ductility and fatigue properties.

1.3 Research objective

The aim of this research study is to develop an optimized surface engineering process for the near β Ti-10V-2Fe-3Al alloy to enhance its wear properties without degradation of its mechanical properties.

An overview of the research scope is given in Figure 1.1. As with any research study, the first stage is a background (literature) review. This review examines titanium alloys, especially β titanium alloys, as well as their mechanical properties and

applications. Surface treatments on β titanium alloys, specifically the nitriding process are studied. The effects of nitriding surface treatment on the microstructure of the β phase titanium alloys are discussed.

1.4 Organization of the thesis

This thesis is organized into six chapters as follows:

Chapter 1 introduces the background information related to this research, as well as the overall objective and organization of the thesis.

Chapter 2 is a background (literature) review. It summarizes various microstructures, mechanical and fatigue properties of titanium and its alloys, in particular those for near β Ti-10V-2Fe-3Al. Surface treatments on Ti-10V-2Fe-3Al alloys specifically nitriding are explained. The effects of the surface treatment on the microstructure and mechanical properties of the alloy are discussed in detail.

Chapter 3 encompasses the experimental procedures used in this study. This chapter elaborates on sample preparation, ion nitriding condition, and mechanical testing, *e.g.* tensile, fatigue and wear tests. The screening tests for choosing the optimized ion nitriding conditions for the Ti-10V-2Fe-3Al alloy are described in detail as well.

Chapter 4 presents series of experimental results including inductively coupled plasma optical emission spectrometry, focused ion beam and high-resolution transmission electron microscopy and scanning electron microscopy. The results of tensile, fatigue and wear tests of ion nitrided Ti-10V-2Fe-3Al are presented and compared with those of the untreated alloy.

Chapter 5 discusses the results presented in Chapter 4. The microstructure-property relations of ion nitrided Ti-10V-2Fe-3Al are discussed. The mechanical properties of the ion nitrided alloy are related to the changes in the microstructure.

Chapter 6 highlights the main findings of this research study, followed by suggestions for future modifications in the ion nitriding treatment of Ti-10V-2Fe-3Al.

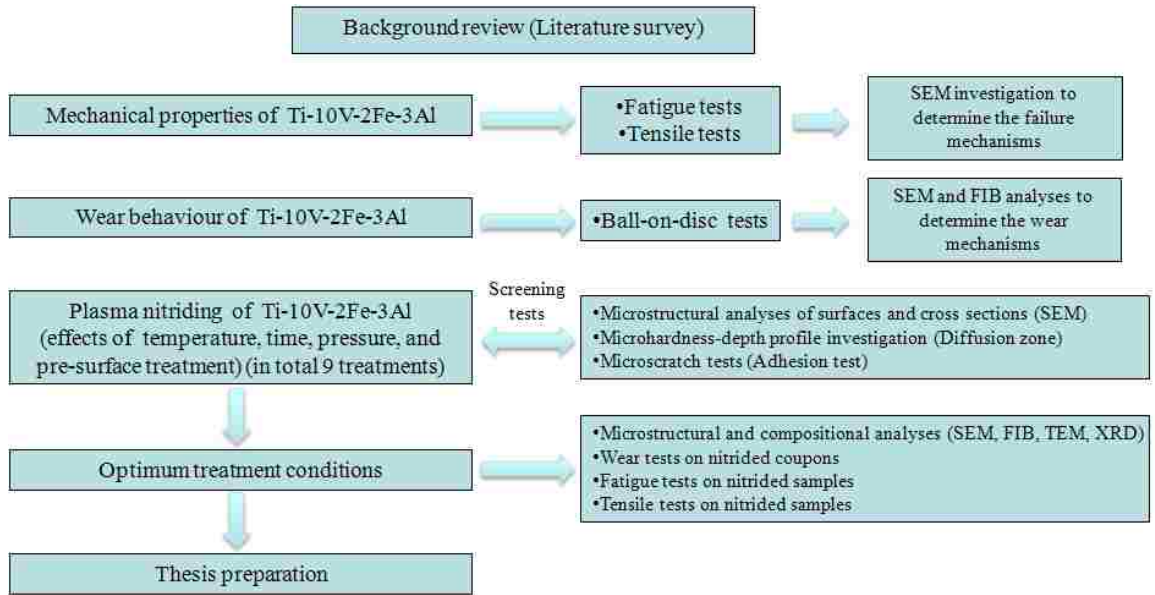


Figure 1.1 This figure shows the methodology used for this research study

CHAPTER 2

REVIEW OF LITERATURE

2.1 Overview

This chapter summarizes various microstructures, mechanical and fatigue properties of titanium and its alloys, in particular those for near β Ti-10V-2Fe-3Al. Surface treatments on Ti-10V-2Fe-3Al alloys specifically nitriding are explained. The effects of the surface treatment on the microstructure and mechanical properties of the alloy are discussed in details.

2.2 Titanium & titanium alloys

Titanium is present in the earth's crust at a level of about 0.6% and therefore is the fourth most abundant structural metal after aluminum, iron, and magnesium. The most important mineral sources are ilmenite (FeTiO_3) and rutile (TiO_2) [1]. The lattice structure of titanium is hcp (α) with a c/a ratio of 1.587 at room temperature, which transfer to bcc (β) when the temperature increases above its transition temperature, 890°C for pure titanium ($795 \pm 15^\circ\text{C}$ for β -Ti alloys). Different alloying elements and various heat treatments generate the different composition of $\alpha + \beta$ phase [2]. Therefore, titanium alloys are metallic materials which contain a mixture of titanium and other chemical elements [3].

Commercial titanium alloys are classified conventionally into three main categories (α , $\alpha + \beta$, and β alloys) according to their position in a pseudo-binary section through α/β isomorphous phase diagram, as well as the microstructure of the alloy at room temperature [1,2].

According to the β -isomorphous phase diagram in β isomorphous phase diagram of titanium alloys[2], α alloys which contain neutral alloying elements (such as Tin (Sn)) and/ or β stabilizers (such as Aluminum (Al), or Oxygen, (O)) only. These are not heat treatable [4]. All α titanium alloys are based on the low temperature, hexagonal allotropic form of titanium. These alloys are substitutional alloying elements (Al or Sn) or interstitial alloying elements (O, C, or N) that are soluble in the hexagonal α phase. These alloys also contain limited quantities of elements that have limited solubility such as Fe, V, and Mo.

$\alpha + \beta$ alloys, which are metastable and generally include some combination of both α and β stabilizers, and which can be heat treated.

In contrast to $\alpha + \beta$ alloys, β alloys do not transform martensitically upon quenching to the room temperature, resulting in a metastable β phase. β alloys, which are metastable and which contain sufficient β stabilizers (such as Molybdenum (Mo), Silicon (Si), and Vanadium (V)) to allow them to maintain the β phase when quenched, and which can also be solution treated and aged to improve the strength [1].

2.3 Beta titanium alloys

An alloy is considered to be a β alloy if it contains sufficient β stabilizer alloying elements to retain the β phase without transformation to martensite on quenching to room temperature [5]. The main characteristic of β or near- β alloys is that they are fully heat treatable and generally weldable; they can be hardened to much higher yield stress levels thus to achieve high strengths; they possess good creep resistance up to an intermediate temperatures and maintain good corrosion resistance as well. They have excellent formability in the solution treated (ST) condition. β titanium alloys are the most versatile

of all commercial titanium alloys because they offer a wide range of strength to ductility ratios [6]. The importance of metastable β titanium alloy has continually increased, mainly because the broad range of complex microstructures enable materials designers to optimize for both strength and toughness [7].

According to the pseudo-binary phase diagram (Figure 2.2) [8], there are two kinds of β alloys; namely “high strength” β alloys and “heavily stabilized” β alloys. “High strength” β alloys are located with their chemical composition close to the β to $\alpha + \beta$ alloy boundary and therefore contain a high volume fraction of α phase. The first group of alloys in Table 2.1 are examples of the “high strength” β alloys. The “Heavily stabilized” β alloys are located more to the right in the pseudo-binary phase diagram, contain a much lower volume fraction of α phase thus possess lower maximum achievable strength compared to the high strength group of β alloys. The second group of alloys in Table 2.1 are examples of “heavily stabilized” β alloys.

Typical β alloys include: Ti-3Al-8V-6Cr-4Mo-4Zr ASTM grade 19; Ti-10V-2Fe-3Al AMS 4983, 4984, 4987; Ti-15V-3Cr-3Al-3Sn AMS 4914; and the titanium alloy Ti-5Al-5Mo-5V-3Cr. Ti-3Al-8V-6Cr-4Mo-4Zr (Beta C) and Ti-15V-3Al-3Cr-3Sn (Ti-15-3) are more highly β -stabilized alloys, whereas the Ti-10V-2Fe-3Al (Ti-10V-2Fe-3Al) are solute-lean β alloys which can be classified as β -rich $\alpha + \beta$ alloys.

The Ti-3Al-8V-6Cr-4Mo-4Zr (Beta C) is equivalent to ATI 38-644 β titanium alloy (UNS R58640). This grade is a metastable β titanium alloy known for its exceptional ductility in the solution treated (annealed) condition, and for its high strength and ductility in the solution treated and aged condition (STA) condition. Improved tensile

properties can be achieved while maintaining good ductility and a low modulus of elasticity. Fatigue strength is also good in the STA condition [9].

The Ti-15V-3Al-3Cr-3Sn (Ti-15-3) is one of the practically used β - titanium alloys, with superior cold deformability in the β solution treated condition and a high mechanical strength after α phase precipitation aging. However, a main limit of this alloy is poor tribological behavior, characterized by high friction coefficients and severe adhesive wear.

The Ti-10V-2Fe-3Al alloy has been developed for aeronautical applications in the 1970s to provide weight savings over high-strength steels in forged aircraft undercarriage components [10]. It's good combination of ductility and fracture-toughness makes its use very attractive. It's fatigue crack growth resistance is reported to be comparable to that of other alloys [11]. The alloy possesses good die forgeability due to a low β transus of $\sim 800^{\circ}\text{C}$, almost 200°C below the β transus of the high-strength $\alpha + \beta$ alloy Ti-6Al-4V [10]; as well as the low thermomechanical processing cost, good hardenability and the excellent formability in comparison to α and $\alpha + \beta$ titanium alloys [12]. A low β transus provides lower forging loads, and enables the forger to use less expensive dies, such as Ni, as opposed to the expensive Mo dies required for the isothermal forging of Ti-6-4 at temperatures around 950°C . Also, energy consumption is decreased, due to the lower forging temperatures and heat up times, so consequently, Ti-10V-2Fe-3Al is more amenable to near net shape isothermal forging than α/β type alloys [13]. Ti-10V-2Fe-3Al is also a good candidate for critical components in the helicopter's rotors due to its excellent mechanical behaviors [14].

The Ti-5Al-5Mo-5V-3Cr (Ti-5-5-5-3) is a relatively new near- β alloy based on the Russian alloy system termed VT22 [15]. Correctly, it is only the metastable β alloys which are heat treatable by solution treatment and ageing. Fully stable β alloys can only be annealed [4].

The “Low-Cost Beta” alloys Ti 6.8Mo–4.5Fe–1.5Al (Ti LCB) is developed by Timetal, USA, with the brand name “Timetal LCB” and the chemical composition Ti 6.8Mo–4.5Fe–1.5Al. Because of high demands on strength and fatigue resistance in suspension structure components, β -Ti alloys offer the most attractive strength-to-density ratio and additionally offer a low Young’s modulus. To challenge the cost competition of these generally very expensive materials, a “Low-Cost Beta” alloy cost saving is thereby mainly accomplished by substituting expensive β stabilizers like vanadium by iron and using a standard Fe-Mo master alloy [16].

TABLE 2.1 List of important β phase titanium alloys

COMMON NAME	ALLOY COMPOSITION (WT %)	T_{β} (°C)	GROUPS OF BETA ALLOYS
Ti-6246	Ti-6AL-2SN-4ZR-6MO	940	HIGH STRENGTH B ALLOYS
Ti-17	Ti-5AL-2SN-2ZR-4MO-4CR	890	
SP-700	Ti-4.5AL-3V-2MO-2FE	900	
BETA-CEZ	Ti-5AL-2SN-2CR-4MO-4ZR-1FE	890	
Ti-10V-2FE-3AL	Ti-10V-2FE-3AL	800	
BETA 21S	Ti-15MO-2.7NB-3AL-0.2SI	810	HEAVILY STABILIZED B ALLOYS
Ti-LCB	Ti-4.5FE-6.8MO-1.5AL	810	
Ti-15-3	Ti-15V-3CR-3AL-3SN	760	
BETA-C	Ti-3AL-8V-6CR-4MO-4ZR	730	
B120VCA	Ti-13V-11CR-3AL	700	

T_{β} is the β transition temperature

2.3.1 β titanium alloys microstructures

2.3.1.1 *Annealed microstructures*

β annealed microstructure can be obtained by following the processing route of homogenization, deformation, recrystallization in the β phase field and aging in the ($\alpha + \beta$) phase field to precipitate the α phase in the form of fine α platelets; which is schematically shown in Figure 2.3 [1]. A continuous α layer will be formed due to the nucleation of α phase at β grain boundary. A precipitate free zone (PFZ) is a zone does not contain any of α platelets located near the continuous α layer; it is relatively soft compared to age-hardened matrix. Yield stress and the β grain size in the matrix and PFZ are two mechanical property parameters influenced by the alloy compositions. High strength β alloys influenced more by continuous α layers than heavily stabilized β alloys.

Heavily stabilized β alloys have relatively low β transus temperature of 800°C or even lower, which allows deformation process performed at lower temperatures [17]. Recrystallization temperature, heating rate, and aging temperature are three important parameters of the recrystallization and aging treatment. Shorter recrystallization time can be expected since no α phase has to be dissolved; thus the smaller β grain size can also be formed.

High strength β alloys have high β transus temperature and the higher volume fraction of α phase. Cooling rate, annealing temperature, and aging temperature are several important parameters need to be considered in processing steps such as recrystallization, annealing and aging. Two alternative approaches are shown in deformation (step II), they are β phase field deformation or ($\alpha + \beta$) phase field deformation. Deformation taken in ($\alpha + \beta$) phase field has beneficial of creating smaller β

grain size in the recrystallization step. The smaller grain size of β alloys are results of the lower β transus temperature. Annealing and aging are two final heat treatment in $(\alpha + \beta)$ phase field for high strength β alloys. Higher processing temperature annealing step precipitate a desired volume fraction of coarse α plates, the decreasing cooling rate from the annealing temperature increases the size and volume fraction of the coarse α plates. Lower processing temperature aging step determine the yield stress level of material due to fixed total volume fraction of α phase. Increasing volume fraction of coarse α plates decreasing the volume fraction and size of the fine α platelets; thus influence the yield stress level of the material.

2.3.1.2 Processed microstructures

In order to obtain the β processed microstructure, a processing route of homogenization, deformation in β phase field, annealing, and aging steps should be followed, which schematically shown in Figure 2.4 [1]. Several important parameters should be considered. Deformation time determines the unrecrystallized structure; deformation mode determines the shape of β grains; deformation degree determines the width of β grains and the geometry of grain boundary α layer. Effect of the cooling rate is very similar in comparison with the one in β annealed microstructure; it determines the grain boundary α layer and “side plates” at grain boundary as well as the unrecrystallized structure.

The recrystallization step is not in the sequence of processing route since an unrecrystallization structure with highly deformed grain boundary is intended to create. Figure 2.5 shows the Ti-6264 microstructure as an example of β processed microstructure [18]. It is obvious that most α layers are segmented to a smaller part on β grain

boundaries. β grain boundaries are strong heterogeneous nucleation sites for α formation. Deformation time is a very important parameter since the continuous operation without reheating for final deformation process is required. The shape of the unrecrystallized β grains are determined by deformation mode, such as ellipsoidal shaped or pancake shaped β grains. Cooling rate has the effect on determining the width of grain boundary α layer and “side-plates”. Following the deformation step, Annealing and aging are two heat treatments that are very similar to those in β annealed microstructure materials. For highly elongated β grains, the width of the β grain is inversely proportional to the maximum size of the coarse α plates.

2.3.1.3 Through-transus processed microstructures

The processing route for this type microstructure is schematically shown in Figure 2.6 [1]. It is similar to that for β processed materials. The recrystallization step is omitted. However, there is a more complicated processing condition for the deformation step. The deformation temperature and time are critical since there is a short time interval near the end of the deformation process that material should only remain in the $\alpha + \beta$ phase region. The α phase is precipitate at the β grain boundaries at the short time interval. The deformation process in $\alpha + \beta$ phase field allows the α phase deformed and recrystallized to globular particles at the boundaries of the unrecrystallized, elongated β grains. “Necklace” microstructure can be used to describe this kind of microstructure since α particles present only at the β grain boundaries [9].

Deformation time in the $\alpha + \beta$ phase region in deformation step is the most important parameter in the processing route for “necklace” microstructure. Figure 2.7 [1] schematically illustrates the time/temperature control of through-transus deformation; the

time should be long enough for α precipitation at the deformed β grain boundary and should be finished before crossing the boundary line for α precipitation in the β matrix. In comparison with β processed microstructure processing route, the cooling rate is no longer an important processing parameter since α phase precipitate at the β grain boundary. Similar final two treatments are observed in through-transus processed microstructures processing route.

2.3.1.4 Bi-modal microstructures

The processing sequence for obtaining bi-modal microstructures is homogenization, deformation, recrystallization, annealing and aging; which are shown schematically in Figure 2.8 [1]. The advantage of bi-modal microstructure is to reduce the effect of α layer on mechanical property by creating small enough β grain size at β grain boundary. Several important parameters including cooling rate, deformation degree, annealing temperature and aging temperature are present.

The recrystallization annealing temperature directly influences the size of the recrystallized equiaxed β grains by alternating the volume fraction of primary α . Both annealing temperature and cooling rate are important in annealing treatment for the purpose of precipitate coarse α plates. Temperature difference between recrystallization annealing temperature and the intermediate annealing temperature determines the volume fraction of coarse α plates. Aging treatment deals with the volume fraction of fine α platelets under the effect of volume fraction of globular primary α and coarse α plates.

2.3.1.5 Thermomechanical processing microstructures

Thermomechanical processing (TMP) techniques such as isothermal forging (IF) (as opposite to conventional forging) are required to fabricate Ti-10V-2Fe-3Al aerospace components because the microstructure is particularly sensitive to temperature, especially close to the β transus. The effect of TMP on the microstructure of Ti-10V-2Fe-3Al around the β transus focuses on the breakup of an initial prior β forged microstructure, consisting of α plates and grain boundary α in and around large β grains. The microstructure involves equiaxed grain morphology, consisting of spheroidized α within a β matrix, with increasing strain. Such microstructural development impacts ductility and superplasticity into the forged product as deformation proceeds [10].

2.3.2 Properties of β titanium alloys

2.3.2.1 Mechanical properties

Mechanical properties of materials including strength, hardness, ductility, toughness, elasticity, plasticity, and brittleness; are used as the measurements of how metals behave under applied loads. Table 2.2 [19] lists the material properties including physical, mechanical and thermal properties of solution treated at 760°C plus aged at 385°C Ti-10V-2Fe-3Al alloy.

Hardness is the measure of the shape change for a solid under applied force in various kinds. [20]. Several methods of measuring hardness can be applied; therefore, the hardness of a material is always specified in terms of the particular test that is used to measure this property. Rockwell, Vickers, or Brinell are three methods mainly performed for hardness testing. Rockwell is the most frequently used among these tests. The basic

principle used in the Rockwell test is that a hard material can penetrate a softer one [21]. Indentation hardness measures the shape change of the material that under permanent plastic deformation resulted from the constant compressive loading using a specific indenter. These measurements are widely applied in the engineering and metallurgy fields. [20]. The term "micro-hardness", which is also known as, the "micro-indentation hardness testing" has been widely performed in the literature research to describe the hardness testing of materials with micro-scale applied loads. In the micro-indentation hardness testing, a diamond indenter of a specific geometry is impressed into the surface of the test specimen using a known applied force (commonly called a "load" or "test load") of 1 to 1000 gf. Micro-indentation tests typically have forces of 2N (roughly 200 gf) and create indentations of about 50 μm . Due to their specificity, the micro-hardness testing can be used to observe changes in hardness on the microscopic scale [22]. Scratch hardness measures the fracture or permanent plastic deformation resulted from friction on the material using a specific indenter [20].

In materials science, strength is the amount of applied stress that the material can withstand before the failure observed. The field of strength of materials deals with loads, deformations and the forces acting on a material. The intensity of the internal force due to the load apply to the material deforms the material. Deformation of the material caused by stress is called strain. The applied stress may be tensile, compressive, or shear. The ultimate strength is the maximum strain a material can withstand before necking. The tensile strength is a measurement of resistance of being stretched apart when placed in a tension load. The compressive strength is opposite to the tensile strength. The fatigue strength is the ability of material to resist fatigue failure under various kinds of rapidly

changing stresses and is expressed by the magnitude of cyclic stress. The impact strength is the ability of a metal to resist suddenly applied loads and is usually measured in foot-pounds of force [21].

The fracture toughness is one of the material abilities to resist fracture while cracks appear. It is a very important property for engineering materials especially for the design application. K_{IC} stands for the linear-elastic fracture toughness of the material determined from the stress intensity factor (K) when the crack starts propagate. J_{IC} in short for plastic-elastic fracture toughness measure the energy required for crack propagation. Typical fracture toughness values (K_{IC}) for titanium alloys varies from 44 to 66 MPa m^{1/2} [23]. Bhattacharjee et al. [24] summarized the fracture toughness values of Ti-10V-2Fe-3Al alloy for different grain sizes, as shown in Table 2.3.

Table 2.2 List of Materials Properties of Ti-10V-2Fe-3Al (ST at 760°C + Aged at 385°C) and Ti-6Al-4V ELI

	Ti-10V-2Fe-3Al (ST 760°C + AGED 385°C)	Ti-6Al-4V ELI (GRADE 23), ANNEALED
PHYSICAL PROPERTIES		
DENSITY	4.65 G/CC	4.43 G/CC
MECHANICAL PROPERTIES		
HARDNESS, VICKERS	475	341
TENSILE STRENGTH, ULTIMATE	1430 MPa	860 MPa
TENSILE STRENGTH, YIELD	1240 MPa	790 MPa
COMPRESSIVE YIELD STRENGTH	1280 MPa	860 MPa
FATIGUE STRENGTH (KT =3.0)	450 MPa @ # OF CYCLES 1.00E + 7	140 MPa @ # OF CYCLES 1.00E + 7
FATIGUE STRENGTH (UNNOTCHED)	830 MPa @ # OF CYCLES 1.00E + 7	300 MPa @ # OF CYCLES 1.00E + 7
SHEAR STRENGTH	760 MPa	550 MPa
FRACTURE TOUGHNESS	131.2 MPa m ^{1/2}	100 MPa m ^{1/2}
THERMAL PROPERTIES		

THERMAL CONDUCTIVITY	7.80W/M-K	6.70 W/M-K
B TRANSUS	760°C	960°C

Table 2.3 Effect of grain size on fracture toughness of Ti-10V-2Fe-3Al

	820°C	900°C	1100°C	1200°C
GRAIN SIZE (D), MM	230	355	530	845
J _{IC} , KJ/M2	174.6	132.6	118.9	105.8
K _{IC} , MPA-M1/2	131.2	114.5	108.5	102.3

C. Sauer et al. [18] performed tensile tests under various inclined angles and in both L- and ST- direction. The highest yield stress and ductility is observed for the alloy Ti-6264 in L direction. The minimum of tensile ductility is observed under 45° orientation. On the other hand, in ST-direction, yield stress and ductility are higher than the value under 45° orientations. Soft grain boundary zones do not influence the yield stress due to the low volume fraction of the zones. However, a texture effect is associated with the orientation dependence of the yield stress. Tensile ductility is determined by two main parameters, crack nucleation resistance and crack propagation resistance. Early crack nucleation and fast crack propagation result the minimum ductility in 45° inclined angle orientation.

W. Chen et al. studied the effect of prestrain on mechanical behavior of aged Ti-10V-2Fe-3Al alloy [25]. The Vickers hardness in both prestrained and unstrained β -ST Ti-10V-2Fe-3Al decreases while an increasing aging time. Vickers hardness of unstrained Ti-10V-2Fe-3Al initiated at 445Hv and decreased to 380 Hv after 8 hours of aging treatment. The prestrained sample, however, has an initial value of 415 Hv and decreased to 350 Hv under the same aging treatments. The tensile yield strength for prestrained and unstrained aged Ti-10V-2Fe-3Al is around 1325 MPa; as the aging time

increase, yield strength of prestrained and unstrained sample decrease to 1150 MPa and 1075 MPa, respectively. Therefore, the yield strength is inversely proportional to aging time with a decrement of 10% for both kinds of sample [26]. Meanwhile, W. Chen et al. observed that prestrained sample has an ability of improving its ductility by 200% under the aging treatment due to lack of grain boundary α film and its lower hardness.

W. Chen et al. studied the influence of the aging process on mechanical properties of Ti-10V-2Fe-3Al as well [27]. Both simplex aging and duplex aging are performed on aged Ti-10V-2Fe-3Al alloy; the Vickers hardness of initial β inner-grain in both aging treatment samples depends on aging time. Under the same aging time, the simplex aging gives higher grain hardness. The curve of aging time versus tensile yield strength show the sufficient decrement of yield strength for simplex and duplex aging; similarly, under the same aging time, the duplex aging generates a lower yield strength compared with simplex aging treatment.

W. Chen et al. also reported the microstructural evolution in primary α phase-containing cold forged Ti-10V-2Fe-3Al under different applied strains [28]. The Vickers hardness of $\alpha + \beta$ ST Ti-10V-2Fe-3Al after cold forging increased as the increase in strains. The Vickers hardness can be as high as 340 Hv when strain increased to 1.2 compare with the original β -ST sample. Hall-Petch effect best explains the increase in Vickers hardness, which is subjected to the microstructure refinement inside the shear band; meanwhile, localized plastic deformation would cause the rapid increase in shear bands.

C. Li et al. studied the influence of α morphology and volume fraction on the stress-induced martensitic transformation in Ti-10V-2Fe-3Al [29]. The stress-strain

curves for the heat treated samples show there is a 10-20% increase in strength for the stress-induced martensitic transformation. Both the β grain size and β phase stability affect the triggering stress of SIM; the triggering stress increased with α volume fraction until the α volume fraction reaches a critical value of 50%; moreover, the globular form of α material generated from $\alpha + \beta$ phase field has a lower second yield stress than the acicular α material which is formed in $\beta + (\alpha + \beta)$ phase field.

Sun et al. investigated the effect of stress-assisted martensite transformation on the mechanical behavior of Ti-10V-2Fe-3Al [30]. Martensite (α'') can be generated in the metastable β microstructure under applied stress. The metastable β microstructure shows the lower strength and ductility compared with solution treated and aged microstructure. Moreover, the martensite transformation ($\beta \rightarrow \alpha''$) does not influence the strength and ductility in Ti-10V-2Fe-3Al alloy.

Bhattacharjee investigated the effect of β grain size on tensile behavior and ductile fracture toughness of Ti-10V-2Fe-3Al [24]. Metastable β titanium alloys Ti-10V-2Fe-3Al alloy subject to SIM transformation during tensile loading in the β -quenched condition. The β grain size has effect on SIM transformation in metastable β titanium alloys Ti-10V-2Fe-3Al alloy. Both the variation of plastic flow and fracture toughness respect to β grain size are reported. Four deformation stage, (1) elastic deformation of metastable β , (2) triggering of SIM α'' under elastic deformation, (3) elastic deformation of β matrix and α'' , and (4) plastic deformation of untransformed β matrix and α'' are observed in deformation of β -ST Ti-10V-2Fe-3Al. As the grain size increased from 230 to 530 μm , the triggering stress for SIM increases; when grain size is larger than 845 μm , no SIM observed. The flow stress is found to obey the Hall-Petch relationship. On the

other hand, when the grain size ranges between 355 to 845 μm ; the fracture toughness linearly depends on the inverse square root of grain size but has no effect of the SIM transformation.

Terlinde et al. studied the three microstructure including $(\alpha + \beta)$ ST plus α -aged; β -ST plus α aged, and ω -aged [28]. The yield strength of three microstructures varies between 900 MPa and 1450 MPa. Both microstructure and yield stress influence the ductility. $(\alpha + \beta)$ ST plus α -aged is observed that the increase in α_p volume fraction decreases the ductility at comparable yield stress. For β -ST plus α aged microstructure, lower ductility is observed than the $(\alpha + \beta)$ ST plus α -aged condition. Macroscopic brittleness change to marked ductility can be observed in ω -aged microstructure. Furuhashi et al. [31] reported the Vickers hardness of the ST Ti-10V-2Fe-3Al alloys is 250Hv.

2.3.2.2 Fatigue behaviour

Fatigue is a kind of mechanical failure modes with the materials progressive and localized structural damage that occurs under cyclic loading. The nominal maximum stress values are expected to be less than both the ultimate tensile stress limit and the yield stress limit of the material [32]. The American Society for Testing and Materials (ASTM) defines fatigue life, N_f , as the number of stress cycles of a specified character that a specimen sustains before failure of a specified nature occurs [33]. The fatigue resistance, for instance the endurance limit, is one of the most important factors for β titanium alloys due to their aerospace applications. However, unlike the other structural alloys, the endurance limit and the tensile strength do not correlate to each other in β titanium alloys. Nevertheless, increased emphasis has been made to β -titanium alloys

applications since they have the ability to optimize microstructure and properties over a wide scope through various mechanical and heat treatments [34].

Jha et al.[32] divided six commercial β -titanium alloys (Ti-8V-8Mo-2Fe-3Al (Ti-8-8-2-3), Ti-10V-2Fe-3Al (Ti-10V-2Fe-3Al), Ti-11.5Mo-6Zr-4.5Sn (Beta III), Ti-3Al-8V-6Cr-4Mo-4Zr (Beta C), Ti-15V-3Cr-3Sn-3Al (Ti-15-3-3-3), and Ti-5Al-2Sn-2Cr-4Mo-4Zr-1Fe (Beta-CEZ)) into three classes (A, B, and C) based on their processing history and resulting microstructures, as shown in Figure 2.9. Class A microstructures generally consist of a high volume fraction of very finely distributed α particles. Class B microstructures consist of coarse primary- α (α_p) and uniformly distributed, fine, secondary- α (α_s) in transformed β matrix. Class C microstructures generally consist of a non-uniform distribution of α phase in the transformed β matrix as well as continuous grain boundary α in some alloys. S-N fatigue curves (common curve relating stress range ($\Delta\sigma$) to the number of cycles to failure (N_f)) are plotted for Ti-10V-2Fe-3Al in Figure 2.10. Overall, microstructures belonging to Class A (forged above the β transus, followed by control cooling and direct aging below β transus) show the highest fatigue limits. Variations of fatigue limits corresponded to variations in the characteristics of α particles. Moreover, the fatigue limits of all three kinds of microstructures are plotted in Figure 2.10, as a function of UTS. Overall fatigue behaviours of β -titanium alloys prove that Class A microstructure with uniformly distributed fine α particles show medium to high fatigue limits; and the fatigue limit does not correspond to the UTS. Finally, Jha reported that the microstructures consist of uniformly distributed fine α particles in the transformed β matrix results the highest high-cycle fatigue resistance.

M. Benedetti [35] summarized the relationship between the microstructure, extrinsic mechanisms and fatigue propagation resistance of β titanium alloys. Microstructural differences depend on the size and the shape of β grains which can be varied by processing. β annealed (lamellar) structure, $\alpha + \beta$ processed (bimodal) structure, and β processed (pancake) structure are three types of the structure for β -CEZ β titanium alloy. In β annealed (lamellar) structure, extensive grain boundary α -layers are formed and their lower mechanical properties as compared to the lamellar matrix reduce the ductility and fracture toughness, thus results the intergranular fracture. $\alpha + \beta$ processed (bimodal) structure, on the other hand, consists much finer β grain size thus effectively restricts the length of the grain boundary α layers. Continuous grain boundary α -layers are segmented into individual drops by a “through-transus” deformation process can be found in β processed (pancake) structure. The microcrack propagation and macrocrack propagation distinguish each other by the route of cracks propagation. The microcrack propagation along the grain boundary α -layers where the macrocracks with much larger crack front length does not follow the grain boundary α -layers due to the smaller plastic zone sizes. Therefore, nearly flat crack paths are generated along the lamellar matrix. The overload fracture conditions are existed when the plastic zone size is greater than β grain size. Cracks propagate along grain boundary α -layers generate microscopically ductile grain boundary fracture. The crack bridging effect and crack closure effect as the secondary extrinsic mechanisms result higher fatigue propagation resistance of the β processed (pancake) structure. Retarding effect points out the inherent crack propagation resistance of the $\alpha + \beta$ processed (bimodal) structure is higher than that of the β processed (pancake) structure. Moreover, the bimodal microstructure with small

β grain sizes shows the best performances in terms of inherent fracture properties. Crack bridging, crack closure, and crack front geometry effects determine the macrocrack propagation resistance.

R. Chait and T.S. DeSisto [36] studied the effect of grain size on the high cycle fatigue crack initiation of Ti-8Mo-8V-2Fe-3Al (Ti-8823), which is a metastable β Ti alloy. They compared the strength ratio, σ_{fs}/σ_{UTS} between two different treatments Ti-8823 alloy, solution treatment and age, and direct age. There is a big difference between the strength ratios of two treatment alloy. They found that individual β grains always correlate with the fracture initiation. Meanwhile, tensile ductility is heavily influenced by the β grain size. The voids are initiated at grain boundaries and coalesce thus forms cracks. They confirmed that the β grain size, as similar to ultimate tensile strength or hardness; dominate on determining the fatigue strength of metastable β -Ti alloys as well. As β grain size increases, fatigues strength decreases accordingly.

In contrary to aforementioned fatigue behaviours, Jha et al. [34] reported an unusual fatigue behavior for β -titanium alloy Ti-10V-2Fe-3Al, $\alpha + \beta$ microstructures. Fatigue data of samples on S-N curves show the duality from cracks nucleated at the surface and subsurface regions. Two separate S-N curves can be plotted according to fatigue crack initiation. The effect of microstructure factors is studied.

The dominant microstructure difference between two groups of specimens is the volume fraction of primary α_p particle. The dual S-N fatigue behaviors (Figure 2.11) are observed from the microstructure contained a low volume fraction (10%) of primary- α (α_p) particles whereas the aspect ratio (length/thickness) is around 1-3 in. It is reported that the specimens that failed by subsurface crack initiation exhibited relatively higher

fatigue lives. On the other hand, a higher stress level of surface crack nucleation compared with the lower stress level of subsurface crack nucleation is observed. Other than dual S-N fatigue behaviors observed from low volume fraction α_p microstructure, a two-stage S-N fatigue behavior (Figure 2.12) can be observed for the microstructure contained a high volume fraction (45%) of primary- α (α_p) particles whereas the aspect ratio (length/thickness) is around 14. Basically, a transition cyclic stress level of failed specimens can be observed above and below the surface and subsurface fatigue crack initiation, respectively.

The main observation of fatigue fracture surface analysis by Jha et al. presents the center of crack region appears a flat faceted region. The size of this region under surface crack nucleation is larger than the primary α particle; but is not corresponding to the stress level and the location of crack initiation; for subsurface surface crack nucleation, however, the size of small faceted region ($10 \times 1 \mu\text{m}$) is corresponding to the α_p particles [37].

Fretting can be defined as the small oscillatory displacements at interfaces due to vibrations in the structure and induces early crack nucleation and propagation. Sliding displacement has an effect on fretting damage on the contacting surface. Gross slip condition and partial slip condition are two levels of sliding amplitude. Wear associates with gross slip condition and generate wear debris, whereas the initiation of fatigue crack is dominant in the partial slip condition. Two kinds of loadings such as fretting loading at the surface and bulk fatigue loading have effect on cracking nucleation and propagation. Fretting loading at the contact surface generates the cracking nucleation and early propagation in mode I; bulk fatigue loading generates the propagation in mode I. are two

kinds of loadings in cracking process. Heredia et al. performed fretting wear test with a cylinder on plane configuration to study tribological behavior and cracking response of Ti-10V-2Fe-3Al. Polished, ground, and shot peened are three surfaces for the investigation. Surface roughness, residual stress, and surface hardness are three parameters for comparison.

Heredia et al. concluded that the different surface treatment process with different surface roughness and compressive residual stress do not affect the sliding regime condition and the coefficient of friction in the partial slip regime. Meanwhile, the sample with residual stress induced by the grinding process is not an obstacle for the crack propagation. Therefore, it is confirmed that the crack nucleation threshold as well as the cracking response of Ti-10V-2Fe-3Al solicited in fretting are independent of the surface roughness or the residual stress under grinding process. Shot peening treatment, on the other hand, has a sufficient effect on preventing crack propagation by compressive residual stress thus has a higher resistance of fatigue or fretting loading on samples [14].

Takeda et al. studied the fretting fatigue characteristics of Ti-4.5Al-3V-2Mo-2Fe annealed at various temperatures in $\alpha + \beta$ field. Both low and high cycle fatigue life regions are observed. The slip and stick regions can be clearly defined in low fatigue region but not in high cycle fatigue life region. Crack initiation sites are different for each region; surface crack initiation is observed in low cycle fatigue life region whereas subsurface crack initiation is observed in high cycle fatigue life region. The fretting fatigue life of Ti-4.5Al-3V-2Mo-2Fe is hardly affected by the volume fraction and diameter of the primary α phase in the low cycle fretting fatigue life region. The fretting fatigue limit of Ti-4.5Al-3V-2Mo-2Fe tends to increase with a decrease in the volume

fraction and average diameter of primary α phase. When volume fraction and average diameter of primary α phase are below certain values, the fretting fatigue limit is lowered by coarsening of the acicular α phase, which precipitates in the β phase region. The fretting fatigue crack of Ti-4.5Al-3V-2Mo-2Fe initiates at the boundary between slip and stick regions at the initial stage of fretting fatigue. After the width and depth of the fretting fatigue crack grow to some extent, the fretting fatigue crack grows in the same manner as the plain fatigue crack [38].

2.3.2.2.1 Fatigue strength enhancement: Mechanical surface treatments

The fatigue strength in metal components can be increased by one of the most common surface treatment, shot peening. Gao studied the influence of shot peening on tension-tension fatigue property of Ti-10V-2Fe-3Al as well as the surface characterization including surface roughness, surface residual stress, and surface layer residual compressive stress. Double shot peening, as an advanced shot peening process, significantly improve fatigue performance as well. Double shot peening includes cast iron shot peening and glass shot peening. The process start with cast iron shot peening to make a deep residual compressive stress field; followed by glass shot peening to decrease the surface roughness and clean the surface thus increase the fatigue limit.

Gao illustrates the improvement in fatigue properties by plotting the residual stress field (Figure 2.13) and the S-N curve (Figure 2.14) for both untreated surface specimen and shot peened surface specimen. Gao stated that residual compressive stress in the surface layer generated during shot peening process plays an important role in improving the fatigue life and fatigue limit. Finally, Gao concluded that the shot peening proves increase the fatigue limit at 1×10^7 cycles of Ti-10V-2Fe-3Al by 29%. Both

surface roughness and residual stress are the main factors influence the fatigue properties of Ti-10V-2Fe-3Al; shot peening and double shot peening processes can improve the fatigue performance by changing the surface integrity of mechanical parts. Both over shot peening and lack of shot peening do not induce the proper residual stress field, only optimal shot peening intensity on different materials produce the best fatigue performance. On the other hand, double shot peening can always improve the fatigue life and fatigue limit significantly [39].

A. Drechsler et al. [40] reported the optimum mechanical surface treatment to improve the fatigue strength of components of Ti-10V-2Fe-3Al. Both shot peening and deep-rolling enhance the fatigue resistance of the notched electropolished reference and the fatigue strength is increased by a factor of 2.5 under the optimum process condition. Variation of primary α (α_p) volume fraction generates different levels of fatigue resistance and the highest fatigue strengths at 10^7 cycles (775 MPa at R=-1 and 1200 MPa at R=0.1) on smooth electropolished specimens are obtained from the material with 15% volume fraction α_p .

2.3.2.3 Wear and friction properties

Wear, friction, and lubrication are three main principles in tribological filed. Figure 2.15 illustrates the tribological process including mechanical and tribochemical changes, as well as material transfer between two contact surfaces [41]. In material science, wear is considered as a loss of dimension on a surface due to plastic deformation when two interacted surfaces sliding against each other [42]. Wear classifications and mechanisms are summarized in Table 2.4[43]. In details, there are five wear mechanisms including, adhesive wear, abrasive wear, surface fatigue, fretting wear, and erosive wear.

Adhesive wear subjects to frictional contact between surfaces and refers to the wear debris transformation during sliding motion of two contact surfaces. Abrasive wear subjects to two sliding surfaces with different surface hardness; the harder surface slides against softer surface causes the loss of materials on the softer surface. Three mechanisms of abrasive wear including plowing, cutting, and fragmentation. Delamination wear also refers to the surface fatigue, subjects to the damage of materials under cyclic loading, which is first stated by Nam P. Suh at M.I.T. in 1973. Three stages of delamination wear are voids nucleation on the surface, voids coalescence parallel to the surface, and detachment of plate like wear particles when the cracks reaches a critical length and breaks through the surface [44]. Fretting wear subjects to the cyclic sliding motion between two contact surfaces, materials can be removed from either one or both surfaces. Erosive wear process is extremely short comparing with the other four wear mechanisms; which is subject to impact of solid or liquid particles against the objects. The materials are removed from the surface due to the cyclic deformation [45].

Table 2.4 Wear classifications and mechanisms

CLASSIFICATION	WEAR MECHANISMS
WEAR DOMINATED BY MECHANICAL BEHAVIOR OF MATERIALS	1. ASPERITY DEFORMATION AND REMOVAL 2. WEAR CAUSED BY PLOWING 3. DELAMINATION WEAR 4. ADHESIVE WEAR 5. ABRASIVE WEAR 6. FRETTING WEAR 7. WEAR BY SOLID PARTICLE IMPINGEMENT
WEAR DOMINATED BY CHEMICAL BEHAVIOR OF MATERIALS	1. SOLUTION WEAR 2. OXIDATION WEAR 3. DIFFUSION WEAR 4. WEAR BY MELTING OF THE SURFACE LAYER 5. ADHESIVE WEAR AT HIGH TEMPERATURES

The surface roughness quantifies the surface texture. It is measured by the vertical deviation of a real surface from its ideal state. Higher surface roughness indicates larger deviations; generates higher coefficient of friction and higher wear rates; but may promote adhesion at the same time. Lower surface roughness indicates smaller deviations and lower friction coefficients. Variation of roughness alters the performance of a mechanical component, since its surface irregularities may form nucleation sites for cracks or corrosion.

The complete tribological process between two contact surfaces in relative motion is shown in Figure 2.16. The process is extremely complex since it involves simultaneously friction, wear and deformation mechanisms at different scale levels and of different types. In order to obtain a holistic understanding of the complete tribological process taking place and to understand the interactions, it is useful to analyze separately the tribological changes of four different types: the macro- and micro-scale mechanical effects, the chemical effects and the material transfer [41].

A. Bloyce summarized the poor tribological behaviour of unalloyed titanium subjected to three aspects. The first is the electron configuration, which allow the metal more reactive and confers a high friction coefficient. The second is the crystallography, since titanium has lattice parameters which allow several slip systems to operate. Lastly, the low tensile and shear strength of titanium due to bonding occurs with other materials. The fracture occurs in the titanium rather than at the junction, resulting in a relatively large amount of metal transfer and hence higher wear rates [46].

Takeda et al. performed the pin-on-disk configuration wear test to study the effect of microstructure on fretting fatigue and sliding wear of β titanium alloy, Ti-4.5Al-3V-

2Mo–2Fe. The weight of wear debris that is swept out from the specimen surface in frictional wear test of Ti–4.5Al–3V–2Mo–2Fe tends to increase with a decreasing hardness. The fretting fatigue life of Ti–4.5Al–3V–2Mo–2Fe tends to decrease with an increasing weight of wear debris that is swept out from the specimen surface in fretting fatigue test and increase in the depth of the crack growth zone caused by contact pressure. The frictional wear characteristics can be summarized as the Vickers hardness of the alloy tends to increase with an increasing annealing temperature up to an annealing temperature of 1123 K; the Vickers hardness then tends to decrease with further increasing annealing. The weight loss tends to increase in the alloy having low Vickers hardness due to the increase in the true contact surface on the boundary of sliding surface by normal load and the increase in friction coefficient with an increase in shear area temperature. The Vickers hardness of the alloy depends on the microstructure, that is, the wear characteristics of the alloy depend on volume fraction and diameter of primary α phase and β phase region and the size of acicular α phase. Takeda et al. also studied the relationship between frictional wear characteristics and fretting fatigue characteristics. Figure 2.17 shows the wear areas caused by sliding friction and fretting wear areas. The variation of wear rates between sliding wear and fretting wear are observed. However, both sliding wear rate and fretting wear rate are depending on the microstructure of heat-treated alloys [38].

A. Marsui studied the effect of the microstructure of titanium-base materials on tribological properties [47]. The dry sliding friction tests with constant normal pressure and sliding speed are performed to observe the friction surface, the cross section, and the state of wear particles. Variations of the coefficient of friction, specimen temperature,

and the displacement of the compression axis are plotted against sliding distance. Marsui observed the axis displacement is opposite to the direction of wear tracks in the case of β -type titanium alloys. The accumulated wear particles are observed on the β -type titanium alloys in micro-scale. Cross sections parallel to the sliding direction show the plastic flow of subsurface layer and wear particles accumulation layer in β -type titanium alloys. Meanwhile, severe wear with the normal pressure dependence wear rate can be established under low PV condition which indicates the poor friction and wear characteristics.

Aging treatment is performed on β -type titanium alloys to improve its friction and wear performance. Precipitation of α -phase after aging strengthening the alloy and increase its hardness. The coefficient of friction of β -type titanium alloys drops by half; black microscopic wear particles indicates observation of the mild wear. Therefore, aging treatment of β -type titanium alloys generates higher friction and wear characteristics.

S. Fayeulle et al. performed fretting wear tests to investigate the precise particle detachment process of β titanium alloy, Ti-15V-3Al-3Cr-3Sn [48]. Tests results show the friction coefficient for β -alloy is higher; the variation of the tangential load attributed to plastic deformation is increase to the peak value and decrease towards the end. Tribologically transformed structure (TSS) is introduced as the localized new structure in the superficial layer of the titanium alloys beside the debris layer, which is formed under the stress-induced transformation mechanism [49]. The structure is observed as a dark area with the maximum depth of 15 μm . Cracks are observed in β -Ti-15V-3Al-3Cr-3Sn below TTS area, cracks propagation results the decrease of elastic slope of the cycles on friction log. As cracks propagate further into the bulk, the detached of wear particles is

observed. Hardness tests proved the TTS area are much harder than the bulk alloys. Tribologically transformed structure properties depend on the properties of initial material as well as the friction and wear mechanism. Finally, the tribological behavior during fretting depends on the formation of TTS and the interface among wear debris, the TTS, and bulk alloy.

2.4 Surface treatment for β titanium alloys

2.4.1 Thermomechanical processes

2.4.1.1 Nitriding technologies

Various surface treatments include the plasma modification, ion implantation, laser modification, and PVD and CVD technologies. The primary surface treatment intends to modify the microstructure of the surface layer and retain its chemical composition by applying rapid heating and cooling rates at high temperature. The secondary surface treatment focuses on the methods of introducing a coating on the bulk material. The tertiary surface treatment considers thermochemical treatment such as nitriding, case carbonizing, and oxidizing on titanium alloys. In the meantime, combinations of various surface treatments draw engineers' attentions in past few decades [50].

According to Matychak et al. [51], kinetics of the nitrogen interacts with near β titanium alloys containing three steps. The first, nitrogen molecules are supplied to the β titanium alloys surface with mass-transfer coefficient, h by physical and chemical adsorptions, dissociations. Secondly, Nitrogen accumulated on interstitial defects in the layer of contact resulted from the chemical interaction between nitrogen and alloy. The

third, the diffusion process took place which allows the nitrogen diffuses into both α -phase and β -phase of β titanium alloys with different diffusion coefficient.

Nitriding technologies include plasma nitriding, laser nitriding, ion nitriding, salt-bath nitriding, gas nitriding, and other processes. The gas and plasma nitriding are among the most widely used thermo-chemical treatments for improving the surface properties of titanium alloys. According to Spies [52], the plasma nitriding of titanium is a state of the art. The thermo expansion coefficient of titanium nitrides is identical to titanium. Formation of the nitrided layer with various structures depends on alloy type and nitriding temperature. The ion nitriding, in general, has a faster growth rate than gas nitriding. The composition of reaction gas plays an important role on layer formation. Nitrogen-hydrogen gas mixture increases the growth rate of compound layer. The formation of the compound layer acts like a diffusion barrier for nitrogen either delays or prevents the diffusion process.

The gas nitrided surface layer formed due to thermochemical treatment consists of two zones. A diffusion zone represented by an α -solid titanium solution supersaturated with nitrogen and alloying elements; and a compound layer lying on top of the diffusion zone and consisting of TiN and Ti₂N titanium nitrides. Change of phase composition and morphology results a hardening effect in gas nitride surface layer. Laser gas nitriding by controlling the amount of nitrogen take-up by the melt pool using a CO₂ laser and incorporates a gas jet blowing nitrogen or nitrogen mixture. The corresponding microstructure after laser gas nitriding often contains TiN dendrites surrounded by nitrogen-rich α -Ti. However, formation of solidification structure may results the cracking, formation of porosity and unacceptably rough surface [46,47].

2.4.1.2 Plasma nitriding of titanium alloys

2.4.1.2.1 Nitriding temperature and time

Ion nitriding temperature influences the $\alpha + \beta$ alloys and β alloys behaviour according to their various β transus temperatures. The β transus is defined as the transition temperature from $\alpha + \beta$ to β . Different alloys have various transus temperature due to elements type and composition. Generally, nitrogen and aluminum extend α phase field whereas vanadium, molybdenum, manganese reduce α phase field. Bacci et al. studied the influence of β transus temperature on α - β titanium alloys behaviour in plasma nitriding process [53]. First of all, physicochemical characteristics of the nitrided layer rely on whether the ion-nitriding treatments are performed above or below the β transus temperature. It has been proved that large α phase crystals are shown in matrix close to nitrided layer without concerning the treatment temperature. However, equiaxed α phase crystals can be obtained underneath the continuous nitrided layer in $\alpha + \beta$ matrix when ion nitriding temperature is below β transus value. Surface layers of plasma nitrided alloys consist both the nitrided layer and the diffusion layer. Nitrided layers include TiN_x and Ti_2N . According to the Ti-N phase diagram, TiN_x has face-centered cubic crystal structure and is defined as phase δ with approximately 30-35 at% of N. Ti_2N , however, has tetragonal structure and defined as phase ϵ with approximately 33 at% of N. The existence of TiN can provide a surface with dramatically tribological properties such as low friction and high wear resistance. However, the plastic deformation of substrate material under high loading condition will result catastrophic premature failure. Therefore, a deep hardened layer is required to sustain high contact stress. [54] Underneath the nitrided layer, is the deep hardened diffusion layer; where an interstitial

solid solution of nitrogen in titanium α (h.c.p structure with 22 at% of N). Interface between the continuous nitrated layer and the metal matrix can be either planar or uneven depends on different alloy compositions. Generally, the continuous nitrated layer is small and α phase crystals are equiaxed and their size are progressively decreasing from the outer layer towards inner core. A.A. Il'in et al. [54] studied the sequence of formation of the surface layer of titanium alloys. It can be stated as following sequence: (1) the textureless δ -TiN nitride; (2) the ϵ -Ti₂N nitride; (3) the solid solution of nitrogen in α -Ti, and (4) α -Ti. With increasing in nitriding duration, nitrides δ -TiN and ϵ -Ti₂N and solid solution of nitrogen increases.

Extent of nitrogen increases the hardness of α phase crystals on the basis of the nitrogen diffusion mechanism in titanium alloys. Nitrogen diffusion coefficient vary in α titanium, β titanium, and nitrides such as phase ϵ and phase δ . Highest nitrogen diffusion coefficient is observed in titanium alloys whereas lowest nitrogen diffusion coefficient is observed in nitrides. As a result, in plasma nitriding process; the nitrogen diffusion rate in nitrides controls growth rate after a thin continuous layer is generated. Faster diffusion is achieved in metal matrix sometimes can be reached hundreds of microns toward the core. As stated before, α phase is rich in nitrogen; nitrogen is more soluble in α phase with relatively large quantity with comparison to β phase. Therefore, nitrogen tends to concentrate in α crystal increasing their hardness. Moreover, no α phase crystals can be observed in the matrix of β alloy while plasma nitriding temperature is above β transus value. Spies concluded that since the diffusion rate in titanium is limited, greater diffusion for a given nitriding time requires higher nitriding temperature [52].

2.4.1.2.2 Nitriding pressure

Chamber pressure plays an important role in ion nitriding of titanium alloys. Researchers pay attention of controlling the working gas pressure during treatment. The optimal treatment pressure is considered as the pressure with the most active gas atmosphere. Spies stated that the degree of ionization and the ion energy increases as the working pressure decreases [52]. Panaioti [55] studied that the effect of the pressure in the gas-discharge chamber on the depth of nitrogen diffusion in plain titanium, VT1-0, and titanium alloy, VT8. Various pressure ranges from 53Pa (0.4 Torr) to 266 Pa (2 Torr) at a constant temperature of 900°C and duration of 3 hours are performed. The thickness of diffusion zone is determined from the microhardness distribution over cross-section of the nitrided samples. By plotting the depth of diffusion zone over applied nitrogen pressure (Figure 2.18), it is observed that; under the study condition, both plain titanium VT1-0 and alloy VT8 obtained their peak diffusion zone when treatment pressure is 80 Pa. The depth of diffusion zone then drops substantially whether the nitrogen pressure increases or decreases. However, the optimal value of pressure is controlled by the distance between the cathode and the anode. Therefore, a relation between optimum pressure and electrodes distance can be established, as shown in Equation 1.



[Equation 1]

Where p_{opt} is the optimum pressure, d is the distance between the electrodes.

Besides, gas pressure in discharge chamber is related to power as well. Specific power of discharge is considered as an additional process factor of ion saturation. As

shown in Equation 2, U is the voltage, I is the current, S is the specimen surface area, and w_{sp} is the specific power of the discharge.



[Equation 2]

Panaioti concluded that nitrogen pressure plays an important role on the depth of diffusion zone. The optimal pressure provided thickest diffusion zone which depended on the distance between the cathode and anode. The optimal nitrogen pressure resulted most effective gas atmosphere thus corresponded to the maximum plasma energy density. The process of plasma nitriding is determined by specific power of discharge.

In the case of age hardening effects, strength deterioration both in static and cyclic occurs due to nitriding. These detrimental effects can be avoided or limited through bulk structure regeneration. Decrease of nitriding temperature to the aging temperature range in association with intensifying the nitriding process and combination of nitriding and solution treatment by means of quenching from the nitriding temperature and subsequent aging [52].

2.4.2 Other surface treatments

Surface engineering has been developed over the past decade. Traditional surface engineering methods are optimized, and modern surface engineering techniques have been commercialized. Meanwhile, hybrid surface engineering and new coating materials are highly innovated [56]. However, above mentioned are classified as the first generation of surface engineering; where the second generation of surface engineering is introduced as duplex surface engineering.

Thermally sprayed coating is built up by overlapping splits of coating materials. Spray coatings can be applied to titanium substrate through plasma spraying, detonation gun, high velocity oxyfuel and vacuum plasma spraying. Sprayed objects contain inherently wear resistance to prevent galling, and possessing a low friction coefficient and have some lubricant retention ability [46]. Applications of sprayed coatings can be found in aero-engines and other gas turbine applications for wear protection. Fretting wear occurred in low-pressure compressor can be protected as well. However, limitation is the cost. High cost of spraying process can be only applied to a localized area instead of the whole surface of large components.

Electroplating and electroless plating are applied to titanium alloys with proper pre-treatment methods. Hard chrome plating is considered as most widely used coating on titanium alloy substrate with their applications on oil seal collars, racing car fly-wheel, and bearing housing and pistons [46].

Plasma immersion ion implantation (PIII) is an advanced surface modification method that relies on plasma concepts, pulsed power techniques and materials science. In PIII, the ions to be implanted into the near surface of materials are extracted directly from the plasma in which the samples or industrial components to be processed are immersed without the need of extraction or acceleration grids.

The plasma oxynitriding treatment allows forming of three compounds (TiN, Ti₂N and TiO₂) obtained by plasma nitriding and plasma oxidizing treatment in a single technical operation with shorter treatment time.

Thermodiffusion nitriding allows engineers to improve acid and wear resistance of titanium alloys [56]. Thermodiffusion nitriding forms nitride phases (δ -TiN, and ϵ -

Ti₂N) in the surface layer; and causes basic texture α -Ti weakening. Nevertheless, both processing temperature and the saturating medium (with nitrogen addition) are concerns of operating status. High temperatures nitriding condition and pure nitrogen are required to avoid the formation of titanium oxides during the treatment. As a result, a large amount of costs will be spent on the controlling of nitrogen purification.

Surface-alloying have been conducted by depositing powders such as TiN, SiC, TiC, and TiB₂ on the titanium alloy substrate and then irradiating high-energy heat sources such as laser beam or electron beam [57-60]. Upon irradiation with laser or electron beams, ceramic powders and substrate are melted, and then ceramic/Ti surface alloyed materials can be fabricated as ceramic elements are penetrated into the substrate and re-precipitated. Particularly, the irradiation of high-energy (several mega electron volts energy range) electron beam generated from an electron beam accelerator holds several advantages: (1) a stronger interface between the melted region and the substrate exists because of melting and solidification of the substrate; (2) it has little influence on the properties of the substrate because of the short irradiation time; and (3) homogeneous heating and cooling [61,62]. Compared with the laser beam method, this method has thermal efficiency which is twice as high, produces a thicker surface-alloyed layer of several millimeters, and enables continuous process in the open air [63].

2.5 Nitriding effect on the titanium alloys

Nitrogen has a high solubility in α -Ti so it strengthens the surface layer significantly. The nitriding process leads commonly to the formation of titanium nitrides TiN_x within the matrix Ti (α)-N solid solution. Therefore, surface nitriding is one of the most effective treatments for improvement of the wear resistance of titanium alloys. It

can be undertaken in numerous processes that have been investigated for many years. The surface improvement of titanium alloys can be achieved in terms of strengthening through solid solution or microstructure changes [64]. In the process, the nitrogen is incorporated into the surface layers of the titanium base alloys at elevated temperatures and yields various combinations of improved properties. Benefits are it is possible to raise the surface hardness, wear resistance, and fatigue resistance and improve the appearance of the surface of treated parts [50]. C. Muller et al. [65] reported that the high-pressure (1500 bar) nitriding of Ti Beta-C at 500°C does not cause nitrides to form; however, the nitrogen concentration in the surface layer increases with nitriding temperature.

2.5.1 Nitriding effect on the near β Ti-10V-2Fe-3Al alloys

2.5.1.1 Microstructure after nitriding

Both gas nitriding and chemical composition influence the microstructure of titanium alloys. Increase in temperature and time increase the grain size as well. After nitriding at a temperature below their β -transus temperatures, the titanium alloys have a homogeneous microstructure; on the other hand, if the nitriding operated at a temperature above their β -transus temperatures, the microstructure changes to inhomogeneous which due to the phase transformations that occur during nitriding at increasing temperature [65].

Malinov et al. [66] studied the microstructure and microhardness of gas nitride surface layer in Ti 10V-2Fe-3Al. Near β Ti-10V-2Fe-3Al alloys are thermochemically treated in a pure nitrogen atmosphere at two different temperature, 950°C and 1050°C,

and for three different periods of time, 1h, 3h and 5h. Ti-10V-2Fe-3Al has the β transus temperature of 790-805°C; $4 \times 4 \times 1.5$ mm coupons are grounded and polished with 0.25 micrometer polishing solution. Differential scanning calorimetry (DSC) is used to heat the samples to 950°C and 1050°C, The heating rate is 50°C/min, isothermally held for 1, 3, 5 hours. Microhardness measurement using Knoop indenter with a load of 0.05 kg and 10 s; step of 20 micrometer taken from the surface to the middle of the sample; totally 100 readings for each sample.

Lakshmi et al. investigated the surface modification and characterization of Ti-Al-V alloys [67]. The effect of plasma nitriding temperature, time and atmosphere on surface hardness, depth of the diffusion layer are analyzed in details by performing the plasma nitriding tests at 800°C and 900°C for 4h, 16h and 32h. The peak surface hardness is 19.65 GPa after nitriding at 900°C for 4 hours. Three layers consisting compound layer, diffusion layer, and core are observed in the microstructure. After 900°C treatment, there is a clear boundary between compound layer and diffusion layer and the grain growth existed. Other than TiN and Ti₂N, TiN_{0.26} is detected for all nitride samples at 800 and 900°C and the formation of the phase depends on treatment time and temperature. Besides, the addition of a small amount of H₂ in the gas mixture can improve the surface hardness by 50 H_v than with pure nitrogen have been elucidated. Meanwhile, both surface hardness and case depth are depending on the temperature and nitriding time. Increase in hardness due to solid solution strengthening in transformed β can be obtained at a temperature above β -transus temperature. Moreover, addition of α -stabilizer Aluminum to the alloy may increase the depth of diffusion zone underneath the compound layer.

Figure 2.19 & Figure 2.20 show the microstructure of Ti-10V-2Fe-3Al alloy before and after nitriding at 900°C for 4 hours.

The creation of nitrated layers during gas nitriding of titanium alloys takes place through a complicated diffusion process. When the samples are in an active nitrogen atmosphere at high temperature, the nitrogen absorbed at the surface diffuses inwards and the material forms different nitrogen compounds. As a result of interaction with nitrogen, a nitrated layer is formed that consists of a compound layer on the surface of the material, which is mainly composed of the titanium nitrides Ti_2N and TiN in the general case, followed by a diffusion zone composed of an interstitial solution of nitrogen in the hcp α -Ti phase. The color of the compound layer is different after the experiments. The color of the sample surface is grey for Ti-10V-2Fe-3Al samples after 1 h of gas nitriding at both temperatures. It becomes red for the samples that gas nitrated for 3h and 5h for both alloys at both temperatures. The red color indicates the simultaneous formation of titanium nitrides. The color depends on the process parameters and the appearance of the new phases.

The compound layer for most of the samples is continuous, and its thickness for the samples nitrated at 950°C and 1050°C for 3h and 5h varies between 5 and 10 μm . Below the compound layer is the diffusion zone. The microstructure of all samples nitrated at 750°C (Figure 2.21) is homogeneous due to the fact that this temperature is below the β transus temperature for this alloy. Similar results are obtained for the other three alloys studied. The samples nitride at 850°C, 950°C and 1050°C had inhomogeneous microstructure. These temperatures are all above the β transus temperature of Ti-10V-2Fe-3Al. The microstructure of the samples nitride at 950°C for

1h, 3h and 5h is given in. The microstructure observed after nitriding at 950°C is similar to the microstructure of the samples nitrided at 850°C and 1050°C.

Figure 2.22 shows the microstructure of Ti 10V-2Fe-3Al after gas nitriding at 950°C and 1050°C for 1h, 3h, and 5h. Three zones formed during nitriding: compound layer, diffusion zone and substrate. There is a clear boundary between the compound layer and the diffusion zone for most of the samples. The compound layer covers the entire sample surface. It is very hard, thin, and brittle. Increases in time and temperature result in an increase in the thickness of the compound layer. For all samples nitrided at a higher temperature than the β transus, the diffusion layer consists of two sublayers. The first one is immediately below the compound layer, which is a continuous α solid solution enriched with nitrogen. There might also be some precipitates of titanium nitrides. In most cases, it is a uniform white layer formed during the process of gas nitriding and further cooling. The solubility of nitrogen in α -Ti is very high according to the Ti-N phase diagram (Figure 2.23). The thickness of this layer can increase with an increase in the duration of nitriding. The second layer, below the first one and above the inner, unaffected substrate, is composed of white, coarse, column-like grains and a finer structure, the latter with the same appearance as the substrate layer. These coarse grains have grown in the depth direction, albeit they are usually inclined, and in some places they grow along the grain boundaries in the substrate. The solubility of nitrogen is much lower in the β than in α phase.

Muller et al. [65] indicated the increase of nitriding time increases the maximum depth of needles found. Surface hardness is measured to be 1000 Hv, 0.005kg which is

significantly lower than the reported value of 1450-1500 HV, 0.05 kg for Ti_2N . Therefore, the acicular features near the surface are found to be α -laths which form in the β grains owing to the α -stabilizing effect of nitrogen, which locally raises the β -transus.

2.5.1.2 Mechanical properties after nitriding

2.5.1.2.1 Tensile properties

W. Chen et al. reported the hardness gradually decreased with aging time in both prestrained and unstrained β -ST Ti-10V-2Fe-3Al samples. It is found lower in the prestrained samples compared to those unstrained samples under the same aging treatments. It is also observed that the yield strength of prestrained samples decreased by about 60 MPa than that of the samples without prestrain at the same aging treatments. In addition, the yield strength of both kinds of samples gradually decreased with aging time. However, the elongation of fracture increased with aging time in both kinds of samples, but it is dramatically improved by about 200% in the prestrained samples compared with the unstrained samples at the same aging treatment. Meanwhile, the ductility improvement effect induced by prestrain can be obviously observed [25].

Muller et al. [65] reported the effect of nitrogen in β alloys is presumably similar to the solid solution strengthening effect of oxygen; under the solution treated condition, nitriding process result an increase in strength and a decrease in ductility. Moreover, the nitrided layer does not change the tensile behaviour of unnotched specimens dramatically; but increases the notched strength significantly for both unaged and aged nitrided specimens, because the proportional limit depends sensitively on material

properties at the notch root [68]. A lower ductility is found in as-SHT material while a severe deterioration is found in aged material.

2.5.1.2.2 Fracture toughness

The fracture behavior in Ti-10V-2Fe-3Al is studied by W. Chen et al. using SEM to examine fracture surfaces after tension. In the prestrained sample aged for 0.5h, the fracture surface consisted of transgranular fracture and tear ridges. As the aging time increased to 8h, only the ductile transgranular fracture feature of tear ridges are observed. This indicated the occurrence of obvious plastic deformation at the tip of cracks in the stage of crack initiation and propagation. The fracture surfaces of the unstrained and 0.5h aged sample mainly exhibited an intergranular fracture mode. Cracks initiated predominantly along grain boundaries, and some transgranular fracture linking the grain boundary cracks took place. On close examination, some microdimples are observed on the transgranular fracture surfaces which indicated microplasticity. When aging time increased to 8h, transgranular fracture increased, and the dimple size became larger and deeper, which are correlated with enhanced ductility [25].

2.5.1.2.3 Hardness

The microhardness and the thickness of the nitrided layers increase with the time prolongation for most of the cases. The thickness of the nitride layers for this alloy varies between 25 μm and 200 μm . With an increase in temperature from 950°C to 1050°C and an increase in time from 1h to 5h, the thickness of the nitrided layers increases. This is because the diffusion coefficient increases with an increase in temperature. The hardness values are very high in the surface layers, and they decrease through the diffusion zones

to approach the basic microhardness of the matrix in the unsaturated core. There is a tendency for microhardness values to increase with the duration and temperature of nitriding for Ti-10V-2Fe-3Al alloy. The increase in microhardness values after nitriding at higher temperatures is due to an increase in the diffusion coefficient [66].

Surface gas nitriding increases the hardness of titanium alloys tremendously. Figure 2.24 shows the microhardness profile of Ti-10V-2Fe-3Al alloy after gas nitriding at (a) 750°C and (b) 850°C. The hardness increases while increasing of nitriding time and temperature. Nevertheless, wear properties of titanium alloys are not related with the surface hardness, which is not improved significantly. The microhardness profiles on titanium alloys after nitriding, prepared on tapered cross sections of the nitride samples, give the information on both the microhardness behavior of the materials and the thickness of the nitrided layers. The increase in surface hardness resulted from the existence of TiN and Ti₂O; which are new phases created during the nitriding process. Nitriding at a temperature below the β transus for titanium alloys is strongly recommended for engineering applications [66].

2.5.1.3 Fatigue

In titanium alloys, although the fatigue limits are slightly improved by nitriding, the overall fatigue strength is reduced compared with the corresponding annealed specimens. In Ti-15Mo-5Zr-3Al alloys, premature crack initiation occurred at a relatively large size in the nitrided specimens; that is, the initiation resistance is significantly decreased by nitriding. The role of the nitrided layer on fatigue behavior depended on the strength of the materials. The improvement in fatigue strength by nitriding is attributed to the enhanced crack initiation resistance if the strength is low, as in pure titanium, while

the reduction in fatigue strength is primarily due to premature crack initiation if the strength is high, as in Ti-15Mo-5Zr-3Al alloys. Overall, the fatigue strength is increased by nitriding for pure titanium alloys, while in the Ti-6Al-4V and Ti-15Mo-5Zr-3Al alloys, the overall fatigue strength tended to be reduced by nitriding. [69]

The Ti-10V-2Fe-3Al has higher fracture toughness K_{IC} compare with the other high strength titanium alloys. The surface roughness and the residual compressive stress caused by shot peening and the effect of shot peening on tension-tension fatigue property of Ti-10V-2Fe-3Al titanium alloy is investigated by Y.K. Gao. The residual compressive stress in the surface layer induced by shot peening is the main factor which can increase the fatigue life and fatigue limit, but the surface roughness also affects the fatigue life. From the experiment, specimens peened preliminarily by cast iron shot and following by glass shot have the longest fatigue life under the same stress level (520 MPa). The fracture surfaces of the specimens had shown the fatigue cracks initiate in surface for all type of specimens. Gao summarized that the fatigue limit at 1×10^7 cycles can be increased by about 27% and 29% by shot peening for Ti-10V-2Fe-3Al titanium alloy; the fatigue properties are sensitive to surface roughness and residual stress and by employing surface modification processes such as shot peening can change the surface integrity of parts to improve the fatigue performance [39].

Muller et al. [65] studied the nitriding effects on fatigue behavior of Ti-3Al-8V-6Cr-4Mo-4Zr (Beta-C) alloy. Fatigue limit in solution heat treated material do not show sufficient changes after gas nitriding with 1500 bar nitrogen pressure at high temperature in a hot isostatic press. The endurance limit increases with strength level, suggesting that the endurance limit is controlled by crack nucleation. However, the poor low cycle

fatigue behaviour of nitrided material can be observed at higher stresses; and more rapid fatigue crack propagation result low ductility which is responsible for the poorer low cycle fatigue behaviour of the nitrided material [70]. Early crack nucleation is thus favored in material with a surface nitride layer, and rapid crack propagation is favored in material whose ductility is reduced. Overall, the material nitrided and aged has the poorest notched fatigue behaviour and worse fatigue resistance. This can be explained by the addition of nitrogen is responsible for an embrittling effect in the near-surface region.

2.5.1.4 Wear and friction

Unlubricated wear tests using pin-on-disk (stainless steel) configuration is performed on near β alloy Beta-C (Ti-3Al-8V-6Cr-4Zr-4Mo) by Ekvall et al. [71] to study tribological behaviour of sliding contact surface. Coefficient of friction is around 0.3 for untreated alloy for 10N loads applied. Nitriding effect allows the coefficient of friction drops to 0.2; as long as the coating can resist the applied load. However, same degree of friction as untreated alloy is resulted from the coating spalling off while the 30N load applied and after long sliding distances. Rolinski et al. [72] focused on the direct-current glow discharge plasma nitriding generated nitrided layers on titanium and its two-phase $\alpha + \beta$ alloys. The compound layer produced by plasma nitriding method have a higher surface hardness, better tribological properties as well as higher abrasion wear resistance compared to the layers produced by gas nitriding method. The reason Rolinski elucidated is there is less extent interaction between traces of carbon compounds and oxygen compounds and titanium in ionized gas condition, rather than in a thermally excited gas.

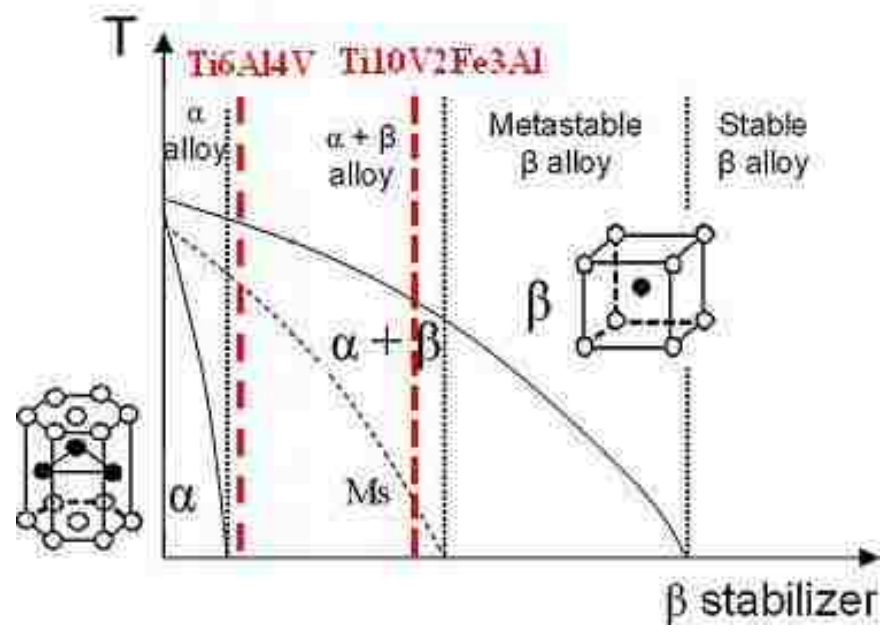


Figure 2.1 β isomorphous phase diagram of titanium alloys

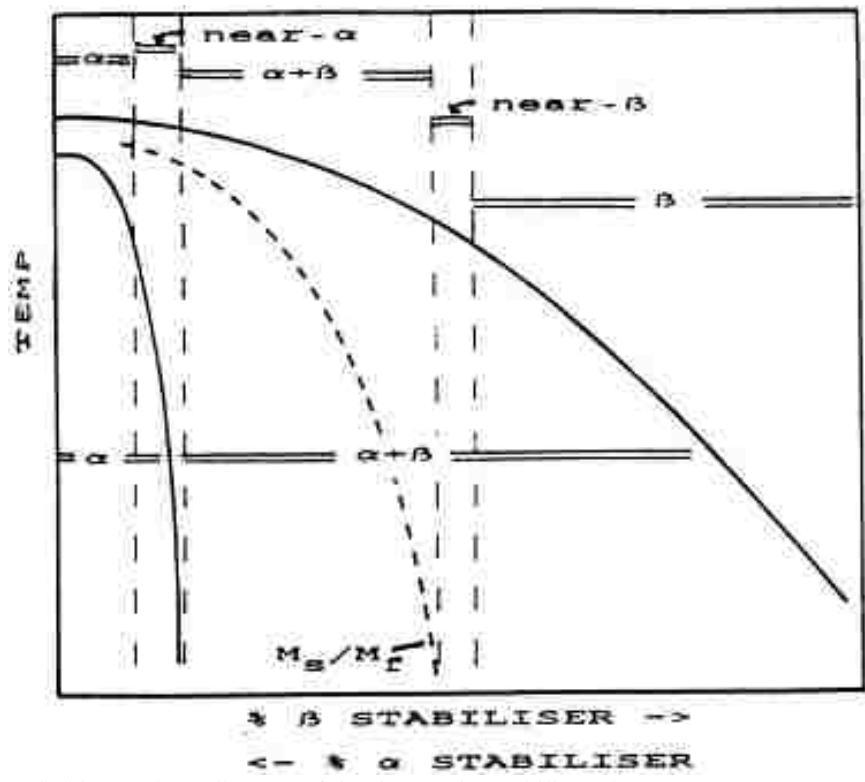


Figure 2.2 Pseudo-binary phase diagram of titanium and α stabilizer element

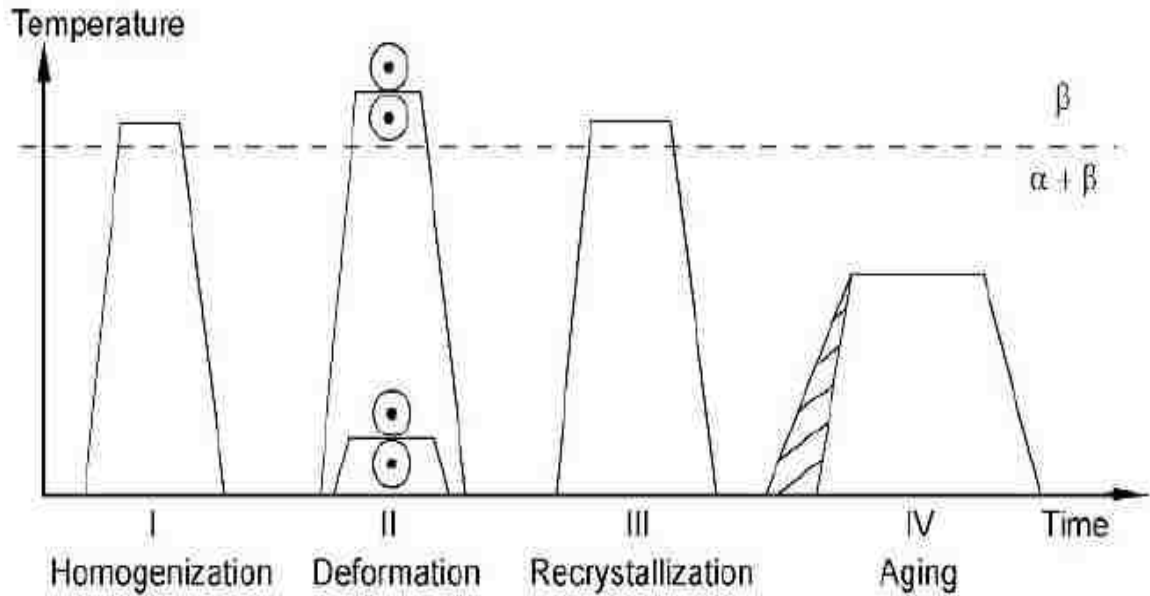


Figure 2.3 Processing route for β annealed microstructure of heavily stabilized β titanium alloys

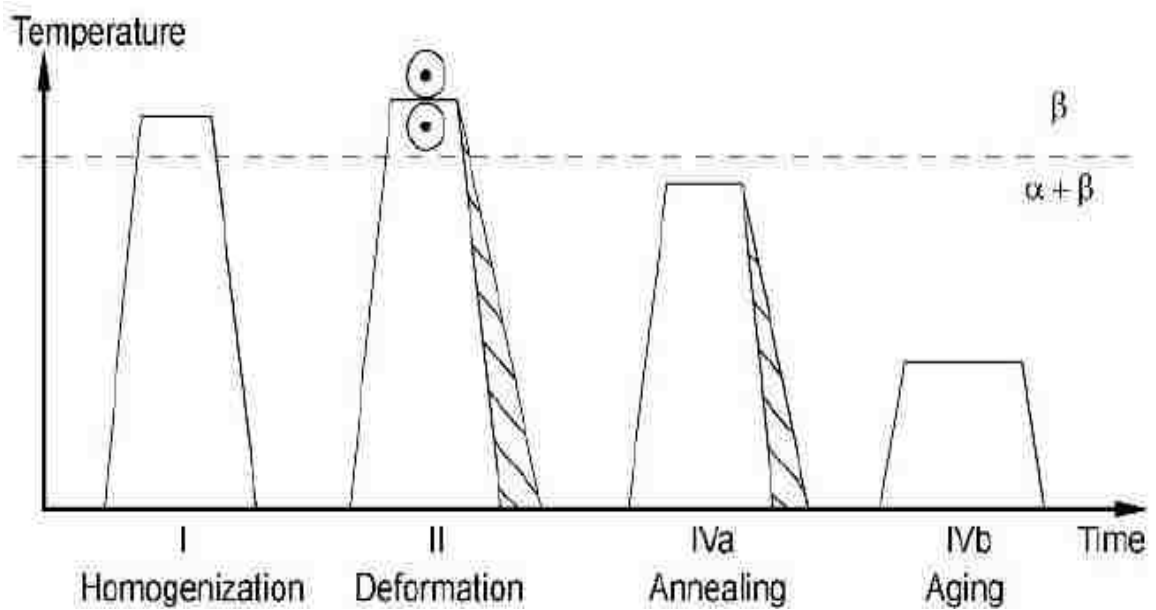


Figure 2.4 Processing route for β processed microstructures of β titanium alloys (schematically)

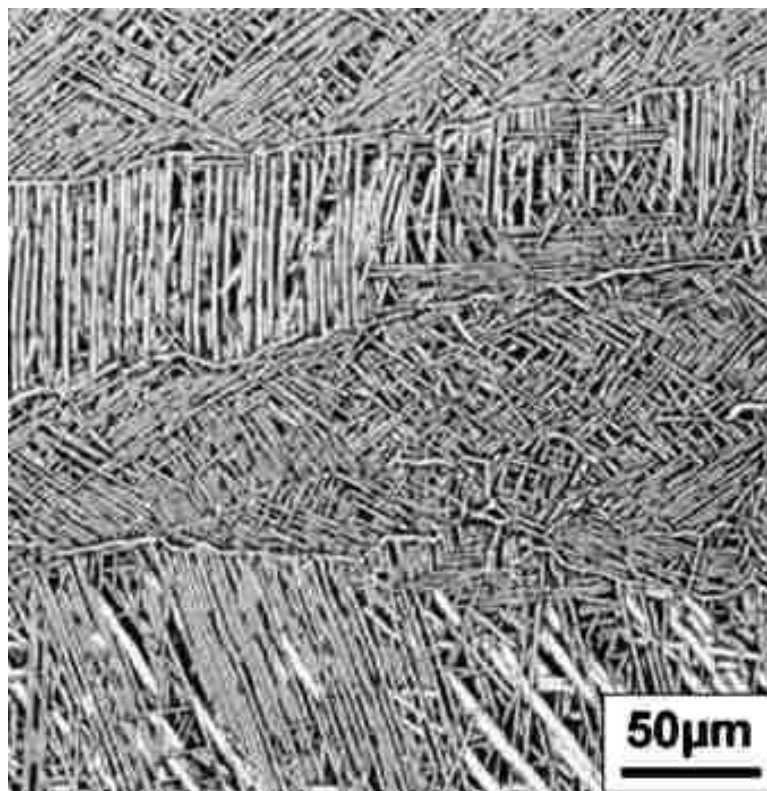


Figure 2.5 Ti-6264 microstructure showing the α layers along the β grain boundaries are partially discontinuous.

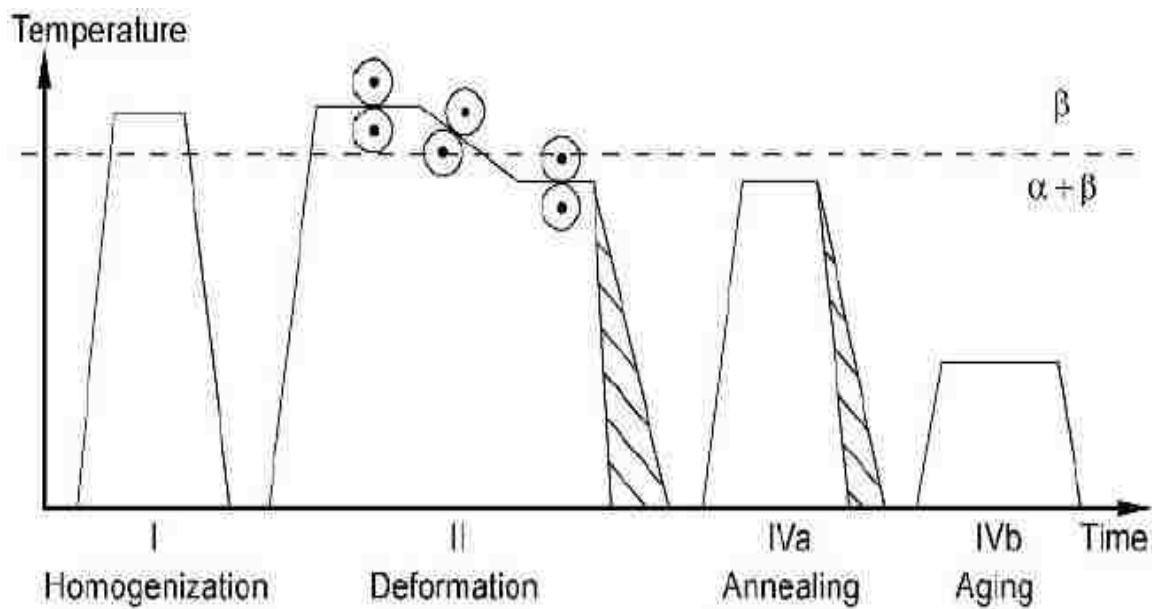


Figure 2.6 Processing route for through-transus processed microstructures of β titanium alloys

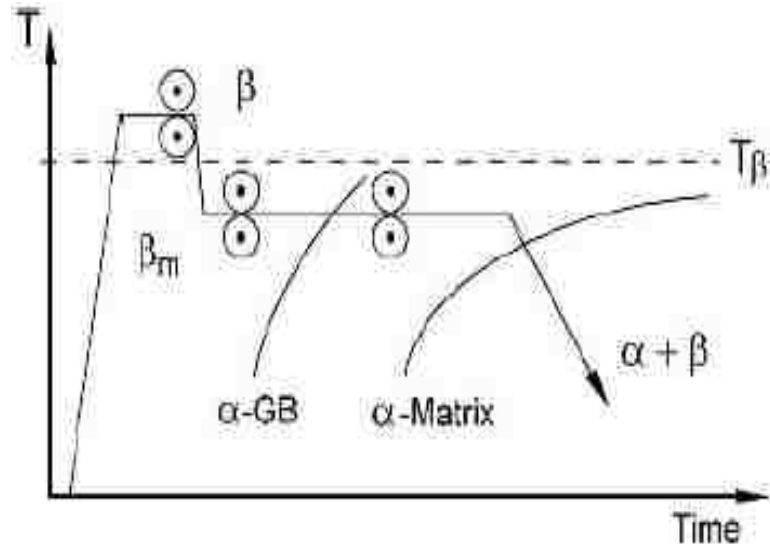


Figure 2.7 Time/temperature control of through-transus deformation (schematically)

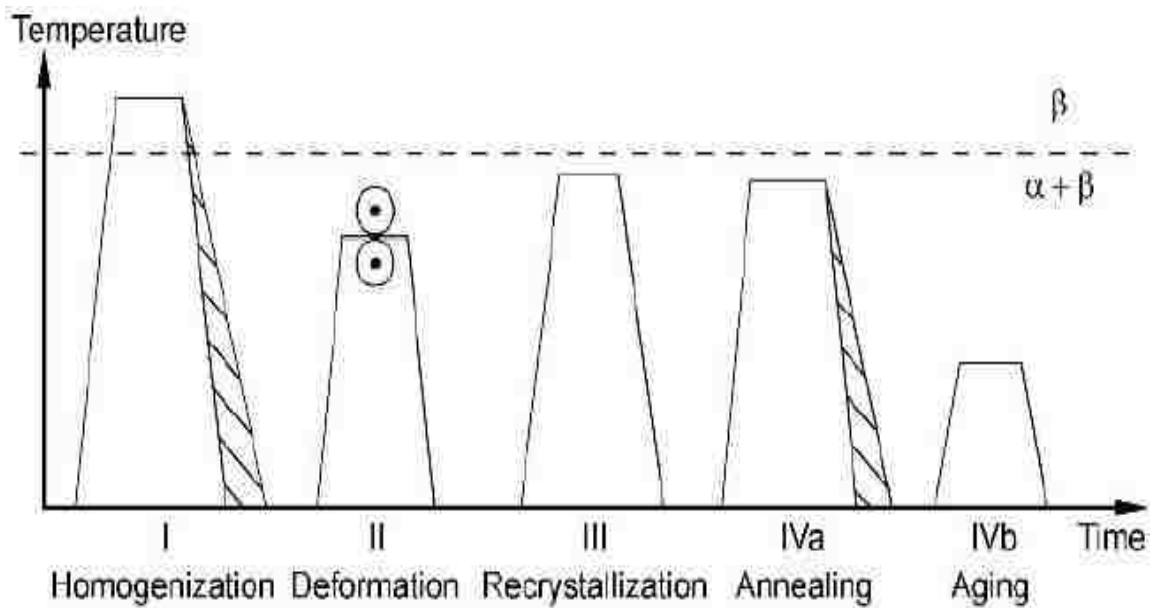


Figure 2.8 Processing route for bi-modal microstructures of β titanium alloys (schematically)

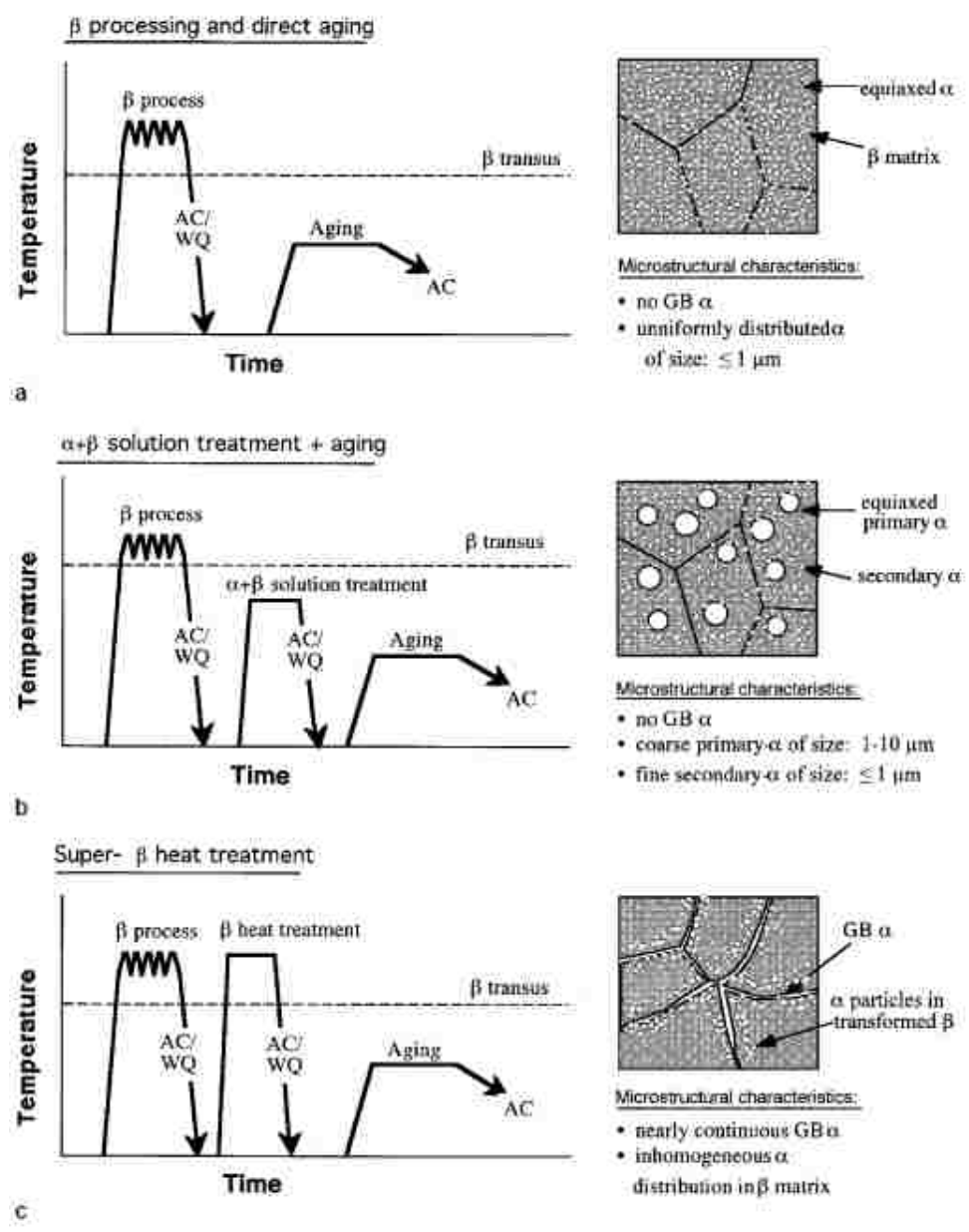


Figure 2.9 Processing, heat treatment, and microstructure of β -titanium alloys in (a) class A, (b) class B, and (c) class C.

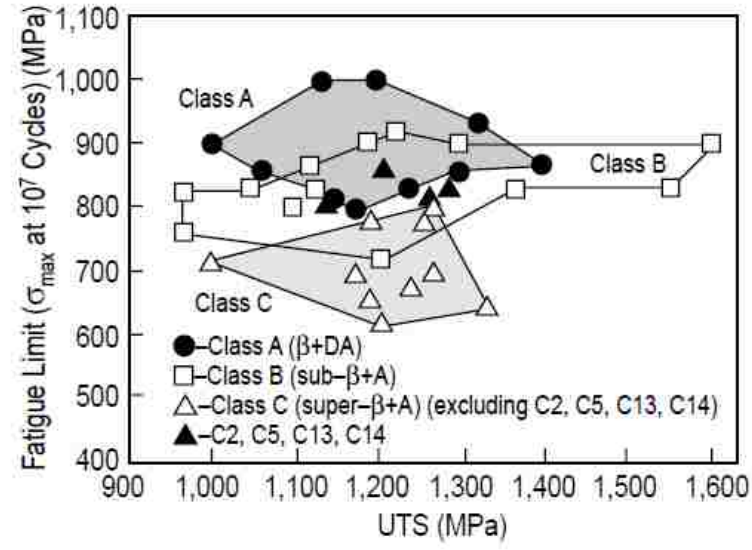


Figure 2.10 The classification of the fatigue behaviour of β -titanium alloys.

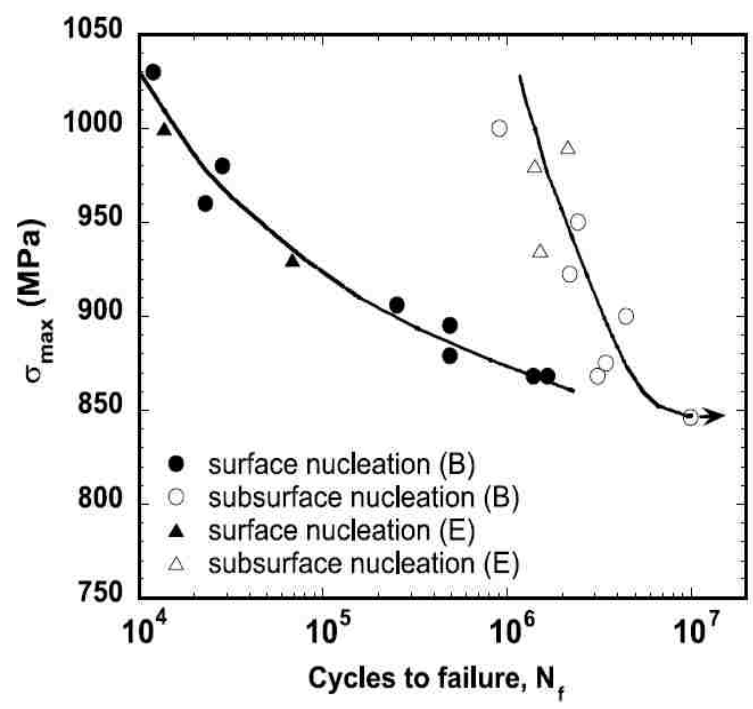


Figure 2.11 The dual S-N fatigue behavior in low volume fraction α_p microstructure

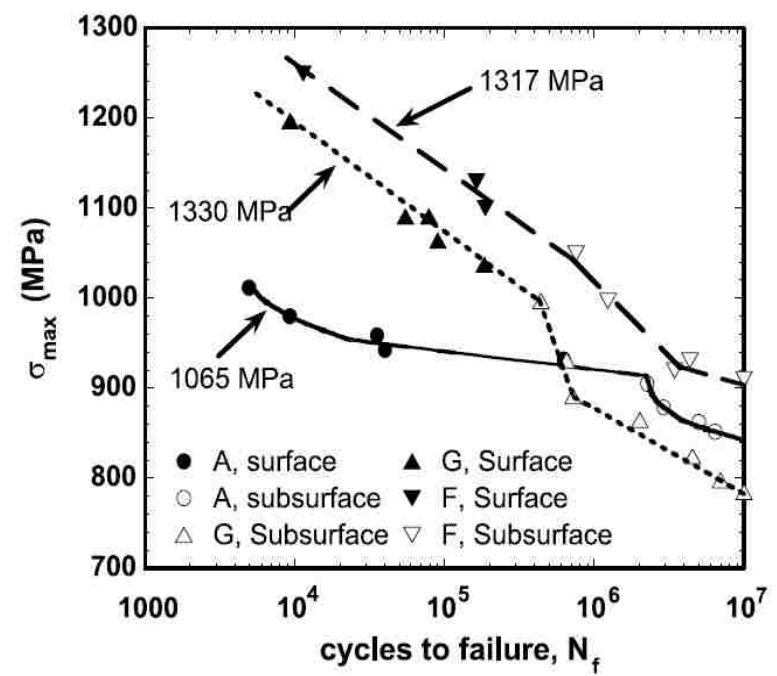


Figure 2.12 The two-stage S-N fatigue behavior in high volume fraction α_p microstructure

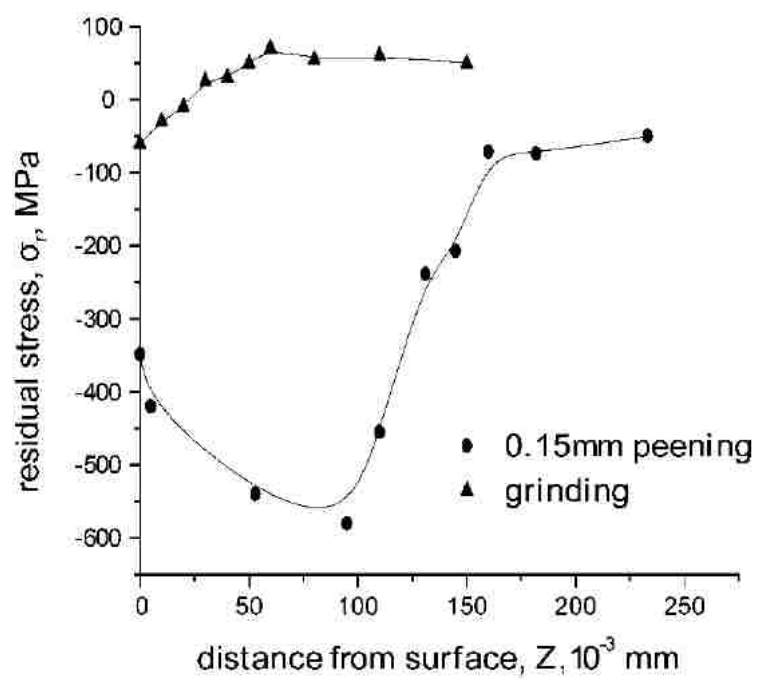


Figure 2.13 Residual stress field in Ti-10V-2Fe-3Al alloy

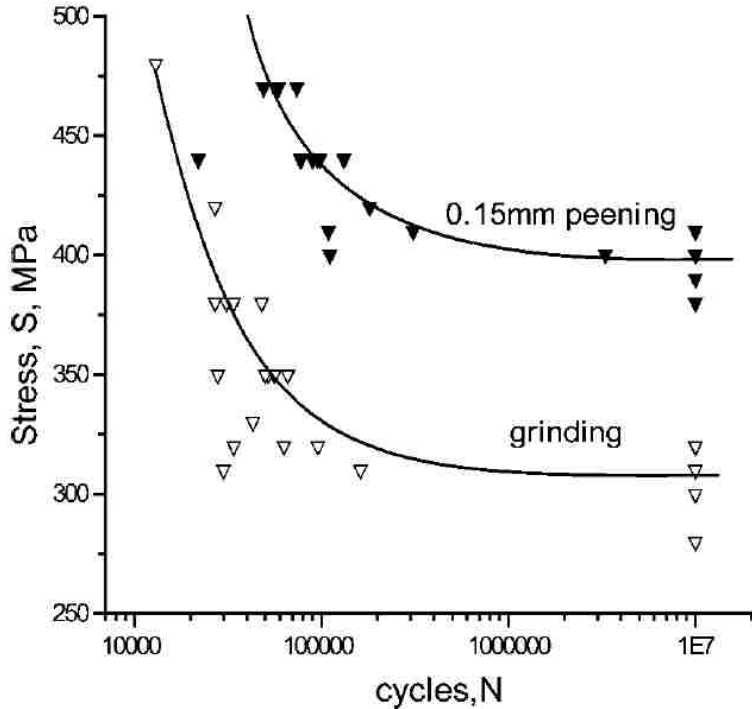


Figure 2.14 S-N curves for ground and shot peened Ti-10V-2Fe-3Al

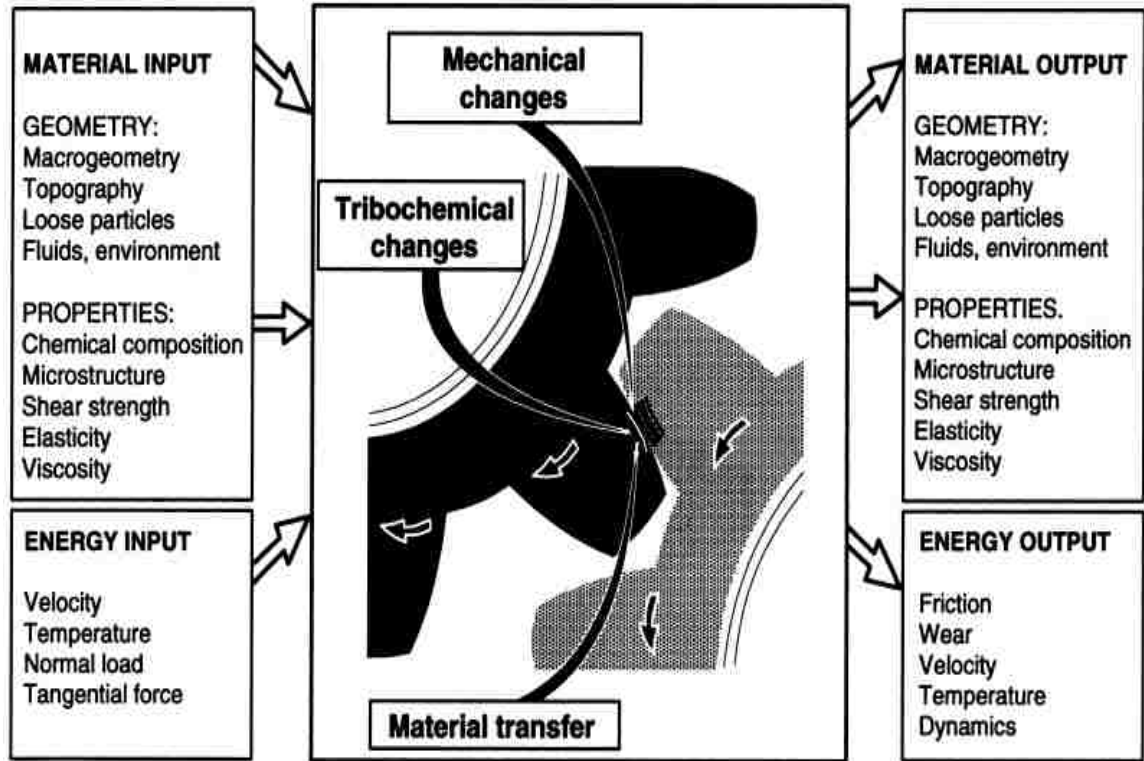


Figure 2.15 The tribological process in a contact between two surfaces includes mechanical and tribochemical changes as well as material transfer

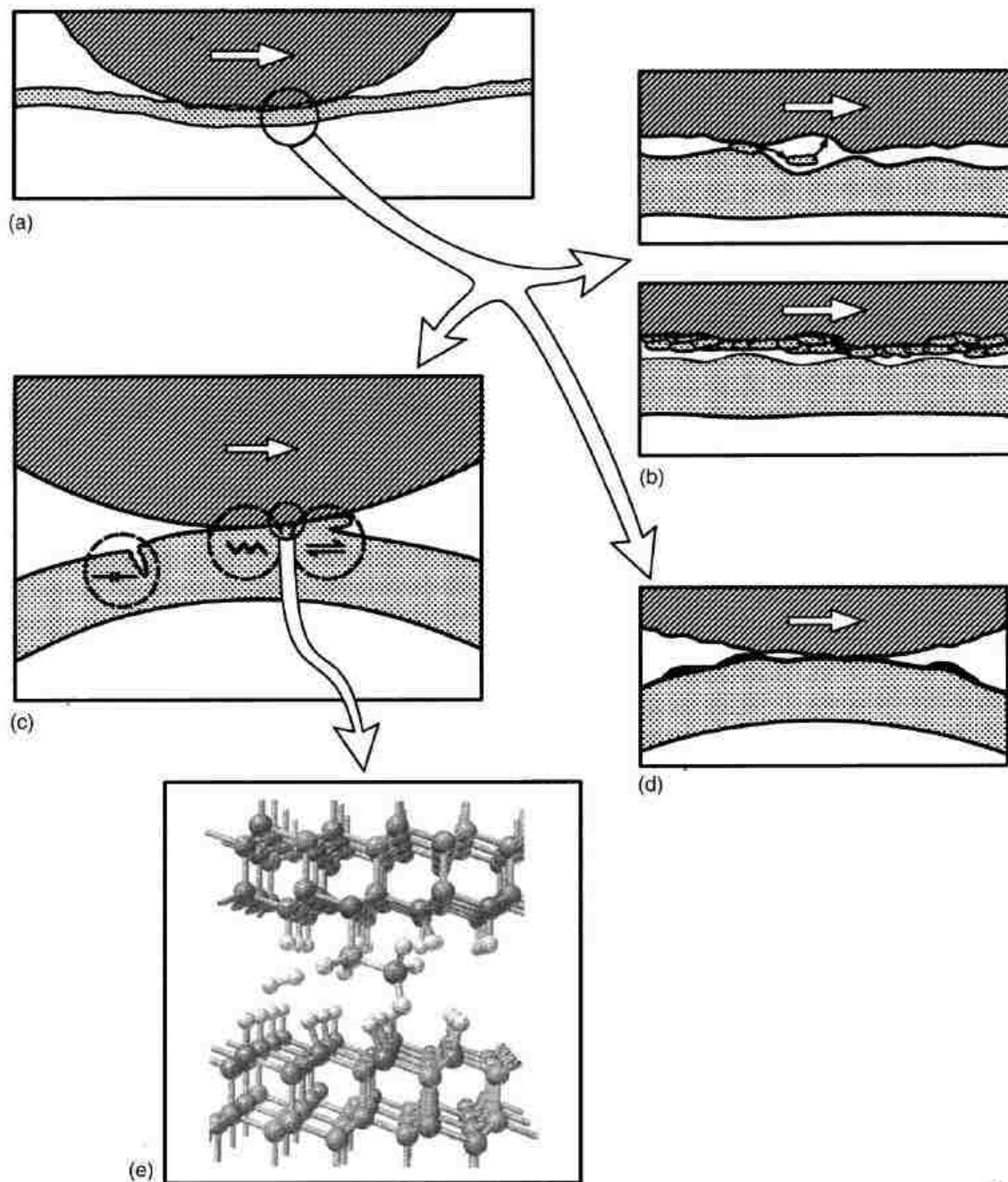


Figure 2.16 Tribological contact mechanisms: (a) macromechanical, (b) material transfer, (c) micromechanical, (d) tribochemical, and (e) nanomechanical contact

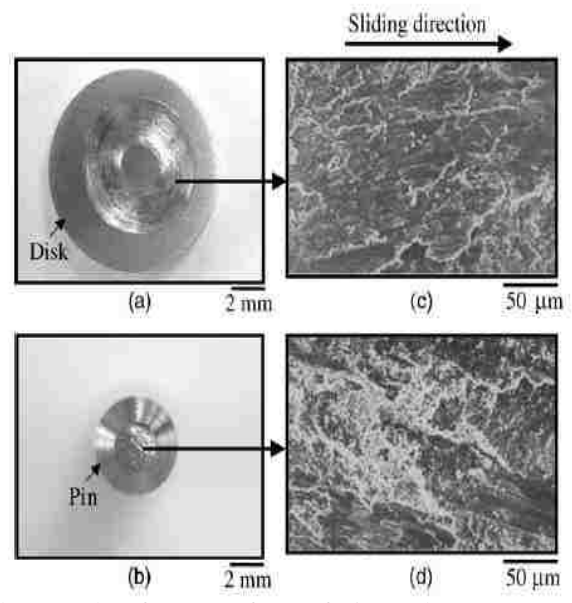


Figure 2.17 Typical light photographs of wear surfaces of Ti-4.5Al-3V-2Mo-2Fe alloy (a) disk and (b) pin, and SEM micrographs of wear surfaces of (c) disk and (d) pin of Ti-4.5Al-3V-2Mo-2Fe annealed at 1083K.

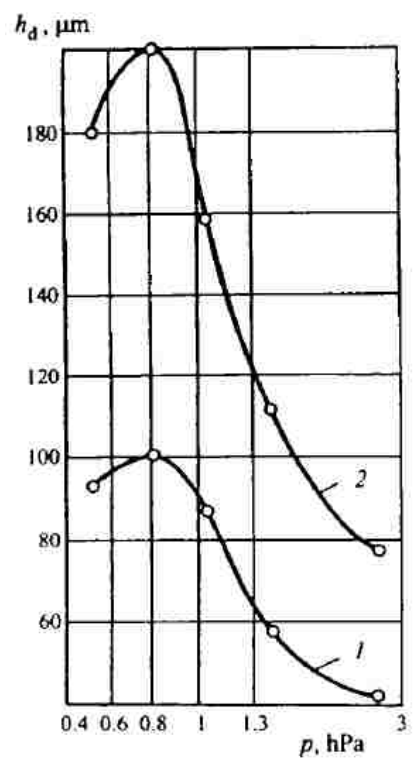


Figure 2.18 Dependence of the thickness of the diffusion zone h_d after ion nitriding of titanium VT10 (1) and alloy VT8 (2) at 900°C for 3 h on the nitrogen pressure p .

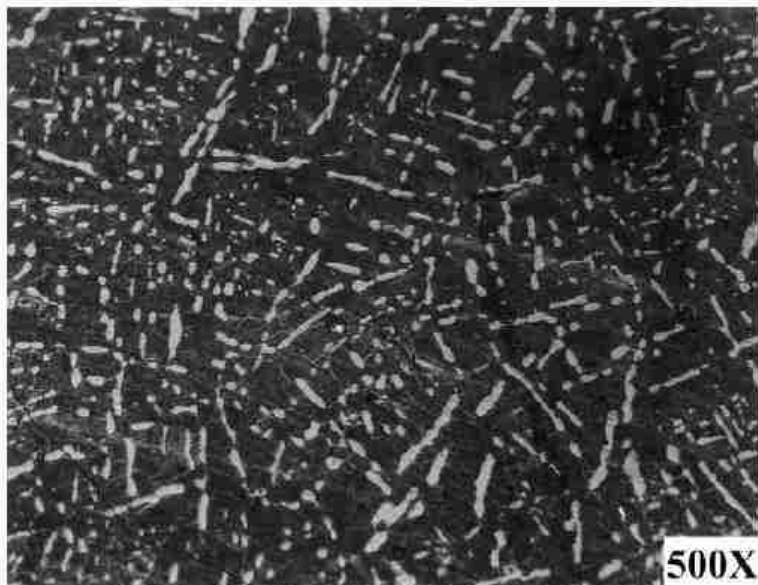


Figure 2.19 Microstructure of Ti-10V-2Fe-3Al alloy before nitriding

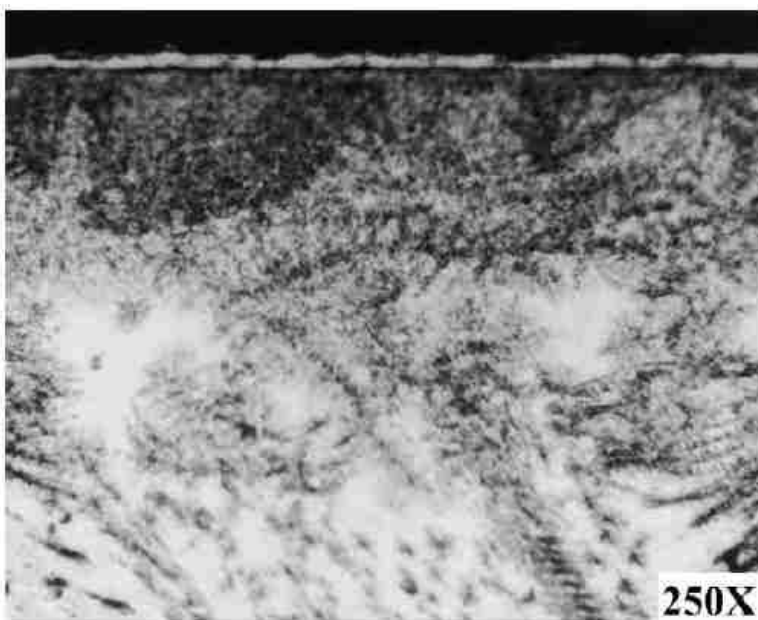


Figure 2.20 Microstructure of Ti-10V-2Fe-3Al alloy after nitriding at 900°C for 4 hours

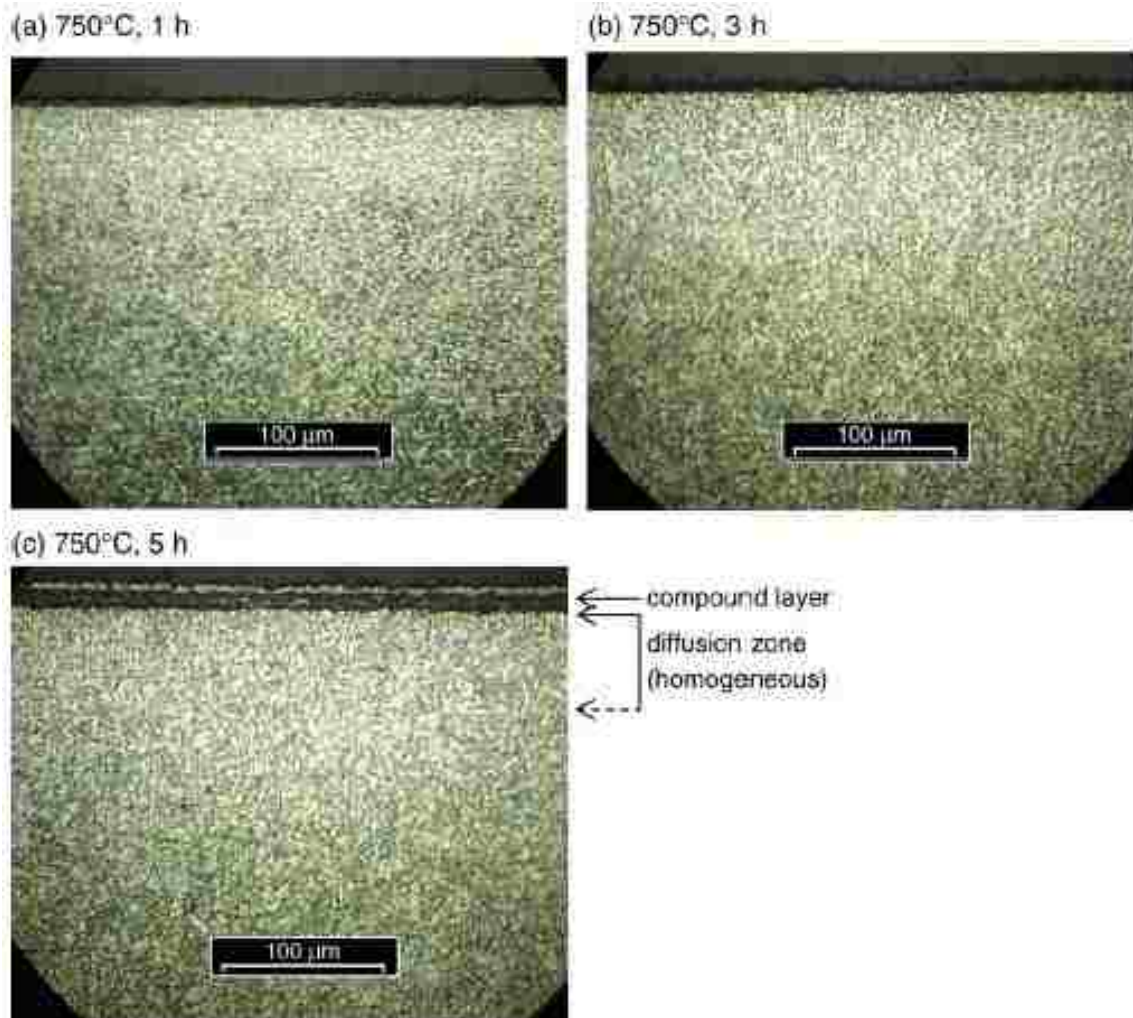


Figure 2.21 Microstructure of the cross-section of Ti-10V-2Fe-3Al alloy after gas nitriding at 750°C for 1h, 3h, and 5 h.

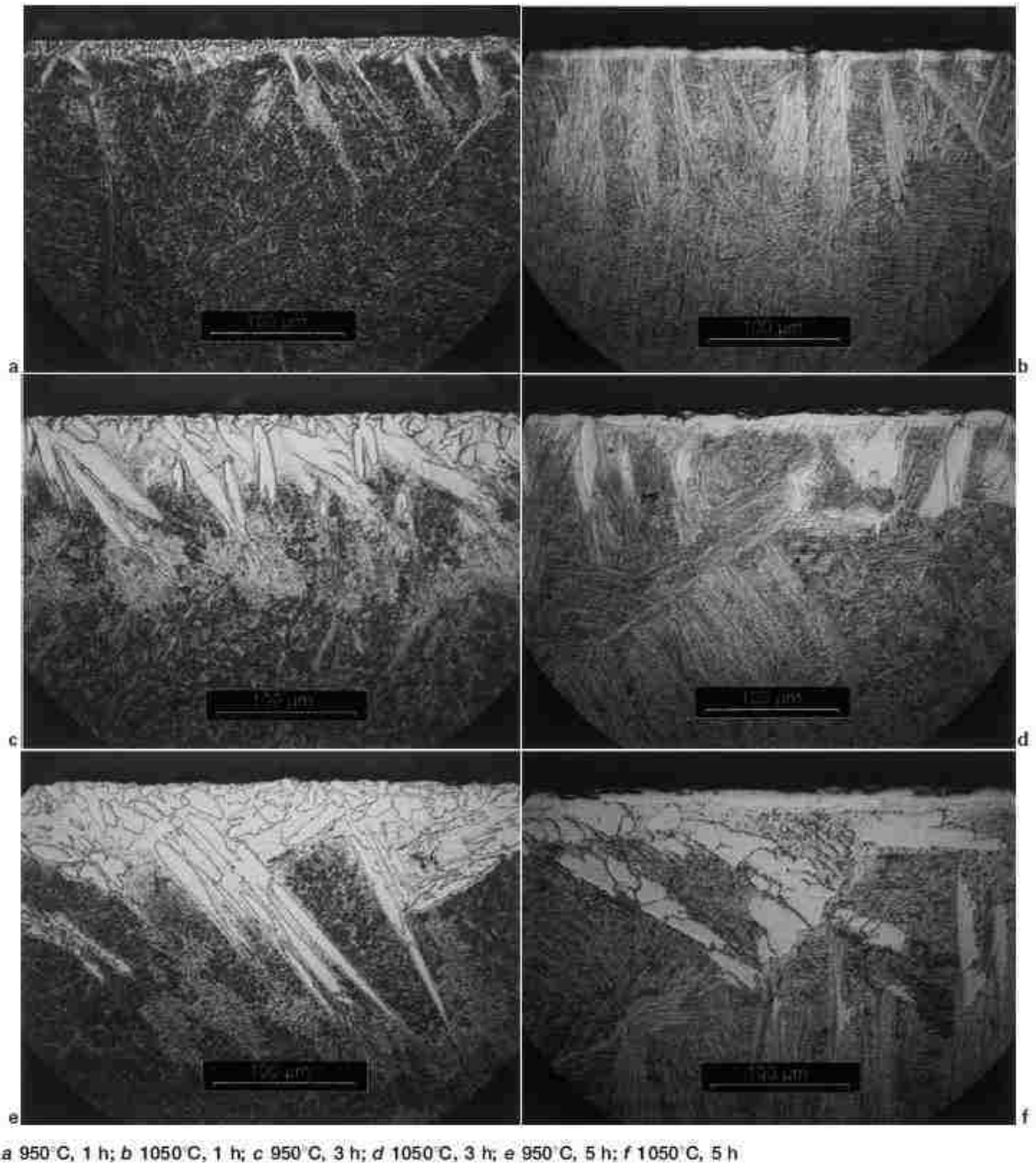


Figure 2.22 Microstructure of Ti 10V-2Fe-3Al after gas nitriding at 950°C and 1050°C for 1, 3, and 5h.

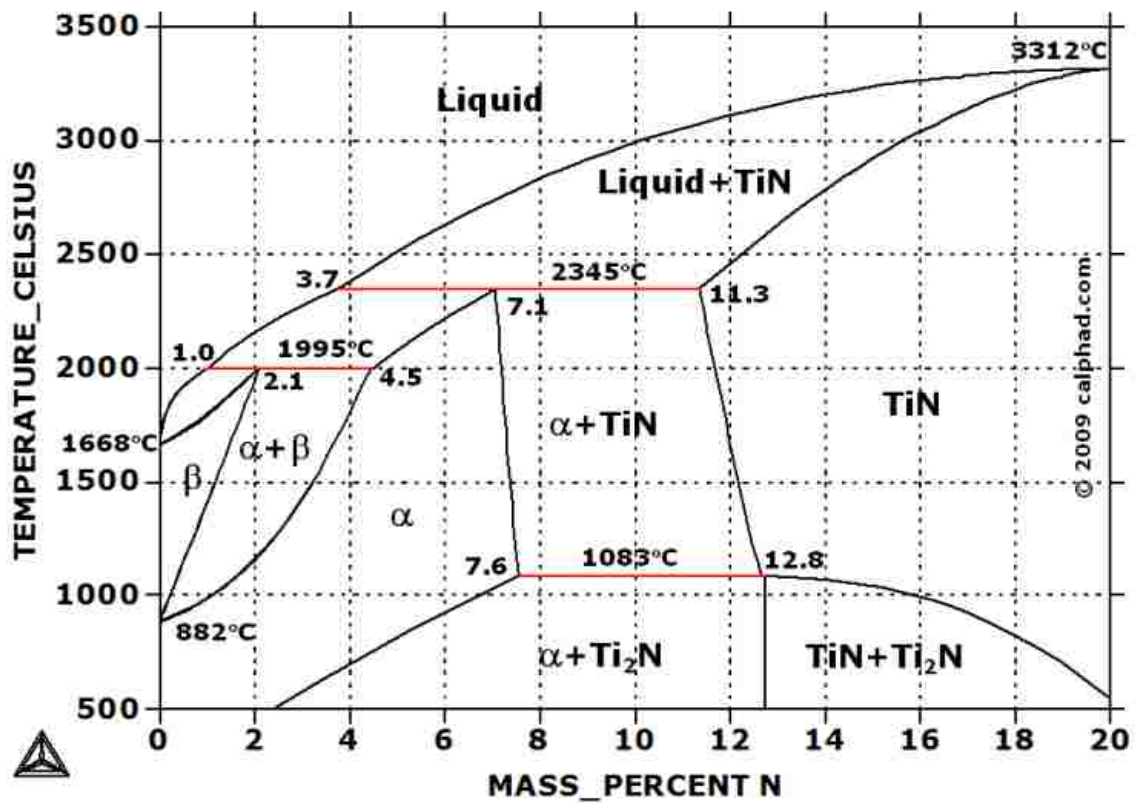


Figure 2.23 Ti-N phase diagram.

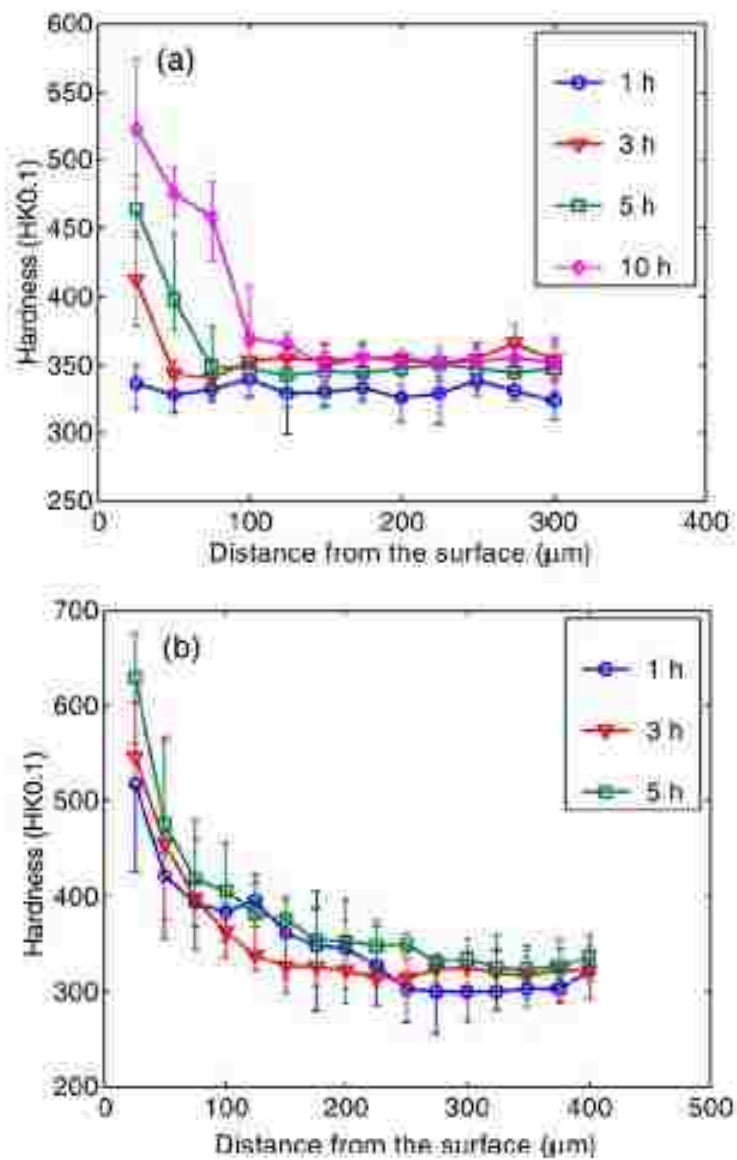


Figure 2.24 Microhardness profile of Ti 10-2-3 alloy after gas nitriding at (a) 750°C and (b) 850°C.

CHAPTER 3

MATERIALS AND EXPERIMENTAL METHODS

3.1 Overview

In this chapter, the mechanical properties, fatigue properties and wear behaviours of near β Ti-10V-2Fe-3Al alloy are studied. Tensile tests are performed using an MTS Criterion Model 43 tensile test machine. Fatigue tests are carried out using an R.R. Moore type reverse bending cyclic fatigue machine. All the wear tests are done using a CETR UMT multi-specimen test system with a ball-on-disc test apparatus. Materials investigations consisted of sample metallographic preparation and as-received material characterization. The experimental methods involved ion nitriding treatments and the characterization of the nitrided alloy, including microstructure observation, surface roughness measurements and micro-indentation hardness measurements.

To study the tensile and fatigue properties, fractured samples are observed under SEM. To evaluate the tribological behaviour, wear track width and depth are measured using a Veeco optical profiler (WYKO). Wear tracks and wear debris are observed under SEM. Along with the SEM examination, the chemical composition at specific locations on wear tracks and wear debris is determined by energy dispersive spectroscopy (EDS). Meanwhile, Ti-10V-2Fe-3Al samples are ion nitrided in collaborator sites to develop optimum surface treatment conditions for Ti-10V-2Fe-3Al to enhance its wear properties and maintain its fatigue properties. After each treatment trial, screening tests such as optical profiling, Vickers micro-indentation hardness testing, scanning electron microscopy (SEM) and micro-scratch testing are applied to characterize the nitrided samples. The effect of nitriding parameters (temperature, time, pressure and pre-

treatment measures) on the surface morphology and cross-sectional microstructure of Ti-10V-2Fe-3Al are summarized. Finally, the optimized nitriding condition is achieved among a series of nitriding treatments.

3.2 Materials

The Ti-10V-2Fe-3Al alloy used in this research is purchased from the Nanjing Shuangsheng Trade Company in China. Four hot-rolled bars with a diameter of 20 mm and a length of 100 cm are received. The bars are segmented into a disc shape with a diameter of 20 mm and thickness of 3 mm using a wire EDM machine (Charmilles Robofil 240 SL). The segmentation process is processed at a low temperature to avoid microstructural change due to elevating temperature during wire cutting.

The chemical composition of the as-received alloy is measured using an inductively coupled plasma optical emission spectrometer (ICP-OES) (Thermo Jarrell Ash IRIS Advantage spectrometer), which is shown in Figure 3.1. The chemical composition (wt%) of the Ti-10V-2Fe-3Al is given in Table 3.1.

Table 3.1 Chemical analysis of Ti-10V-2Fe-3Al alloy

ELEMENT (WT %)	V	FE	AL	Ti
COMPOSITION	10.65	1.73	2.99	BALANCE

3.3 Ion nitriding of Ti-10V-2Fe-3Al

3.3.1 Sample preparation

Ti-10V-2Fe-3Al samples are prepared with dimensions of 20 mm in diameter and 3 mm in thickness and are schematically presented in Figure 3.2. Subsequently, Ti-10V-2Fe-3Al samples are ground and polished following the metallographic preparation steps for titanium alloys. According to the Buehler standard of the β titanium alloy UNS R54610 Ti-10V-2Fe-3Al (Table 3.2), silicon carbide papers (CarbiMet 2 abrasive disk)

with a grit size from P400 to P1500 are used during the grinding procedure. The samples are polished to a surface finish of 0.5 μm and cleaned in an ultrasonic ethanol bath prior to storage. The cleaned samples are then carefully packed into Petri dishes and stored in the desiccators to minimize the oxidation of the polished samples.

Table 3.2 List of metallographic preparation parameters of Ti-10V-2Fe-3Al coupons [73]

SURFACE	ABRASIVE/SIZE	LOAD LB. (N)/SPECIMEN	BASE SPEED (RPM)/DIRECTION	TIME (MIN : SEC)
CARBIMET 2 ABRASIVE DISCS	320 (P400) GRIT SiC WATER COOLED	6 (27)	250 COMP.	UNTIL PLANE
ULTRAPOL CLOTH	9 MM METADI SUPREME DIAMOND SUSPENSION*	6(27)	150 CONTRA	10:00
MICROCLOTH CLOTH	~0.5 MM MASTERMET COLLOIDAL SILICA PLUS ATTACK POLISH AGENT	6 (27)	150 CONTRA	10:00

*Plus MetaDi Fluid extender as desired

Comp. = complementary (platen and specimen holder both rotate in the same direction)

Contra = platen and specimen holder rotate in opposite directions

3.3.2 Ion nitriding process

The nitriding of Ti-10V-2Fe-3Al samples are performed in a collaborator laboratory (Exactatherm Limited) located outside the University of Windsor. First, all the samples are properly located in a titanium cage inside the vacuum chamber. The purpose of using the titanium cage during nitriding is to intensify the ion nitriding and every component inside the chamber is made of titanium to avoid the contamination of the samples. DC voltage is applied between the sample (cathode) and the chamber wall (anode). Then, the chamber is backfilled with an Ar-H₂ gas mixture to sputter-clean the surfaces of the samples. Meanwhile, the temperature is raised until it reached the desired treatment temperature. In addition, a gas mixture of N₂-H₂ is injected inside the chamber. The electrostatic field between the cathode and anode ionized the gas, forming glow discharge plasma at the sample surface. Positively charged ions of hydrogen and nitrogen

are attracted by the negatively charged sample. They are accelerated by the electric field. The nitrogen ions moved toward the samples and bombarded their surfaces, where they dissolved and chemically reacted with the Ti-10V-2Fe-3Al samples. The treatment pressure and the flow rate are controlled at certain values according to the treatment details. After the treatment, the chamber is cooled under the vacuum. The treatment set-up is shown in Figure 3.3. Temperature, time and pressure are considered variable parameters and are precisely controlled during each operation. All series of nitriding treatments with parameters are listed in Table 3.3.

Table 3.3 List of ion nitriding treatment parameters for Ti-10V-2Fe-3Al

TRIAL #	TEMPERATURE (°C)	PRESSURE (PA)	DURATION (HOUR)	PRE-TREATMENT MEASURES
1	600	67	24	PICKLED WITH 1% HF + 15% HNO ₃ AQUEOUS SOLUTION FOR 5 MINUTES
2	600	67	24	PLASMA GAS ACTIVATED FORM ROOM TEMPERATURE TO 600°C
3	600	520	24	PLASMA GAS ACTIVATED FORM ROOM TEMPERATURE TO 600°C
4	600	67	8	PLASMA GAS ACTIVATED FORM ROOM TEMPERATURE TO 600°C
5	800	67	8	PLASMA GAS ACTIVATED FORM ROOM TEMPERATURE TO 600°C
6	800	67	24	PLASMA GAS ACTIVATED FORM ROOM TEMPERATURE TO 800°C
7	600	67	24	PLASMA GAS ACTIVATED FORM ROOM TEMPERATURE TO 600°C AND PROLONGED FOR 2 HOURS AT 600°C
8	600	67	24	PLASMA GAS ACTIVATED FORM ROOM TEMPERATURE TO 600°C AND PROLONGED FOR 3 HOURS AT 600°C
9	600	67	8	PLASMA GAS ACTIVATED FORM ROOM TEMPERATURE TO 600°C AND PROLONGED FOR 3 HOURS AT 600°C

3.3.3 Surface analysis of ion nitrided samples

3.3.3.1 Surface morphology

The surface roughness of each ion nitrided sample is measured using a Veeco Wyko NT1100 optical profiling system from the research group of Dr. A. Alpas at the University of Windsor. The Veeco Wyko NT1100 [74] is an optical profiler providing three-dimensional surface profile measurements without contact. The phase shift interference (PSI) mode, based on optical phase-shifting, is dedicated to roughness measurements with a maximum 150 nm peak-to-valley topography. Figure 3.4 shows the Veeco Wyko NT1100 optical profiler at the Tribological Research Center at the University of Windsor. The obtained average surface roughness and root-mean-squared roughness are compared between each ion nitriding treatment trial.

3.3.3.2 Compositional analysis by the X-ray diffraction method

The phase compositions on the sample surface that nitrided with the optimum treatment condition are investigated using a Rigaku MiniFlex x-ray diffractometer (XRD) with Cu K_α radiation. The Rigaku MiniFlex enabled faster analysis and improved overall throughput. The PDXL, Rigaku's full-function powder diffraction analysis package, offered a fundamental parameter (FP) method for more accurate peak calculation and phase identification [75]. Subsequently, the calculated d-spacings and the obtained integrated intensities are compared point by point with the MatNavi NIMS materials database to identify each peak in the diffraction pattern.

3.3.4 Cross-sectional microstructure analysis

3.3.4.1 Cross-sectional sample preparation

The cross-sectional microstructures of nitrided Ti-10V-2Fe-3Al are attained from cross-sectional samples cold-mounted in Lecoset cold-curing resin. Prior to cold mounting, the samples are nickel-plated to ensure that no edge damage would occur during the cross-sectional polishing stages. The electroless nickel plating process is an auto-catalytic chemical technique that deposits nickel metal ions in solution with the aid of a reducing agent (phosphorous) that reacts with the ions to deposit nickel onto a metal surface. To ensure that a uniform nickel coating would form, cross-sectional samples are coated in a thin layer of gold prior to the electroless process. The electroless nickel-plating process is performed by submerging the samples in an acid-nickel bath supplied by Buehler EdgeMet Kit at a temperature of 85°C for two hours or longer. The samples are hung from copper wire in the middle of a beaker full of the acid-nickel solution to ensure that temperature fluctuations at the bottom of the beaker, near the hot plate, would not interfere with the plating process, which can potentially produce blisters on the nickel plating. These samples are subsequently ground with 220, 600, 800, 1200 and 1500 SiC grit paper, followed by polishing with 0.05 µm colloidal silica paste, and finally washed in ethanol. Finally, the cold mounted samples are etched in HF + glycerol (1:1) solution (swabbed for 15 seconds) and studied under SEM.

3.3.4.2 Scanning electron microscopy analysis

An FEI Quanta 200 FEG scanning electron microscope (SEM) equipped with an energy-dispersive X-ray spectroscopy (EDS) system is used to characterize the cross-

sectional microstructure from the nitrated samples and thus to evaluate the microstructure of the nitrated layer (Figure 3.5 & Figure 3.6). The system is designed with a single window user interface, allowing a straightforward and flexible analysis. Secondary electron and back-scattered electron SEM images at various magnifications taken from the cross-sectional samples to observe the compound layer and the diffusion zone.

3.3.4.3 Transmission electron microscopy and focused ion beam techniques

Transmission electron microscopy analysis combined with convergent beam electron diffraction (CBED) in the nitrated sample is carried out using the focused ion beam (FIB) technique using a gallium ion source at 30 KV with a Zeiss NVision 40 milling instrument, followed by transmission electron microscope (TEM) lifting techniques using an FEI Titan 80-300HB transmission electron microscope operating at 300 KV [76]. A cross-beam instrument, namely a Zeiss NVision 40, is composed of a field emission gun (FEG) filament SEM (Schottky) and a focused ion beam (FIB) milling instrument. Nanostructures can be characterized under high resolution with a large probe current at a small probe diameter SEM. An FIB milling instrument allows micro-machining, TEM thin foil specimen preparation, 3D tomographic image production, etc. A scanning transmission electron microscopy (STEM) detector can be combined with TEM grids and an SE detector. An energy dispersive spectrometer (EDS) allowed imaging and composition analysis to operate simultaneously. Figure 3.7 shows the FIB milling process on a nitrated sample. A tungsten layer is deposited on the surface to protect it from damage during the milling process (Figure 3.7-a). After ion milling on both sides of the sample, a 2 μm thick milled sample is generated and readied to be

trimmed for TEM lifting (Figure 3.7-c). Figure 3.8 summarizes the FIB in-situ lift-out process for TEM sample preparation.

3.3.4.4 Micro-indentation hardness measurements

The micro-indentation hardness of the nitrated layer, including the compound layer, the diffusion zone and the nitrated surface are measured using a CSM-MicroCombi tester by micro-indentations made with a diamond Vickers tip at a normal load of 245 mN. This tester is ideally suited to the characterization of hard coatings, thick, soft coatings and bulk materials. It provides accurate and reproducible values for the hardness of a variety of materials and coatings of greatly varying thickness and hardness values. It is equipped with an automated optical microscope and high-resolution camera and a PC software package for data acquisition, storage and analysis. With the high-resolution camera, micro-indentations on the specific desired points or phases, such as the extreme thin compound layer (less than 1 μm) and α phase in the β matrix can be achieved. The micro-indentation hardness profile from the compound layer/diffusion zone interface to its bulk material is obtained by performing micro-indentation hardness tests with a diamond Vickers indenter with a maximum load of 245 mN (25 grf) on a mounted cross section tapered at an angle of 10° , giving a magnification of the subsurface region of 5.9 times. The Oliver and Pharr method [77] is used to calculate the hardness value based on the loading and unloading curve slopes. Figure 3.9 shows an example of the load curve used to calculate the microhardness. Curve #1 corresponds to the loading process. Curve #2 is the unloading process. #3 shows the shape of the pyramid indentation. The Vickers diamond pyramid microhardness value is the applied load (kgf) divided by the surface area of the indentation (mm^2) (ASTM E384-11 [78]):



where HV is the Vickers hardness, P is the load in kgf and d is the arithmetic mean of the two diagonals in mm.

3.4 Wear testing

3.4.1 Ball-on-disk wear testing process

Ball-on-disk wear tests on untreated and ion nitrided Ti-10V-2Fe-3Al are performed using a CETR UMT multi-specimen test machine at room temperature under dry sliding conditions, schematically shown in Figure 3.10. The surfaces of Ti-10V-2Fe-3Al disks (20 mm diameter \times 3 mm thickness) are polished to an average roughness of 0.1 μm and cleaned ultrasonically in ethanol. AISI 52100 steel balls of 6 mm in diameter are used as the counterface material. The properties of AISI 52100 steel balls are given in Table 3.4. The tests are carried out at different normal loads of 0.8N, 1.2N, 2N, 3.5N and 5N for a total sliding distance of 200 m (5,000 cycles) at 0.1 m/sec (160 rpm). Coefficients of friction (COF) values are recorded during each test. The wear rates are calculated based on mass loss measurements by weighing the samples before and after each test. Weight measurements are performed using a high-precision balance to 0.01 mg.

Table 3.4 Characteristics of AISI 52100 steel counterface [79]

MATERIAL	AISI 52100 STEEL BALL
DIAMETER	6 MM
DENSITY ($\times 1000$ KG/M ³)	7.7-8.03
POISSON'S RATIO	0.30
HARDNESS	800 HV
ELASTIC MODULUS (GPA)	210
TENSILE STRENGTH (GPA)	2.2
YIELD STRENGTH	2.03
COMPRESSIVE STRENGTH	300,000 PSI (2068MPA)
THERMAL EXPANSION (10-6/ $^{\circ}$ C)	11.9

3.4.2 Scanning electron microscopy analysis of worn materials

After the wear tests, wear tracks and wear debris particles are examined using an SEM (FEI Quanta 200 FEG) equipped with an energy dispersive X-ray spectrometer (EDS). Plain views of the wear tracks and wear debris are observed to identify the morphology of the worn surface under each loading condition. EDS is used to determine quantitatively the composition of the wear debris and selected locations on the wear tracks.

3.4.3 Subsurface analysis of worn Ti-10V-2Fe-3Al

A sub-surface cross-sectional analysis of wear tracks is performed to study the transfer layers and subsurface deformation by the focused ion beam (FIB) milling technique. The milling process is performed using Ga ions at 30 kV, and a thin layer of tungsten is deposited on the milling location to protect the surfaces from damage by Ga ions during the milling process.

3.5 Micro-scratch testing

A sliding contact examination is employed using micro-scratch tests to study the friction behaviour of nitrided surfaces. A CSM Instruments Micro-Combi tester with a Rockwell diamond stylus with a radius of 200 μm is used to perform both (a) progressively increasing load tests with the applied load gradually increased from 0 to 20N and (b) constant load tests (loads selected according to the critical loads determined in the previous load tests). The loading rate and lateral displacement speed are 100 N/min and 10 mm/min, respectively. Variations in the coefficient of friction (COF) and acoustic emission signals are recorded during each test. The critical loads corresponding to the onset of each failure are identified using acoustic emission signals. Micro-scratch tests conducted at constant loads of 1N, 5N, 10N, and 20N are specifically performed to analyze the friction behaviour and the sliding mechanisms of the nitrided surfaces.

3.6 Tensile testing

3.6.1 Tensile sample preparation

According to ASTM E8/E8M, for standard test methods for tension testing of round tension metallic test specimens, the gauge length for the measurement of elongation should be four times the diameter of the specimen when following E8 and five times the diameter of the specimen when following E8M. As a result, tensile tests samples are prepared with their dimension list in Table 3.5. The bars (20 mm in diameter) are segmented with a length of around 9 cm and then hollowed into two smaller bars with a diameter of 9 mm using a wire EDM machine. After the segmentation process, each smaller bar is then computer numerical control (CNC) machined into the exact

dimensions listed. Coolant is applied throughout the machining process to avoid microstructure changes from rising temperature. Figure 3.11 gives schematic and real views of a Ti-10V-2Fe-3Al tensile sample.

Table 3.5 Dimension of tensile test samples according to ASTM E8 [80]

UNIT	G GAGE LENGTH	D DIAMETER	R RADIUS OF FILLET, MIN	A LENGTH OF REDUCED SECTION, MIN
MM	24.0 ± 0.1	6.4 ± 0.1	4.6	30
IN.	1 ± 0.005	0.250 ± 0.005	0.188	1.25

After the machining process, Ti-10V-2Fe-3Al tensile samples are polished using a CNC drill machine (Black & Decker). Samples are ground and polished to a surface finish of 1 μm and cleaned in an ultrasonic ethanol bath. The cleaned tensile samples are then carefully packed into a screw cap tube and stored in the desiccators to minimize the oxidation of the polished samples.

During the nitriding process, tensile samples prepared according to ASTM E8 are polished and hung in the chamber to minimize the effect of residual stress during the machining process. The optimized nitriding condition is applied to the tensile samples. Nitrided tensile samples are shown in Figure 3.12-a. The overall nitriding effect on the tensile samples is very good. No wobbling of the samples is detected, which means that no residue stress is accumulated on the samples' surface during the nitriding process.

3.6.2 Tensile testing process

The mechanical properties are studied through tensile tests performed at room temperature. Tensile tests are performed on cylindrical specimens with a gauge length four times the diameter (24 mm gauge length and 6 mm in diameter). Three untreated and three ion nitrided Ti-10V-2Fe-3Al tensile samples are tested using an MTS Criterion

Model 43 tensile test machine. The tests are conducted at a constant loading rate of 0.5 mm/min, and a clip-on strain gauge is mounted on samples for strain measurements. After the tests, the fractured surfaces are investigated under an SEM. Surface areas near the fractures are etched using Kroll's solution and swabbed for 20 seconds to reveal the microstructure changes on the polished surface. Figure 3.13 shows a nitrided tensile sample under the aforementioned testing conditions above.

3.7 Fatigue testing

3.7.1 Fatigue sample preparation

According to ASTM E466-07, in standard practice for conducting force controlled constant amplitude axial fatigue tests on metallic specimens with a continuous radius between ends, the radius of the curvature should be no less than eight times the minimum diameter of the test section. The reduced section length should be greater than three times the minimum test section diameter. Therefore, fatigue test samples are prepared with the dimensions listed in Table 3.6. The received bars (20 mm in diameter) are segmented with a length of around 12 cm and then hollowed into four smaller bars with a diameter of 6.4 mm using a wire EDM machine. After the segmentation process, each smaller bar is then CNC machined into the exact dimensions listed. Coolants are applied throughout the machining process to avoid microstructure changes from rising temperature. Figure 3.14 shows the fatigue sample prepared with the conventional metallographic process.

Table 3.6 Dimension of fatigue test samples according to ASTM E466-07 [81]

UNIT	L GAGE LENGTH	D DIAMETER	R RADIUS OF FILLET MIN	LG GRIP LENGTH	DG GRIP DIAMETER
IN.	1.875	0.167	1.333	1.23	0.25
MM	47.6	4.23	33.9	31.2	6.4

After the machining process, Ti-10V-2Fe-3Al fatigue samples are polished using a CNC drill machine (Black & Decker). The samples are ground and polished to a surface finish of 1 μm and cleaned in an ultrasonic ethanol bath. The cleaned tensile samples are then carefully packed into a screw cap tube and stored in the desiccators to minimize the oxidation of the polished samples.

The optimized nitriding condition is applied to fatigue samples in a process similar to that previously described for the ion nitriding of tensile samples. The overall nitriding effect on the fatigue samples is very good, as shown in Figure 3.12-b.

3.7.2 Fatigue testing process

Bending rotation fatigue tests ($R = -1$) are performed on untreated Ti-10V-2Fe-3Al at a frequency of 50 Hz at room temperature using an R. R. Moore type reverse bending cyclic fatigue machine (Figure 3.15). According to the Instron machine manual [82] and based on the rotating beam principle, the specimen is considered a simple beam during function, and symmetrical loadings are applied at two points. Stress is applied to the specimen using deadweights to ensure precise loading. When a half revolution is made, the stresses in the fibers originally below the neutral axis are reversed from tension to compression and vice versa. Upon completing the revolution, the stresses are again reversed so that, during one revolution, the test specimen passes through a complete cycle of flexural stress (tension and compression). Subsequently, the fractured surfaces are

analyzed using SEM. A fatigue specimen that does not break at 10^7 cycles is considered to indicate that the stress magnitude does not reach the fatigue limit.



Figure 3.1 Thermo Jarrell Ash IRIS Advantage optical emission spectrometer

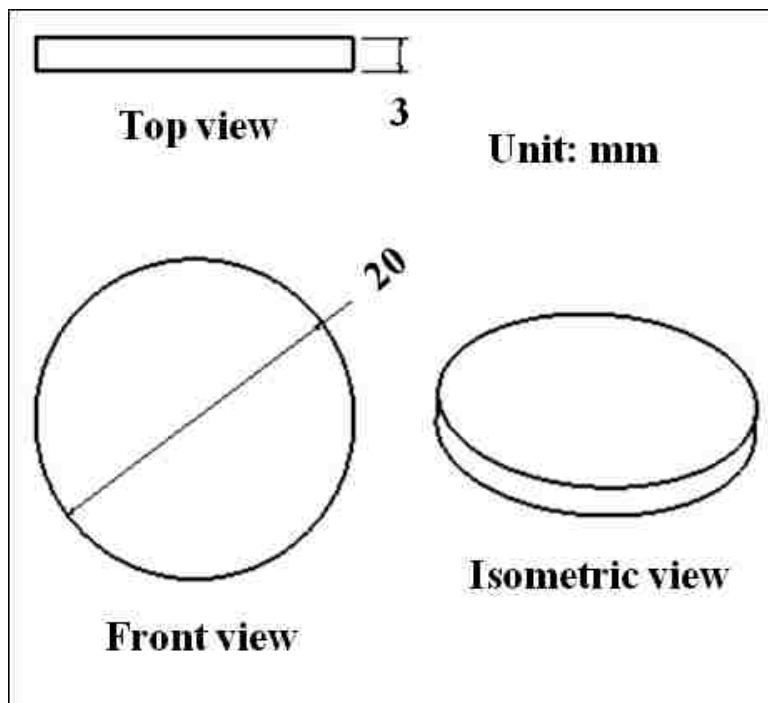


Figure 3.2 Schematic presentation of Ti-10V-2Fe-3Al coupons

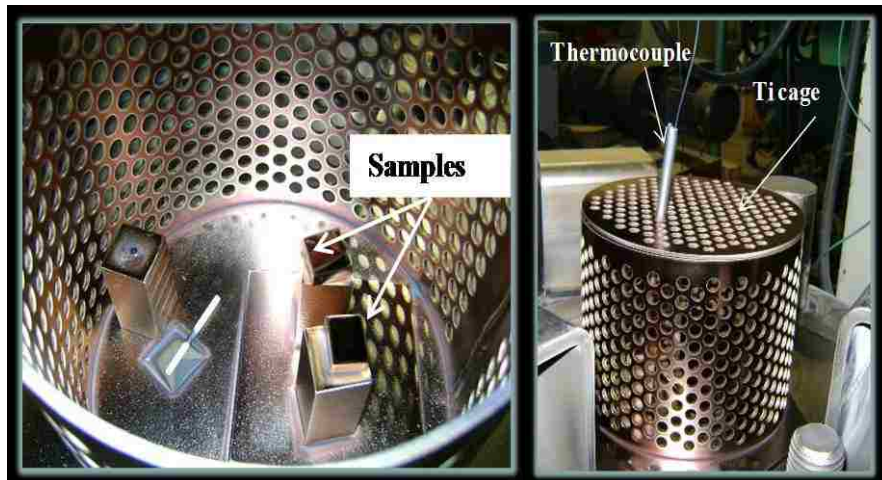


Figure 3.3 Treatment set-up showing the titanium samples are located in a titanium cage [83]



Figure 3.4 Effective NT1100 offers all the advantages of industry-standard WYKO optical profiling, including the full Wyko Vision® analytical software package [74].



Figure 3.5 Scanning electron microscopy used in research objective from Great Lakes Institute for Environmental Research at University of Windsor

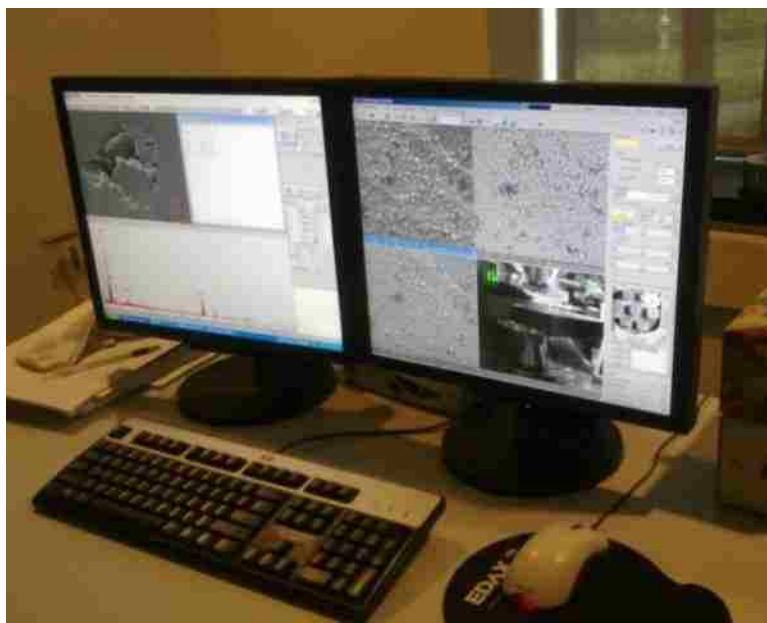


Figure 3.6 The user interface of EDS coupled with SEM

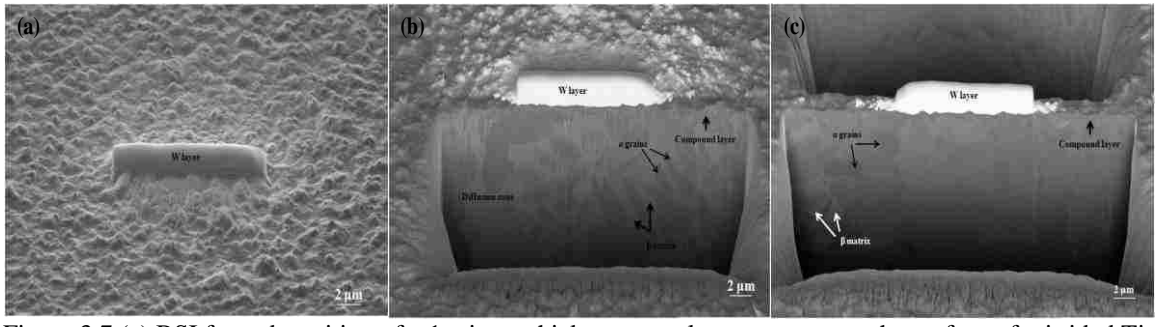


Figure 3.7 (a) BSI from deposition of a 1 micron thick tungsten layer to preserve the surface of nitrided Ti-10V-2Fe-3Al during milling, (b) BSI of ion milling of the sample on one side of subsurface region, and (c) BSI from ion milling of the sample on both sides of subsurface region

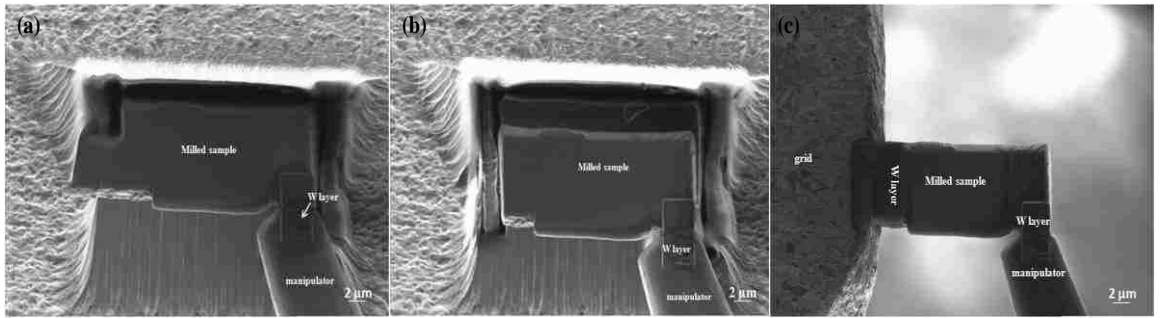


Figure 3.8 (a) BSI of the manipulator approaches the sample until they touch and then attached to the sample by sputtering a small W layer, (b) BSI of lifted sample from base materials by a manipulator, and (c) BSI shows the sample is taken to the grid by the manipulator and attached to the grid with W layer deposition.

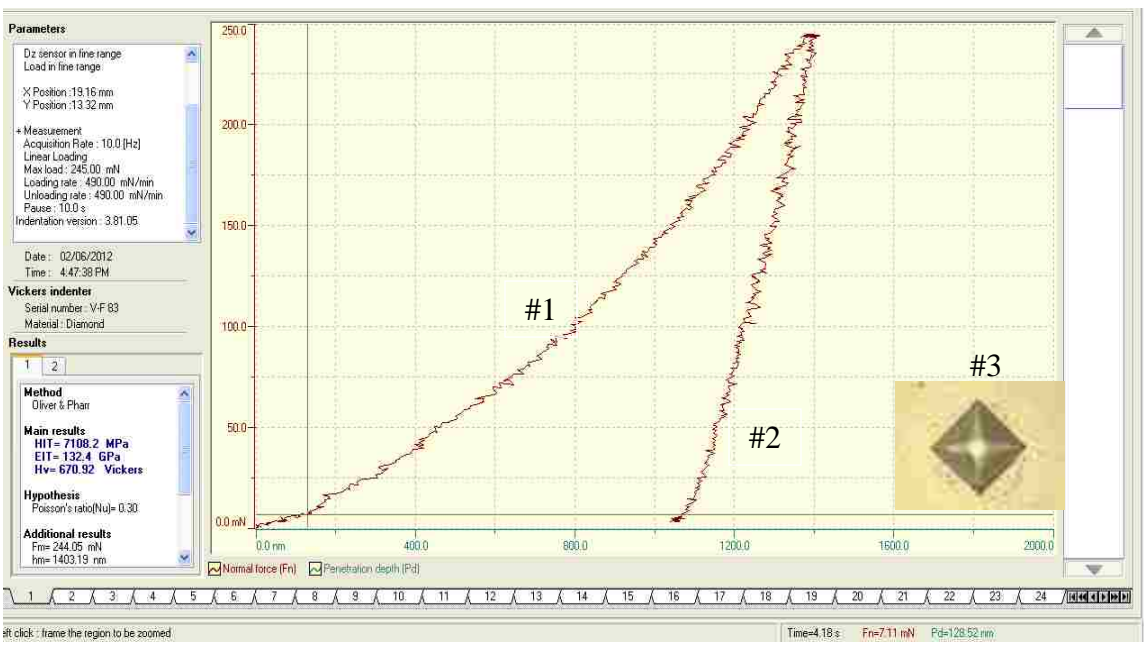


Figure 3.9 Illustration of loading/ unloading curves during microhardness measurement

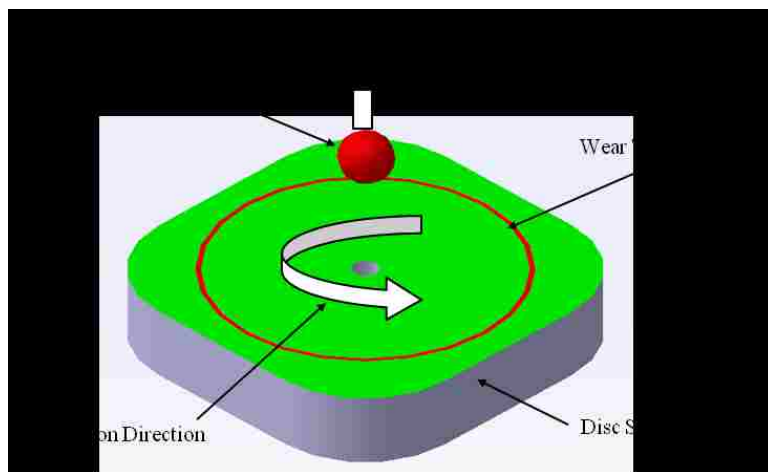


Figure 3.10 Schematic presentation of ball-on-disc wear test apparatus

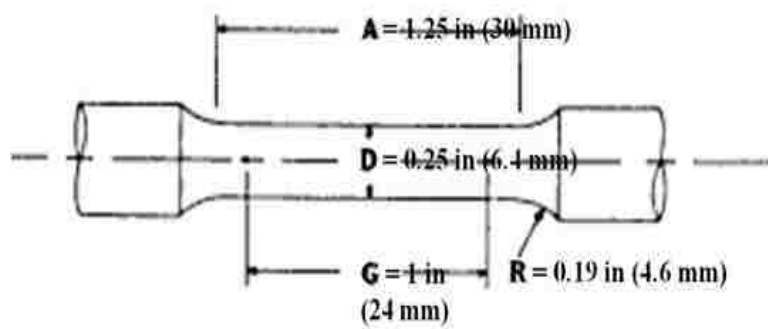


Figure 3.11 Schematic presentation and real image shown of a tensile test sample



Figure 3.12 Real image shown of (a) the tensile test sample, and (b) fatigue test sample which have been ion nitrided according to optimized nitriding condition selected from Section 3.5.



Figure 3.13 Uni-axial tensile testing on Ti-10V-2Fe-3Al using MTS Criterion Model 43 tensile testing machine with loading rate of 0.5 mm/min.

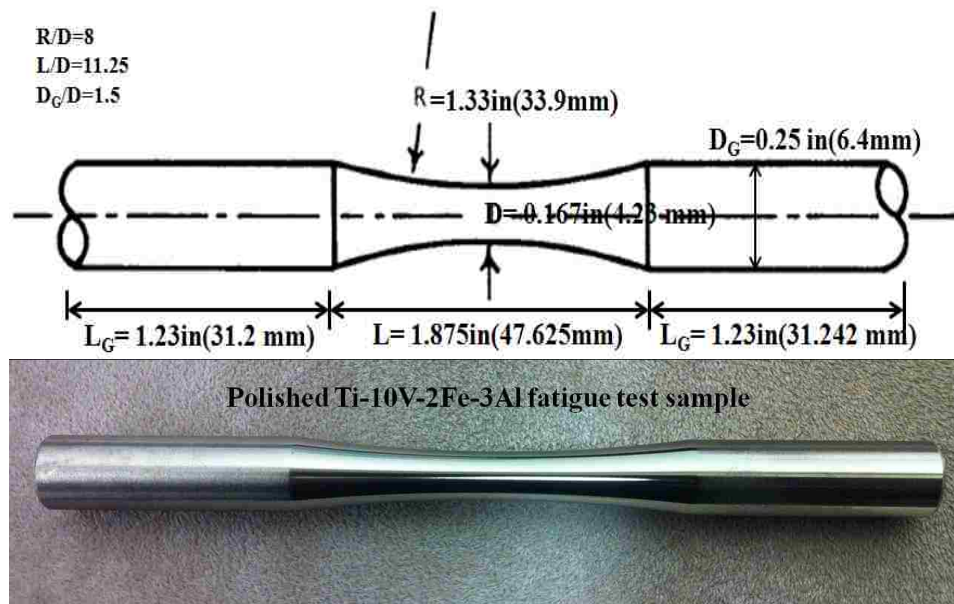


Figure 3.14 Schematic presentation and real image shown of a fatigue test sample



Figure 3.15 Bending rotation fatigue tests ($R = -1$) are performed on untreated Ti-10V-2Fe-3Al using R.R. Moore type fatigue machine at the 50 Hz in room temperature.

CHAPTER 4

EXPERIMENTAL RESULTS

4.1 Overview

This chapter is classified into two major sections. The characterization of the as-received Ti-10V-2Fe-3Al, including microstructure evaluation, plus mechanical, fatigue, and wear properties of Ti-10V-2Fe-3Al. The effect of ion nitriding parameters, such as temperature, time and pressure on microstructural features is stated. Surface roughness, measurements on the compound layer thickness and diffusion zone depth, the cross-sectional microstructure evaluation, and the scratch resistance of the nitrided layer are presented as the screening tests to develop an optimized nitriding condition of Ti-10V-2Fe-3Al. Additionally, ion nitrided Ti-10V-2Fe-3Al and their corresponding tensile and fatigue properties are given. Tensile testing results for both untreated and ion nitrided Ti-10V-2Fe-3Al are also compared. The fractured surface and the sample surfaces near the fracture region are observed using SEM. Meanwhile, fatigue testing results, including a plot of S-N curves and fractured surface observations on both untreated and ion nitrided samples, are analyzed. Characterization of worn tracks, and wear debris after wear testing is performed, and the results with corresponding wear mechanisms are discussed.

4.2 Characterization of Ti-10V-2Fe-3Al as-received

4.2.1 Microstructure evaluation on Ti-10V-2Fe-3Al

The typical top surface microstructures of as-received material at various magnifications are shown in Figure 4.1. Conventional metallographic preparation techniques for Ti alloys are followed, and the surfaces are etched in Kroll's reagent. Specimens had a homogeneous structure perpendicular and parallel to the rolling

direction consisting of rod-like α grains with various sizes in a matrix of the β phase. Figure 4.2 shows the cross-sectional microstructure of untreated Ti-10V-2Fe-3Al alloy at different magnifications. Several β grains are revealed from the grain boundaries with an average grain size of $256 \pm 58.3 \mu\text{m}^2$. The average β phase content is determined by an image analyzing software, “Omnimet 8.9[®]” (OmniMet Image Analysis-BUEHLER), which is according to ASTM standard [84,85]. β phase composition in the cross-sectional microstructure and top surface microstructure is 65.5% and 60%, respectively. Figure 4.3 shows the top surface and the cross-sectional microstructure processed by Omnimet 8.9[®] image processing software.

4.3 Ion nitriding of Ti-10V-2Fe-3Al

A series of ion nitriding treatments (nine in total) are performed at Exactatherm Ltd. (research project collaborator). Ion nitriding temperature, time, pressure and pre-treatment measures are four variables and are compared accordingly. Only one variable is compared each time. For instance, when comparing ion nitriding temperature, rest of ion nitriding parameters such as time, pressure and pre-treatment measures remained constant. Moreover, all other treatment parameters, such as plasma gas composition, remained constant. Measurements of surface roughness, compound layer thickness and depth of the diffusion zone are presented as the screening tests to determine the optimized nitriding treatment parameter for Ti-10V-2Fe-3Al. Since thin compound layers could minimize the residual stress and give the coating better adhesion to the substrate, thick diffusion zones provided better mechanical support to the coating.

First, the pre-treatment measure is varied between acidic pickling, plasma gas sputtering and elongated plasma sputtering. The optimized pre-treatment method is the

elongated plasma sputtering process. Second, the ion nitriding temperature is compared between 600°C and 800°C. The optimized ion nitriding temperature is selected as 600°C. Third, the ion nitriding time is varied between 8 hours and 24 hours. The duration of optimized treatment is selected as 8 hours. Last, but not least, ion nitriding pressure is compared between 67 Pa and 520 Pa. The optimized nitriding pressure for Ti-10V-2Fe-3Al is 67 Pa. Details of comparison results are presented in sections 4.3.1–4.3.5. Section 4.3.6 summarizes the optimized ion nitriding condition for Ti-10V-2Fe-3Al.

4.3.1 Effect of pre-treatment methods on surface roughness and cross-sectional microstructure

To study the effect of pre-treatment measures on microstructure features, nitriding temperature, time and pressure need to remain constant. The depth of the diffusion zone, compound layer thickness, and surface roughness are compared for coupons nitrided under different pressures. Table 4.1 lists nitriding parameters for Ti-10V-2Fe-3Al with various pre-treatment methods.

Table 4.1 List of ion nitriding parameters for Ti-10V-2Fe-3Al with different pre-treatment methods

TEMPERATURE	600°C
TIME	24 HOURS
COOLING	UNDER VACUUM
GAS COMPOSITION	2.9% N ₂ - BALANCE H ₂
PRESSURE	67 PA (0.5 TORR)
PRE-TREATMENT METHODS	CHEMICAL PICKLING, PLASMA SPUTTERING, ELONGATED PLASMA SPUTTERING

4.3.1.1 Surface roughness

Optical 3D profiles from surface topography of Ti-10V-2Fe-3Al are given in Figure 4.4. The average surface roughness (R_a) and the root-mean-squared roughness (R_q) are measured and compared in Figure 4.5. It shows that the prolonged gas-sputtering method provides the lowest surface roughness among three pre-treatment methods.

4.3.1.2 Cross-sectional microstructure, depth of diffusion zone and compound layer thickness

Cross-sectional microstructure observations are given in Figure 4.6. The compound layer is uniformly distributed for a sample activated with sputtering gas. In contrast, a discontinuity thin compound layer is shown in a sample activated with an acidic pickling solution. Figure 4.7 compares the depth of the diffusion zone and the compound layer thickness for samples nitrided with various pre-treatment measures. It shows the sputtering-gas-activated sample has a much higher depth of diffusion zone. In contrast, only the prolonged gas-sputtering-activated sample has a thinner compound layer, which is 49% less than the sputtering-gas-activated sample and the acidic pickling solution sample.

4.3.1.3 Micro-indentation hardness profile

Figure 4.8 compares the micro-indentation hardness depth profile between samples with different pre-treatment measures. For the sample pickled with a chemical solution and plasma gas sputtering, the depth of the diffusion zone is measured much lower than the value obtained from the sample pre-treated with elongated gas sputtering. To summarize, the increasing gas-sputtering duration resulted in a smoother surface.

Prolonged gas sputtering is considered as an optimized pre-treatment measure since it offers a smoother surface, a sufficient depth of diffusion zone and a thinner compound layer.

4.3.2 Effect of nitriding temperatures on surface roughness and cross-sectional microstructures

To study the effect of nitriding temperatures on microstructure features, nitriding pressure and nitriding times need to remain constant. Depth of diffusion zone, compound layer thickness and surface roughness are compared for coupons nitrided at different temperatures. Table 4.2 lists nitriding parameters for Ti-10V-2Fe-3Al with various nitriding temperatures.

Table 4.2 List of ion nitriding parameters for Ti-10V-2Fe-3Al with different nitriding temperature

PRESSURE	67 PA (0.5 TORR)
TIME	24 HOURS
COOLING	UNDER VACUUM
GAS COMPOSITION	2.9% N ₂ - BALANCE H ₂
TEMPERATURE	600°C & 800°C

4.3.2.1 Surface roughness

Optical 3D profiles from surface topography of Ti-10V-2Fe-3Al are given in Figure 4.9. The average surface roughness (R_a) and the root-mean-squared roughness (R_q) are measured and compared in Figure 4.10. It shows that with a rise in nitriding temperature, the average surface roughness and the root-mean-squared roughness increased by 34.7% and 35.3%, respectively.

4.3.2.2 Cross-sectional microstructure, depth of diffusion zone and compound layer thickness

Cross-sectional microstructure observations are given in Figure 4.11. The compound layer is uniformly distributed for a sample nitrided at 600°C. In contrast, a discontinuity thick compound layer is shown in a sample nitrided at 800°C. Figure 4.12 compares the depth of diffusion zone and compound layer thickness for samples nitrided at 600°C and 800°C. It shows that the depth of diffusion zone and compound layer thickness of the sample treated at 800°C increased by 38% and 131%, respectively.

4.3.2.3 Micro-indentation hardness profile

Figure 4.13 compares the micro-indentation hardness depth profile between samples treated at 600°C and 800°C. For the sample treated at 600°C, the depth of diffusion zone is measured as 21 μm ; which is much lower than 48 μm obtained from the sample treated at 800°C. Although the sample treated at 800°C gives a higher depth of diffusion zone, a discontinuous and thick compound layer is generated at 800°C, which is not preferable since it could result in brittle cracking and premature failure. Meanwhile, increasing the nitriding temperature led to an increase in average surface roughness. As a result, the optimized nitriding temperature should be 600°C.

4.3.3 Effect of nitriding time on surface roughness and cross-sectional microstructure

To study the effect of nitriding time on a microstructure feature, nitriding pressure and nitriding temperature need to remain constant. Depth of diffusion zone, compound layer thickness and surface roughness are compared for coupons nitrided with different

duration. Table 4.3 lists the nitriding parameters for Ti-10V-2Fe-3Al with various nitriding times.

Table 4.3 List of ion nitriding parameters for Ti-10V-2Fe-3Al with different nitriding durations

PRESSURE	67 PA (0.5 TORR)
TEMPERATURE	600°C
COOLING	UNDER VACUUM
GAS COMPOSITION	2.9% N ₂ - BALANCE H ₂
TIME	8 & 24 HOURS

4.3.3.1 Surface roughness

Optical 3D profiles from the surface topography of Ti-10V-2Fe-3Al are given in Figure 4.14. The average surface roughness (R_a) and the root-mean-squared roughness (R_q) are measured and compared in Figure 4.15. It shows that with an increase in the nitriding time, the average surface roughness and the root-mean-squared roughness increased by 21.3% and 22.8%, respectively.

4.3.3.2 Cross-sectional microstructure, depth of diffusion zone and compound layer thickness

Cross-sectional microstructure observations are given in Figure 4.16. The compound layers are uniformly distributed in both samples. Figure 4.17 compares the depth of diffusion zone and compound layer thickness for samples nitrided for 8 hours and 24 hours. It shows that the depth of diffusion zone and the compound layer thickness of the sample treated at 800°C increased by 197% and 74%, respectively.

4.3.3.3 *Micro-indentation hardness profile*

Figure 4.18 compares the micro-indentation hardness depth profile between samples treated for 8 hours and 24 hours. For the 8-hour sample, the depth of diffusion zone is measured as 9 μm , which is much lower than 21 μm obtained from the sample treated for 24 hours. In summary, the nitriding time enhances the diffusion of nitrogen with minor effects on the substrate microstructure. The sample nitrided for 24 hours gives a higher depth of diffusion zone and a continuous compound layer. Meanwhile, increasing nitriding time led to an increase in the average surface roughness. Therefore, both the 8-hour and 24-hour durations can be considered optimized conditions.

4.3.4 **Effect of nitriding pressure on surface roughness and cross-sectional microstructure**

To study the effect of nitriding pressure on microstructure features, nitriding temperature and nitriding times need to remain constant. Depth of diffusion zone, compound layer thickness and surface roughness are compared for coupons nitrided under different pressure. Table 4.4 lists nitriding parameters for Ti-10V-2Fe-3Al with various nitriding pressures.

Table 4.4 List of ion nitriding parameters for Ti-10V-2Fe-3Al with different nitriding pressures

TEMPERATURE	600°C
TIME	24 HOURS
COOLING	UNDER VACUUM
GAS COMPOSITION	2.9% N ₂ - BALANCE H ₂
PRESSURE	67 PA (0.5 TORR) & 520 PA (3.9 TORR)

4.3.4.1 Surface roughness

Optical 3D profiles from surface topography of Ti-10V-2Fe-3Al are given in Figure 4.19. The average surface roughness (R_a) and the root-mean-squared roughness (R_q) are measured and compared in Figure 4.20. It shows that with an increase in nitriding pressure, the average surface roughness and the root-mean-squared roughness decreased by 67.3% and 66.7%, respectively. Increasing nitriding pressure gave rise to a smoother sample surface.

4.3.4.2 Cross-sectional microstructure, depth of diffusion zone and compound layer thickness

Cross-sectional microstructure observations are given in Figure 4.21. The compound layer is uniformly distributed for the sample nitrided at 600°C. In contrast, a discontinuity thick compound layer is shown in the sample nitrided at 800°C. Figure 4.22 compares the depth of diffusion zone and the compound layer thickness for samples nitrided under 67 Pa and 520 Pa. It shows that the depth of diffusion zone and the compound layer thickness of the sample treated under 520 Pa decreased by 74% and 63%, respectively.

4.3.4.3 Micro-indentation hardness profile

Figure 4.23 compares the micro-indentation hardness depth profile between samples treated under 67 Pa and 520 Pa. For the sample treated under 67 Pa, the depth of diffusion zone is measured as 21 μm ; which is much higher than the 9 μm obtained from the sample treated under 520 Pa. In general, increasing the nitriding pressure resulted in surfaces that are smoother, but it also impaired diffusion of N atoms within the Ti

substrate. The depth of diffusion zone of the sample nitrided under 520 Pa is too thin to be selected as an optimized condition. Therefore, treatment under 67 Pa is the optimized nitriding pressure.

4.3.5 Effect of nitriding time on surface roughness and cross-sectional microstructure of samples pre-treated with prolonged gas sputtering

To study the effect of nitriding time on samples pre-treated with prolonged gas sputtering, nitriding pressure and nitriding temperature need to remain constant. Depth of diffusion zone, compound layer thickness and surface roughness are compared for coupons nitrided for different durations. Table 4.5 lists nitriding parameters for Ti-10V-2Fe-3Al with various nitriding times.

Table 4.5 List of ion nitriding parameters for Ti-10V-2Fe-3Al with different nitriding duration

PRE-TREATMENT METHOD	GAS SPUTTERING AT 600°C FOR 2.5 HOURS
PRESSURE	67 PA (0.5 TORR)
TEMPERATURE	600°C
COOLING	UNDER VACUUM
GAS COMPOSITION	2.9% N ₂ - BALANCE H ₂
TIME	8 & 24 HOURS

4.3.5.1 Surface roughness

Optical 3D profiles from surface topography of Ti-10V-2Fe-3Al are given in Figure 4.24. The average surface roughness (R_a) and the root-mean-squared roughness (R_q) are measured and compared in Figure 4.25. It shows that the surface roughness of nitrided samples are slightly higher than the untreated sample. However, there is no

difference in surface roughness between the samples nitrided for 8 hours and 24 hours with the pre-treatment method of gas sputtering at 600°C for 3 hours.

4.3.5.2 Cross-sectional microstructure, depth of diffusion zone and compound layer thickness

Cross-sectional microstructure observations are given in Figure 4.26. The compound layers are uniformly distributed for both samples nitrided for 8 hours and 24 hours. Figure 4.27 compares the depth of diffusion zone and the compound layer thickness for samples nitrided for 8 hours and 24 hours. It shows that the 8-hour sample has a slightly lower depth of diffusion zone. However, the compound layer thickness for the sample nitrided for 8 hours is 60% less than the value of the sample nitrided for 24 hours.

4.3.5.3 Micro-hardness profile

Figure 4.28 compares the micro-hardness depth profile between samples treated for 8 hours and 24 hours. For the 8-hour sample, the depth of diffusion zone is measured as 40 μm ; which is much lower than 44 μm obtained from the sample treated for 24 hours. In summary, increasing nitriding time resulted in an increase in the thickness of the compound layer and the depth of diffusion zone. However, 8 hours treatment time is sufficiently long combined with prolonged gas-sputtering duration and not only generates a thick diffusion zone, but also a thin compound layer.

4.3.6 Optimized ion nitriding conditions for Ti-10V-2Fe-3Al

By comparing previous trials of nitriding treatment and summarizing the effect of nitriding parameters on microstructure features; the selected treatment condition for Ti-

10V-2Fe-3Al is summarized in Table 4.6 and selected as a temperature of 600°C for the duration of 8 hours with a diluted nitrogen gas mixture and a pressure close to 67 Pa. In the meantime, the elongated plasma gas activation method is applied prior to the nitriding process. (The prolonged gas activation process is created by using an active gas composition of 2.9% nitrogen balance hydrogen at 600°C for an extra 3 hours before nitriding.)

Table 4.6 Treatment conditions, compound layer thicknesses and diffusion zone depths

TREATMENT CONDITIONS				THICKNESS OF COMPOUND LAYER (MM)	DEPTH OF DIFFUSION ZONE (MM)
TEMPERATURE (°C)	TIME (H)	PRESSURE (PA)	PRE-TREATMENT ACTIVATION		
600	8	67	PLASMA GAS WITH ELONGATED DURATION	0.37 ± 0.1	40

4.3.6.1 Surface characterizations (WYKO, SEM, XRD)

The surface morphology of nitrided Ti-10V-2Fe-3Al is shown in Figure 4.29. The average surface roughness (R_a) and the root-mean-squared surface roughness (R_q) of nitrided Ti-10V-2Fe-3Al over an area of $91.2 \times 119.9 \mu\text{m}^2$ at a magnification of 50X are 0.196 ± 0.005 and $0.241 \pm 0.006 \mu\text{m}$, respectively. The optical 3D profile for nitrided Ti-10V-2Fe-3Al shown in Figure 4.30 reveals a relatively low roughness of the nitrided surface. Surface hardness of the nitrided sample is measured at 330 Hv (200 gf), which is tremendously increased by 25% compared to untreated Ti-10V-2Fe-3Al. X-ray diffraction (XRD) analysis on nitrided Ti-10V-2Fe-3Al is performed and revealed the Ti_2N as the major phase, with the presence of several peaks corresponding to TiN , V_2N and Fe_8N . The presence of V_2N and Fe_8N in the nitrided surface resulted from a high percentage of vanadium in bulk materials. α -Ti peaks are reflections from the substrate

due to the X-ray depth of penetration All the possibilities for indexing the diffraction pattern are illustrated in Figure 4.31.

4.3.6.2 Cross-sectional microstructure analysis (SEM, TEM, FIB)

Untreated Ti-10V-2Fe-3Al contains both α and β phases. Various sized rod-like α grains are randomly distributed in β matrix, with an average of 42.0% α phase composition measured using Omnimet 8.9[®] software. Ion nitriding of Ti-10V-2Fe-3Al resulted in a different cross-sectional microstructure, which consists of a thin compound layer uniformly distributed on the top surface, a thick diffusion zone right underneath the compound layer with an average thickness of 40 μm and a bulk region. The thickness of the compound layer and the depth of diffusion zone are measured from an SEM image at a magnification of 3000X (Figure 4.32) and are presented in Table 4.6. A cross-sectional microstructure of nitrided Ti-10V-2Fe-3Al shows the nickel coating is piled up on the compound layer to prevent coating damage during the polishing process. Less than 1 μm in thickness of the compound layer restricts brittle cracking and premature failure of the nitrided surface under sliding movements in aerospace applications. The thin but tough compound layer mainly consists of TiN and Ti₂N, proved by XRD and TEM analysis. During the nitriding process, α phase stabilizers, such as Al, allow the α phase form and penetrate to bulk material on the nitrogen diffusion path. Therefore, the diffusion zone contain interstitial nitrogen solid solution is formed. Meanwhile, β transus temperature for Ti-10V-2Fe-3Al is between 790°C and 805°C [10,12]. Thus, for the treatment conducted below the transus temperature, α grains at a distance several μm from the sample surface can be observed in the diffusion zone as well.

The FIB milling technique is applied to observe the subsurface microstructure at higher magnifications, as shown in Figure 4.33. On both sides of the subsurface region, needle-like α grains are arranged in the β matrix. At higher magnification, a thin compound layer adheres on top of the sample without any voids, as shown in Figure 4.34 and Figure 4.35. Analytical TEM observation performed on cross-sectional thin film proves the formation of a compound layer under glow discharge. The combination of dark field TEM images (DF-TEM) and CBED patterns reveal the presence of α and β phases in the diffusion zone as shown in Figure 4.35. Meanwhile, a close observation on the selected area in Figure 4.36 reveals the formation of cubic TiN, tetragonal Ti₂N and hexagonal V₂N in the compound layer. Figure 4.37 showing a subsurface region of the compound layer area with its corresponding element distribution map, which is recorded using the STEM-EDS method, shows the nitrogen-enriched compound layer and an enrichment of vanadium in β phase that exists in the diffusion zone. The TEM investigation on the cross-sectional bulk microstructure of nitrided Ti-10V-2Fe-3Al in Figure 4.38 revealed the presence of α and β grains after nitriding treatment.

4.3.6.3 Microhardness profile

The microhardness depth profile shown in Figure 4.39 indicates the depth of nitrogen interstitials reached during the nitriding process. A very high microhardness value is obtained at the compound layer interface, approximately 330 Hv (200 gf), gradually decreases until it reaches the average bulk hardness value, 265 Hv (200 gf). The depth of the gradually decreased profile indicates the nitrogen diffusion zone and is estimated at approximately 40 μm . Further SEM observation on nitrided cross-sectional

microstructure confirms the measurement and reveals the hardening effect of nitrogen interstitials diffused in the α phase.

4.4 Microscratch analysis

A series of microscratch tests under constant loading conditions are utilized to study the nitriding treatment effect on a nitrided surface under sliding contact. Each cracking event during a progressively increasing load scratch test had an acoustic emission output whose magnitude is proportional to the area of crack that generated it. Figure 4.40 is a plot of the acoustic emission for the progressively increasing load test on nitrided Ti-10V-2Fe-3Al. The progressively increasing load test scratch path is shown in Figure 4.41-a. The figure shows that the path width expands as the load increases from 0 to 20N. Figure 4.41-b is the location where the first micro-crack is observed. Tensile cracks are closely distributed near the area where the 10N load applies (Figure 4.41-c) and semi-circular cracks are all found near the area of 20N of load applied (Figure 4.41-d).

The variations of the coefficient of friction (COF) of the treated and untreated alloy tested at each constant load are given in Figure 4.42. The figures indicate that nitrided Ti-10V-2Fe-3Al led to a much smoother COF curve compared to the untreated alloy at each loading condition. Meanwhile, there is a tremendous reduction in the average coefficient of friction value (72% with applied load of 5N) of Ti-10V-2Fe-3Al for all loading conditions (Figure 4.43).

The scratch path under progressively loading observation in Figure 4.44 revealed that the compound layer is peeled near the edge of the path near the area where 20N of

load is applied. Acoustic emission signals are also recorded during progressively increasing load scratch tests and indicate the occurrence of a severe surface displacement at 17.2N of load applied. Further investigation of the constant load test (20N) scratch path confirmed the existence of compound layer delamination, as shown in Figure 4.45. However, at 10N loading conditions, there are tensile cracks found on the scratch path but no flake-off of coatings is observed (Figure 4.46). Therefore, both the scratch path observation and the acoustic emission signals justify that a well-bonded compound layer possesses considerable adhesive strength to the substrate when the sliding contact load is less than 17.2N, which has an equivalent mean contact pressure (p_m) of 10.82 GPa. The average depth of penetration of the Rockwell stylus is reported while constant loading scratch tests are underway; for 10N and 20N loading conditions, they are $4.97 \pm 0.12 \mu\text{m}$ and $9.21 \pm 0.30 \mu\text{m}$, respectively.

4.5 Wear behaviour of Ti-10V-2Fe-3Al

4.5.1 Wear behaviour of Ti-10V-2Fe-3Al as-received

Variations of wear rates with the applied load of both Ti-10V-2Fe-3Al and Ti-6Al-4V are plotted in Figure 4.47. The rising trend of wear rate with the applied load appears to occur at a faster pace up to 3.5N, and above this load the increase in wear rate slows down. The wear rate rising trend of Ti-6Al-4V, in general, is similar to Ti-10V-2Fe-3Al. The wear rate of Ti-6Al-4V from 0.8N to 2N is relatively higher. Nevertheless, at 3.5N, the wear rates for both alloys are almost the same. A further increase to 5N, Ti-6Al-4V shows a higher wear rate again. The average COF values at the steady state condition are plotted against the applied normal load during wear tests in Figure 4.48. It can be observed that average COF values are remaining constant to the applied load for

Ti-10V-2Fe-3Al. The highest COF value corresponds to the test at 0.8N and gradually decreases upon increasing the load. However, it appears that above 3.5N, the average COF value remains more or less the same for both alloys.

In Figure 4.49, variation of the COF with sliding distance is plotted for 0.8N and 5N wear tests. A longer running-in period (~70 m) is observed for wear tests at higher applied load of 5N before the steady-state condition is reached. However, in the wear test at 0.8N, the steady-state condition is reached after ~45 m and the COF vs. sliding distance shows a smoother trend with a lower extent of fluctuations.

Representative three- and two-dimensional optical profiles from the 0.8N and 5N wear tracks are given in Figure 4.50 and Figure 4.51, respectively. It is evident that a wear test at a higher applied load resulted in a deeper and wider wear track with significant material pile up on the sides of the track.

The SEM micrograph from typical morphology of worn surfaces of the Ti-10V-2Fe-3Al coupons after sliding at 0.8N is shown in Figure 4.52-a. The wear track consisted of abraded regions with continuous grooves and ploughing marks along the sliding direction (Figure 4.52-b) and areas that contained a layer of accumulated material surrounded by fine wear debris particles (Figure 4.52-c). Closer examination revealed the presence of micro-cracks on the surface of accumulated layers. Elemental analysis of these layers by EDS indicates that they mainly consisted of elements from the substrate (Ti, V, Al and Fe) as well as oxygen.

The generated wear debris at 0.8N are carefully collected and examined by the SEM/EDS. These particles are in the form of compacted platelets (Figure 4.53-a), fine equiaxed particles (Figure 4.53-b) with the same elemental composition (Ti, Al, V, Fe

and O) and belt-like particles resembling micro-cutting chips with the same composition as substrate alloy (Ti, Al, V and Fe) (Figure 4.53-c).

Back-scattered electron (BSE) SEM image indicates that the location of FIB analysis is chosen on the area where the accumulation of wear particles presents on the Ti-10V-2Fe-3Al coupon after a wear test at 0.8N. Therefore, the wear track cross-section is parallel to the sliding direction to observe the microstructure and element analysis underneath the worn surface. Figure 4.54-a shows the location of ion milling on one of the plateaus on the wear track surrounded by very fine debris particles. After ion milling, the cross section of the indicated plateau on the wear track contains the mechanically mixed layer (MML) and the deformed substrate, as shown in Figure 4.54-b. The MML under high magnification (as shown in Figure 4.54-b) had an average thickness of $7.3 \pm 0.2 \mu\text{m}$. This layer is exfoliated from the Ti alloy substrate. The micrographs illustrate the morphology of the MML, such as the presence of pores and the mixing of α and β phases in this layer, as well as its spallation from the substrate. Meanwhile, plastic deformation of the substrate in the sliding direction can be seen.

The wear scar on the steel counter-face after the 0.8N test had a circular shape 600 μm in diameter, as shown in Figure 4.55-a, and mainly consisted of accumulated material (Figure 4.55-b). Their chemical composition is similar to that of accumulated layers on the wear track of the Ti-10V-2Fe-3Al coupon (Figure 4.52-c).

Figure 4.56 is a secondary electron SEM image showing the wear track from the worn surface of a Ti-10V-2Fe-3Al sample tested at 5N normal load. Similar to 0.8N worn surface, there are micro-ploughing marks in the abraded area (Figure 4.56-b) and wear debris piled-up area (Figure 4.56-c). More and wider longitudinal micro-ploughing marks

filled with oxide particles (10 μm wide) can be observed on the wear track. Besides, micro-cracks normal to the sliding direction are observed on the worn surface shown in Figure 4.56-c. Wear debris generated at a 5N load consisted of Ti plates and two morphologies of oxides, which are the TiO flakes and the TiO fine particles illustrated in Figure 4.57.

The location of ion milling is chosen on the wear track surrounded by very fine debris particles. Figure 4.58-a illustrates the morphology of MML on the cross section of the wear track on the Ti-10V-2Fe-3Al coupon after a wear test at 5N. Pores and the mixing of α and β phases are present in this layer, which is indicated in the EDS map as shown in Figure 4.59. Mechanically mixed layer thickness is measured at $9.3 \pm 0.63 \mu\text{m}$. Meanwhile, substrate plastic deformation can be proved from the deformed β grains (Figure 4.58-b).

The wear mark on the worn surface of SAE 52100 steel ball counter-face after a test at 5N is approximately 1 mm in diameter, which is twice as big as the 0.8N wear mark. Figure 4.60-a shows the most part of the wear mark are piled up with oxides. Wide ploughing marks are visible due to the increase of the real area of contact during the sliding process when the load increased from 0.8N to 5N. The cracks and debonding of the particles are observable in the accumulated area of the SAE 52100 steel ball after a wear test at 5N (Figure 4.60-b).

4.5.2 Wear behaviour of ion nitrided Ti-10V-2Fe-3Al

Variations of wear rates with the applied load of both untreated and ion nitrided Ti-10V-2Fe-3Al are plotted in Figure 4.61. Wear rates of ion nitrided samples are much lower compare with untreated values. The wear rate of 2N ion nitrided sample is

negative, which indicates that there is no wearing on the sample surface and there are wear debris generated from the counterface. The wear rates for both alloys are almost the same. A further increase to 3.5N and 5N, ion nitrided Ti-10V-2Fe-3Al samples show a relatively higher wear rate. However, compare with the wear rates of untreated samples, ion nitrided wear rates at 3.5N and 5N are decreased by 55% and 47%, respectively. The average COF values at the steady state condition are plotted against the applied normal load during wear tests in Figure 4.62. It can be observed that average COF values remain constant for both untreated and ion nitrided Ti-10V-2Fe-3Al. The average COFs for ion nitrided Ti-10V-2Fe-3Al, in general, is less than the COFs for untreated Ti-10V-2Fe-3Al. In Figure 4.63 and Figure 4.64, variation of the COF with sliding distance is plotted for 2N and 3.5N wear tests, respectively. From the figures, COF curves for ion nitrided samples are much smoother compare to untreated samples' curves. A longer running-in period (~70 m) is observed for wear tests at 3.5N on the untreated sample before the steady-state condition is reached. However, for the wear tests at 2N, the steady-state condition is reached after ~45 m for both untreated and ion nitrided samples.

4.6 Tensile properties of Ti-10V-2Fe-3Al

4.6.1 Tensile properties of Ti-10V-2Fe-3Al as-received

Stress-strain curves for each trial of the tensile test are plotted in Figure 4.65. Tensile properties, including yield strength, ultimate tensile strength, elastic modulus and percentage of elongation are listed in Table 4.7. To study the microstructure-initiated behaviour in titanium alloys, tensile properties of Ti-10V-2Fe-3Al are compared with ELI Ti-6Al-4V, which is the most widely commercially used titanium alloy. ELI Ti-6Al-4V alloy has a mill-annealed structure containing equiaxed interconnected α grains, grain

boundary β particles and fine recrystallized β particles inside the α grains. Initial α phase grain size is around 3 μm in diameter, and has an average 20% volume fraction of the β phase.

Table 4.7 List of tensile properties for Ti-10V-2Fe-3Al and Ti-6Al-4V [5,86,87]

SAMPLE #	YIELD STRENGTH (MPA)	UTS (MPA)	ELASTIC MODULUS (GPA)	ELONGATION (%)
Ti-10V-2Fe-3Al	821.5	881	92	18.9
ELI Ti-6Al-4V	827	896	94	10

The results plotted in Figure 4.66 reveal that the Ti-10V-2Fe-3Al alloy generally shows similar strength and stiffness compared to the Ti-6Al-4V alloy. The ultimate tensile strength and yield strength ($\sigma_{y 0.2}$) of this alloy is approximately 1.7% and 0.7% lower than those of Ti-6Al-4V, respectively. However, a 47% increment of elongation percentage value indicates a significantly superior ductility of the near- β titanium alloy.

SEM fractographs of Ti-10V-2Fe-3Al samples after tensile tests show the ductile cup-and-cone type of fracture morphology (Figure 4.67) consisting of shear lips and a central rupture region. Several cracks (approximately 100 μm long) are expanded to over 10 μm in width and are shown in Figure 4.67-b. The formation of these cracks resulted from the coalescence of micro-cracks generated at grain boundary α phase in β matrix. Figure 4.68-b is an SEM micrograph showing the population of dimples (3 μm < dimple diameter < 10 μm) with irregular shapes in the ruptured region; which is a typical ductile fracture mode. There are shallow micro-voids shown (about 5 μm in diameter) in Figure 4.68-b, which indicate shear deformation during the tensile test. Figure 4.69 shows the microstructure features of this region after etching. Observation of the skin of the samples revealed the formation of elongated α grains distributed near the fracture region as shown

in Figure 4.69-b and reveals surface microstructure change under tensile loading. An array of α grains are stretched in the tensile loading direction, which resulted from high tensile ductility of the Ti-10V-2Fe-3Al alloy compared to the Ti-6Al-4V alloy.

4.6.2 Tensile properties of ion nitrided Ti-10V-2Fe-3Al

The plot of stress–strain curves for untreated and ion nitrided Ti-10V-2Fe-3Al is given in Figure 4.70. Tensile properties of untreated and ion nitrided Ti-10V-2Fe-3Al are listed in Table 4.8 and compared in Figure 4.71. The yield and ultimate tensile strength of the ion nitrided alloy compared to the untreated alloy increased by 6% and 5%, respectively. However, it is found that elongation of the ion nitrided alloy decreased from 18.9% to 15.9%.

Table 4.8 Comparison of tensile properties between untreated and ion nitrided Ti-10V-2Fe-3Al

Ti-10V-2Fe-3Al	0.2 % YIELD STRENGTH ($\Sigma_{0.2}$), MPa	ULTIMATE TENSILE STRENGTH (Σ_{UTS}), MPa	ELONGATION (Φ), %	ELASTIC MODULUS (E), GPa
UNTREATED	821.5 \pm 4.2	88.01 \pm 5.1	18.9 \pm 0.3	92.0 \pm 4.0
ION NITRIDED	873.0 \pm 5.3	922.5 \pm 11.7	15.9 \pm 0.44	95.0 \pm 5.2

The resulting fractographs for both untreated and ion nitrided Ti-10V-2Fe-3Al are given in Figure 4.72. Both samples show the cup-and-cone-shaped ductile type of fracture. The untreated alloy (Figure 4.73-a) has a ductile fractured region and a sheared region. Dimples with an average size of 12.3 μm^2 are shown in Figure 4.73-b. The area fraction of ductile fractured to the overall fractured region for untreated alloy and ion nitrided alloy is 39% and 43%, respectively.

A diffusion zone with an average depth of 30 μm from the nitrided surface is formed, as shown in Figure 4.74-a. Dimples in the ductile fractured region had an

average size of $3.5 \mu\text{m}^2$; they are smaller than those in the sheared region, which have an average size of $13.8 \mu\text{m}^2$ as shown in Figure 4.74-a. Meanwhile, a close observation on the diffusion zone is given in Figure 4.74-b, showing micro-voids initiated from α/β interface. The average grain size in the diffusion zone is measured as $6 \mu\text{m}^2$.

4.7 Fatigue properties of Ti-10V-2Fe-3Al

4.7.1 Fatigue properties of Ti-10V-2Fe-3Al as-received

S-N fatigue curves of untreated Ti-10V-2Fe-3Al and Ti-6Al-4V in rotating beam loading at a stress ratio ($R = -1$) is shown in Figure 4.75. The fatigue strength of untreated Ti-10V-2Fe-3Al at 10^7 cycles is near 800 MPa, which is higher than 625 MPa and 525 MPa, the fatigue strength of untreated Ti-6Al-4V at 10^7 cycles, increased by 28% and 52%, respectively.

Fracture surfaces of fatigue samples that had failed at different stress levels of 797 MPa, 827 MPa and 887 MPa are examined under the SEM to study fatigue crack initiation and propagation. Fatigue crack initiation sites at various stress levels are shown in figures range from Figure 4.76 to Figure 4.79. It appears that in all the samples, cracks have initiated close to the surfaces mostly from a single point of origin. Nevertheless, multiple fracture origins are observed on the fatigue sample that failed at the highest applied stress of 887 MPa.

Figure 4.76 reveals some interesting details near the crack initiation on the sample fractured at 797 MPa. There are micro-voids and micro-cracks randomly distributed on the initiation site. This is due to the simultaneous formation of multiple slip steps. Slip steps increase while the loading cycles increase. Micro-voids are believed to initiate from the relatively equally spaced slip steps, which are shallow with a thickness of several

grains resulting from repeated bending rotating cycles [88]. Coalescence of micro-voids form micro-cracks and further coalescence of micro-cracks to form cracks that cause fatigue fracture. Figure 4.77 shows the crack initiation of Ti-10V-2Fe-3Al fatigue sample that failed at a maximum stress level of 827 MPa. The fatigue crack is initiated from an inclusion with a length of 10 μm and a width of 2 μm as shown in Figure 4.77-c. A 40 μm long crack observed in Figure 4.77-b tends to expand further by joining other micro-cracks around it on the initiation site.

Figure 4.78 exposes several interesting details at a higher cyclic loading stress level, 887 MPa. Micro-voids and fatigue striations are obvious; however, cracks are not obvious on the primary initiation site (Figure 4.78-b). This means the coalescence of micro-cracks is rare, which can be explained as the fast crack propagation process at a high magnitude of maximum cyclic loading stress. Micro-cracks do not have enough time to reach their critical flaw size. In contrast, cyclic loading stress exceeds the load-bearing limit of the rest material in a very short duration thus resulting in a catastrophic failure of the fatigue sample in a relatively smaller amount of cycles. Figure 4.79 shows a secondary local crack initiation site, which is very close to the primary crack initiation site shown in Figure 4.78. Micro-cracks are lying perpendicular to the local origin and their length increased as further to the origin, as shown in Figure 4.79-c. Therefore, the Ti-10V-2Fe-3Al fatigue sample under high-level stress (887 MPa) is subject to multiple fatigue fracture initiation sites. Plateaus shown in Figure 4.79-a are ratchet marks, which are evidence of the common fracture by the joining of multiple initiation sites.

Figure 4.80 to Figure 4.82 represent details of the crack propagation process at high magnifications for each stress level from 797 MPa to 887 MPa. Figure 4.80 clearly

displays striations in the crack propagation region. The striations are evenly spaced (pointed by arrows) in Figure 4.80-c. Evenly-spaced striations again reveal highly repeatable constant amplitude loading on the sample. Since the stress amplitude is constant, Figure 4.81 best illustrates the existence of consistent and evenly-spaced striations in the crack propagation region. The width of each striation is measured at 6 μm under a constant loading of 827 MPa.

Figure 4.82 illustrates the crack propagation area on the Ti-10V-2Fe-3Al fracture surface at a high amplitude of cyclic loading, 887 MPa. Ascending spaced striations resulted from the fast crack propagation process (Figure 4.82-c).

Fatigue fracture is the fastest and final fatigue stage which always occurs all of a sudden. Dimple rupture found in titanium fracture surface reveals the ductile type of fracture in titanium alloys. When cyclic stress exceeds the bearing capacity of the rest portion on a fatigue sample it fractures and leaves a certain amount of dimples. These dimples may vary in size. FIGURE 4.83 shows a ductile overload fracture surface of Ti-10V-2Fe-3Al at a maximum stress level of 797 MPa. Similar dimple rupture phenomenon can be observed on other fracture surfaces of Ti-10V-2Fe-3Al, which failed at a different stress level.

4.7.2 Fatigue properties of ion nitrided Ti-10V-2Fe-3Al

Fatigue tests are performed on ion nitrided alloy under optimized conditions (600C, 8 hours, 67 Pa and plasma gas sputtered for 3 hours). The S-N fatigue curve of untreated and ion nitrided Ti-10V-2Fe-3Al in a rotating beam loading at a stress ratio ($R = -1$) is shown in Figure 4.84. The fatigue endurance limit of ion nitrided Ti-10V-2Fe-3Al is 527 MPa. From the S-N curve, it is obvious that nitrided Ti-10V-2Fe-3Al contains

both high- and low-cycle fatigue. When applied cyclic stress is higher than 544 MPa, low-cycle fatigue behaviour of Ti-10V-2Fe-3Al is shown. The maximum cyclic fatigue life is 26,750 cycles when 544 MPa is applied. On the other hand, when applied cyclic stress is below 526.5 MPa, high cycle fatigue is observed where all fatigue samples exceeded 10^7 cycles. Figure 4.85 compares the fatigue test results obtained in this investigation with those nitrided Ti-6Al-4V results found in the literature. It is clear that the fatigue endurance limit of nitrided Ti-10V-2Fe-3Al is 527 MPa, which is higher than the 475 MPa of nitrided Ti-6Al-4V, which has increased by 11%.

SEM fractographs of nitrided fatigue samples fractured at 544 MPa and 744 MPa are given in Figure 4.86 and Figure 4.87. Figure 4.86-a shows the crack initiation region near the sample surface. There is a crack ($\sim 3 \mu\text{m}$) initiated right underneath the compound layer observed in the crack initiation region as shown in Figure 4.86-b. Meanwhile, traces of crack tips that remained in this region revealed multiple crack initiation sites. The crack propagation region is close to the crack initiation region. In Figure 4.86-c, striations are found propagated inside α grains and the orientation of these striations are found altered at the β -grain boundary (Figure 4.86-d).

Figure 4.87-a shows a clear boundary between crack initiation and propagation regions on the fractured surface, as marked by white line. The crack initiation region is bigger compared with the region observed on the fatigue sample broken at 54 MPa. A higher magnification SEM image (Figure 4.87-b) from the crack initiation region shows cracks nucleated from the compound layer, and transgranular cracks are found inside α grains. Traces of crack tips are observed in this region as well. The fatigue crack propagation region consists of enlarged β grains (average size of $332 \mu\text{m}^2$) containing

striations. These striations propagated inside each of the β grains and are stopped at the grain boundary, as shown in Figure 4.87-c and Figure 4.83-d.

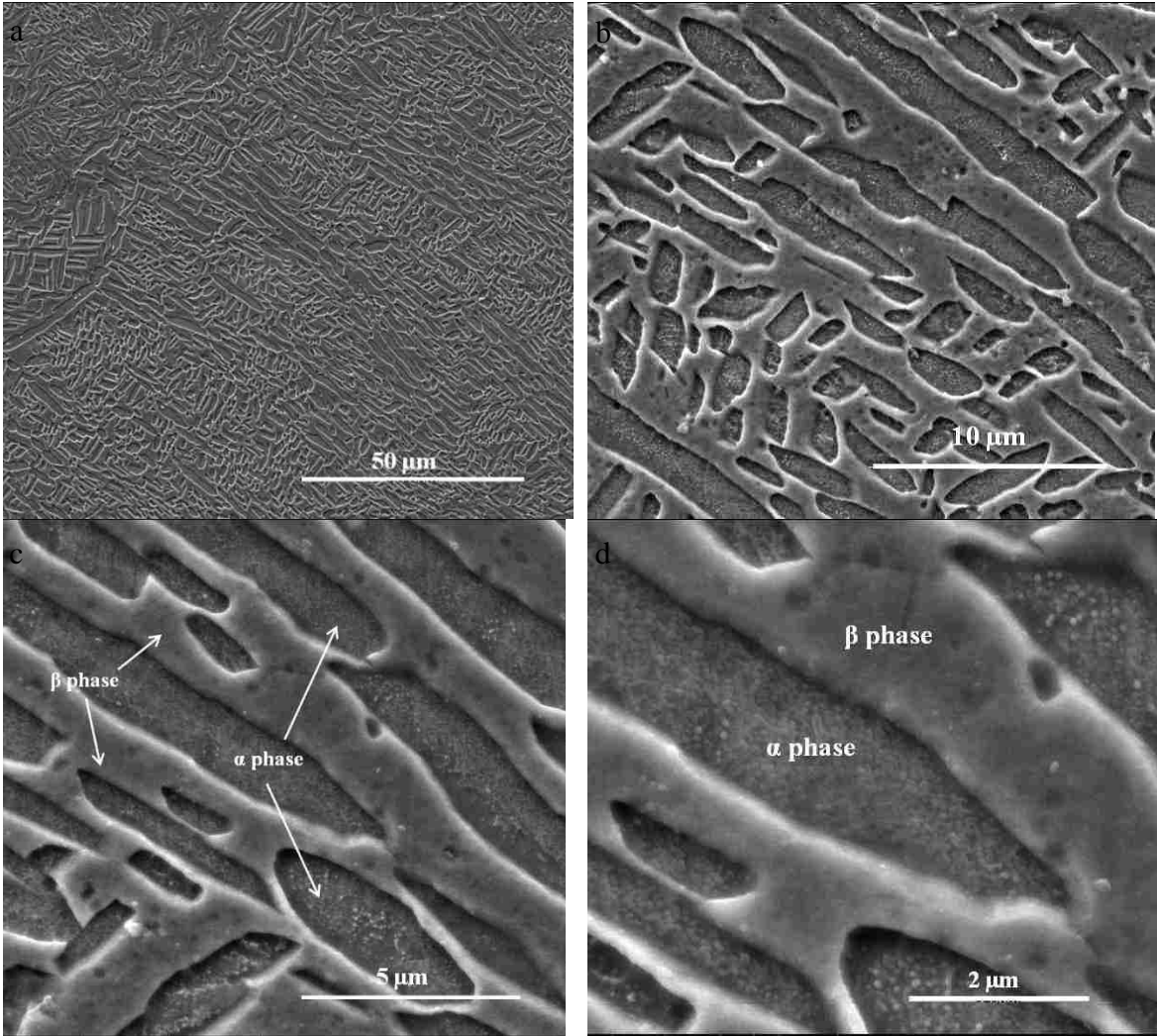


Figure 4.1 Secondary electron SEM image (SI) showing top surface microstructure of untreated Ti-10V-2Fe-3Al alloy at various magnification (a) 1000X, (b) 5000X, (c) 10000X, and (d) 20000X

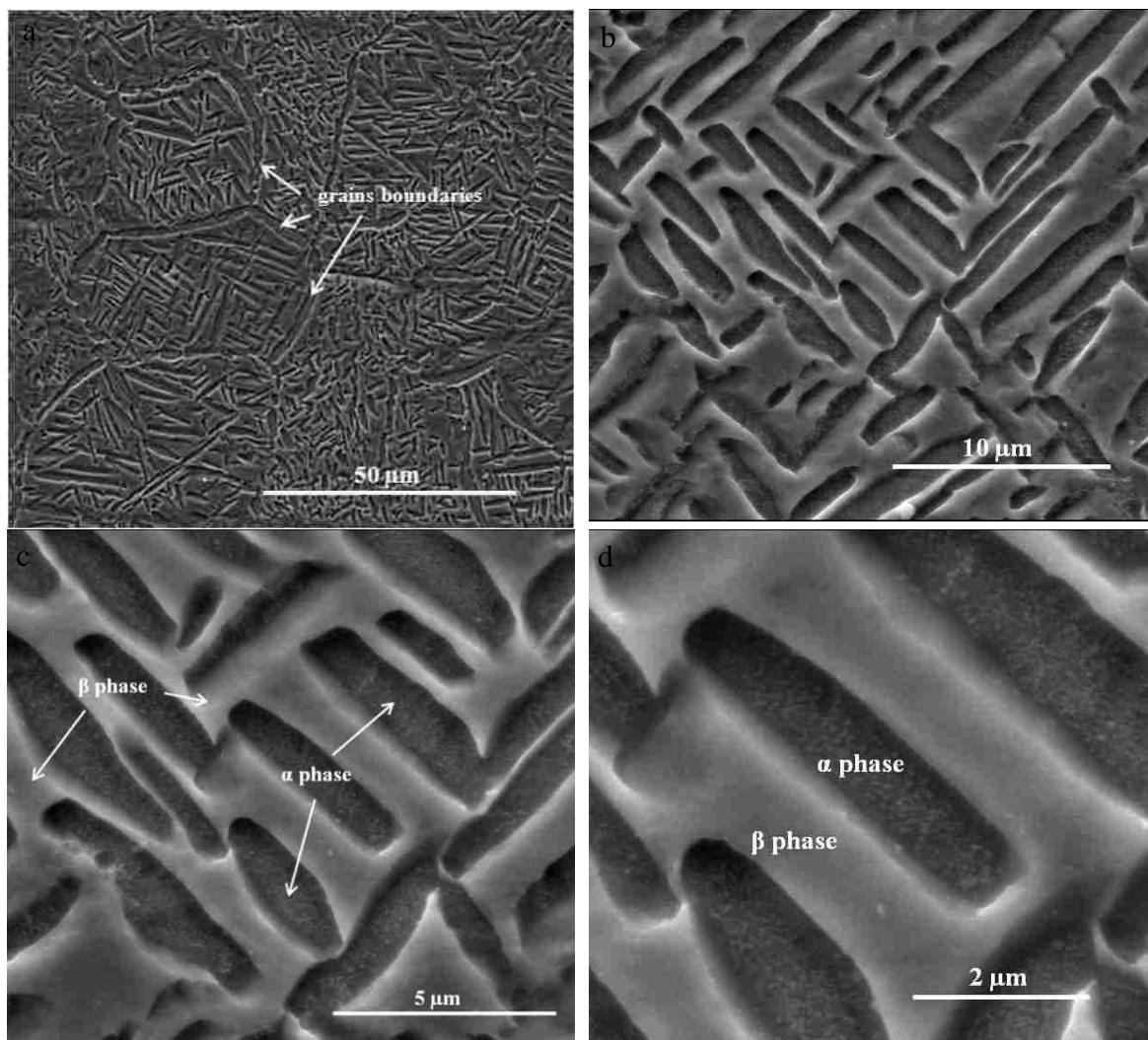


Figure 4.2 Secondary electron SEM image (SI) showing cross-sectional microstructure of untreated Ti-10V-2Fe-3Al alloy at various magnification (a) 1000X, (b) 5000X, (c) 10000X, and (d) 20000X.

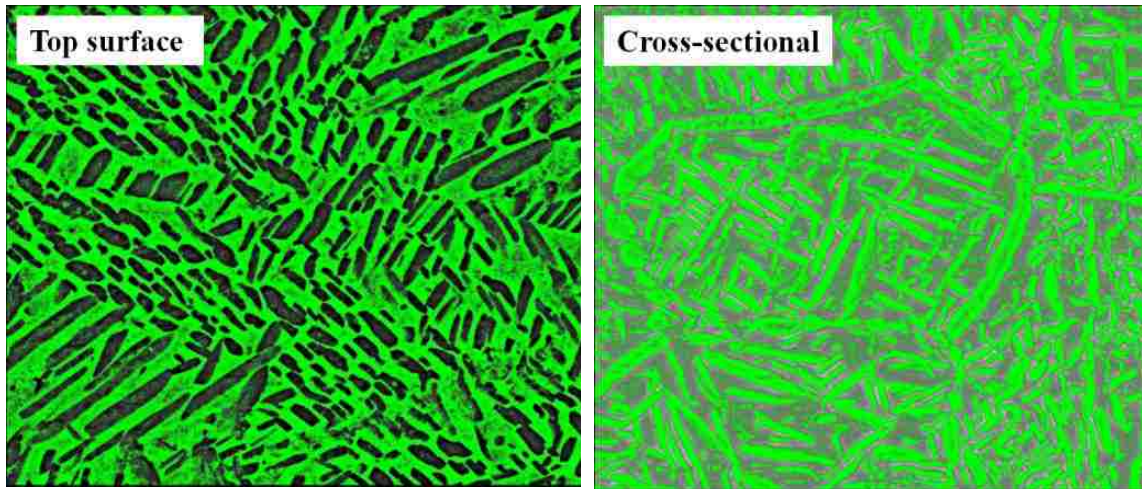


Figure 4.3 Phase composition analysis using “Omnimet 8.9[®]” software showing β phase percentage constituents in untreated alloy.

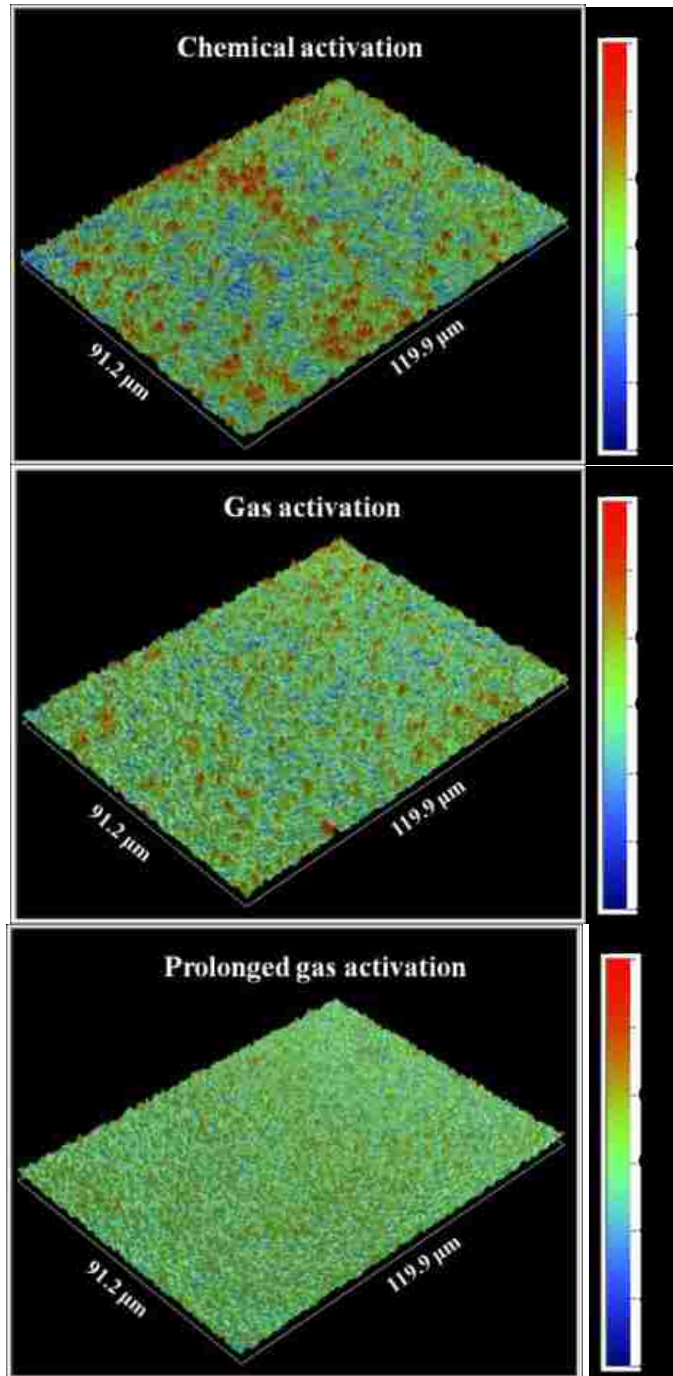


Figure 4.4 Optical 3D profile from surface topography of Ti-10V-2Fe-3Al with pre-treatment method of chemical activation, gas activation, and elongated gas activation

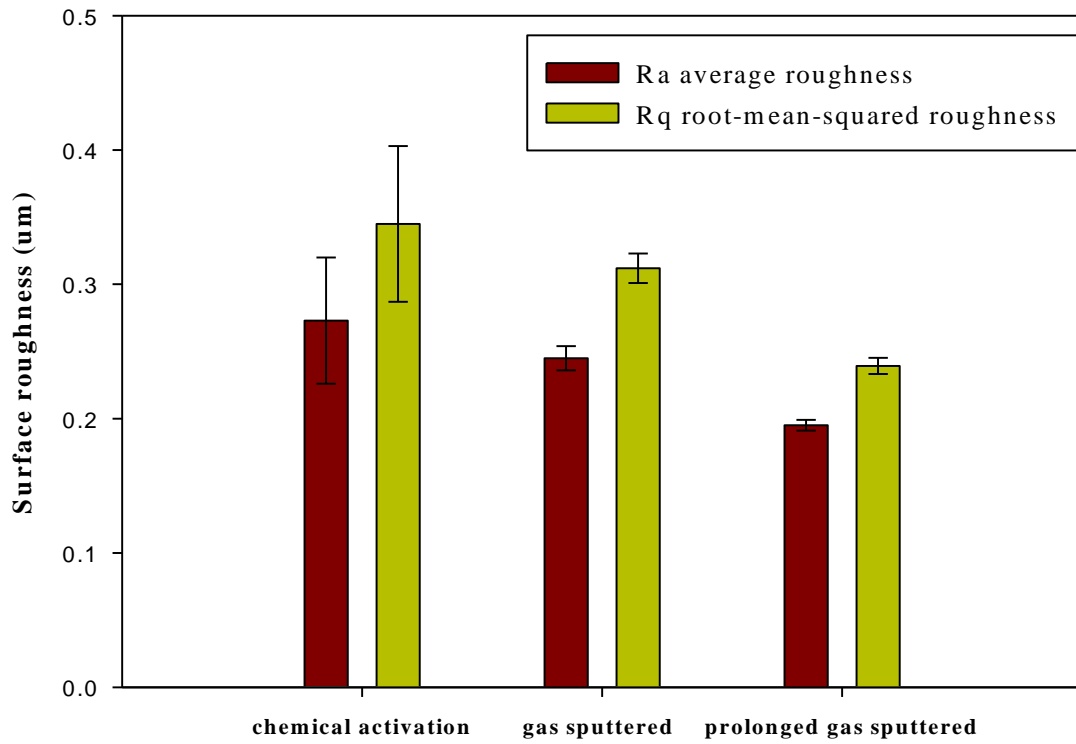


Figure 4.5 Variation of surface roughness with nitriding pressure on ion nitrided Ti-10V-2Fe-3Al

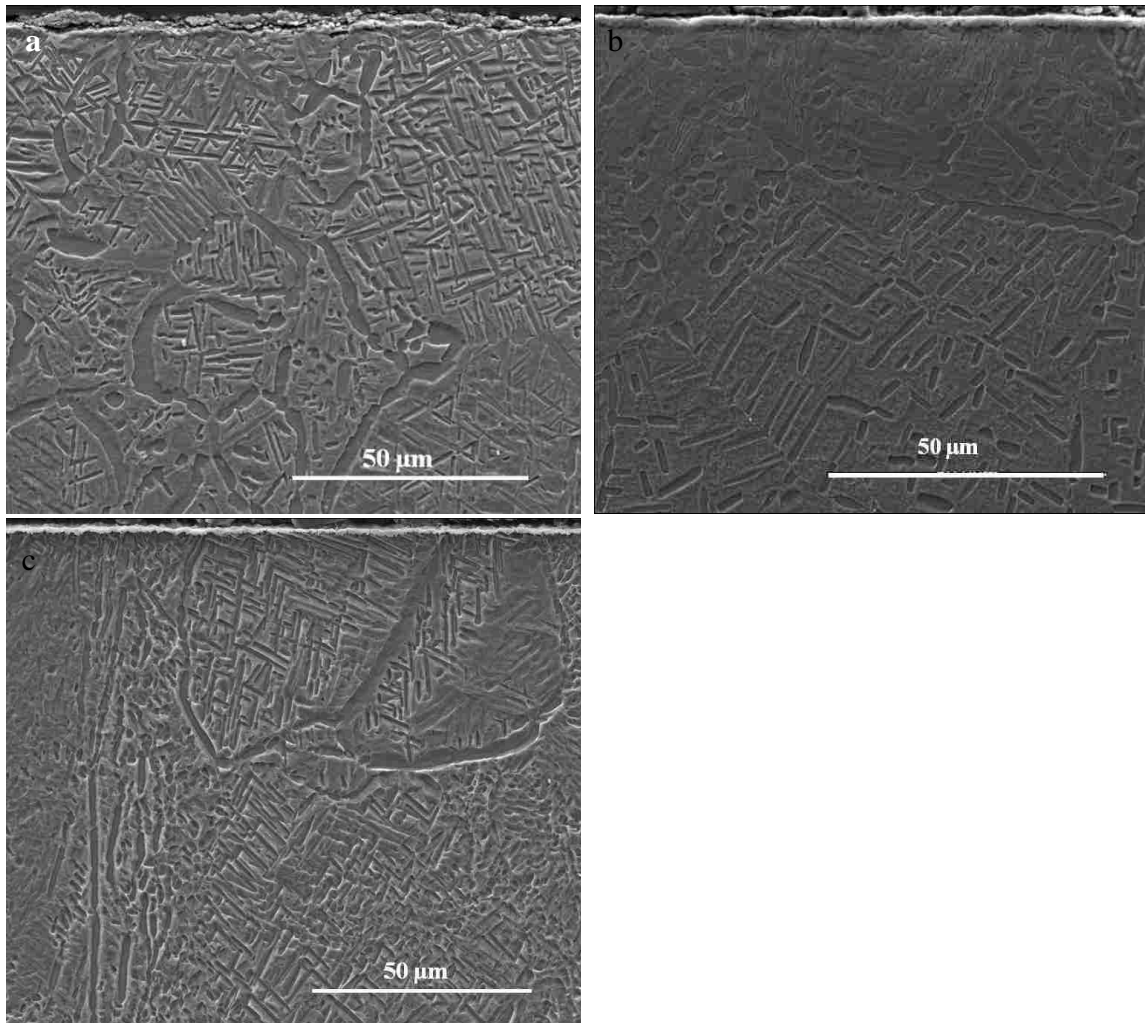


Figure 4.6 Secondary electron SEM image (SI) showing the cross-sectional microstructure of nitrided Ti-10V-2Fe-3Al pre-treated with (a) chemical pickling, (b) gas sputtering, and (c) prolonged gas sputtering

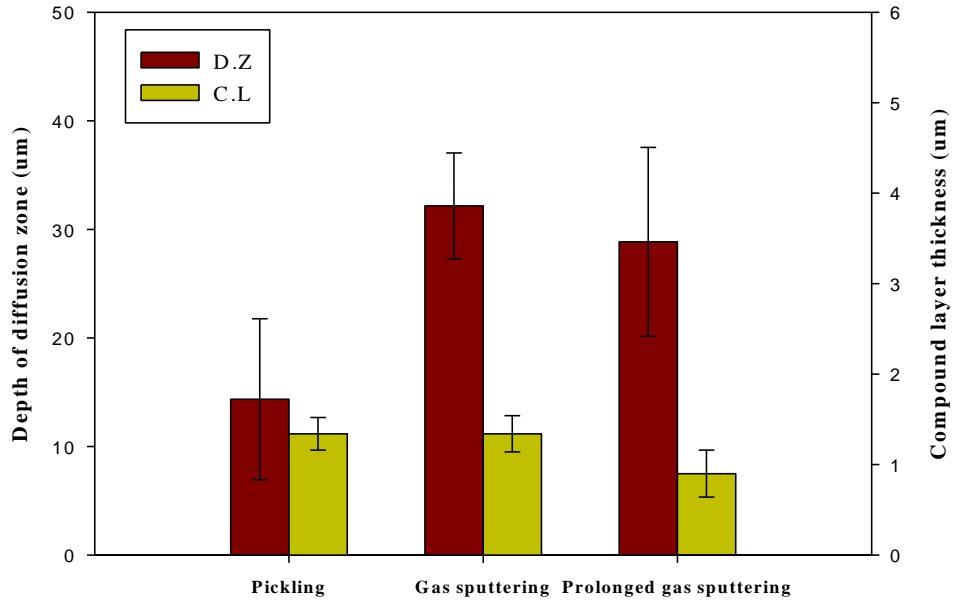


Figure 4.7 Variation of depth of diffusion zone and thickness of compound layer with pre-treatment measures

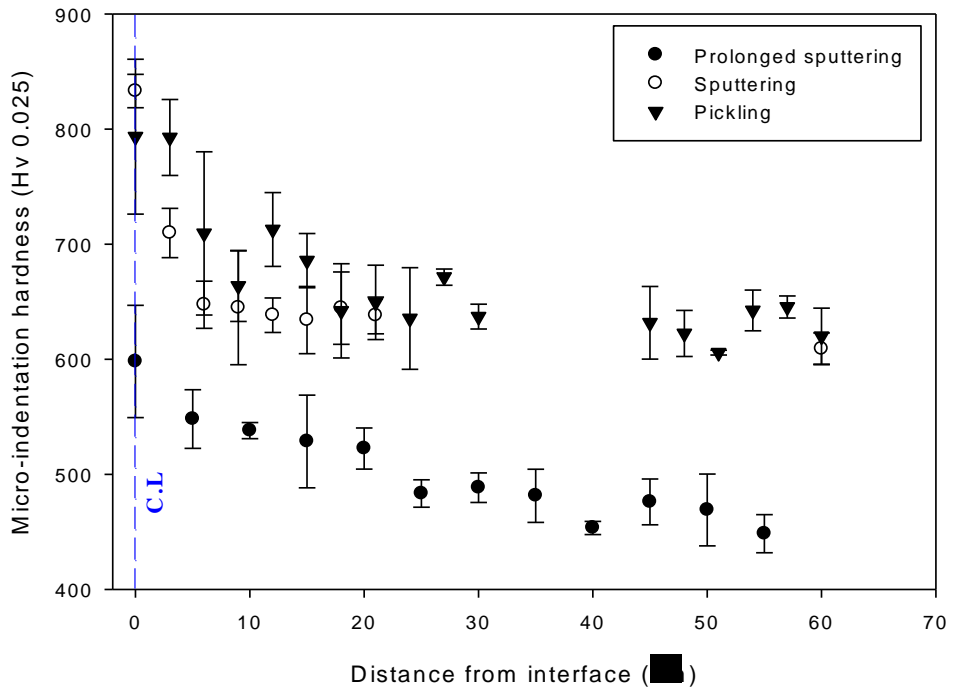


Figure 4.8 Micro-indentation hardness depth profiles of Ti-10V-2Fe-3Al nitrided at 600C with various pre-treatment measures

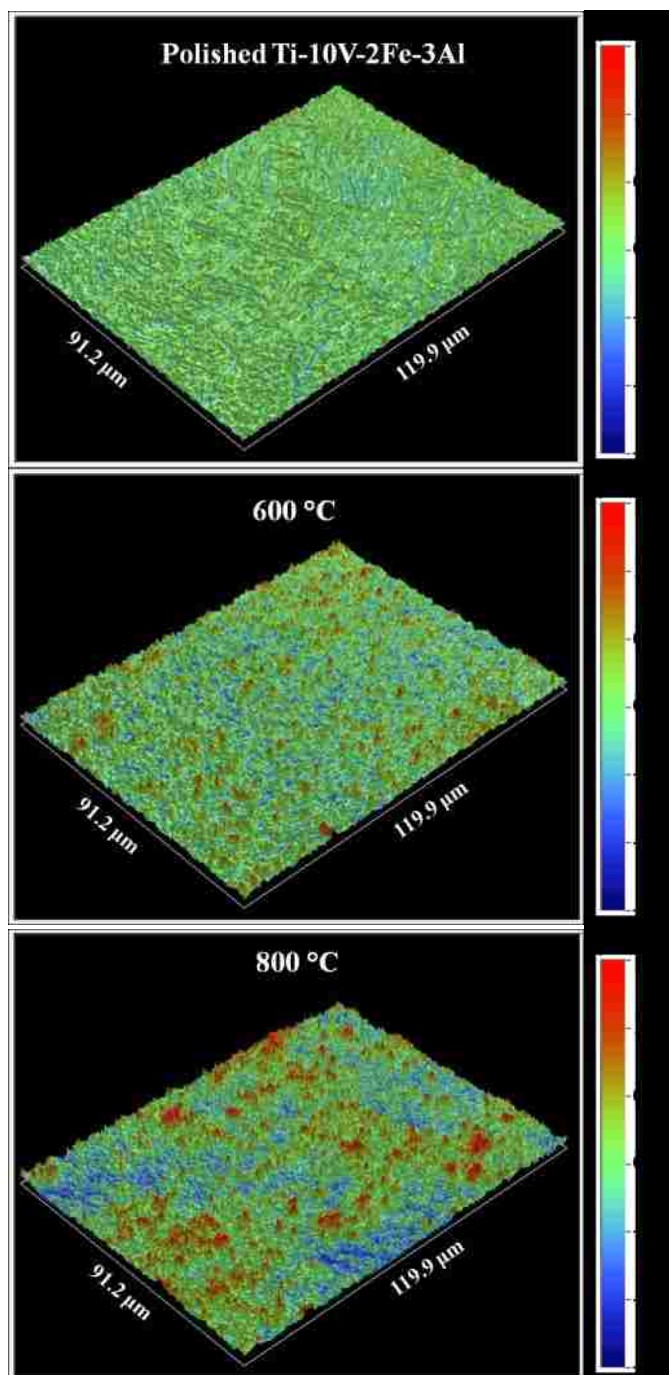


Figure 4.9 Optical 3D profile from surface topography of Ti-10V-2Fe-3Al untreated, nitrided at 600°C and 800°C

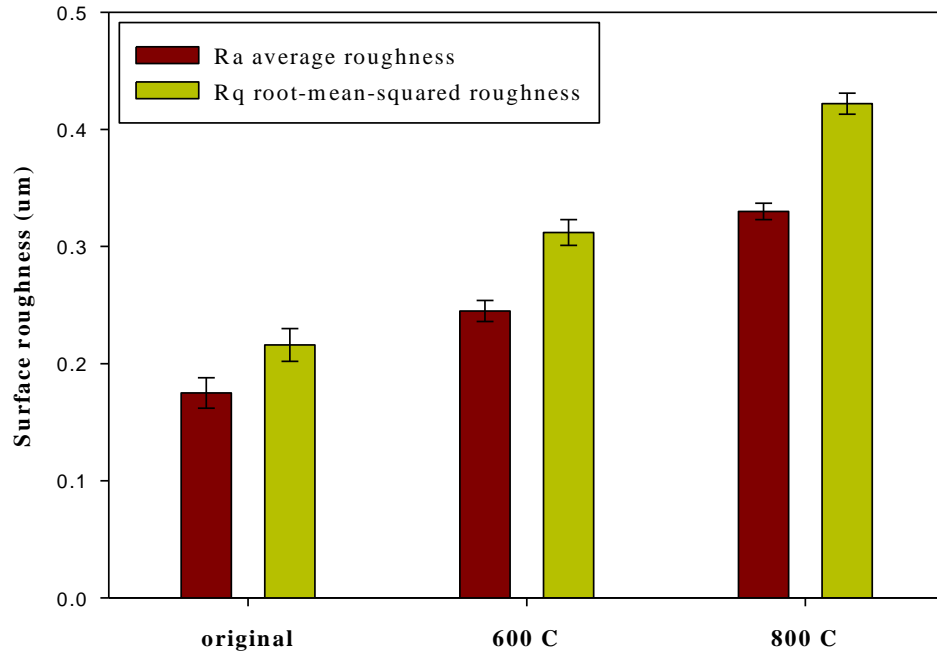


Figure 4.10 Variation of surface roughness with nitriding temperature

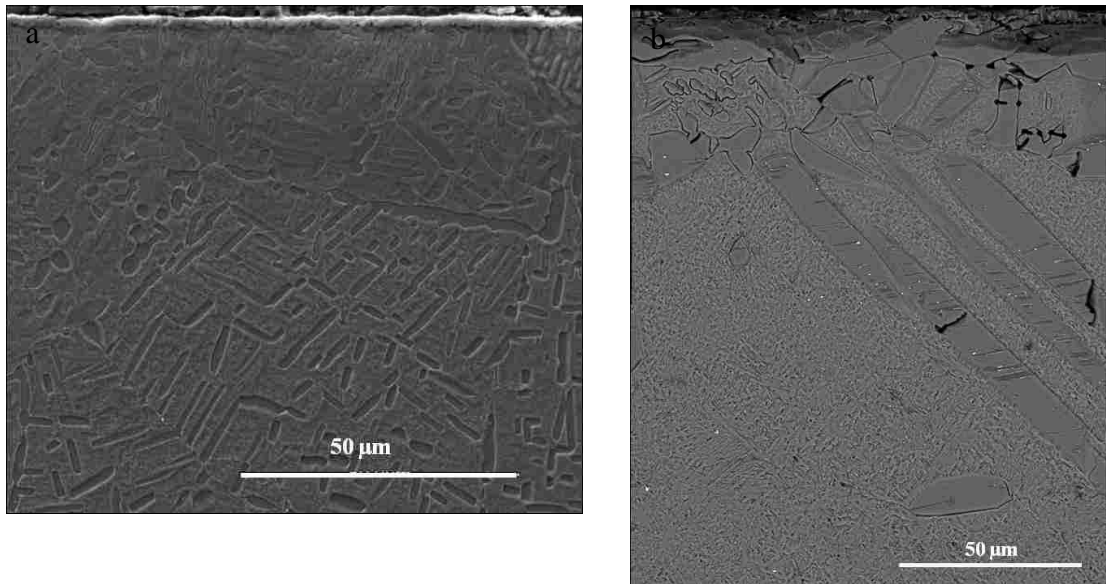


Figure 4.11 Secondary electron SEM image (SI) showing the cross-sectional microstructure of Ti-10V-2Fe-3Al nitrided at (a) 600°C and (b) 800°C.

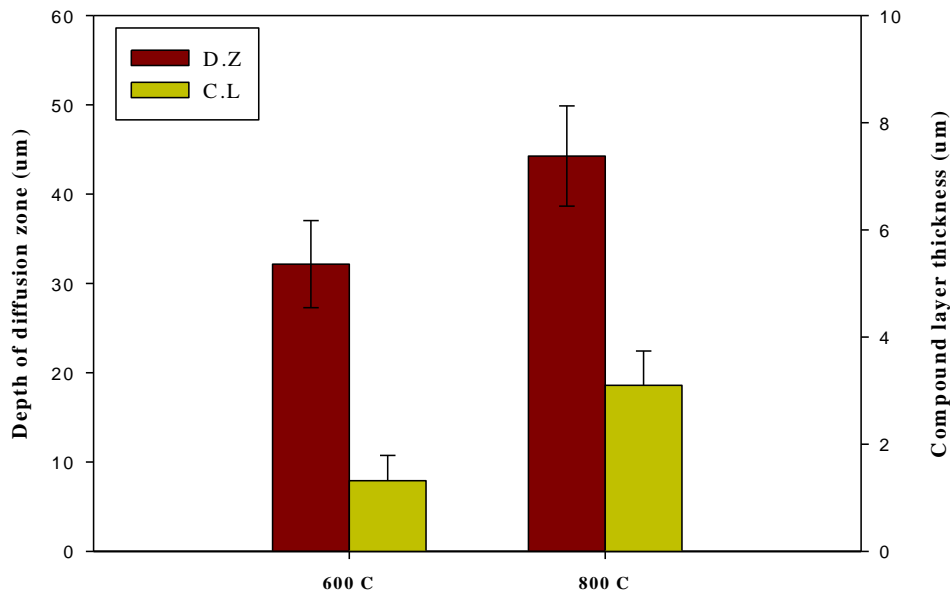


Figure 4.12 Variation of depth of diffusion zone and thickness of compound layer with nitriding temperature

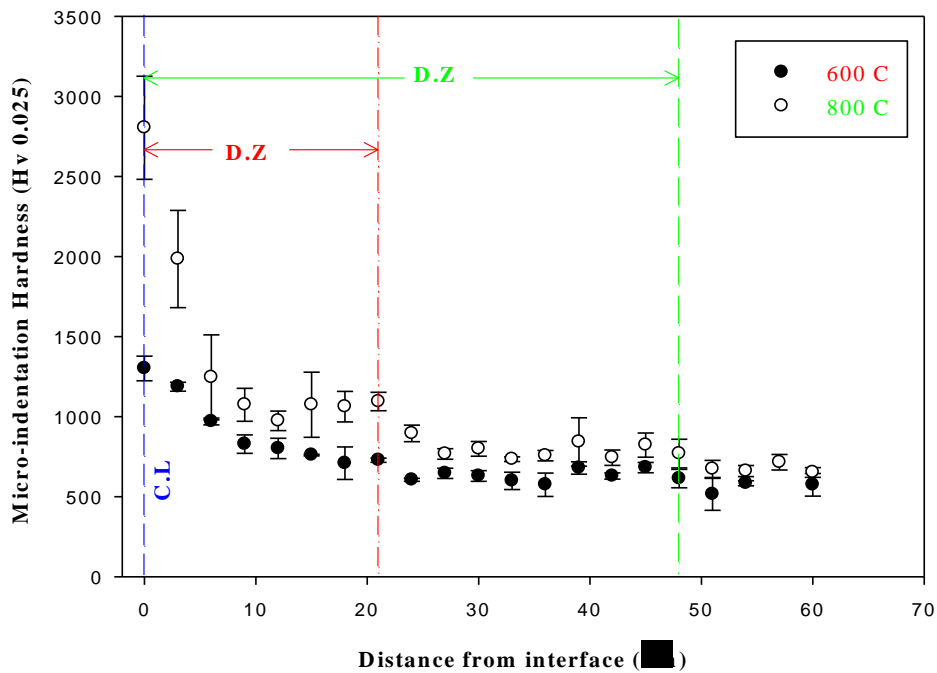


Figure 4.13 Micro-indentation hardness depth profiles of Ti-10V-2Fe-3Al nitrided at 600°C & 800°C.

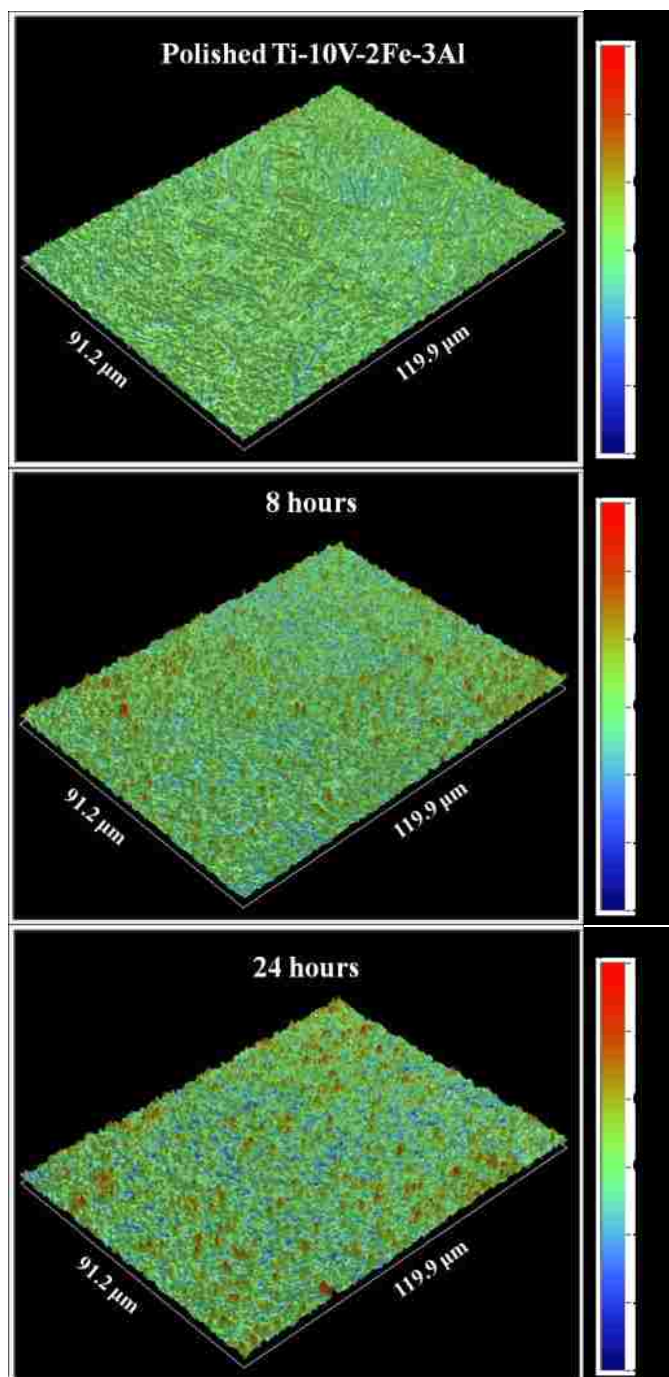


Figure 4.14 Optical 3D profile from surface topography of Ti-10V-2Fe-3Al untreated, nitrided at 8 hours and 24 hours

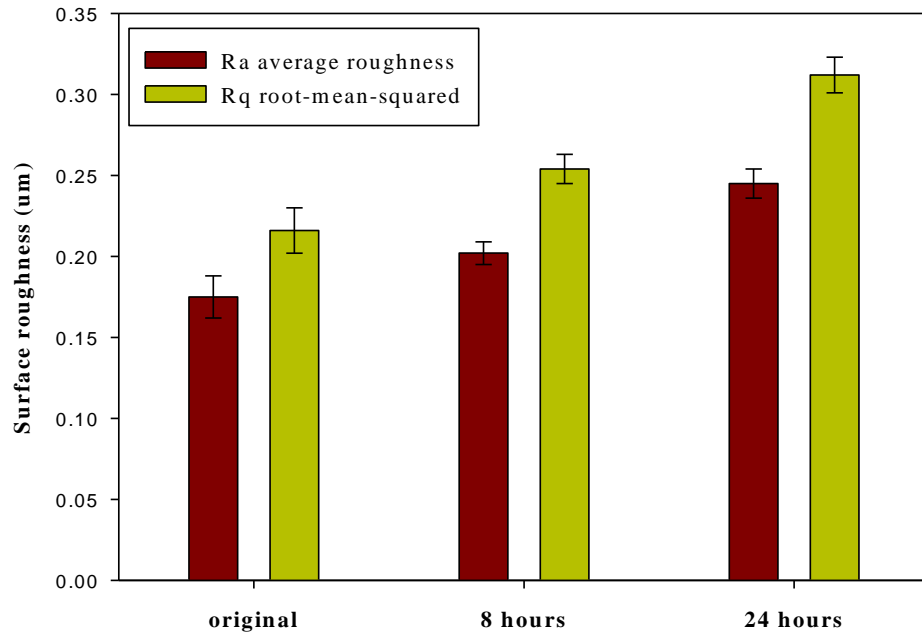


Figure 4.15 Variation of surface roughness with nitriding time

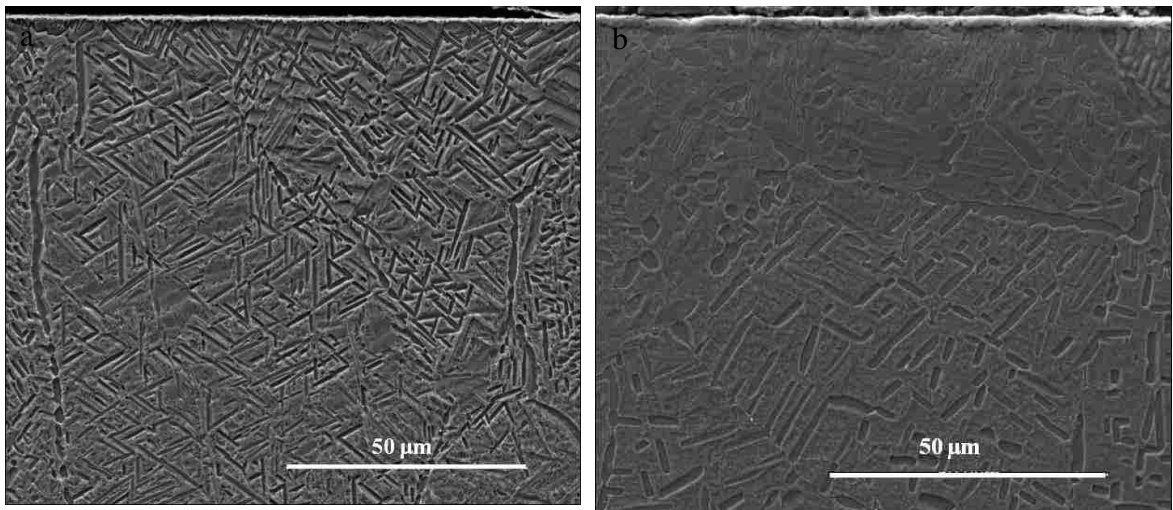


Figure 4.16 Secondary electron SEM image (SI) showing the cross-sectional microstructure of Ti-10V-2Fe-3Al nitrided at (a) 8 hours and (b) 24 hours.

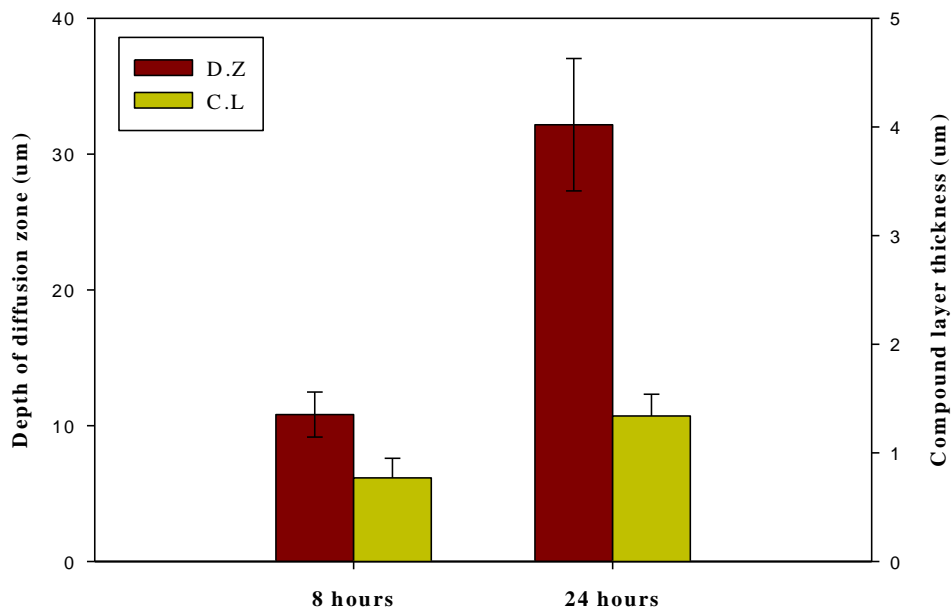


Figure 4.17 Variation of depth of diffusion zone and thickness of compound layer with nitriding time

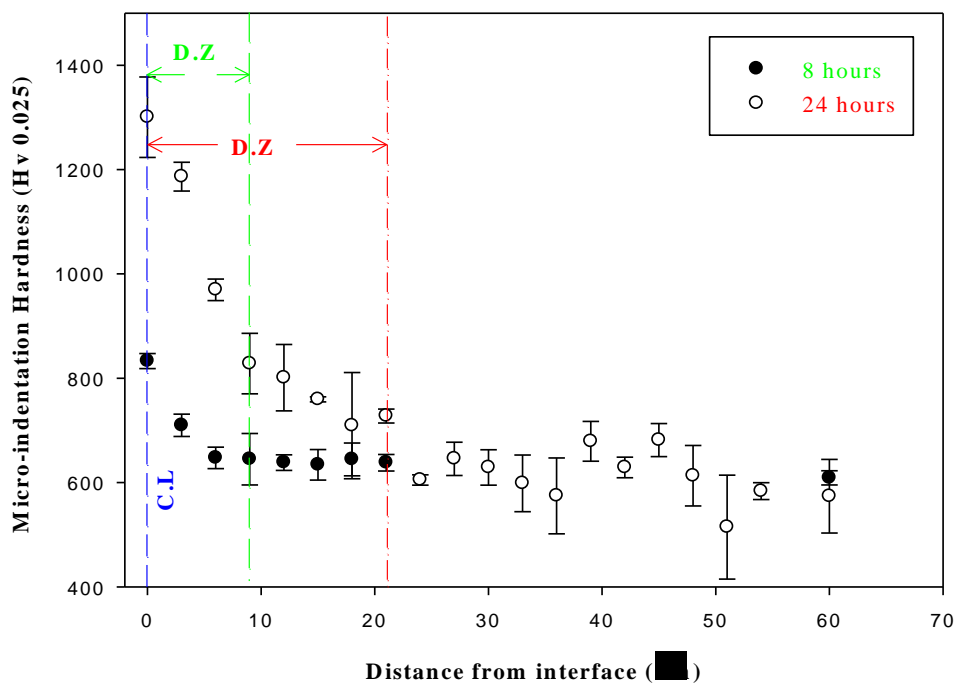


Figure 4.18 Micro-indentation hardness depth profiles of Ti-10V-2Fe-3Al nitrided for 8 & 24 hours

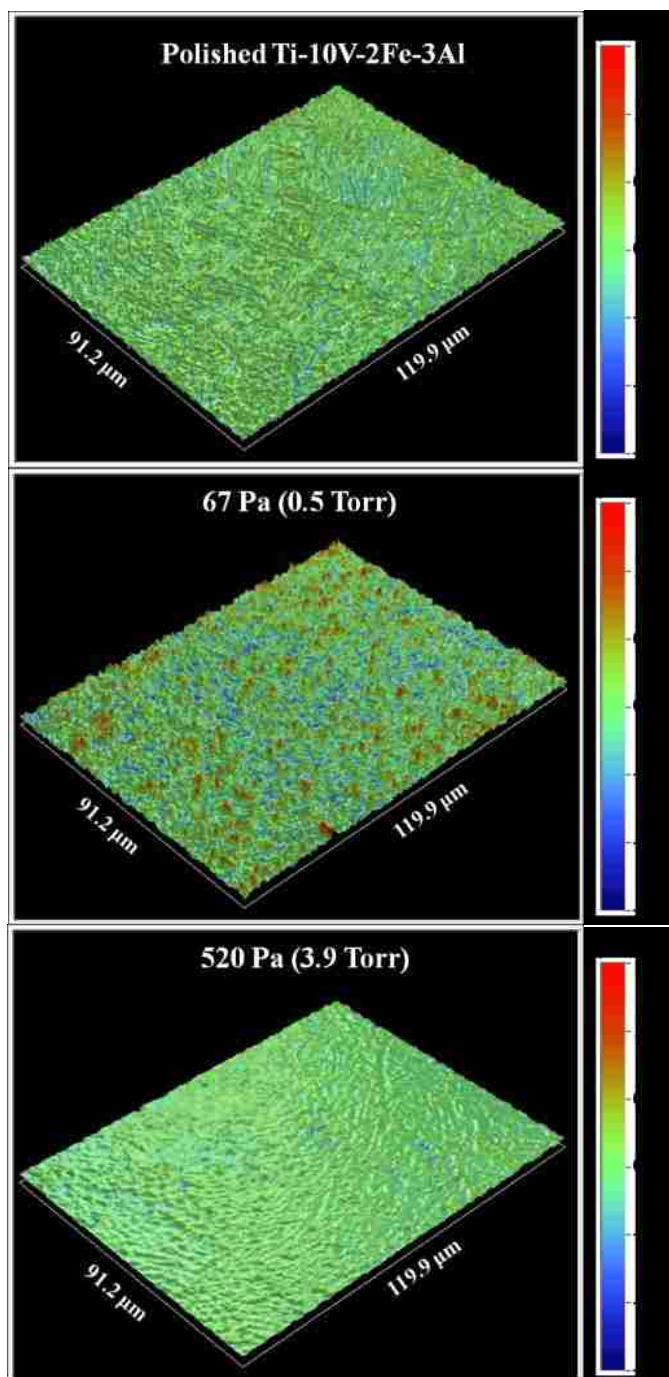


Figure 4.19 Optical 3D profile from surface topography of Ti-10V-2Fe-3Al untreated, nitrided at 600°C and 800°C

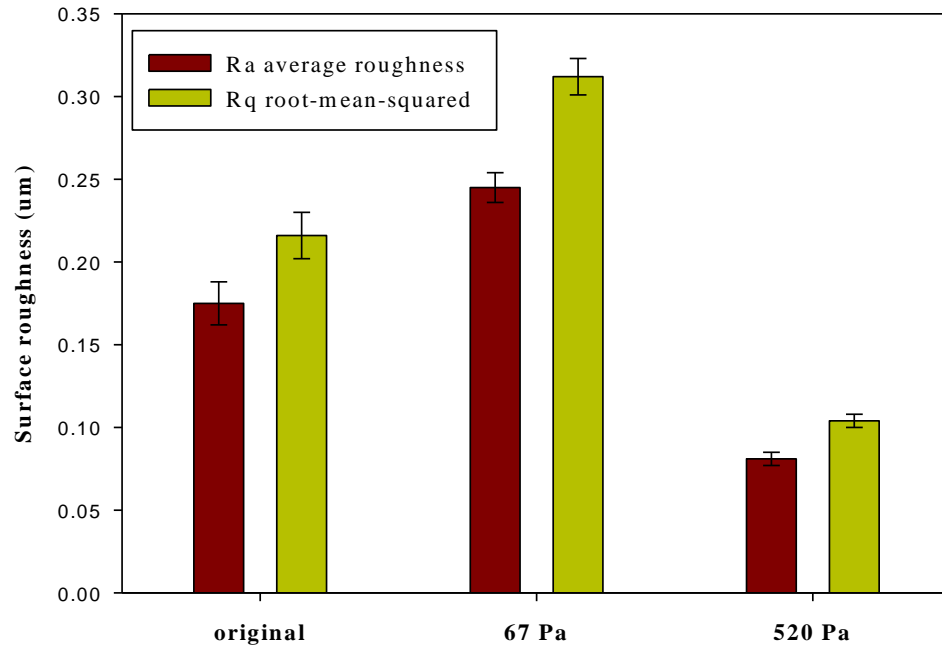


Figure 4.20 Variation of surface roughness with nitriding pressure

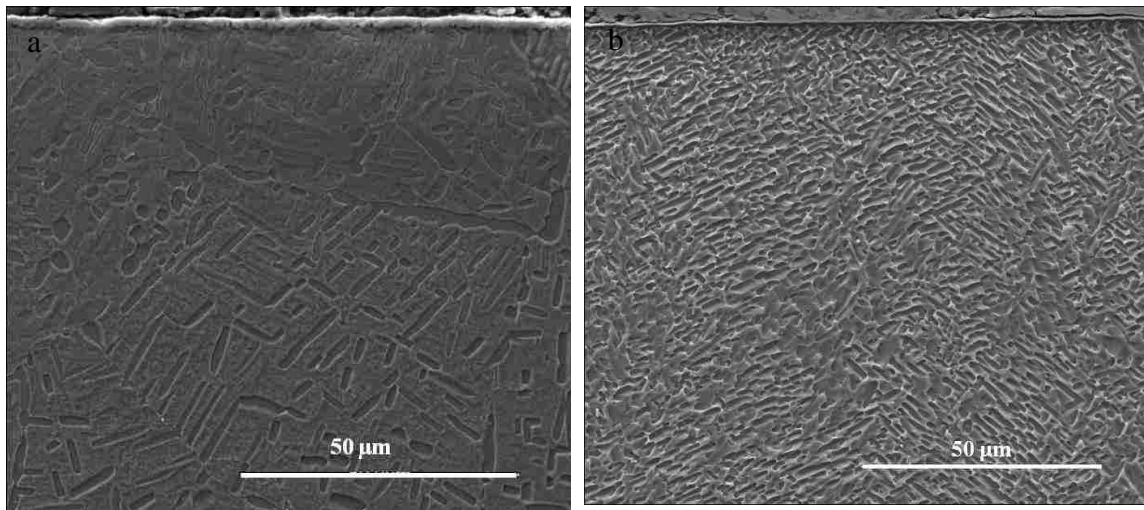


Figure 4.21 Secondary electron SEM image (SI) showing the cross-sectional microstructure of Ti-10V-2Fe-3Al nitrided at (a) 67 Pa and (b) 520 Pa.

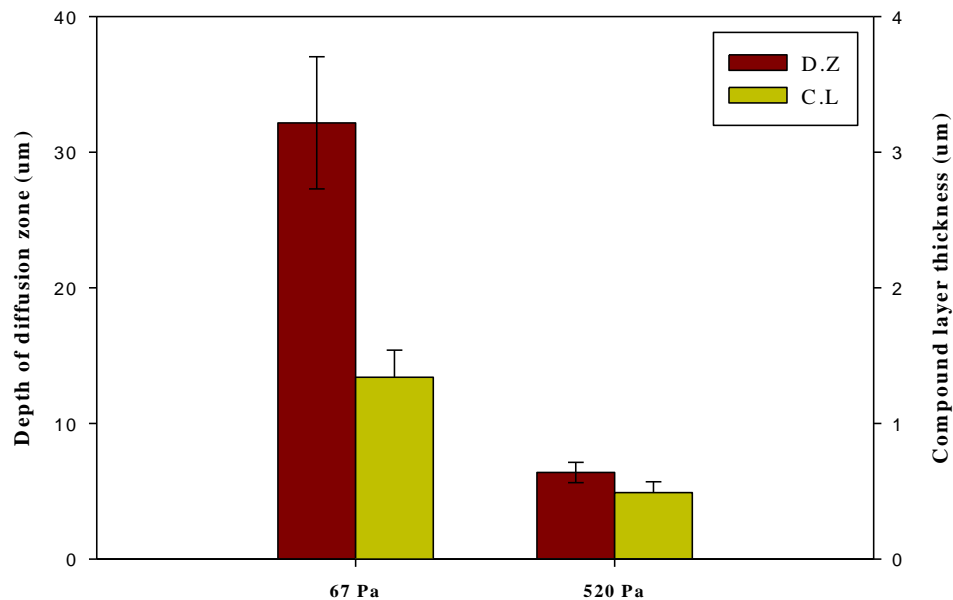


Figure 4.22 Variation of depth of diffusion zone and thickness of compound layer with nitriding pressure

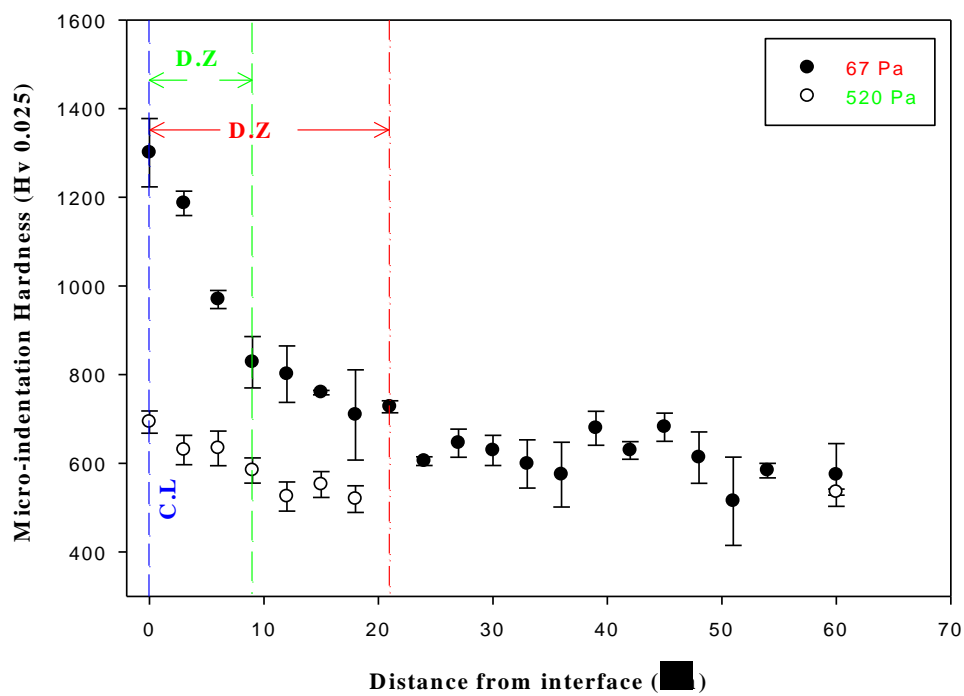


Figure 4.23 Micro-indentation hardness depth profiles of Ti-10V-2Fe-3Al nitrided under 67 & 520 Pa

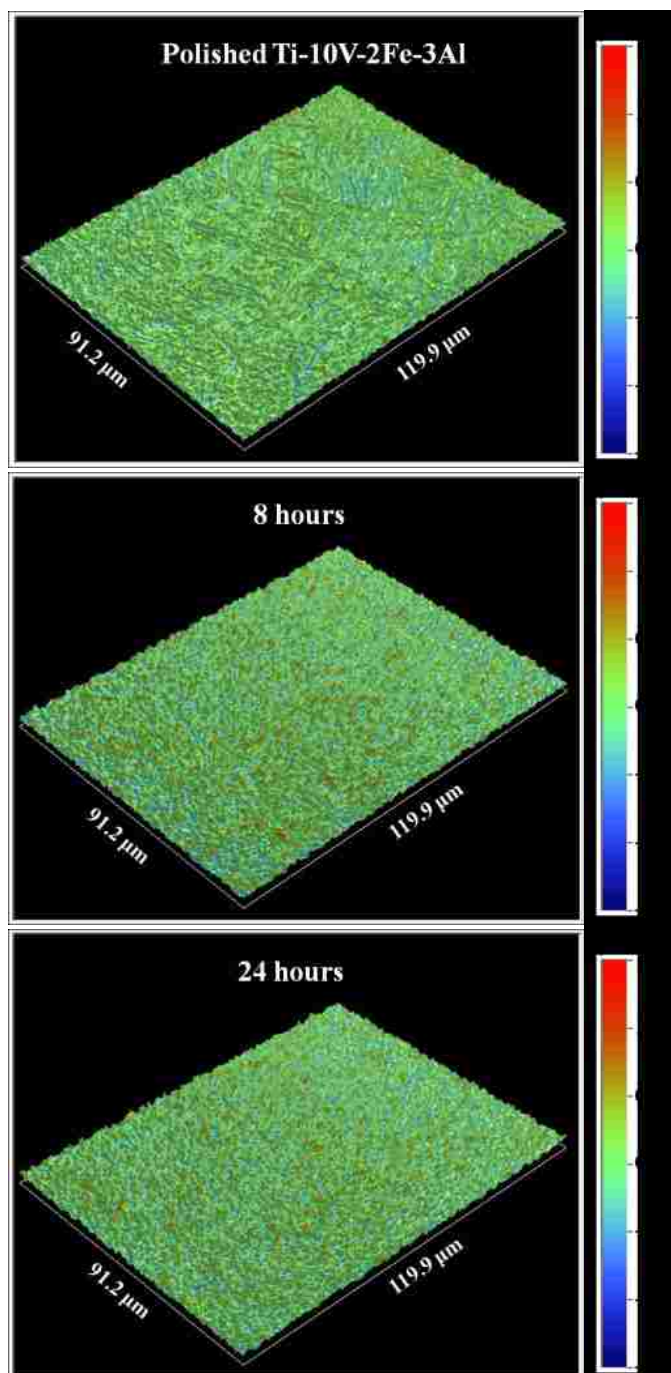


Figure 4.24 Optical 3D profiles from surface topography of Ti-10V-2Fe-3Al untreated, nitrided at 8 hours, and 24 hours

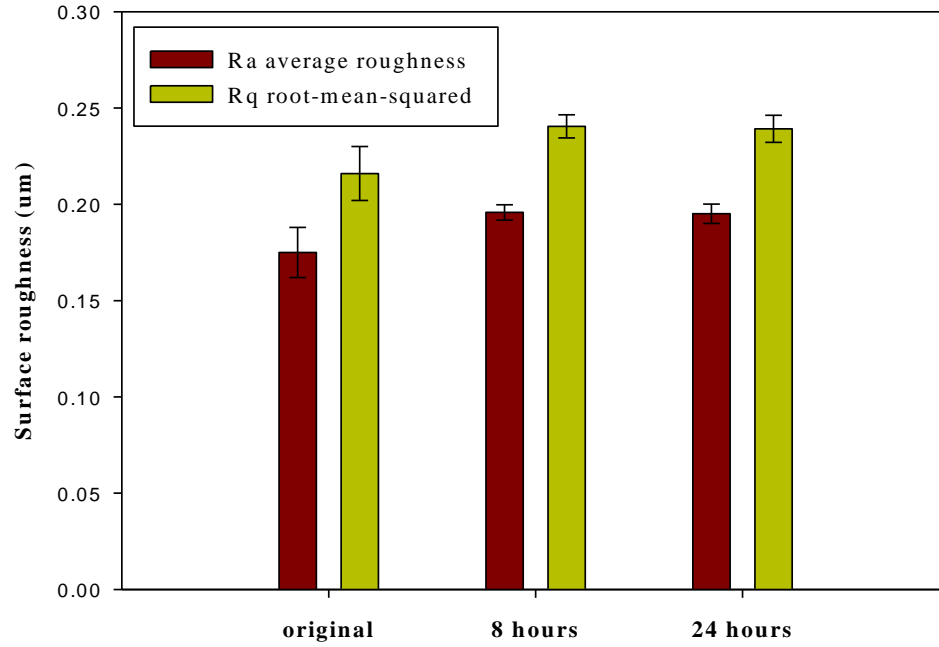


Figure 4.25 Variation of surface roughness with nitriding time

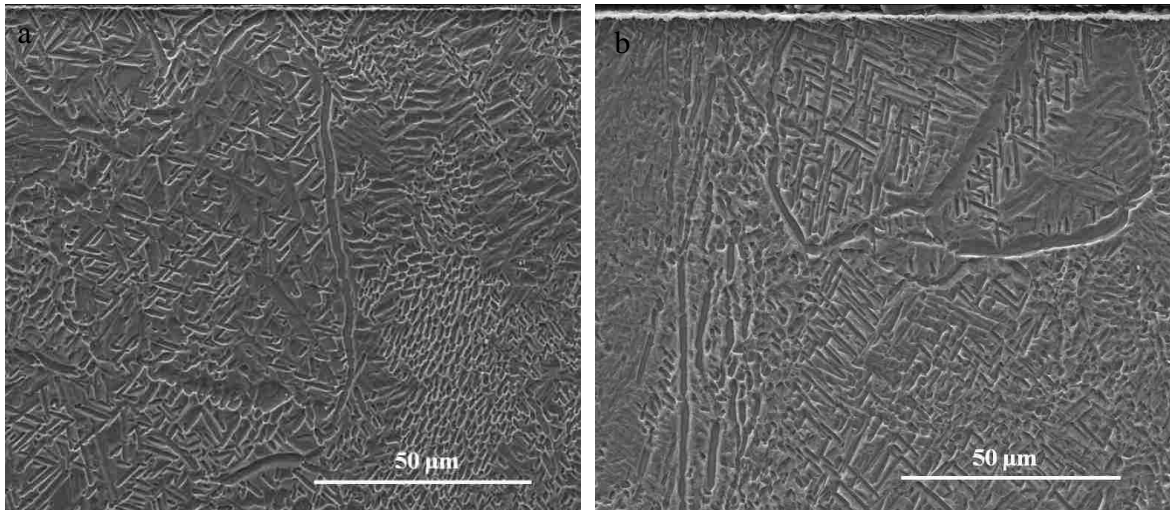


Figure 4.26 Secondary electron SEM image (SI) showing the cross-sectional microstructure of Ti-10V-2Fe-3Al nitrided at (a) 8 hours and (b) 24 hours with prolonged gas sputtering pre-treatment.

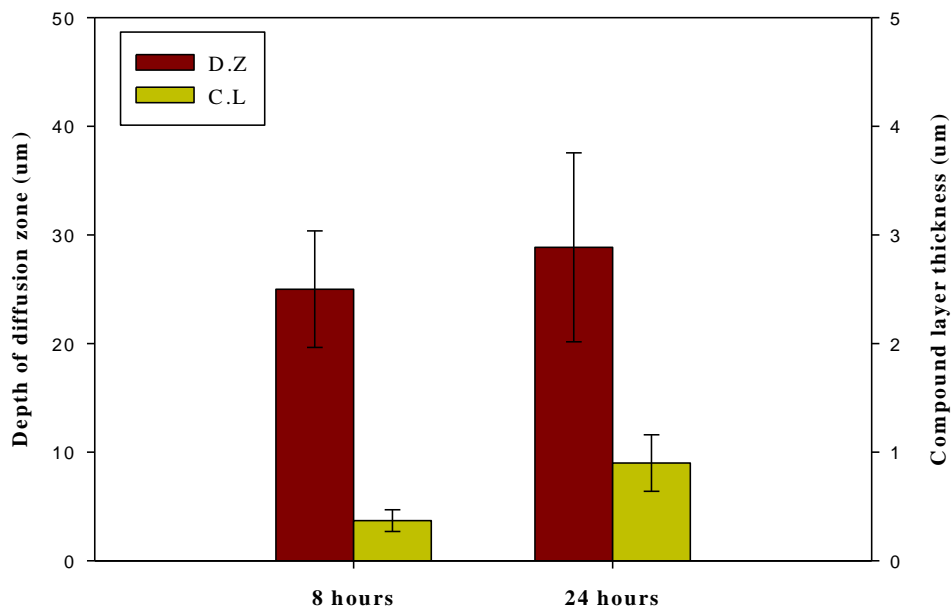


Figure 4.27 Variation of depth of the diffusion zone and thickness of the compound layer with nitriding duration.

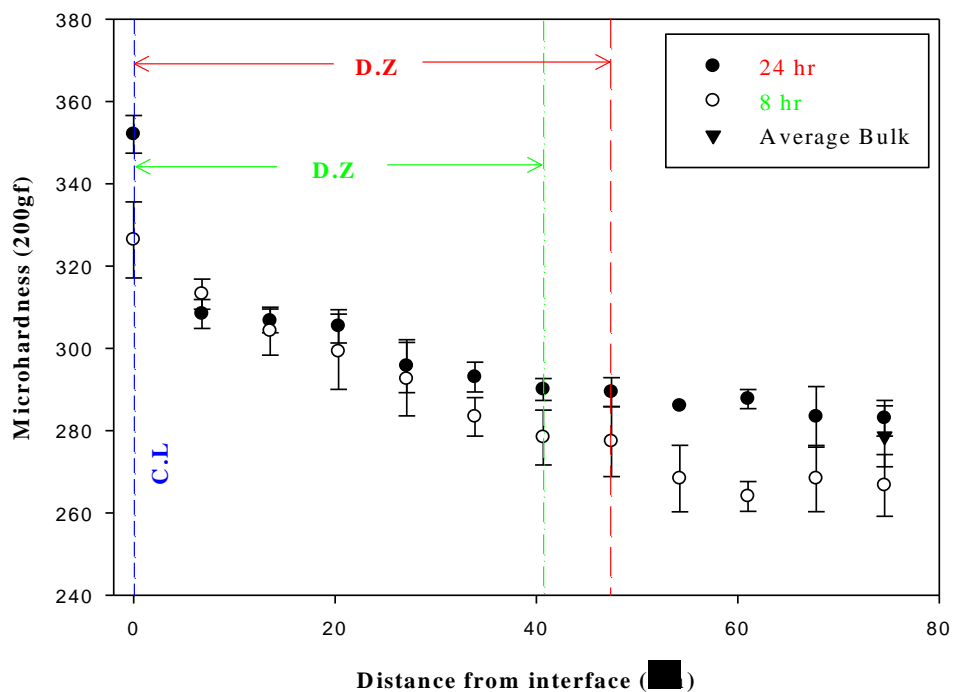


Figure 4.28 Microhardness depth profiles of Ti-10V-2Fe-3Al nitrided for 8 & 24 hours

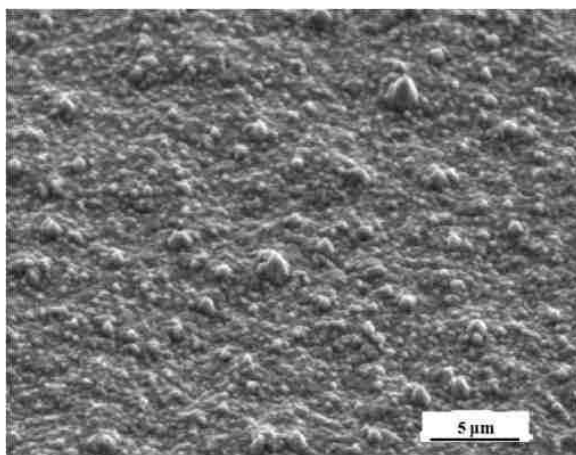


Figure 4.29 Back scatter electron SEM image (BSI) from surface morphology of Ti-10V-2Fe-3Al after ion nitriding (tilt angle: 54°).

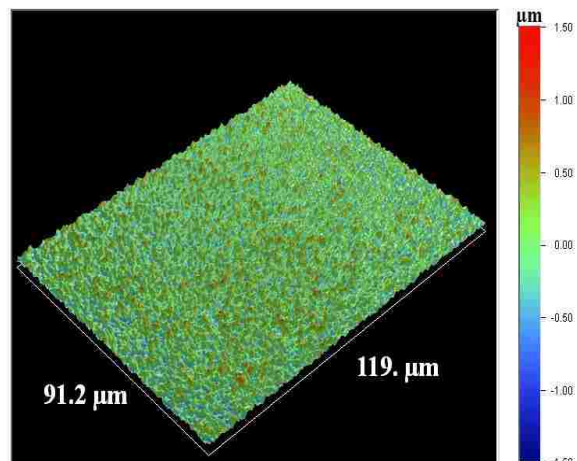


Figure 4.30 Optical 3D profile from surface topography of Ti-10V-2Fe-3Al after ion nitriding

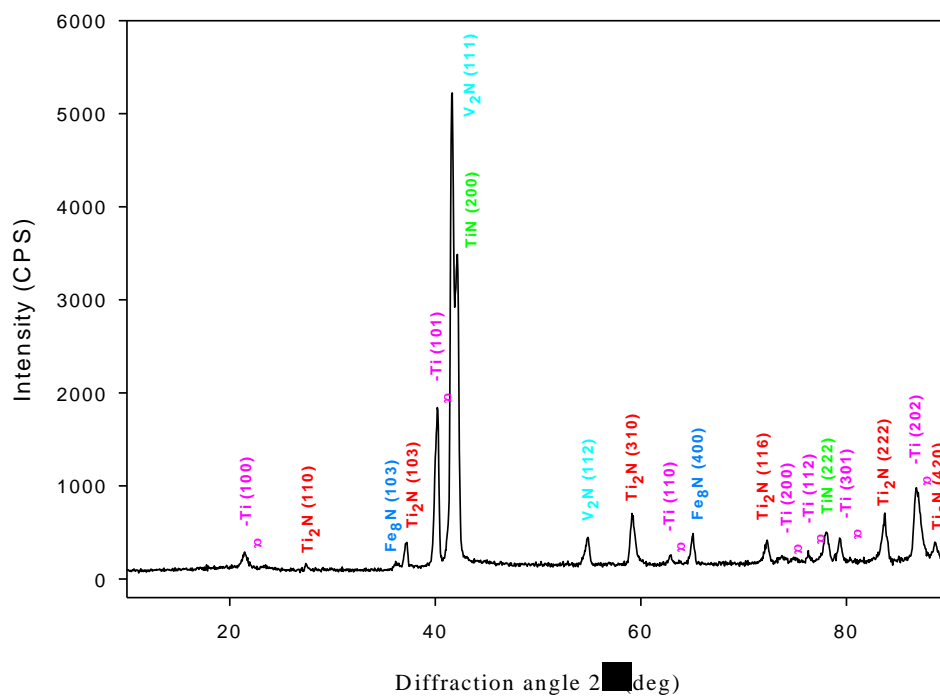


Figure 4.31 X-ray diffraction pattern of nitrided Ti-10V-2Fe-3Al showing Ti_2N as the major phase.

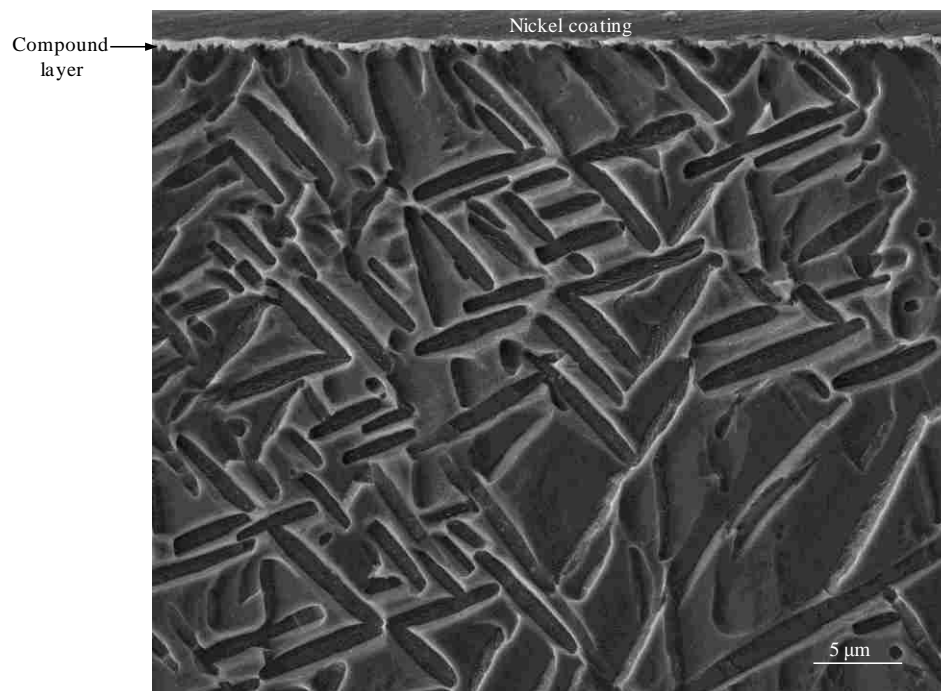


Figure 4.32 SEM MICROGRAPH FROM CROSS-SECTIONAL STRUCTURE OF NITRIDED Ti-10V-2Fe-3Al SURFACE SHOWING A THIN COMPOUND LAYER DEPOSITED ON THE DIFFUSED REGION.

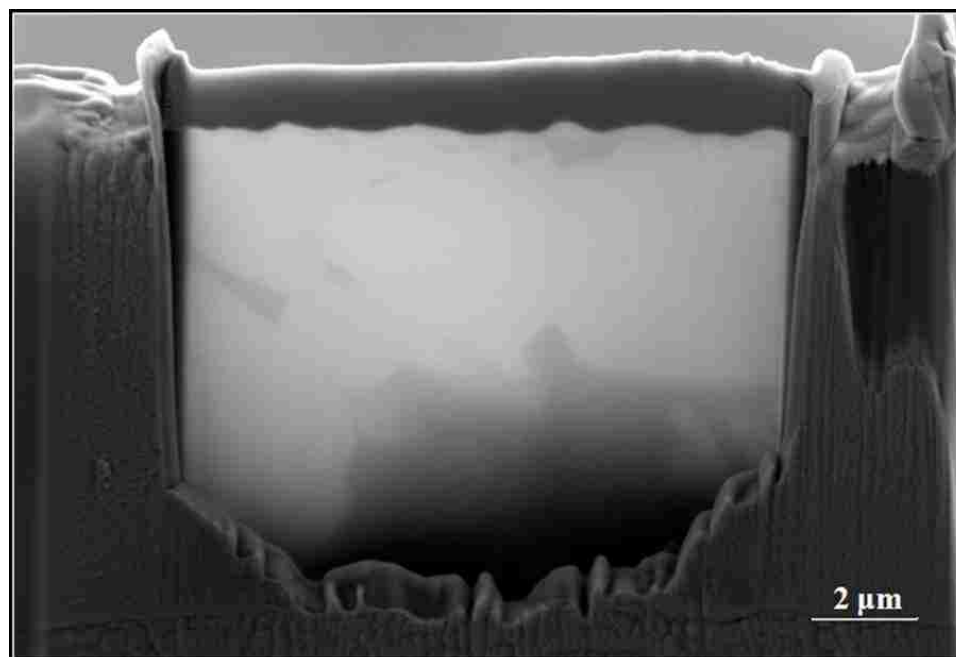


Figure 4.33 BSI shows milled sample is thinned with 300 pA, 150 pA and 40 pA ion beam sizes respectively and reached electron transparent (< 100 nm thick)

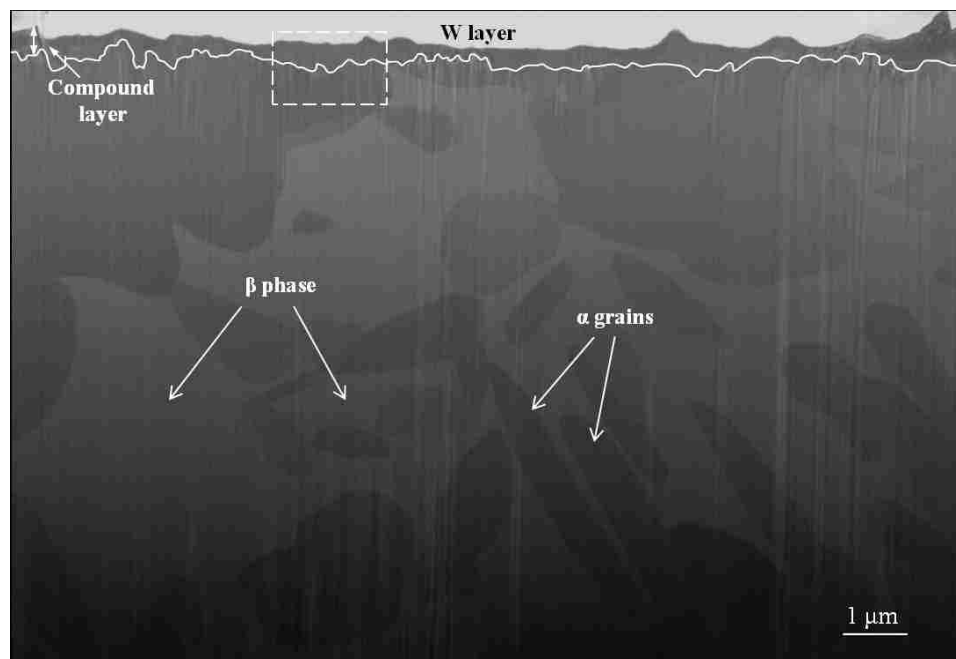


Figure 4.34 BSI from subsurface region of nitrated Ti-10V-2Fe-3Al.

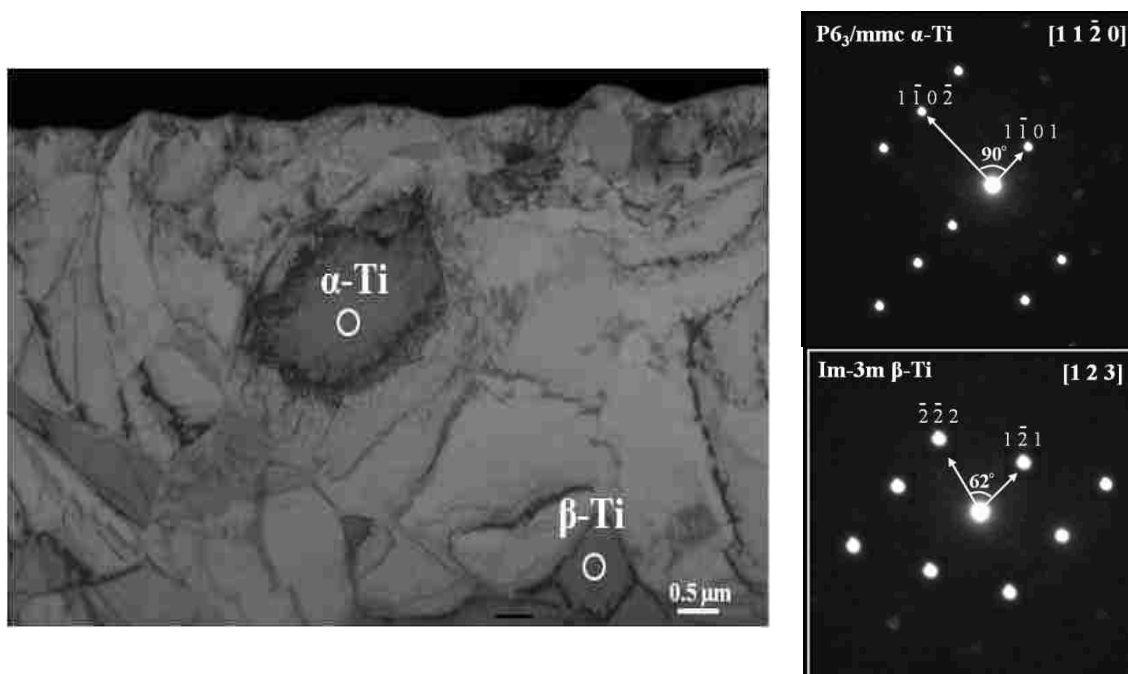


Figure 4.35 A typical cross-sectional dark field transmission electron micrograph (DF-TEM) of overview cross-section on nitrated Ti-10V-2Fe-3Al sample with corresponding CBED patterns taken from α and β phase.

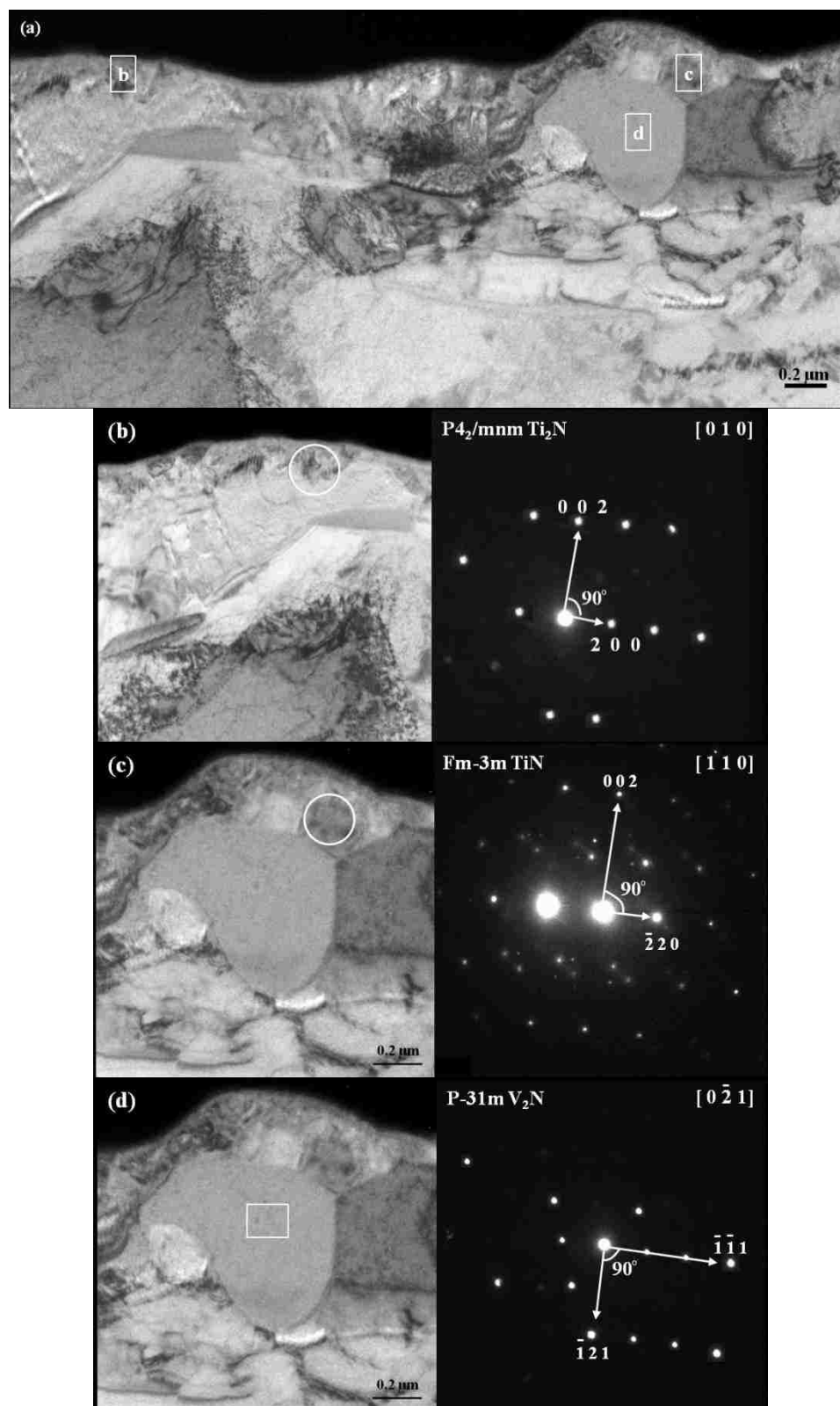


Figure 4.36 A typical cross-sectional bright field transmission electron micrograph (BF-TEM) showing the compound layer morphology and corresponding CBED patterns taken from different layers labeled as b, c, and d

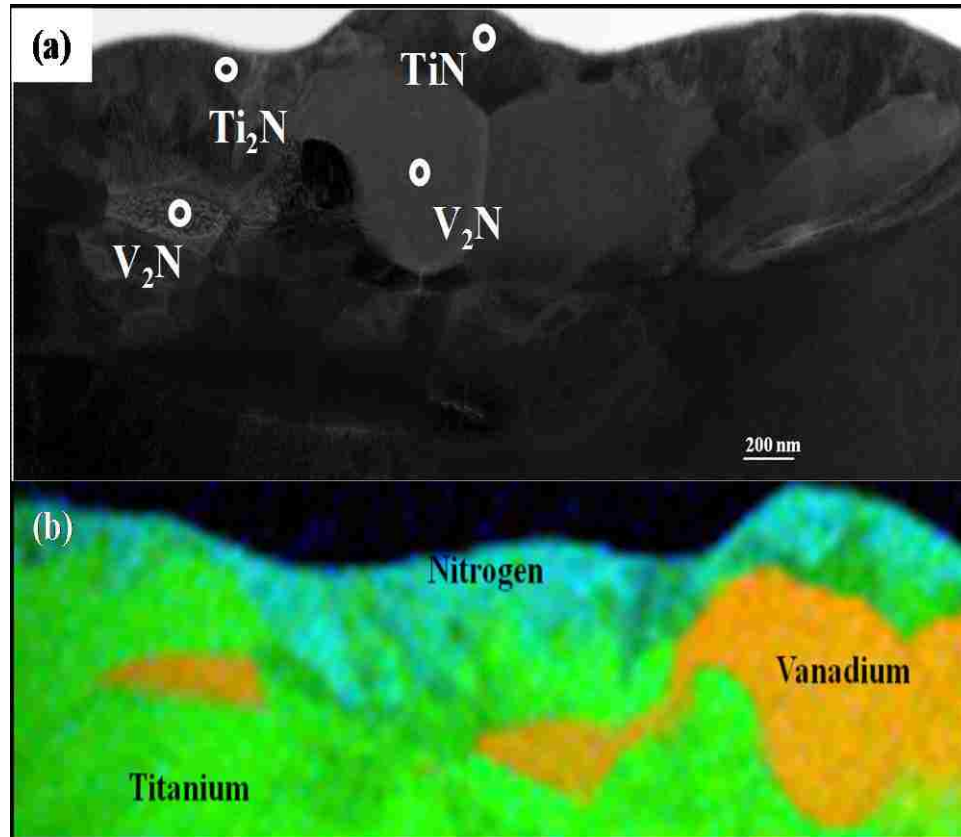


Figure 4.37 (a) Dark field TEM image (DF-TEM) from subsurface region of nitrated Ti-10V-2Fe-3Al, and (b) its corresponding element distribution map.

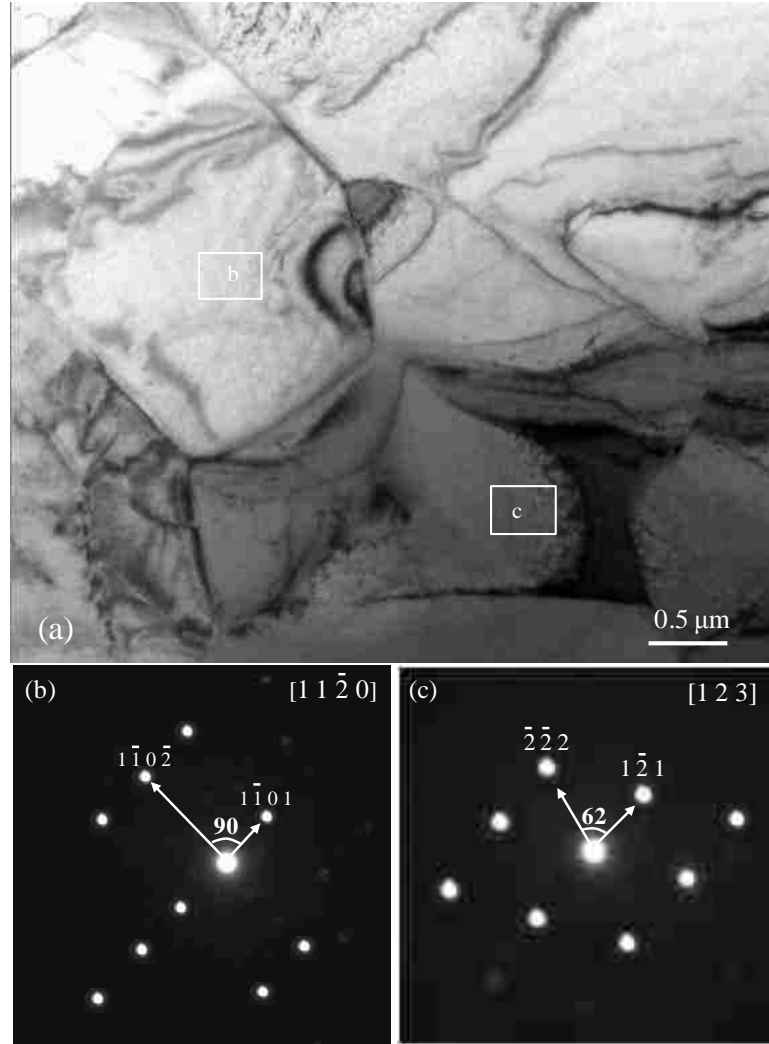


Figure 4.38 (a) A cross-sectional bright field TEM image (BF-TEM) from an area located at approximately 3 μm below the nitride grains, (b) A typical diffraction pattern corresponding to α-Ti from the location marked as “a” in Figure 4.68-a. (c) A typical diffraction pattern corresponding to β-Ti from the location marked as “b” in Figure 4.68-a.

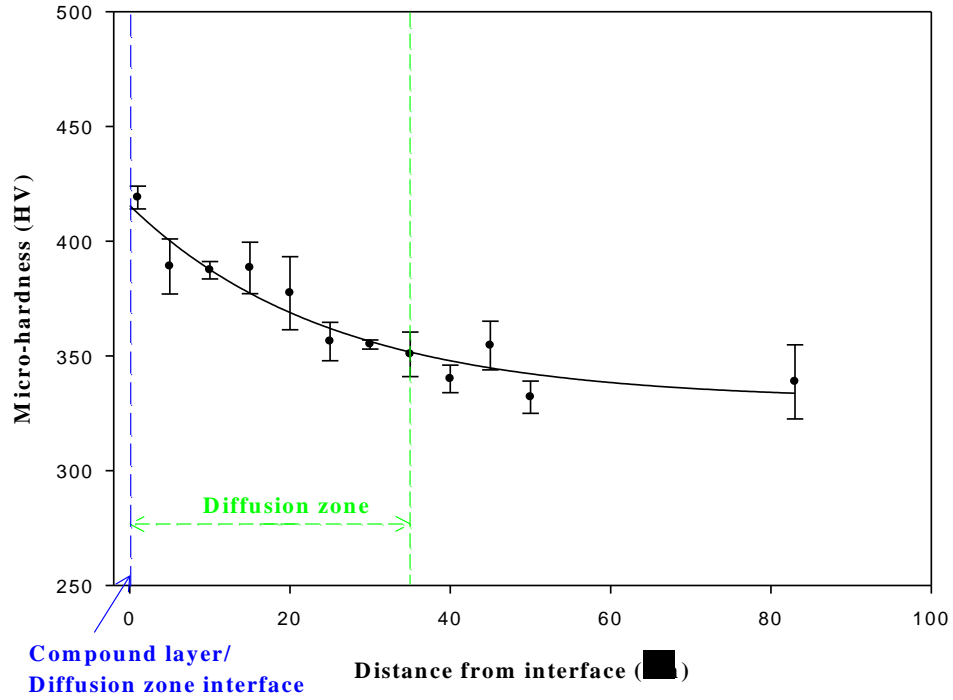


Figure 4.39 Microhardness-depth profile of nitrided Ti-10V-2Fe-3Al showing the significant hardening of diffusion zone resulted from nitrogen interstitials diffusion effect.

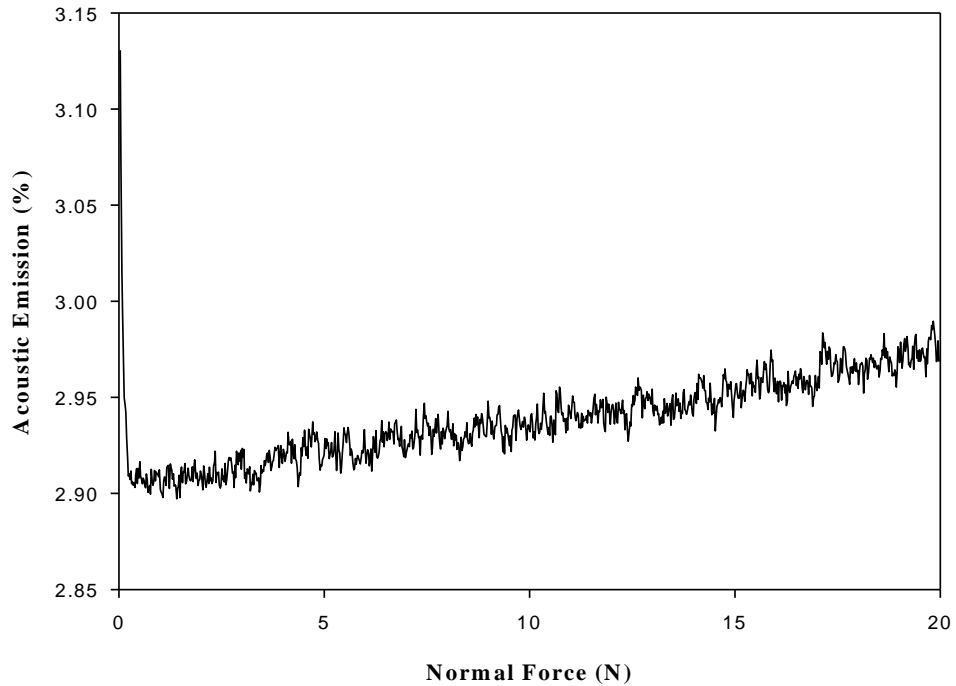


Figure 4.40 Each cracking event (angular/ tensile/ transverse crack) during scratch test has an acoustic emission output whose magnitude is proportional to the area of crack generated it. Testing conditions: applied load: 0-20 N; loading rate: 10 N/min, and lateral sliding speed: 1 mm/min.

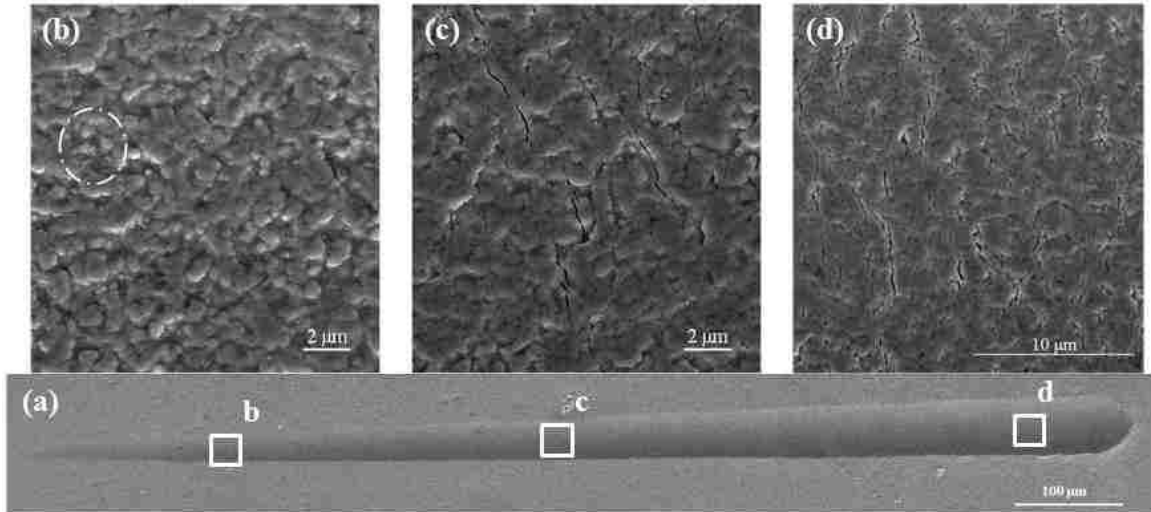


Figure 4.41 SEM micrographs showing (a) scratch path of progressive increasing load test and corresponding cracking event showing in (b) to (d); (b) from the first micro-crack observed area, (c) tensile cracks observed near the area of 10N load applied, and (d) semi-circular cracks existed near the area of 20N applied.

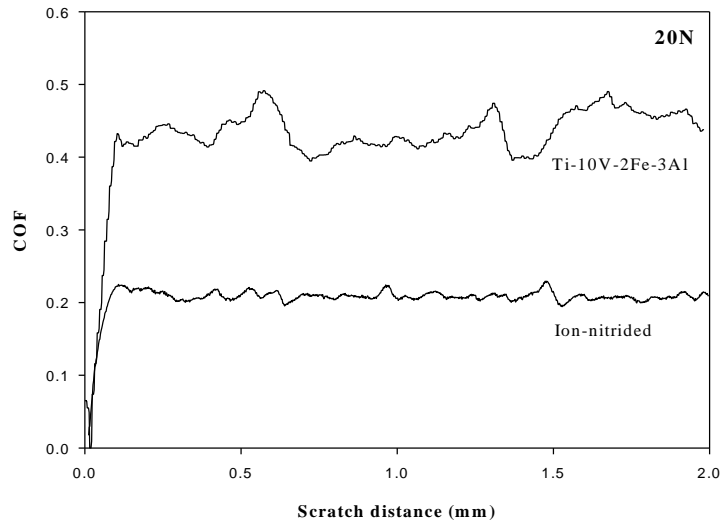
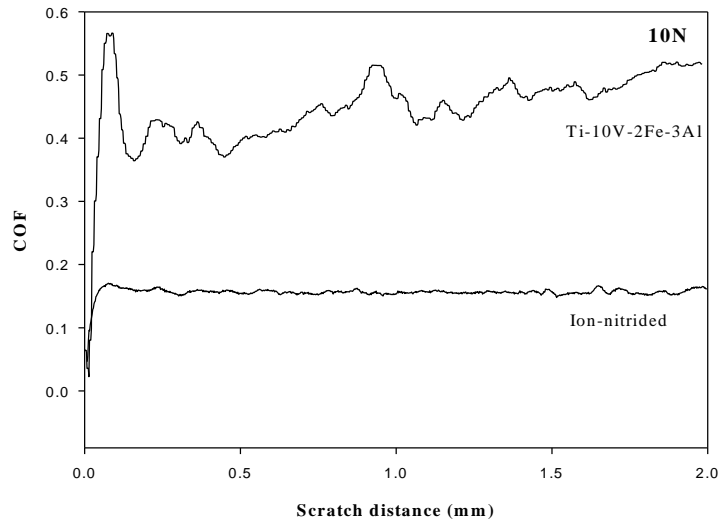
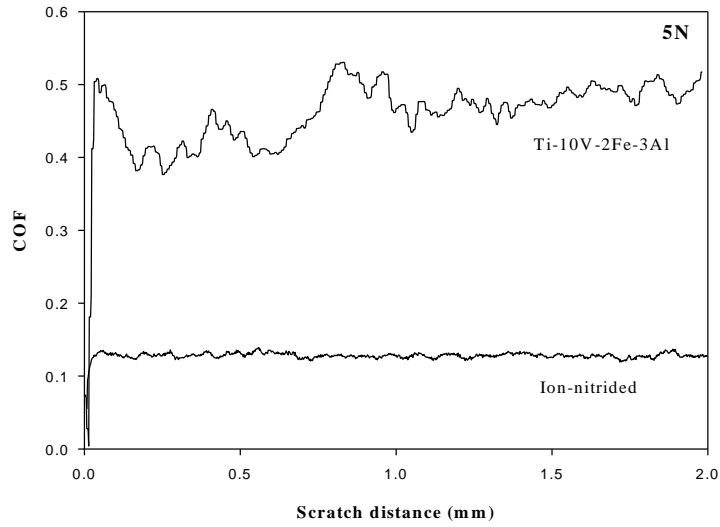


Figure 4.42 Coefficient of friction versus scratch distance for untreated and ion-nitrided Ti-10V-2Fe-3Al at (a) 5N, (b) 10N, and (c) 20N.

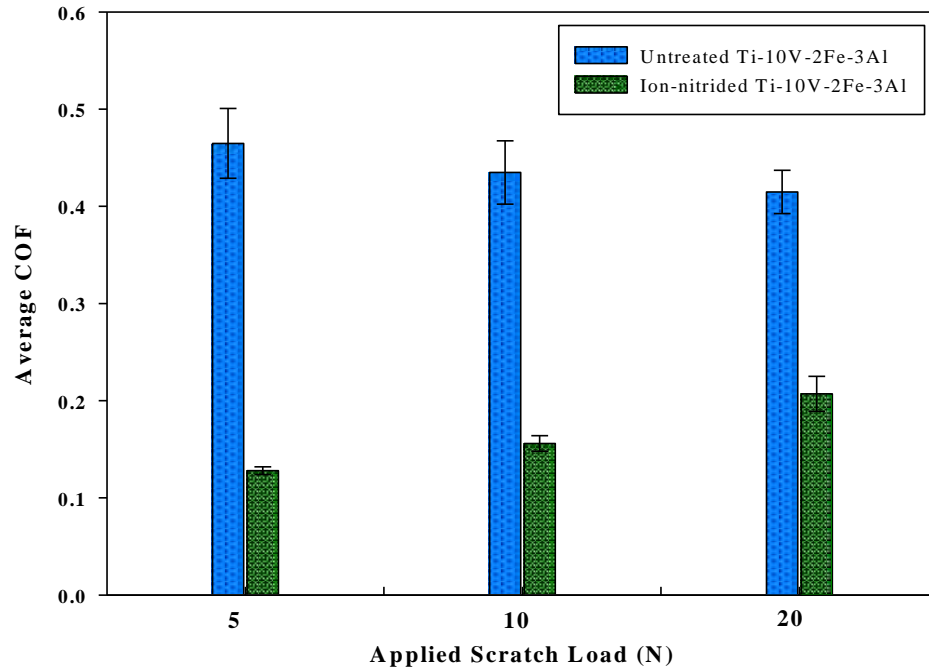


Figure 4.43 Variation of coefficient of friction with applied load for untreated and ion-nitrided Ti-10V-2Fe-3Al at (a) 5N, (b) 10N, and (c) 20N.

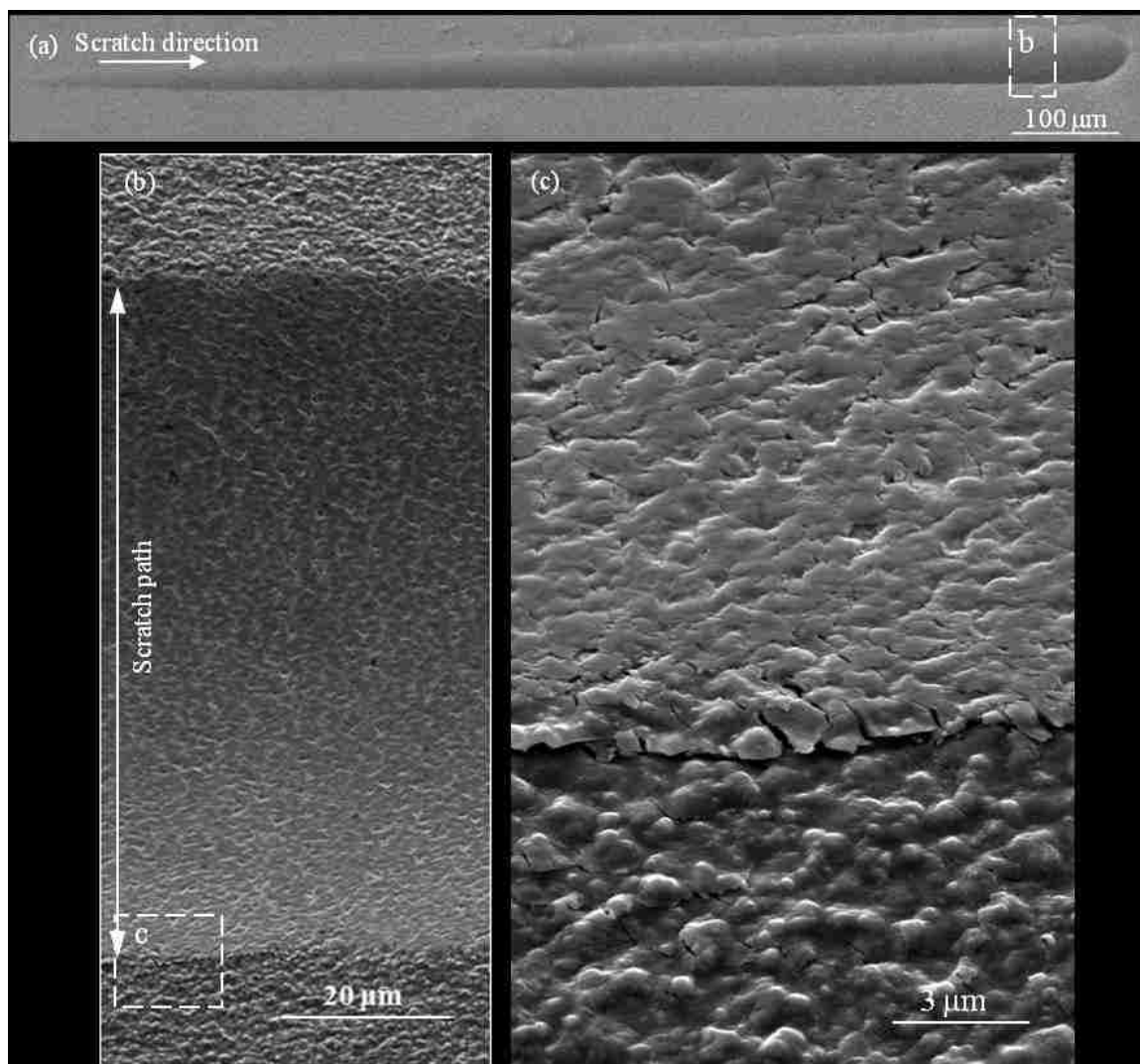


Figure 4.44 Secondary electron SEM micrograph (SEI) from scratch path where 17.2 N of load applied showing coating delaminated. (a) Overall progressively loading scratch path, (b) a higher magnification of the path where delamination observed, and (c) coating delamination existed near the edge of scratch path.

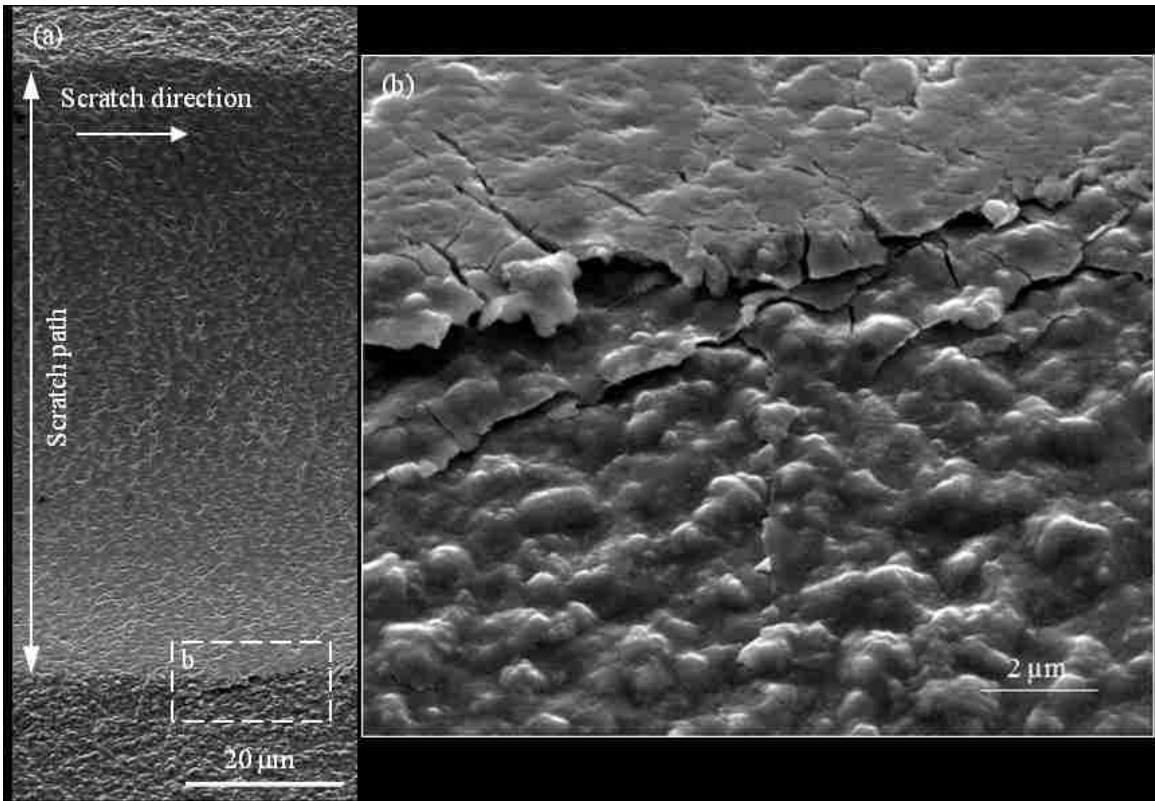


Figure 4.45 Secondary electron SEM micrograph (SEI) from scratch path of constant loading of 20N showing coating delaminates near the edge of the path.

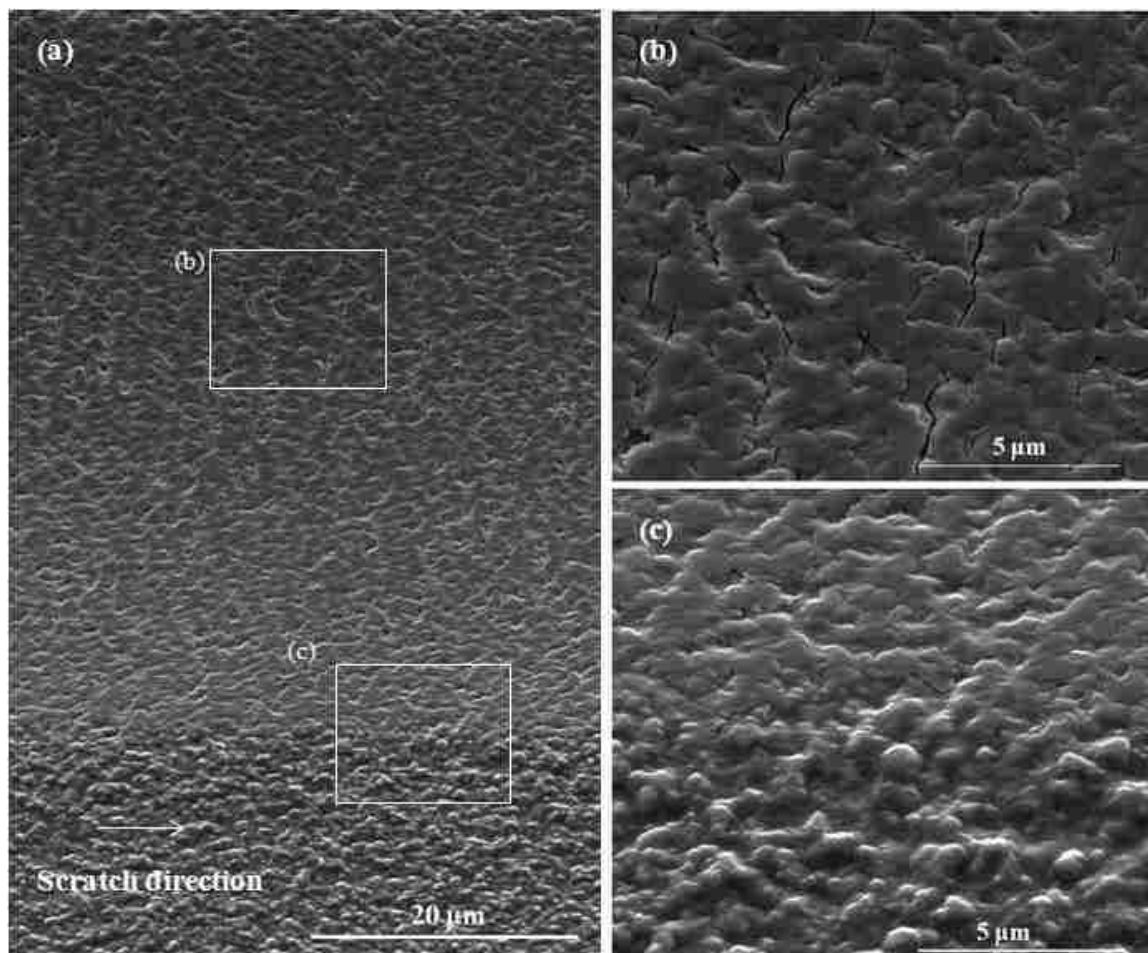


Figure 4.46 Secondary electron SEM micrograph (SEI) from scratch path of constant loading of 10N showing tensile cracks distributed (b) in the middle and (c) near the edge of the path.

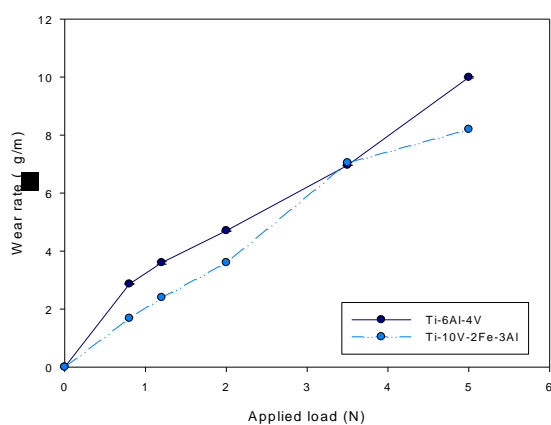


Figure 4.47 Variation of wear rate with applied normal load for Ti-10V-2Fe-3Al and ELI Ti-6Al-4V [83]

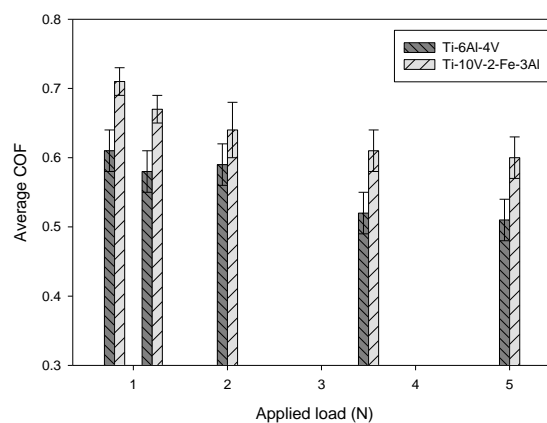


Figure 4.48 Average steady-state COF for different loading conditions for Ti-10V-2Fe-3Al and ELI Ti-6Al-4V [83]

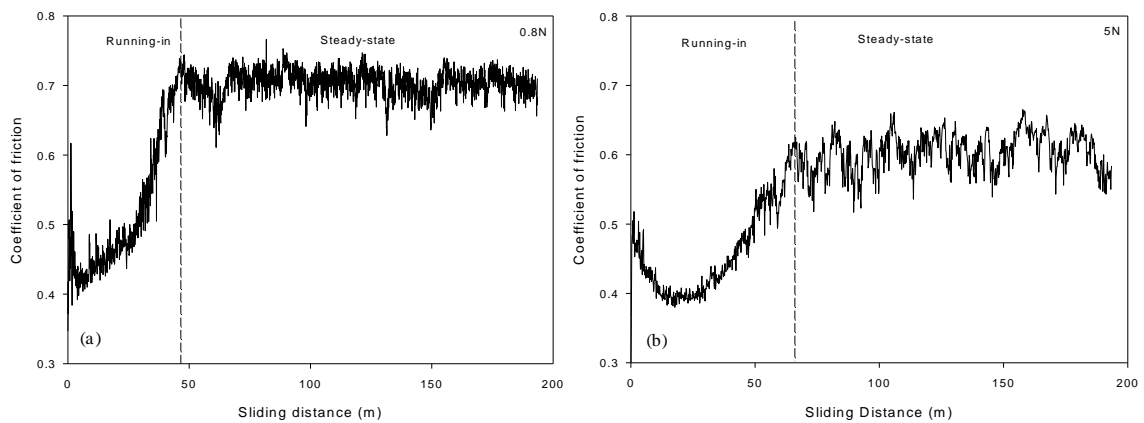


Figure 4.49 Variation of COF with sliding distance during wear tests at (a) 0.8N and (b) 5N.

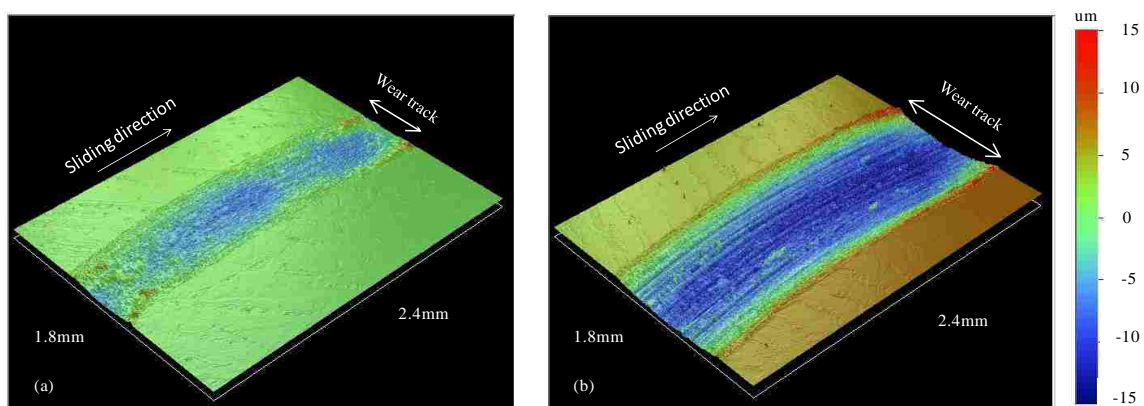


Figure 4.50 Three-dimensional surface profiles from wear tracks at (a) 0.8N and (b) 5N.

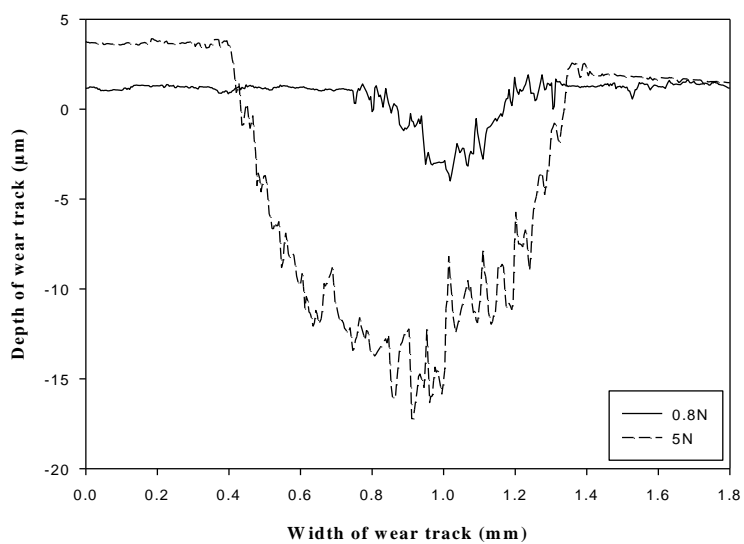


Figure 4.51 Two-dimensional profiles illustrating depth and width of the wear tracks at (a) 0.8N and (b) 5N.

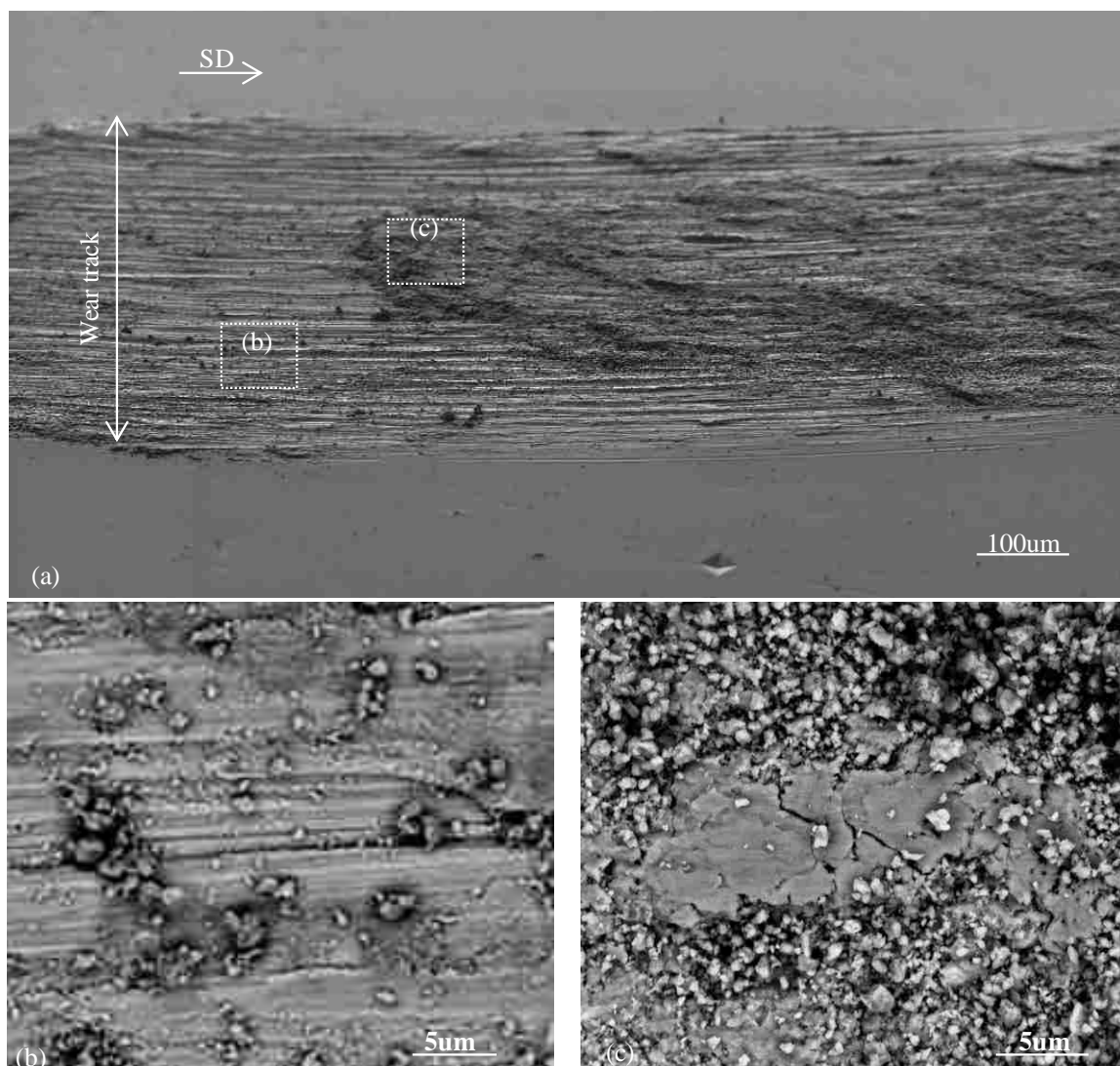


Figure 4.52 (a) BSE micrographs from (a) wear track morphology after wear test at 0.8N (tilted at 52°), (b) ploughing marks covered with fine debris particles and (c) fractured plateau surrounded by fine debris particles. The sliding direction is marked “SD”.

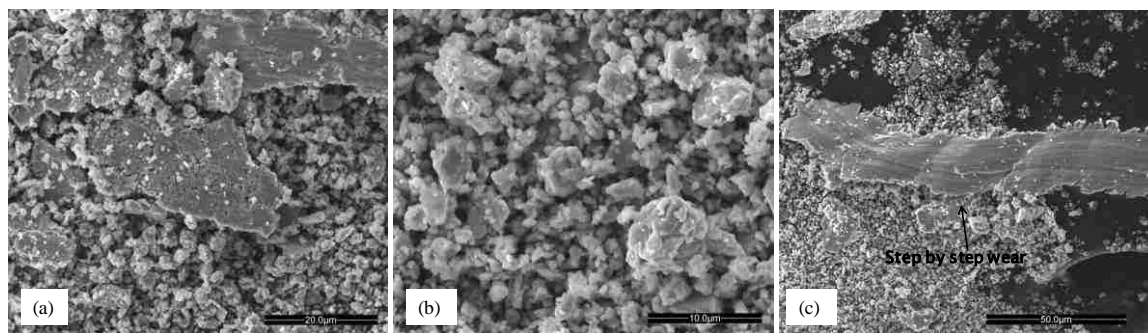


Figure 4.53 SE micrographs from wear debris particles generated during wear test at 0.8N. (a) compacted plates, (b) fine equiaxed particles and (c) metallic belt-like particles.

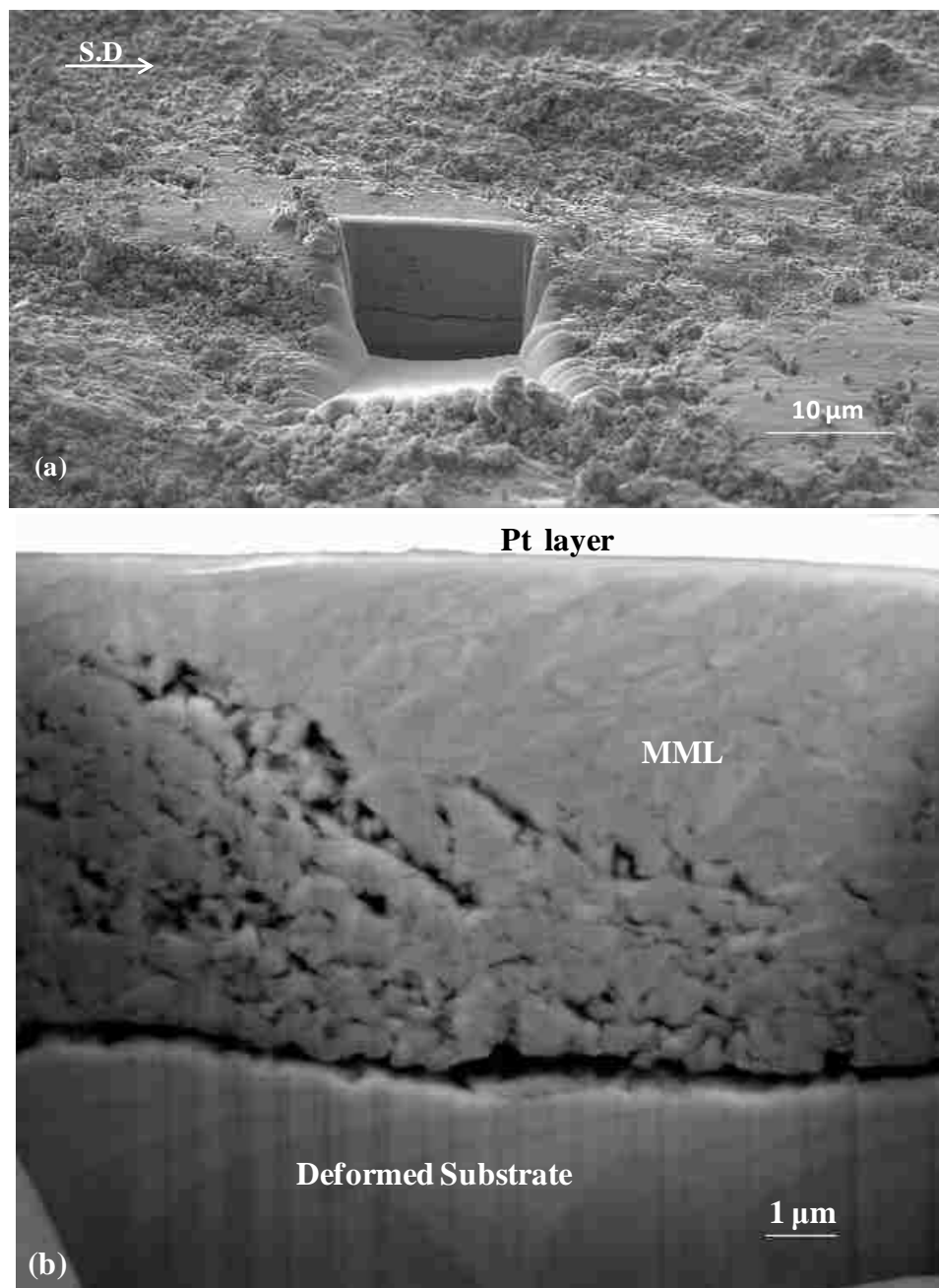


Figure 4.54(a) BSE micrographs from the location of FIB milling on the 0.8N wear track on the Ti-10V-2Fe-3Al test coupon after ion milling (tilt angle: 52°), (b) Cross-sectional BSE micrograph from the MML and subsurface plastic deformation.

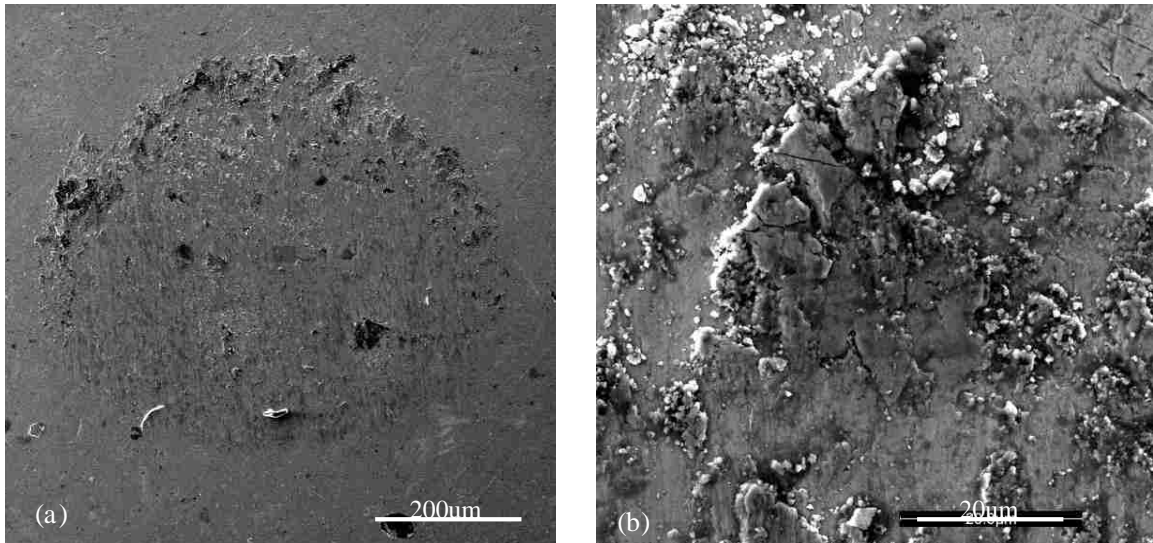


Figure 4.55 SE micrographs from (a) wear scar on the steel counterface ball after wear test at 0.8N and (b) transferred material from Ti-10V-2Fe-3Al surface to the counterface.

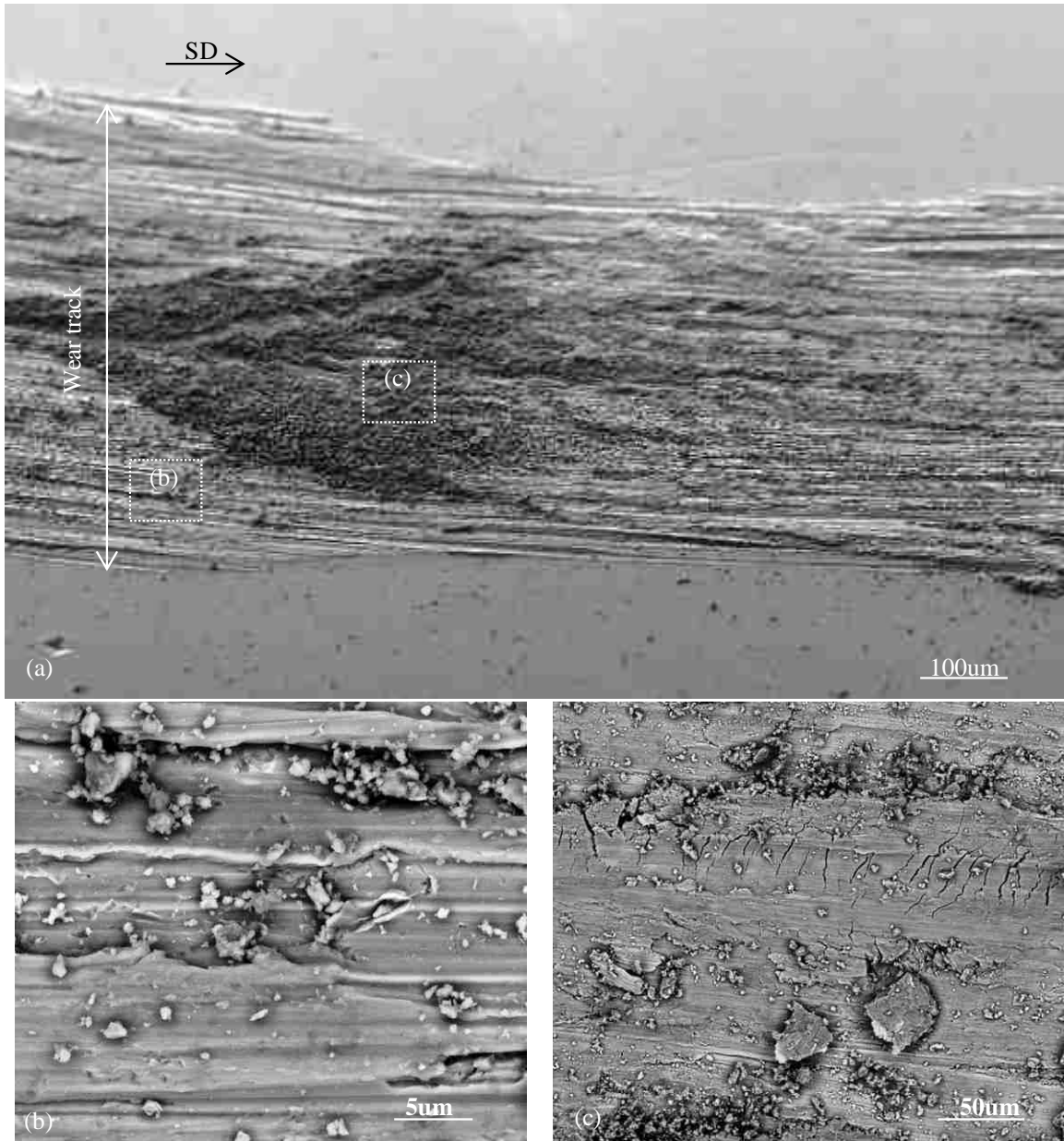


Figure 4.56 (a) BSE micrographs from (a) wear track morphology after wear test at 5N (tilted at 52°), (b) ploughing marks with some plastic deformation and (c) parallel cracks on a plateau and small platelets spalled off from the plateau. The sliding direction is marked “SD”.

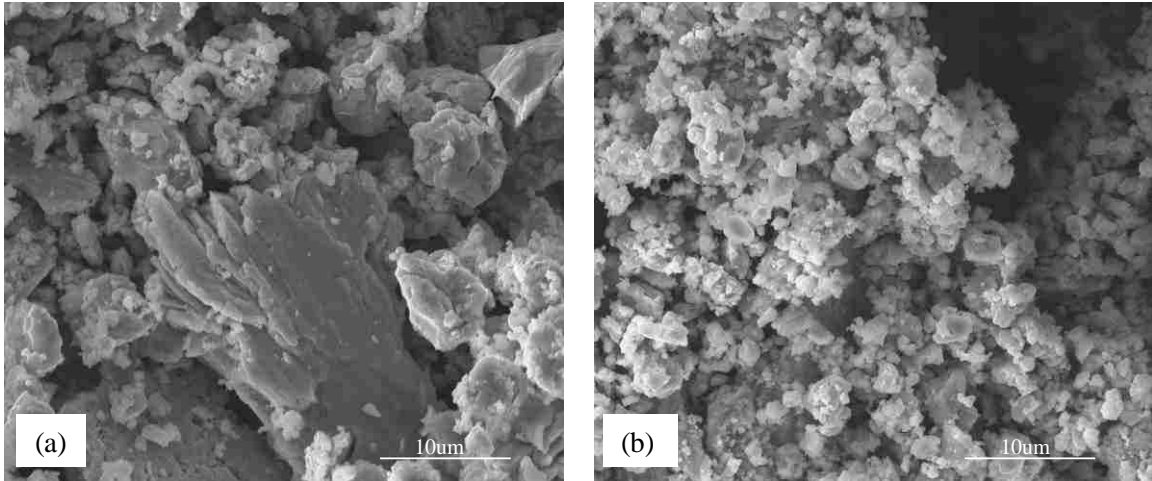


Figure 4.57 SE micrographs from wear debris particles generated during wear test at 5N. (a) platelets with layered morphology, corresponding EDS spectrum indicates presence of Ti, Al, V, O and Fe in the platelets (b) fine particles, also containing the same elements as platelets only with higher oxygen content.

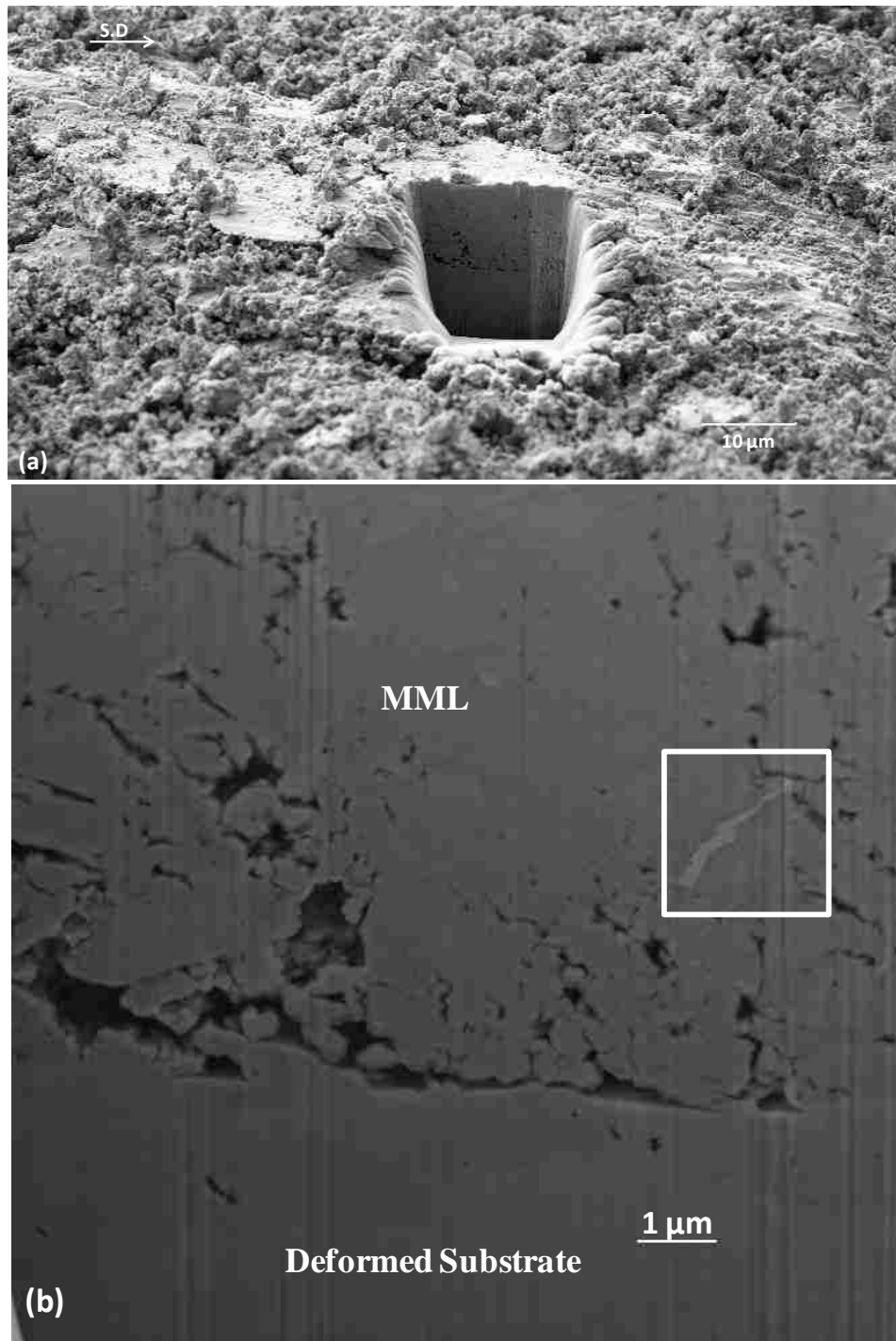


Figure 4.58 (a) BSE micrographs from the location of FIB milling on the 5N wear track on the Ti-10V-2Fe-3Al wear track (tilt angle: 52°), (b) Cross-sectional BSE micrograph from the MML and subsurface plastic deformation.

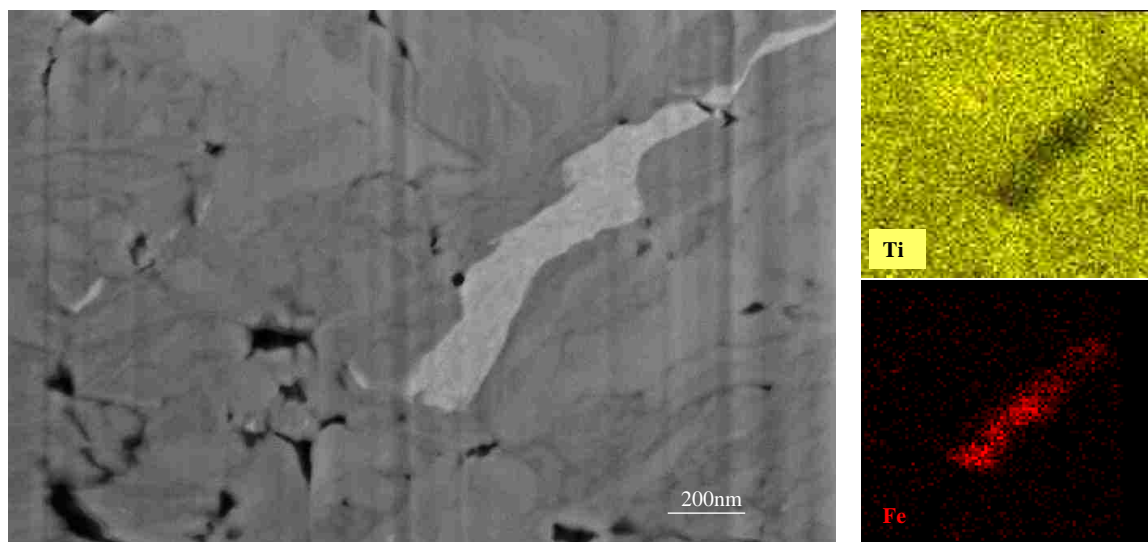


Figure 4.59 BSE micrograph and corresponding EDS mapping from an iron-rich layer within the MML layer on 5N wear track.

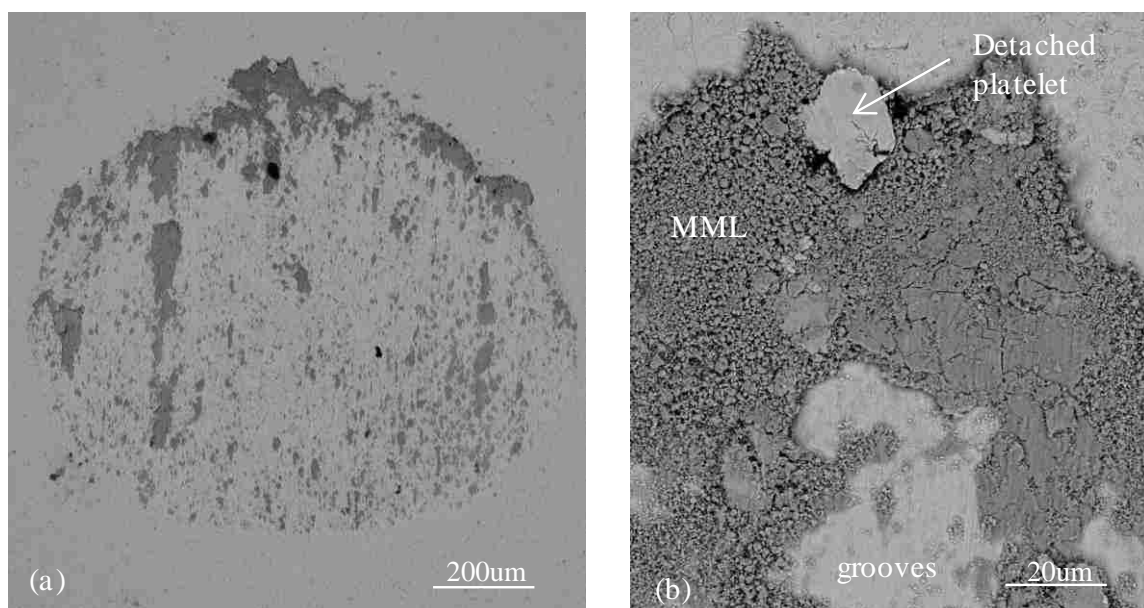


Figure 4.60 SE micrographs from (a) wear scar on the steel counterface ball after wear test at 5N and (b) the wear scar consisted of transferred material (MML), abraded grooves and platelets that have spalled off.

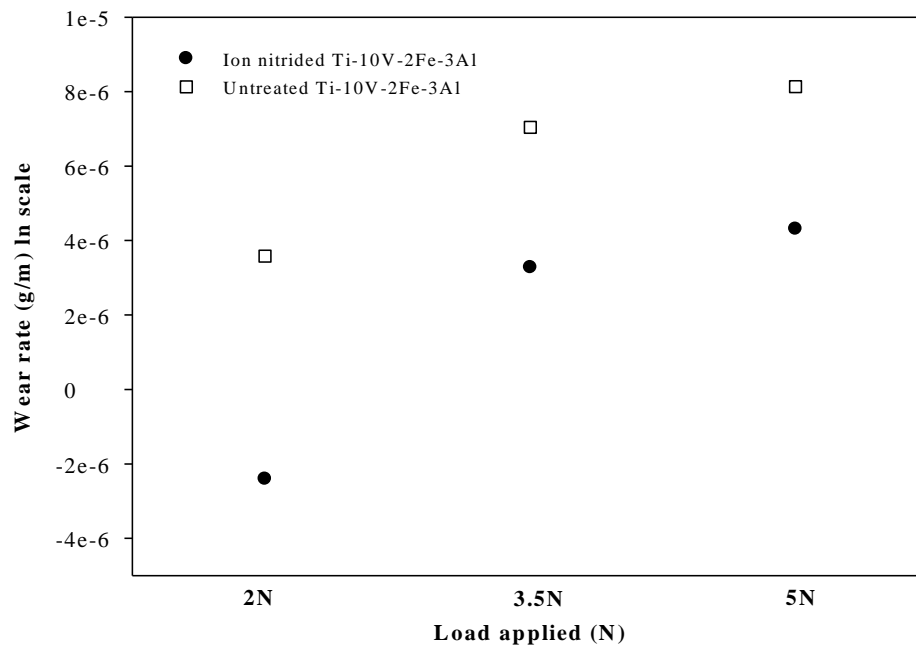


Figure 4.61 Variation of wear rate with applied normal load for untreated and ion nitrided Ti-10V-2Fe-3Al

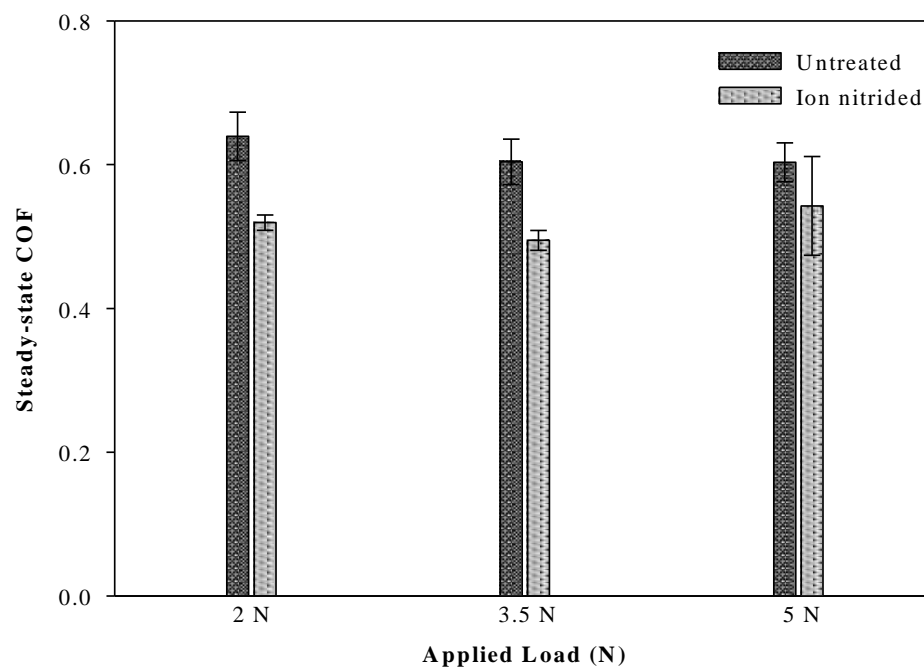


Figure 4.62 Average steady-state COF for different loading conditions for untreated and ion nitrided Ti-10V-2Fe-3Al

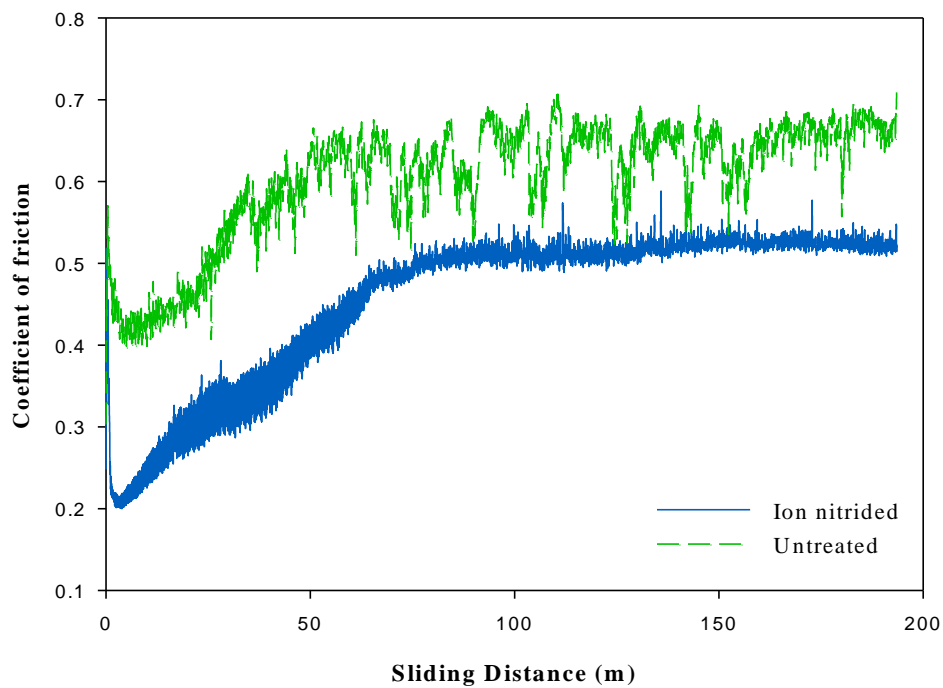


Figure 4.63 Variation of COF with sliding distance during wear tests at 2N

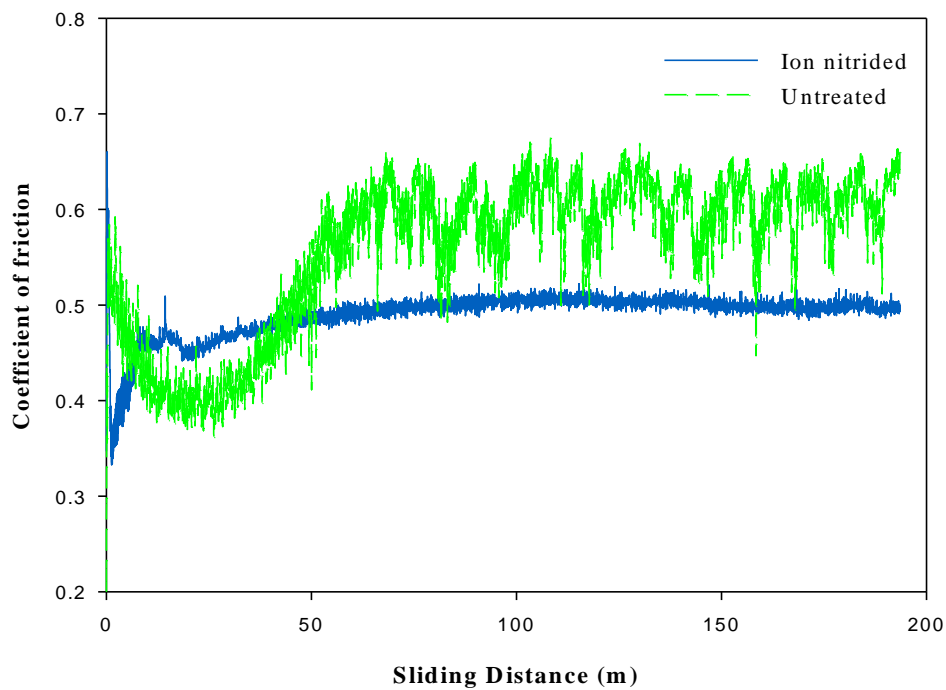


Figure 4.64 Variation of COF with sliding distance during wear tests at 3.5N

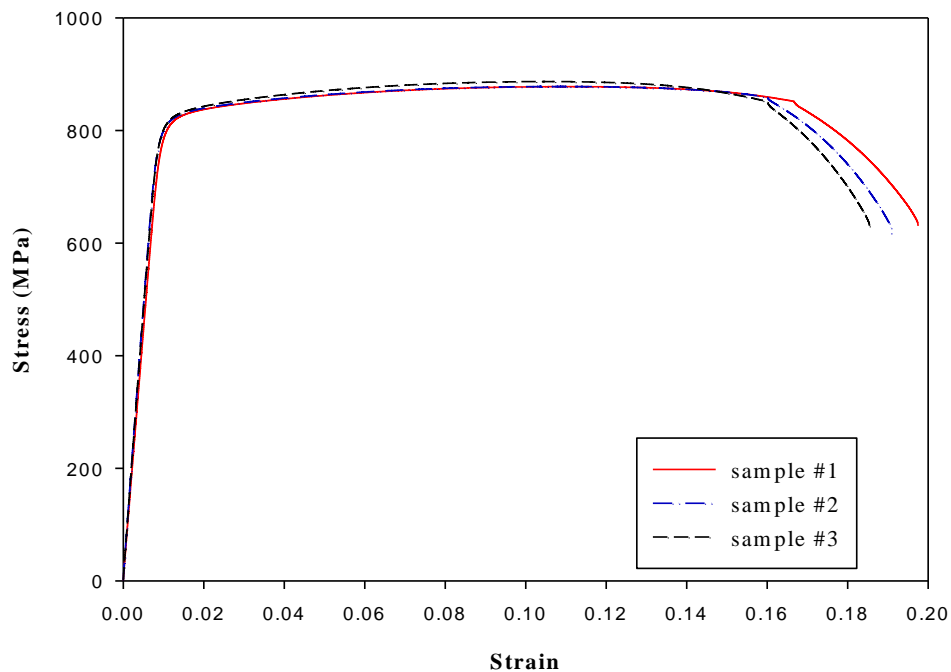


Figure 4.65 Plot of stress-strain curves for each tensile test sample

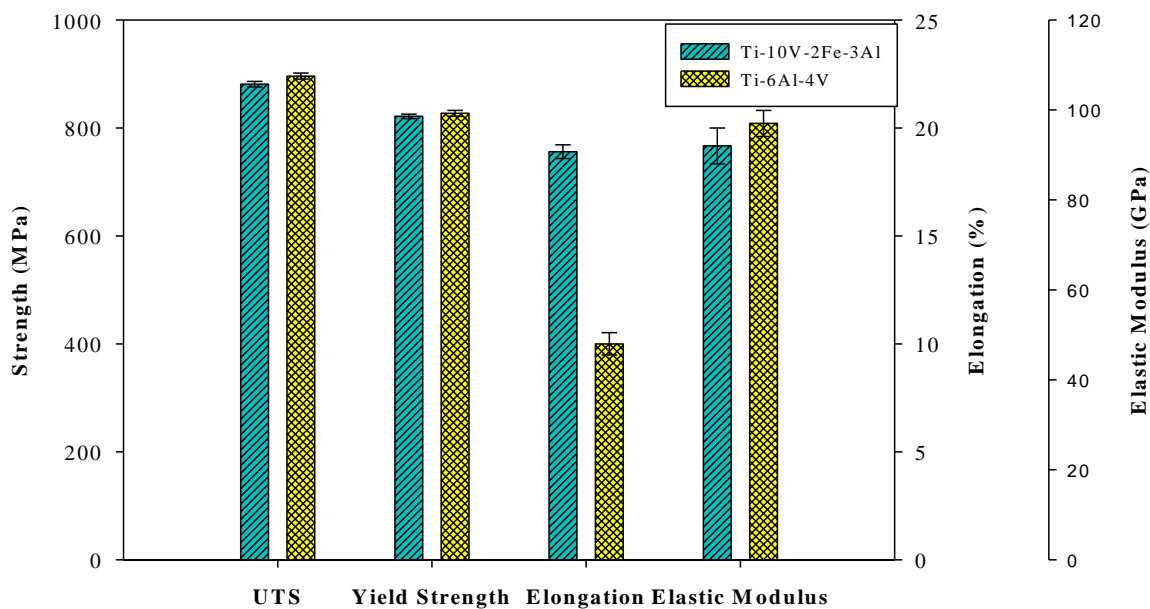


Figure 4.66 Comparison of tensile properties between Ti-10V-2Fe-3Al alloys and Ti-6Al-4V

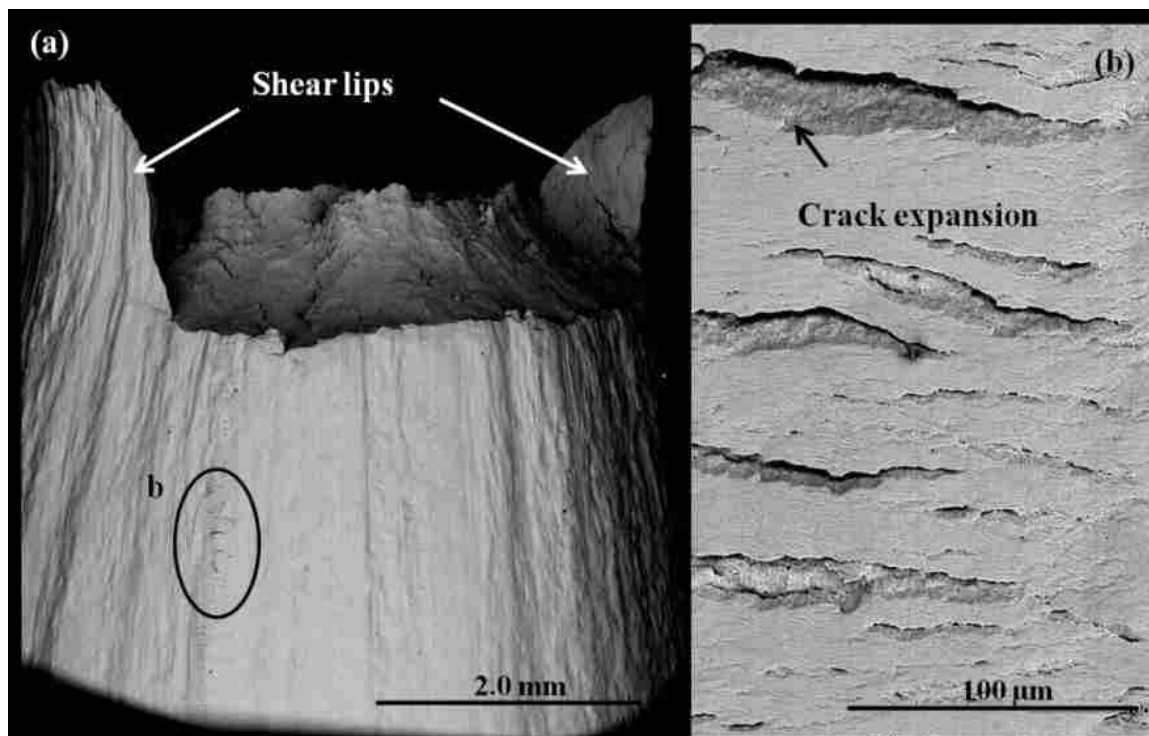
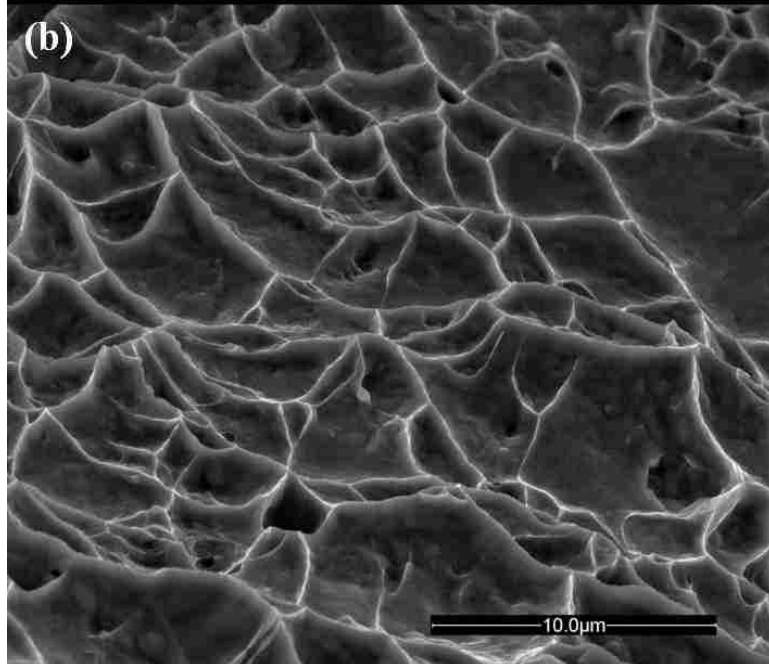
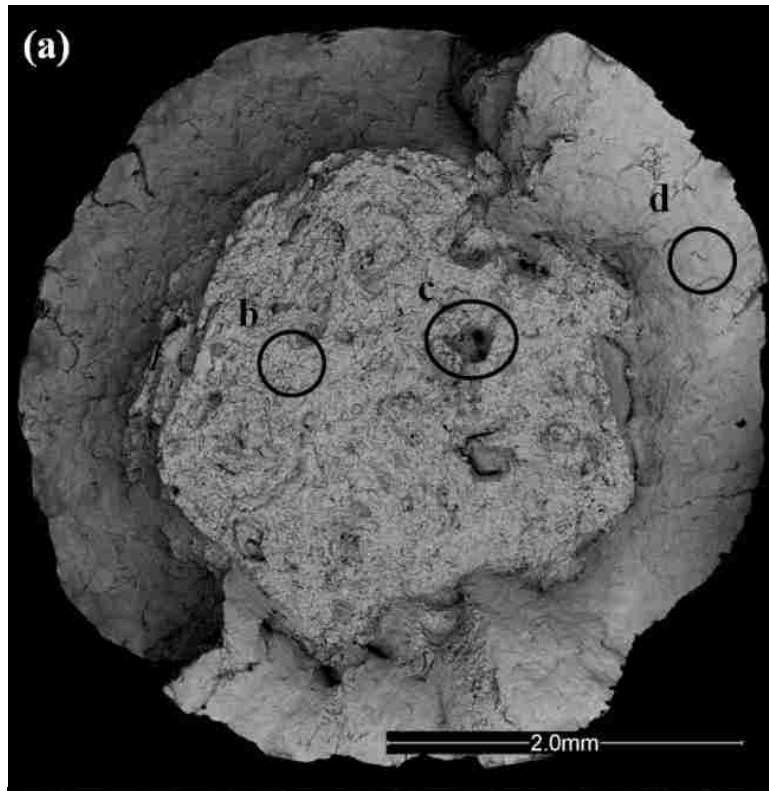


Figure 4.67 Back-scattered electron image (BSI) from Ti-10V-2Fe-3Al tensile specimens with local macro-cracks near fracture surface.



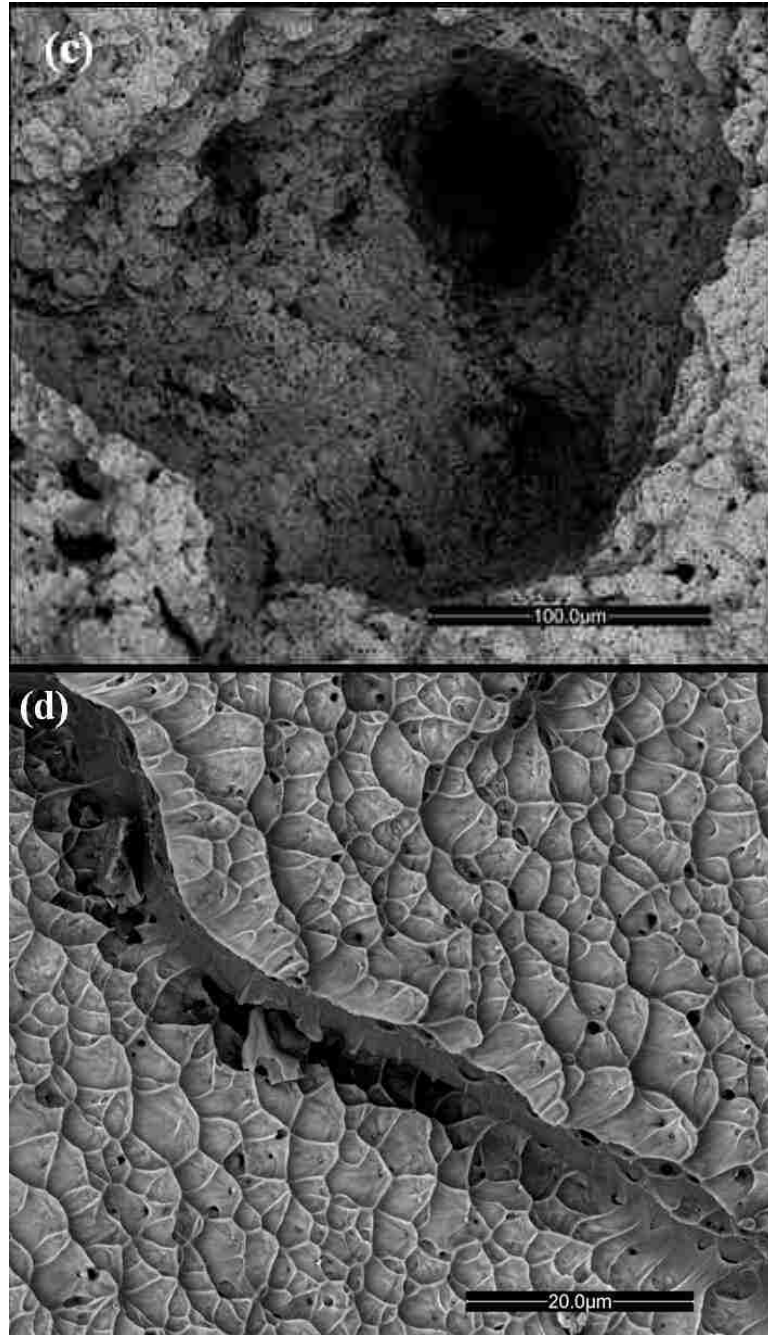


Figure 4.68 Scanning electron fractographs showing (a) tensile fracture surface of Ti-10V-2Fe-3Al, (b) micro-voids and dimples in the dimple rupture region, (c) coalescence of microscopic voids surrounded by shallow dimples in overload region; and (d) crack formation in overload region.

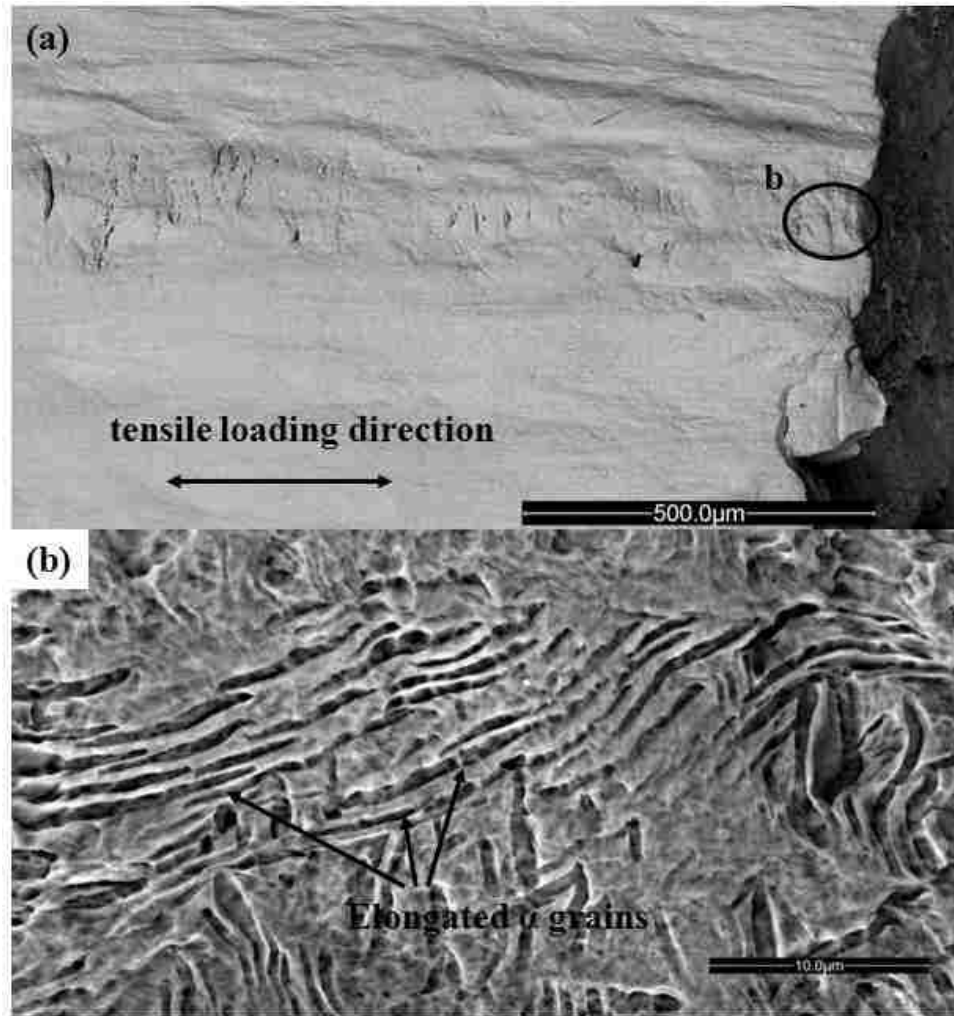


Figure 4.69 Secondary electron images (SEI) from etched Ti-10V-2Fe-3Al tensile specimen surface near fracture region showing microstructure change

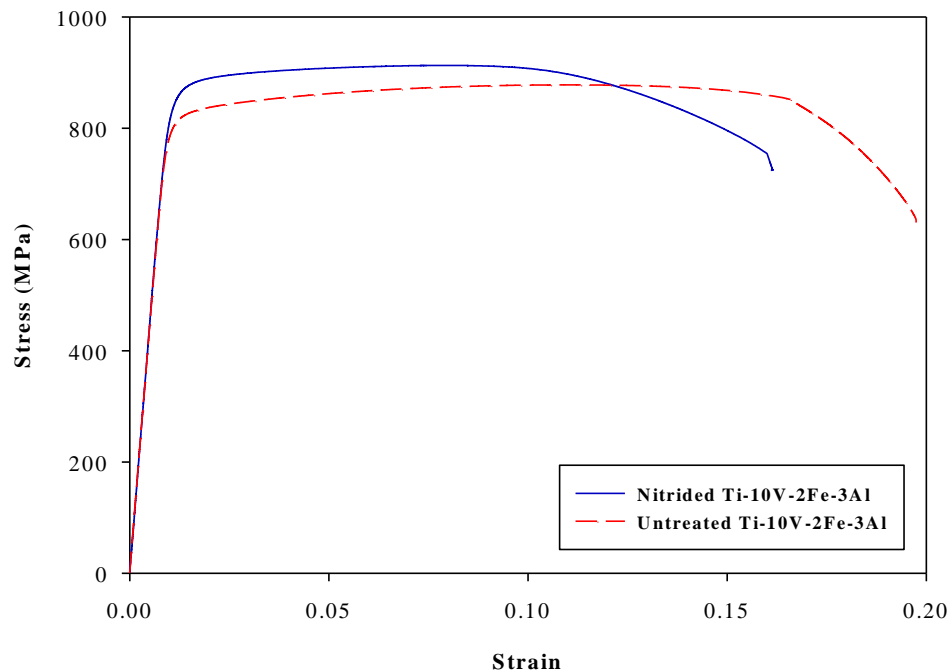


Figure 4.70 Plot of stress-strain curves for each of untreated and ion nitrided tensile test sample

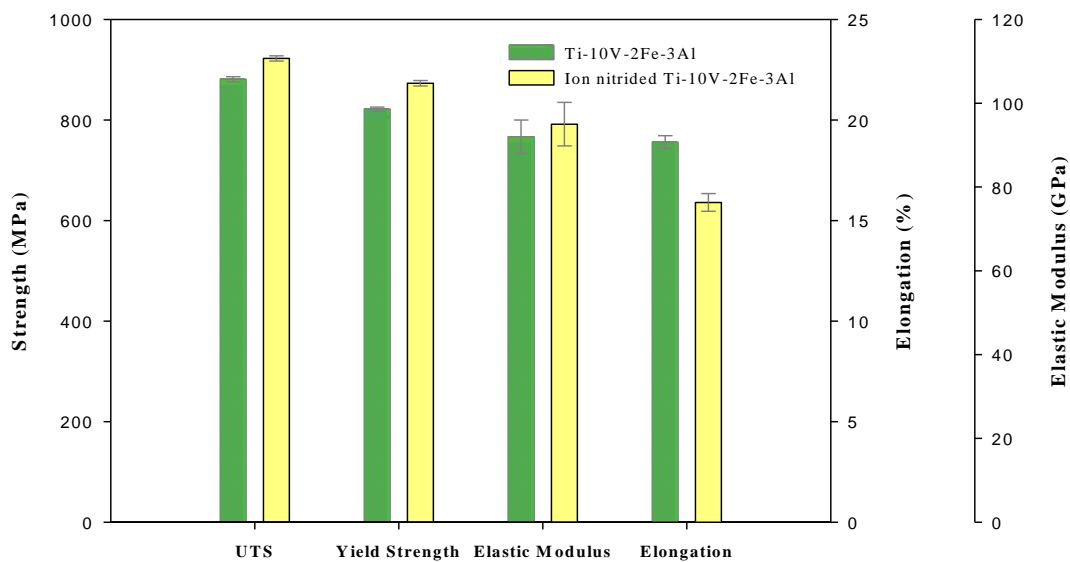


Figure 4.71 Comparison of tensile properties of untreated and ion nitrided Ti-10V-2Fe-3Al.

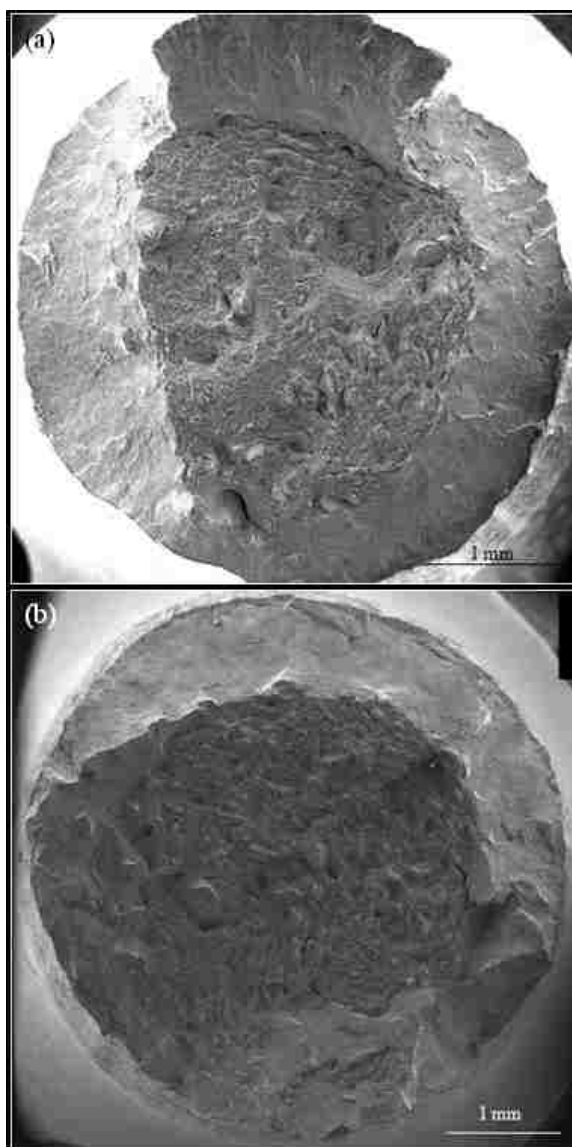


Figure 4.72 Secondary electron SEM images (SEI) showing fractured surface of (a) untreated and (b) ion nitrided alloys. The area fraction of ductile fractured region to overall fractured region for untreated alloy and ion nitrided alloy is 39% and 43%, respectively.

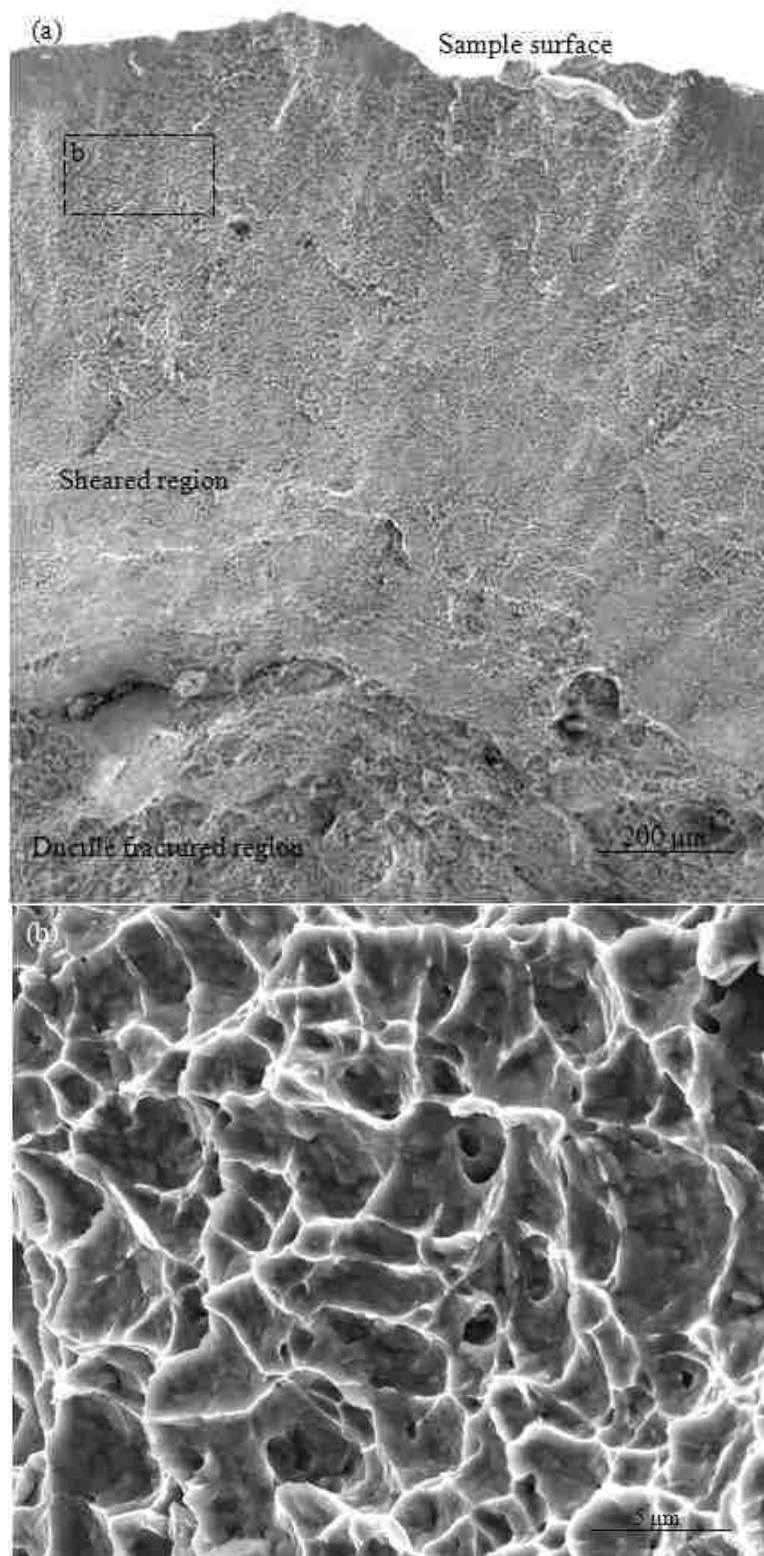


Figure 4.73 Secondary electron SEM image (SEI) showing near surface area from fractured surface of untreated Ti-10V-2Fe-3Al. Enclosed area is the location where higher magnification images are taken. (b) Secondary electron SEM image (SEI) showing sheared region containing dimples with average size of $12.3 \mu\text{m}^2$.

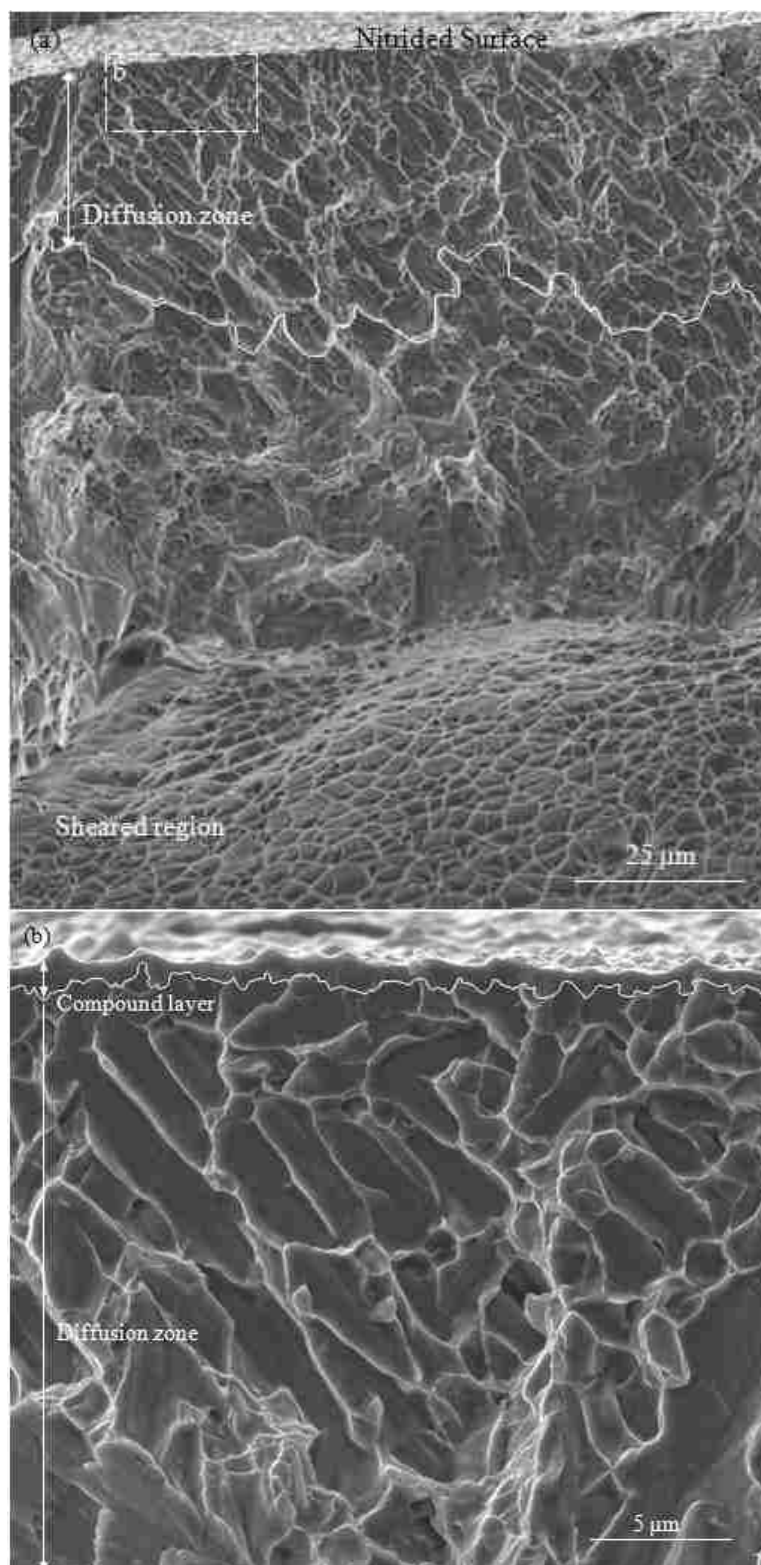


Figure 4.74 Secondary electron SEM image (SEI) illustrating a diffusion zone underneath compound layer observed from fractured surface of nitrided alloy. Enclosed area is the location where higher magnification images are taken. (b) Secondary electron SEM image (SEI) showing compound layer and diffusion zone.

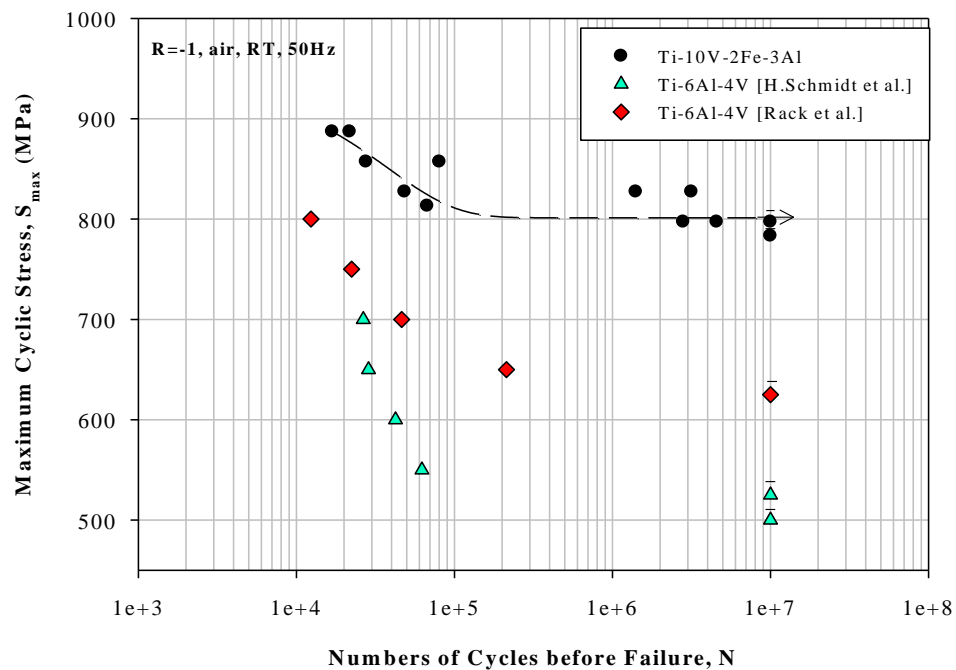


Figure 4.75 Comparison of S-N curves of Ti-10V-2Fe-3Al and Ti-6Al-4V in rotating beam loading ($R=-1$) [89,90]

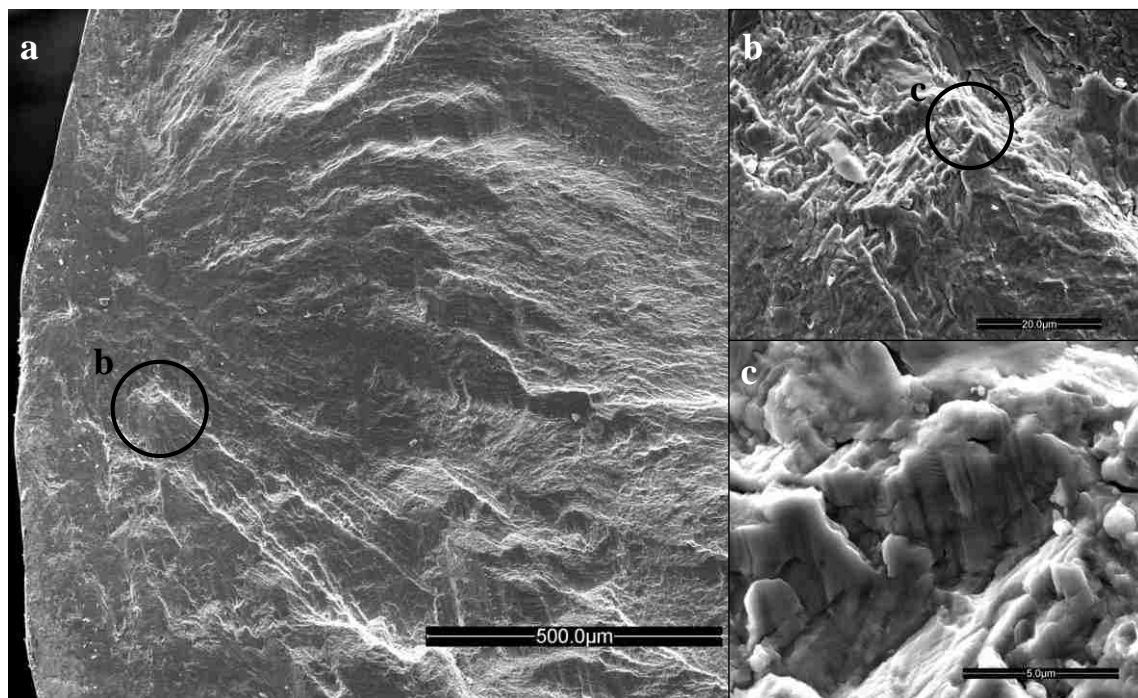


Figure 4.76 Secondary electron image (SEI) shows fatigue crack initiation at various magnifications for Ti-10V-2Fe-3Al fractured at maximum stress level of 797 MPa.

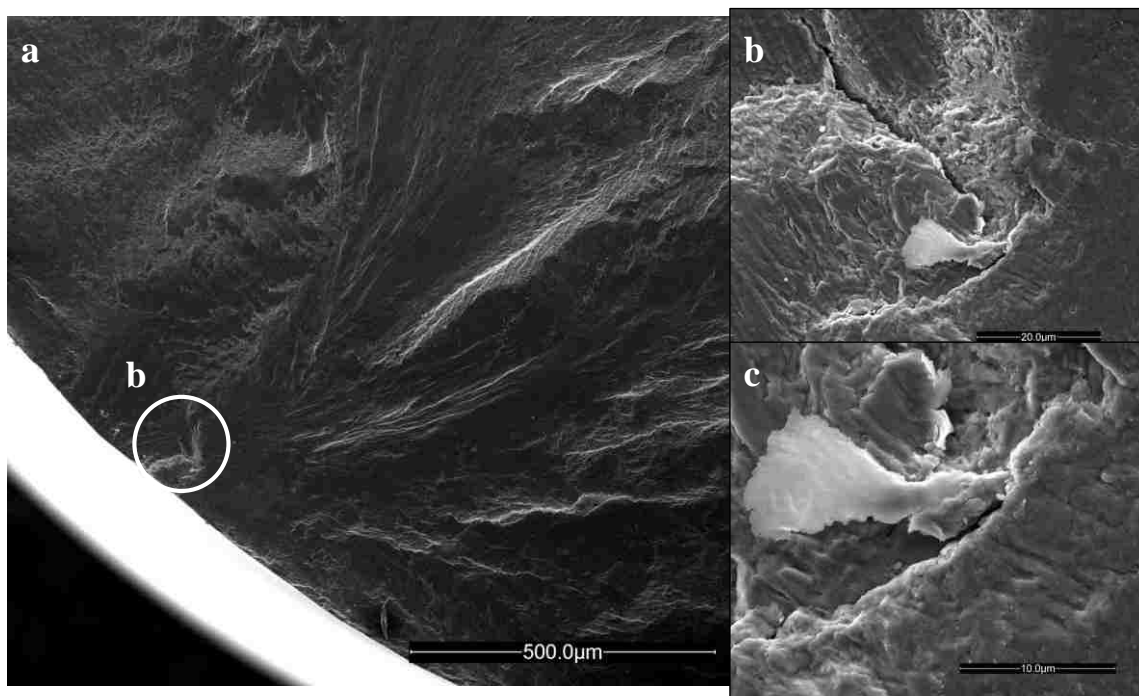


Figure 4.77 Secondary electron image (SEI) shows fatigue crack initiation at various magnifications for Ti-10V-2Fe-3Al fractured at maximum stress level of 827 MPa.

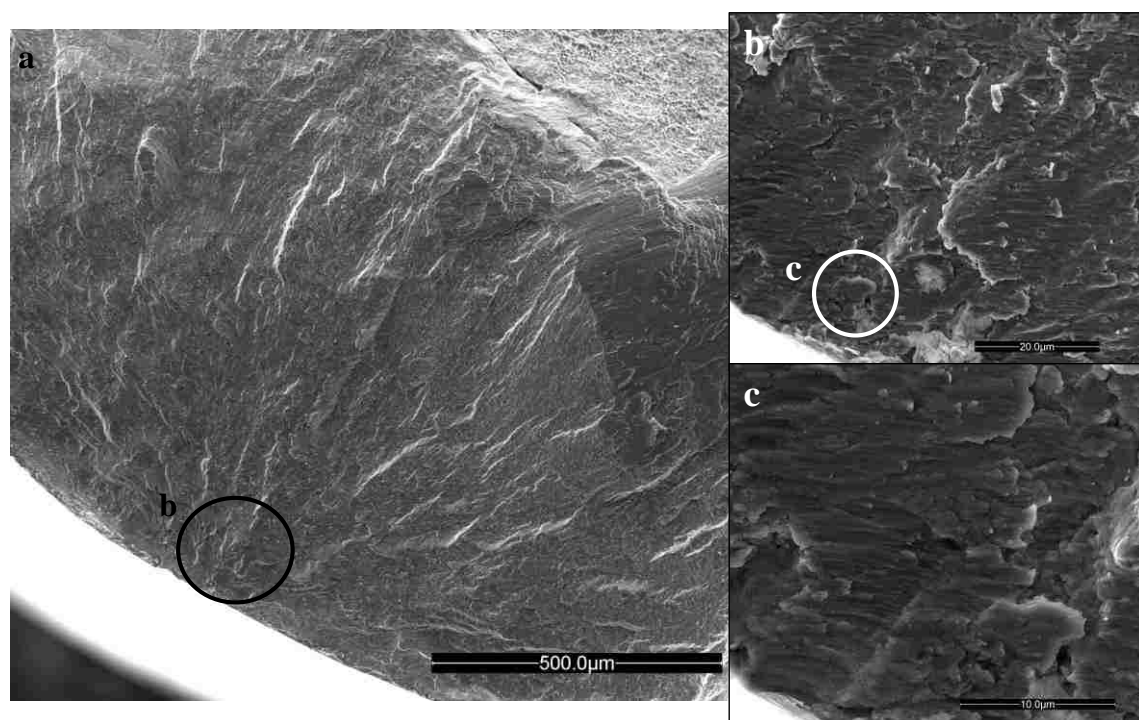


Figure 4.78 Secondary electron image (SEI) shows primary fatigue crack initiation at various magnifications for Ti-10V-2Fe-3Al fractured at maximum stress level of 887 MPa.

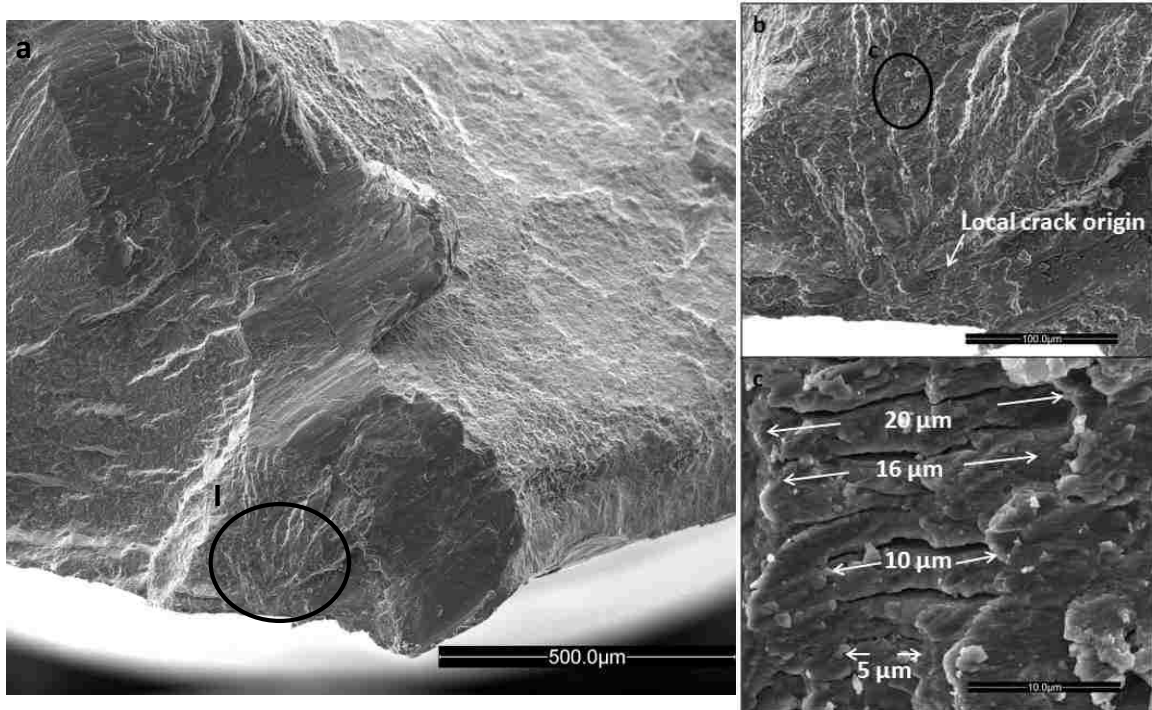


Figure 4.79 Secondary electron image (SEI) shows secondary fatigue crack initiation at various magnifications for Ti-10V-2Fe-3Al fractured at maximum stress level of 887 MPa.

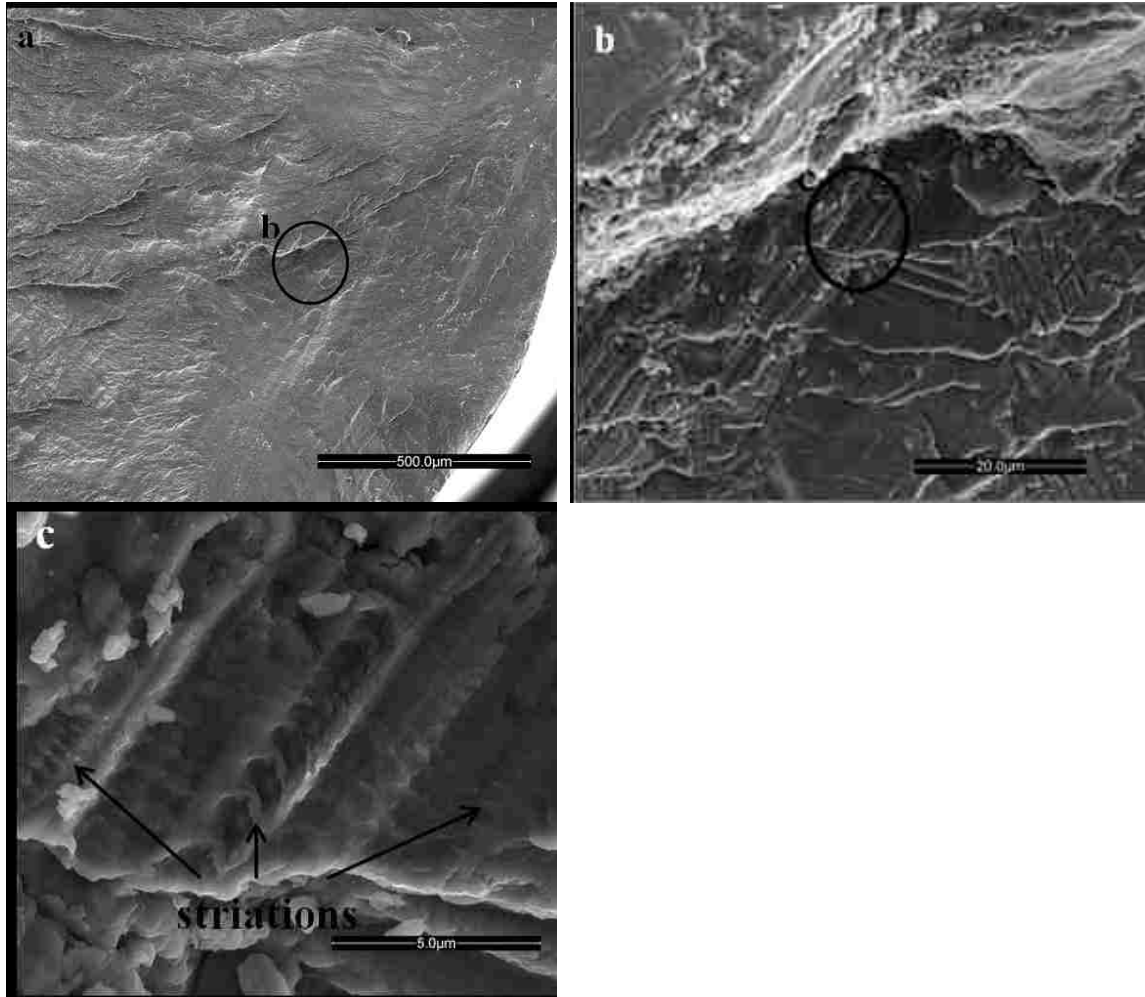


Figure 4.80 Secondary electron image (SEI) shows fatigue crack propagation at various magnifications for Ti-10V-2Fe-3Al fractured at maximum stress level of 797 MPa.

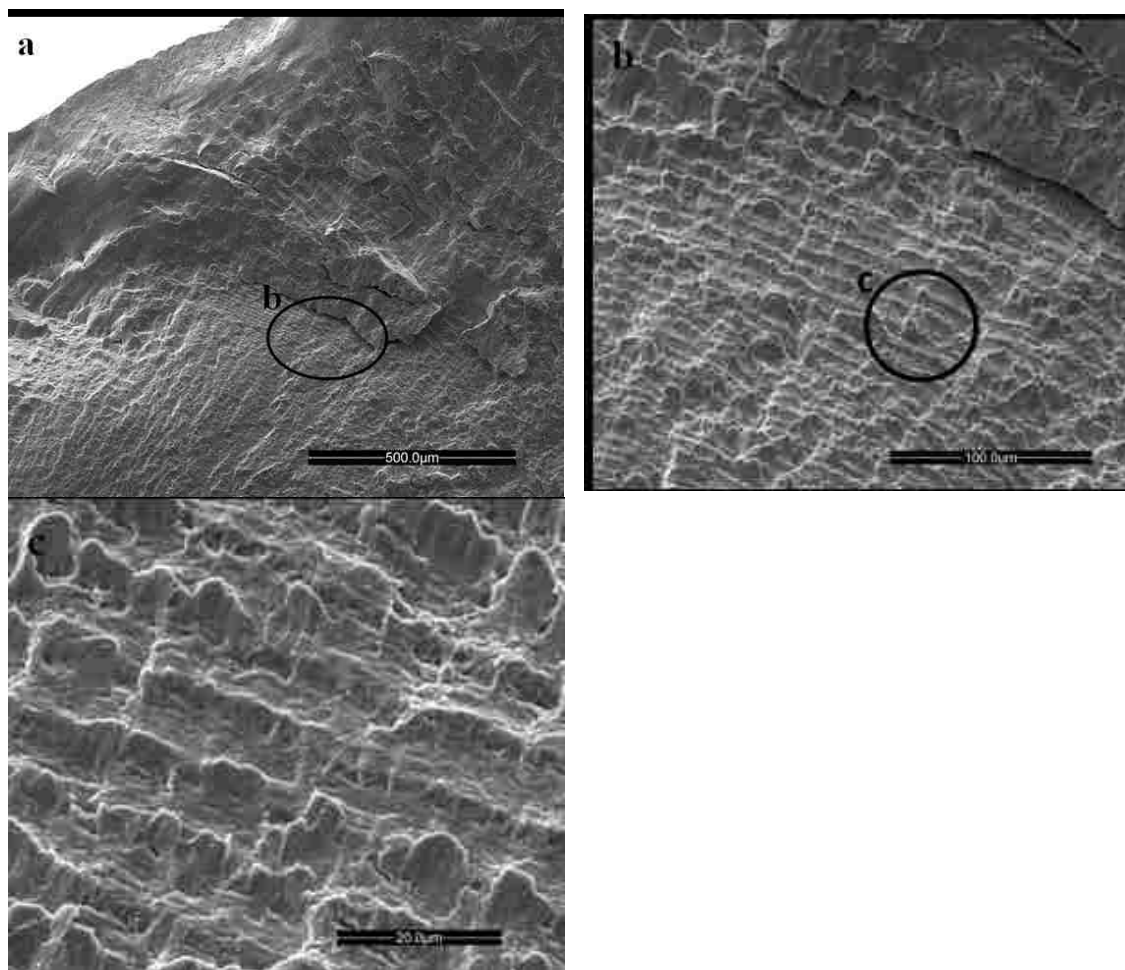


Figure 4.81 Secondary electron image (SEI) shows the region of fatigue crack propagation at various magnifications for Ti-10V-2Fe-3Al fractured at maximum stress level of 827 MPa.

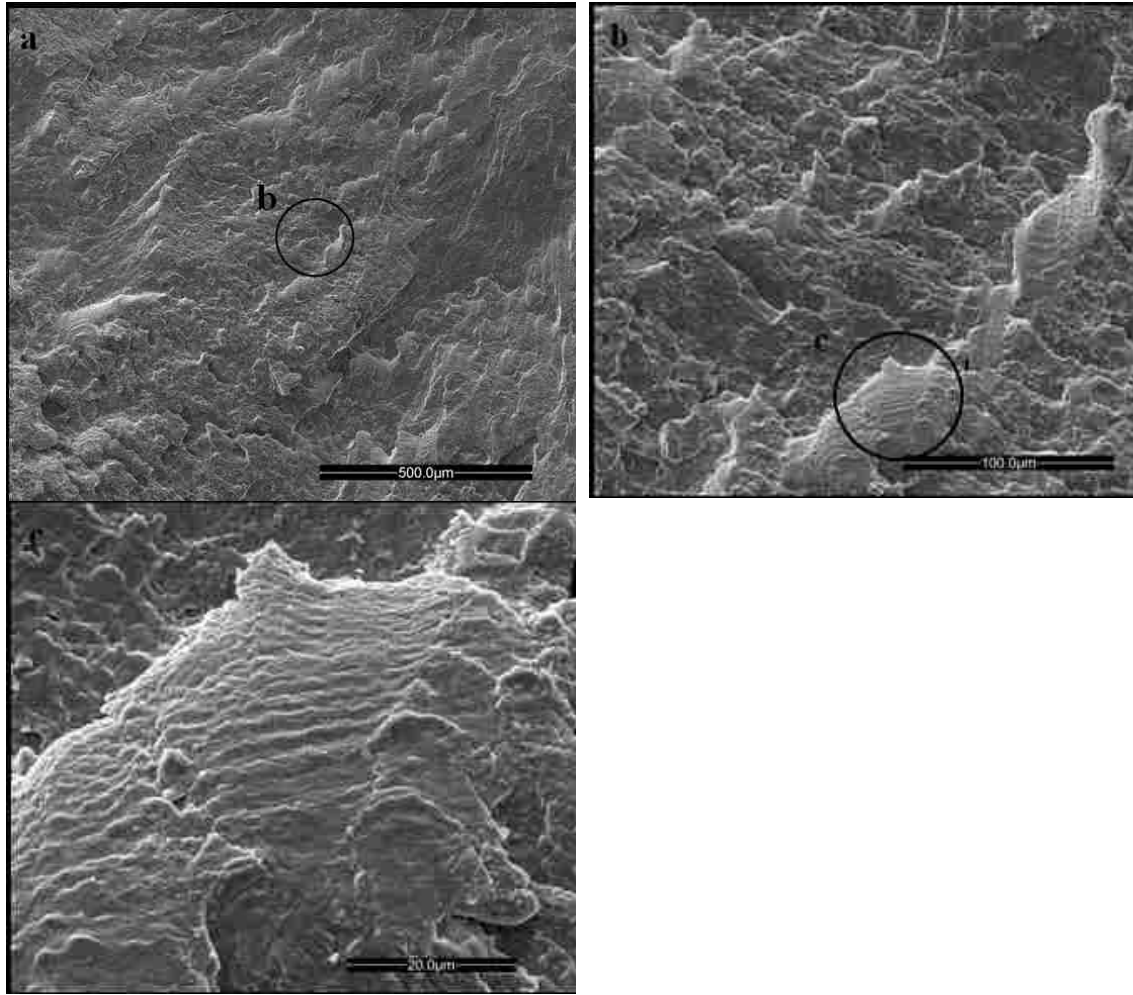


Figure 4.82 Secondary electron image (SEI) shows fatigue crack propagation at various magnifications for Ti-10V-2Fe-3Al fractured at maximum stress level of 887 MPa.

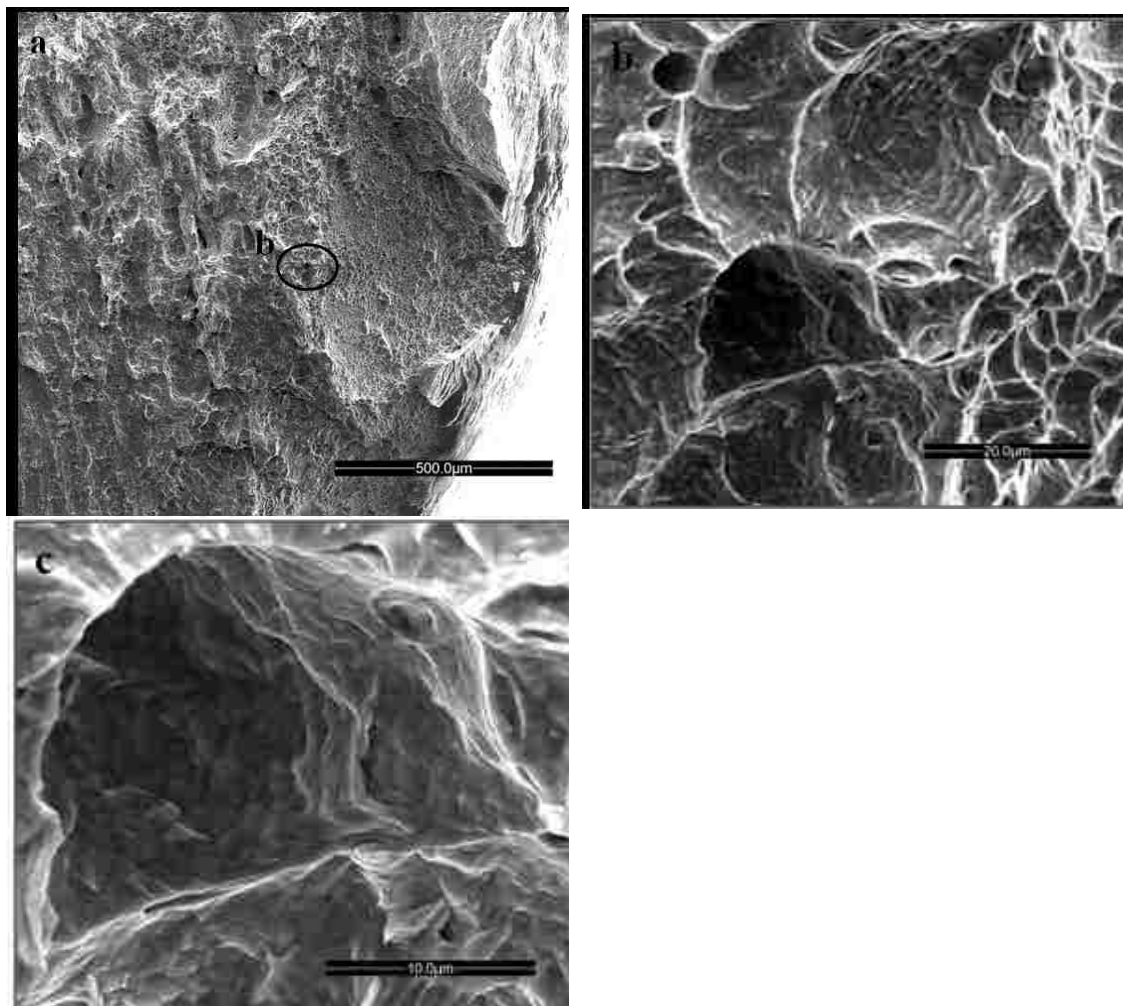


FIGURE 4.83 SECONDARY ELECTRON IMAGE (SEI) SHOWS DUCTILE OVERLOAD FRACTURE (DIMPLES) AT DIFFERENT MAGNIFICATIONS FOR Ti-10V-2Fe-3Al FRACTURED AT MAXIMUM STRESS LEVEL OF 797 MPa.

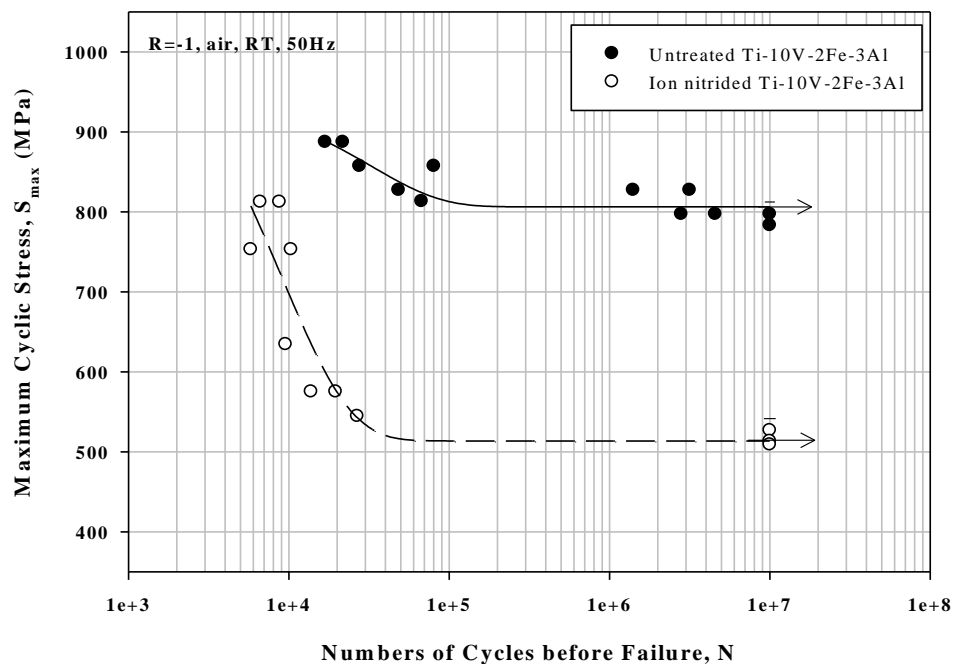


Figure 4.84 Comparison of S-N curves for untreated and ion nitrided Ti-10V-2Fe-3Al.

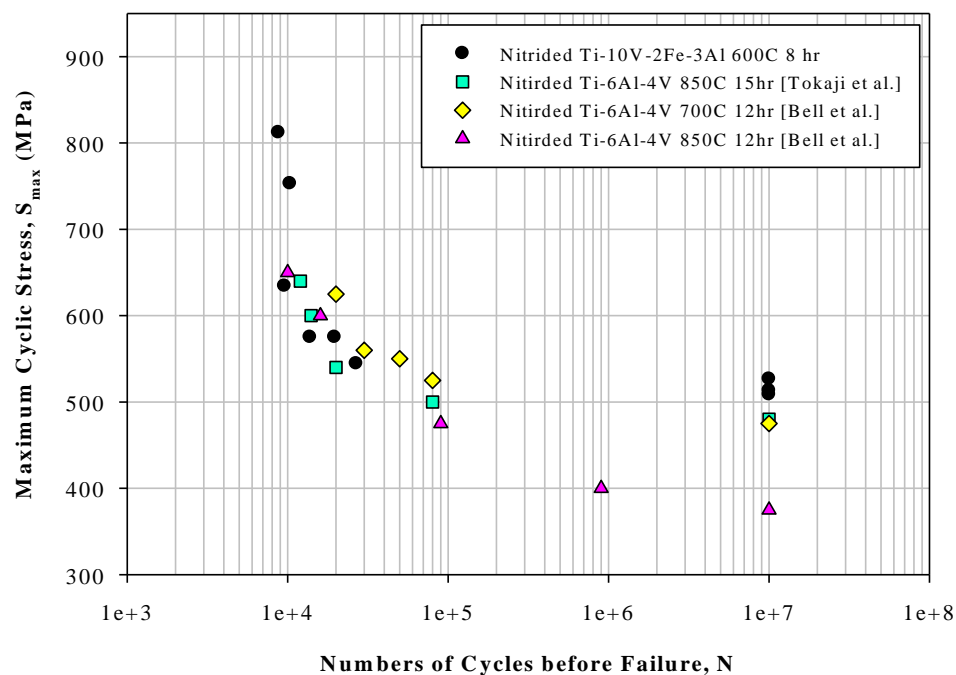
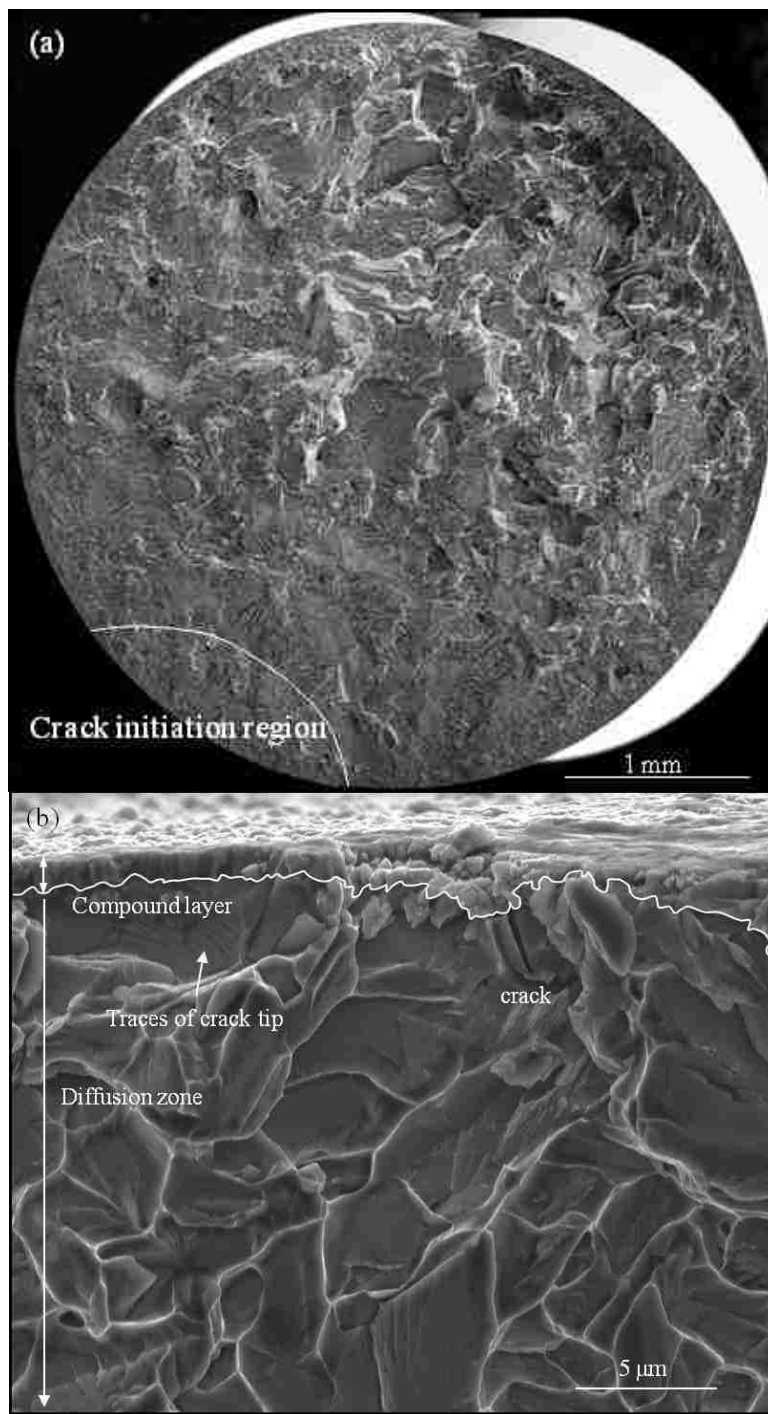


Figure 4.85 Comparison of fatigue test results obtained in this investigation with those found in the literature [56,70,91]. The fatigue limit has increased by approximately 10% compared to those treated at 700C.



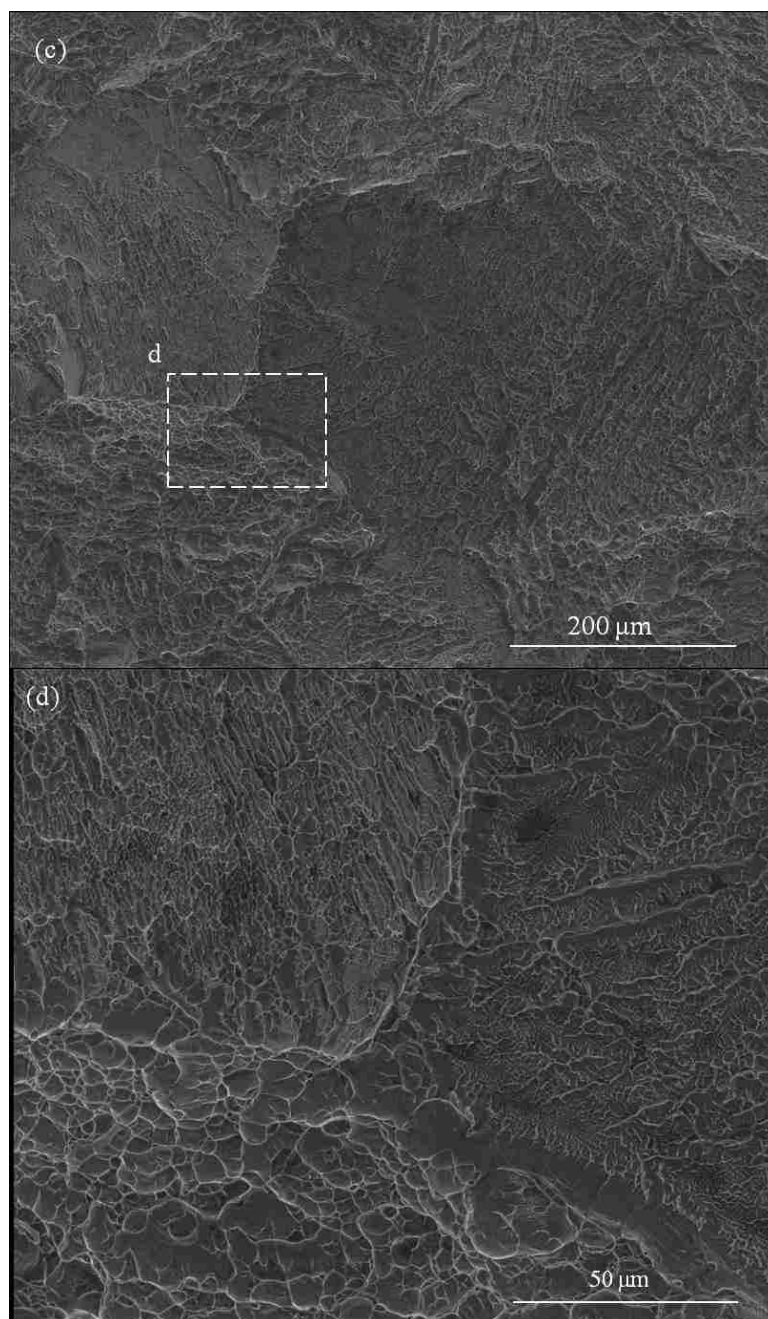
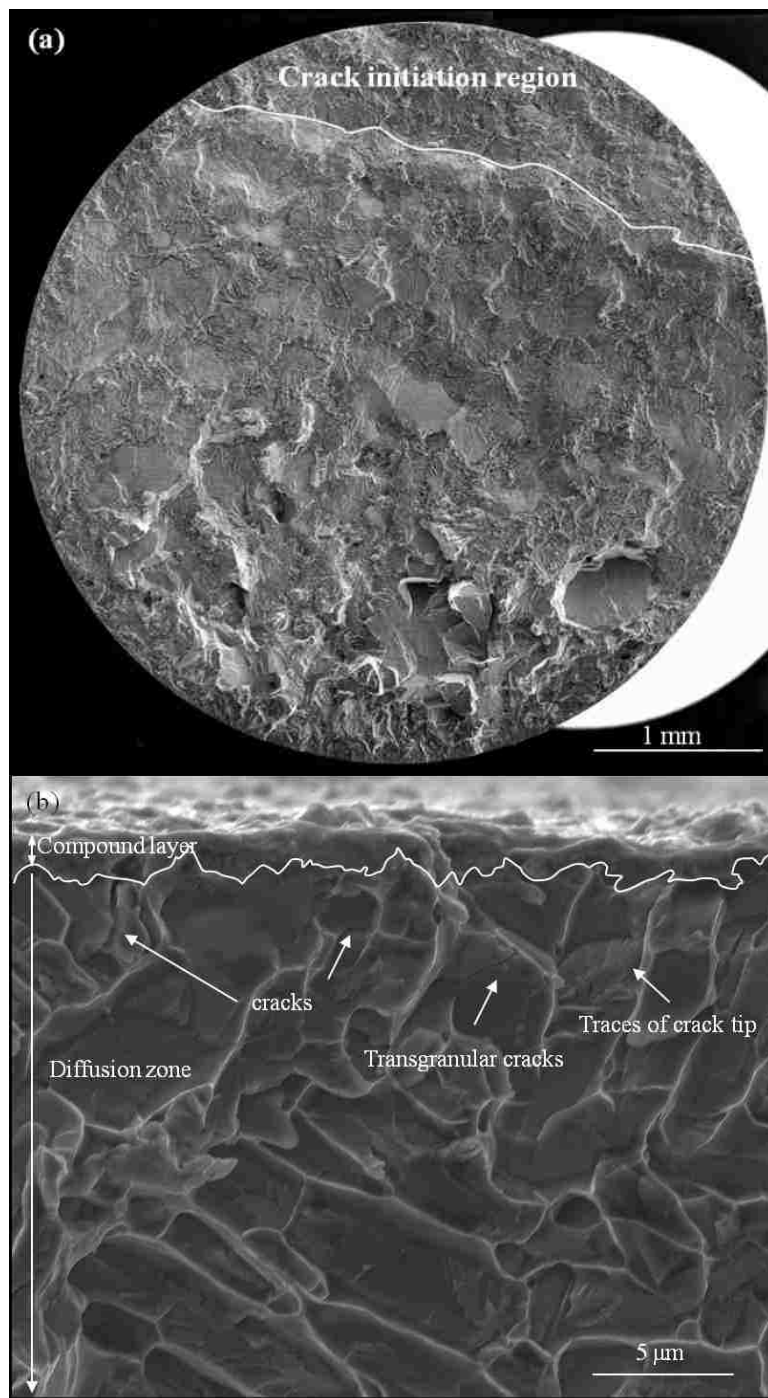


Figure 4.86 Secondary electron SEM image (SEI) showing (a) cross-sectional fracture surfaces of the nitrided sample broken at 544 MPa, (b) a close observation of crack initiation region showing the compound layer and diffusion zone. A crack is initiated underneath the compound layer reveals the surface crack initiation, (c) β grains consists of α grains in crack propagation zone, and (d) different orientation of grain morphologies.



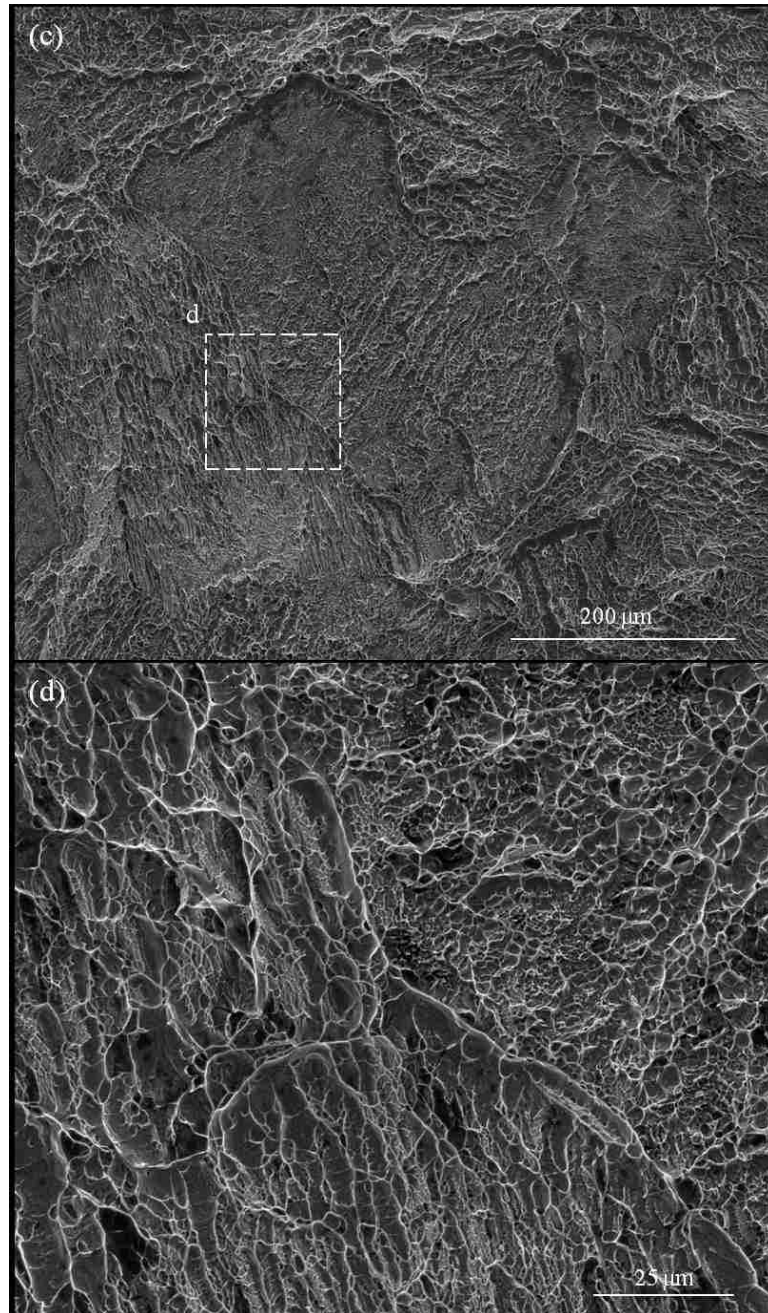


Figure 4.87 Secondary electron SEM image (SEI) showing (a) cross-sectional fracture surfaces of the nitrided sample broken at 744 MPa, (b) a close observation of crack initiation region showing the compound layer and diffusion zone. Several cracks are initiated underneath the compound layer reveals the surface crack initiation, (c) β grains consists of α grains in crack propagation zone, and (d) different orientation of grain morphologies.

CHAPTER 5
DISCUSSIONS

5.1 Ion nitriding of Ti-10V-2Fe-3Al

5.1.1 Effect of nitriding parameters on surface morphology and cross-sectional microstructure

Pre-surface treatment measures such as surface passivation and sputter cleaning, etc., played an important role during the nitriding treatment since proper treatments can remove surface contaminants and enhance the diffusion of nitrogen atoms. Chemical pickling, plasma gas sputtering and elongated plasma gas sputtering are compared. In general, the surface roughness caused by elongated plasma sputtering is the lowest among the three measures (Figure 4.5). The depth of the diffusion zone for both plasma sputtered samples reached 30 μm . Meanwhile, the thinnest compound layer (0.9 μm) is found on the elongated gas sputtered sample, which can be explained by the fact that surface sputtering cleaning helps to improve coating adhesion, and the coating exhibits higher hardness and a higher critical load of failure [92,93].

The results of the ion nitriding of Ti-10V-2Fe-3Al at 600°C and 800°C for 24 hours are compared. Higher surface roughness is found in the 800°C sample (Figure 4.10) because the increase in surface roughness depends mainly on the nitriding gas composition as well as the treatment time and temperature [94,95]. Meanwhile, coarse elongated α -stabilized grains are formed in the diffusion zone of the sample treated at 800°C (Figure 4.11-b); which is due to the $\alpha \leftrightarrow \beta$ phase transformation for the sample treated above the β transus temperature of Ti-10V-2Fe-3Al (795 \pm 3°C) [12,66,96]. Nevertheless, the formation of coarse elongated α -stabilized grains should be avoided

since a detrimental microstructure change can result in the loss of its good mechanical support for the compound layer and thus lead to coating failures [83].

At a constant nitriding temperature, 600°C, Ti-10V-2Fe-3Al is treated for 8 and 24 hours. According to Sha et al., microhardness, the thickness of the compound layer and the depth of the diffusion zone increase with the increase of nitriding duration [17,66]. The cross-sectional microstructure for both samples is homogeneous; the compound layer is continuous, and no coarse elongated α -stabilized grains are formed in the diffusion zone (Figure 4.16) since the nitriding temperature is lower than the β transus temperature of Ti-10V-2Fe-3Al ($795 \pm 3^\circ\text{C}$). The compound layer thickness of the sample treated at 800°C is increased by 74% (Figure 4.17); however, the formation of a thick compound layer should be avoided since the higher residual stresses result in longer nitriding duration, which can harm the adhesion of the coating to the substrate and further affect the fatigue resistance [17,97-99]. Chipping ($\sim 15 \mu\text{m}$ in width) is also observed on the micro-scratch path on the sample nitrided for 24 hours (Figure 5.1).

For a constant nitriding temperature (600°C) and duration (24 hours), a higher nitriding pressure (520 Pa) resulted in a much thinner diffusion zone (decreased by 57%) compared with samples treated under 67 Pa (Figure 4.22). Loss of diffusion depth results from the insufficient diffusion of nitrogen under high nitriding pressure. A high pressure gives rise to the decrease in the energy of bombarding ions [100]; Panaioti et al. further proved that a lower pressure can boost the energy of the bombarding nitrogen ions, which facilitated the formation of vacancies in the subsurface layer of the target, thus accelerating the nitrogen diffusion process. Nevertheless, the aim of this investigation is to develop a thick diffusion zone on nitrided samples since a thick diffusion zone (~ 30

μm) provides better mechanical support for the coating to avoid poor interfacial bonding between the compound layer and its substrate. Furthermore, a strengthened diffusion zone can also increase the load-bearing capacity significantly [101].

5.1.2 Microstructure analysis of ion nitrided Ti-10V-2Fe-3Al

The initial microstructure of the Ti-10V-2Fe-Al alloy used in this investigation consisted of rod-like α grains (35% α phase content) randomly distributed in the β phase matrix (Figure 4.2-a). After nitriding, a layered microstructure composed of a compound layer and a diffusion zone is formed on the surface, as schematically shown in Figure 5.2.

With its low β transus temperature (800 °C), a near β Ti-10V-2Fe-3Al alloy poses several challenges during surface modification treatments, especially nitriding, which is a potential means of improving the sliding behavior of Ti-10V-2Fe-3Al. These challenges include microstructural transformations in the bulk, e.g. formation of a α phase at the grain boundaries and inhomogeneous surface layers, e.g. coarse elongated α -stabilized grains [17]. Therefore, the nitriding of Ti-10V-2Fe-3Al should be performed under controlled treatment conditions, especially temperature and time, to avoid detrimental changes to its microstructure. In this research, the ion nitriding of Ti-10V-2Fe-3Al is conducted at a low temperature of 600°C for 8 hours in a low-pressure (67 Pa) dilute nitriding atmosphere (3% N_2). Meanwhile, microstructural analysis of the subsurface regions confirmed that, by adopting a low nitriding temperature of 600°C, the β phase is retained inside the diffusion zone, and no evidence for the formation of a α -stabilized layer is found in the substrate (Figure 4.32). According to Farokhzadeh et al. [83], the presence of ductile β particles in the DZ deflected and stopped the microcracks that initiated from the surface during scratch testing. Moreover, the ω precipitation

temperature (250-450°C) [1,12,102,103] is avoided in the treatments. Neither the TEM observations (Figure 4.34) nor the tensile results (Figure 4.71) indicate the formation of these brittle features.

The TEM observations from the near surface region show that the compound layer is composed of grains with different sizes (0.1-0.7 μm) and crystal structures. High-magnification TEM micrographs coupled with the corresponding electron energy loss spectroscopy EELS maps and electron diffraction patterns revealed that the compound layer is ~ 0.5 μm thick and consisted of TiN, Ti₂N and V₂N (Figure 4.36). The composition and phase configuration of the compound layer are studied using EELS and CBED patterns and confirmed by XRD results. The EELS spectra demonstrated the presence of nitrogen, vanadium and titanium close to the surface, and constructed EELS maps based on the collected data indicate that some grains in the compound layer are richer in nitrogen, while others are richer in titanium and vanadium (Figure 4.37-b). CBED patterns from the same locations indicate that the grains that are richer in nitrogen are composed of TiN (Fm-3m) crystals, and those richer in vanadium and titanium are V₂N (P-31m) and Ti₂N (P42-mnm) crystals, respectively, as illustrated in Figure 4.36. Titanium nitrides are commonly observed in the compound layer after the ion nitriding of titanium alloys [53,83,104,105]; however, vanadium nitrides are rarely reported. The formation of vanadium nitride along titanium nitride grain boundaries in this research is a functional diffusivity. The diffusion rate of substitutional V atoms in the Ti structure is slower than Ti self-diffusion and follows a non-Arrhenius trend at low temperatures (less than 750°C) [106]. At these temperatures, diffusion likely occurs along a short-circuit path, e.g. dislocations and grain boundaries [107], which is in agreement of the detection

of V_2N at the grain boundaries in this investigation, as shown in Figure 4.37-a. Furthermore, according to the XRD results (Figure 4.31), in addition to titanium and vanadium nitrides, the compound layer also contained traces of iron nitride, Fe_3N . Iron is a fast-diffusing element in titanium [1], and fine iron nitride grains are likely generated on the top surface of the compound layer and are not detectable in TEM observations.

α grains are observed in the diffusion zone located approximately 4 μm below the compound layer. Dislocation cell structures developed in some of these grains. The abundance of dislocations and their arrangement in the form of sub-grains is likely due to the plastic deformation imposed on these grains during the sputtering pretreatment with heavy Ar atoms. The diffusion of nitrogen atoms follows different patterns in the α and β phases. It is known that nitrogen diffuses faster through the β phase but has a higher solubility limit in the α phase [51,104,105]. Consequently, the abundance of the β phase in the microstructure resulted in the fast diffusion of nitrogen, as confirmed by a deep diffusion zone extending to a depth of 35 μm underneath the compound layer (Figure 4.39). On the other hand, the dissolution of nitrogen atoms in the α phase resulted in solution hardening of this phase, as evidenced by the formation of bending contours due to microstrains accumulated in the α grains in this region (Figure 4.38).

TEM observations also show a well-bonded interface between the compound layer and the diffusion zone; no micro-voids are detected in the interfacial region (Figure 4.36-a, Figure 4.37-a). The resulting microstructure exhibited improvements in the surface properties of the Ti-10V-2Fe-3Al. According to the micro-scratch test results, the ion nitriding process resulted in a considerable reduction in the average value and fluctuations of the coefficient of friction under the range of applied loads used in this

investigation (Figure 4.42 and Figure 4.43). Similar findings are reported after ion nitriding is performed on the Ti-6Al-4V alloy [83]. The improvement observed in the friction behavior can be attributed to the formation of the compound layer on the surface of ion nitrided Ti-10V-2Fe-3Al (Figure 4.32). The titanium nitrides (TiN, Ti₂N) effectively suppressed the tendency of the Ti alloy to adhere and transfer to the slider due to their high hardness and chemical inertness [108,109]. Furthermore, the presence of V₂N in the compound layer (Figure 4.36, Figure 4.37 and Figure 4.31) may have also contributed to the improved friction properties due to its high hardness and adhesion resistance [110,111].

5.1.3 Microscratch behaviour of ion nitrided Ti-10V-2Fe-3Al

During micro-scratch tests under progressive loading, the compound layer maintained good adhesion to the substrate up to a normal load of 17N, corresponding to a mean contact pressure of 10.8 GPa (Figure 4.41). At applied normal loads less than the critical value, the compound layer can conform to the deflection of its substrate albeit with the formation of some tensile cracks within the scratch paths (Figure 4.44). This high load-bearing capacity of the nitrided surfaces appear to be a combined effect of the thin compound layer (Figure 4.32) and the deep diffusion zone (Figure 4.39). The thin compound layer does not experience any buckling or delamination under sliding conditions due to the low level of residual stresses and mechanical support from the diffusion zone. Similar observations have also been reported by several researchers [109,112-114]. Nevertheless, when the applied load during micro-scratch tests exceeded the critical value, the compound layer experienced delamination and is detached from the substrate around the scratch path edges (Figure 4.45).

The deep diffusion zone contributed to the high critical load of 17N during sliding (Figure 4.44) by minimizing abrupt changes in stress distribution at the interface and providing good mechanical support for the compound layer [113,115-117]. The diffusion zone had a microhardness profile that gradually decreased from 425 HV to 340 HV (Figure 4.39). This zone mitigated the significant difference in the deformation behavior of the compound layer [118] and the Ti-10V-2Fe-3Al substrate like a “functionally-graded interface” [119]. As a result, the nitrided surfaces performed well under sliding contact and do not experience any premature failures caused by stress concentrations at the interface [56,120,121]. The enhanced nitrogen diffusion kinetics in Ti-10V-2Fe-3Al evidenced by the deep diffusion zone (Figure 4.39) is due to the 65% β phase content with high nitrogen diffusivity [51,104,105,114]. The prolonged (3-hour) sputtering of the surfaces prior to the nitriding treatment in this research also accelerated the nitrogen diffusion by the formation of several dislocations inside the α -grains. It has also been reported that the Ar+H₂ sputtering increased the nitriding kinetics in ferrous alloys by providing easy diffusion paths for nitrogen interstitials, e.g. dislocations and eliminating inherent surface oxides [122,123]. The absence of oxygen and oxides in the TEM-EELS and XRD results (Figure 4.37-b and Figure 4.31) and the formation of a deep diffusion zone (Figure 4.39) suggested that nitrogen diffusion is accelerated in Ti-10V-2Fe-3Al with mechanisms similar to those of the ferrous alloys [122,123].

5.2 Wear behaviour of Ti-10V-2Fe-3Al

Wear rates and the average steady-state COF are two main parameters that indicate the difference between two distinguished wear behaviours for Ti-10V-2Fe-3Al samples, namely low (0.8N) and high loads (5N). Two wear mechanisms, delamination wear and oxidational wear, are observed for both low and high loads; however, oxidational wear dominated at low loads and delamination wear dominated at high loads.

The wear rates of Ti-10V-2Fe-3Al increased sharply at lower loads (from 0.8N to 3.5N) and increased moderately when approaching higher loads (from 3.5N to 5N). The COF is the expression of the energy consumed from the heat dissipation. The COF recorded is low during the running-in period and increased abruptly until it reached the steady-state condition (Figure 4.49). The lower initial COF in the running-in period can be explained by the fact that the titanium oxides that accumulated on the surface of polished Ti-10V-2Fe-3Al provided wear resistance in the beginning of the test. The higher COFs recorded in the steady-state conditions are attributed to the breach of thin titanium oxides and the beginning of plastic deformation [124]. The motivation of the abrupt increase in the COF is unclear, and the running-in period for different loading conditions varies. The higher value of the steady-state COF presented by the 0.8N sample than that of the 5N sample resulted from the changes in the mechanical and metallurgical properties of the asperities' contact on the sliding surfaces. When two surfaces slid against each other, the frictional heat generated at the contact points oxidized the sliding surfaces. The instantaneous temperature at contact asperities, also known as the flash temperature (T_f), and the average surface temperature, also known as the bulk temperature (T_b), are calculated for each loading condition according to the simplified

temperature equations developed in Engineering Tribology and by Lim and Ashby [44,125]. A list of parameters for the calculation of the flash and bulk temperatures during wear tests can be found in Appendix 1. At 0.8N, the bulk temperature is determined to be 26°C, and the flash temperature is 53°C. The bulk temperature at 5N is very similar to the value at 0.8N, which is 29°C, but a much higher flash temperature of 196°C is obtained in the high load conditions. Therefore, a heavily oxidized surface is formed at high loads due to the higher flash temperature. The drop in the average steady-state COF value from 0.8N to 5N is due to the increase in the oxidized layer thickness between two contact surfaces [125,126]. On the other hand, the increase in the COF in the steady-state conditions compared with the running-in state resulted from the entrapment of wear debris that reacted with oxygen in the atmosphere, forming titanium oxides (TiO) that accumulated on the wear samples. This is due to the low thermal conductivity of Ti-10V-2Fe-3Al, which caused heat to dissipate slower than the heat generated from the unlubricated sliding process. Therefore, an adiabatic shear band formed under dry sliding conditions [127-129]. A fluctuating COF is observed during steady-state friction, which depended on the delamination of the oxide layer. If titanium oxides formed and attached on the wear track, they acted like a lubricant between the bulk Ti-10V-2Fe-3Al and the counterface 52100 steel ball, resulting in a drop in COF. However, the titanium oxides are not stable, so they are forced to break and disappear. Therefore, the COF increased again, and as the heat increased, a new layer of oxides formed, which lowered the COF again.

At low loads (0.8N), the flash temperature caused the growth of oxides at asperity contacts; as the sliding process continued, the thin oxide film generated at the asperities

expanded and adhered to the mechanically mixed layer. The wear debris attached to the wear track consisted mainly of titanium oxides, which are generated by flash heating between two sliding surfaces [125]. Two forms of oxides are observed, plate-like oxide flakes (Figure 4.53-a) and ultrafine oxide particles (Figure.4.53-b). A further sliding process resulted in the formation of cracks within oxide flakes, as shown in Figure 4.52-c, which illustrated repeating fragmentation of oxide flakes, which formed tiny oxide particles.

FIB analysis shows the subsurface morphology of a Ti-10V-2Fe-3Al wear test sample that contained a continuous mechanically mixed layer that consisted of pores and the mixing of the α and β phases, as well as its spallation from the substrate, as shown in Figure 4.54. A combination of mechanical mixing and crack propagation are found in this layer under further sliding conditions. The mechanically mixed layer exfoliated from the Ti-10V-2Fe-3Al substrate shows the crack propagation and coalescence. As stated before, titanium oxides generated at one place within the mechanically mixed layer are expanded and thickened but not trapped between two sliding surfaces due to low contact pressure. Instead, titanium oxides in the form of fine particles or plate-like debris are dragged longitudinal to the wear test sliding direction. Therefore, the transferable oxides stayed on the wear track for the further sliding process, resulting in a high steady-state COF. Moreover, deformed β grains are shown in Figure 4.54-b; they indicate plastic deformation in the substrate during the sliding process. This is in agreement with T. Bell et al., who stated that plastic deformation, in general, initiates from the substrate near the interface of the coating and the substrate first [101].

In the high loading condition (5N), although the wear rate is high, the average steady-state COF is lower compared to the value of the COF in the low loading conditions. A transition of the wear regime from local damage of titanium oxides to the delamination of a mechanically mixed layer is reported under high normal force [130]. The direct metallic contact always kept the COF low. Nevertheless, higher temperatures are generated at higher loads. The oxidation effect is stronger; therefore, titanium oxides are formed on most parts of the wear track. These thin but tough titanium oxides are trapped between two sliding surfaces due to high contact pressure, thus providing wear resistance locally and increasing the COF. However, continuing applied high normal force breached the titanium oxides, again resulting in delamination of the mechanically mixed layer. Therefore, a large fluctuation in the steady-state COF, shown in Figure 4.49-b, indicates the frequent transition between delamination of the mechanically mixed layer and local damage of titanium oxides. A large amount of wear debris is also observed on wear tracks, including fine oxide particles, small-scale TiO flakes (Figure 4.57-a) and large-scale Ti-plate debris (Figure 4.57-b). The EDS analysis, shown in Figure 4.59, demonstrated plate-like wear debris does not contain any oxygen, which indicates the presence of Ti plates. The Ti plate composition is very close to the tribolayer on the Ti-10V-2Fe-3Al wear sample. Rigney et al. reported that the flake-like wear debris produced by delamination is attributed to lamellar extrusion [131]. Overall, the delamination of the mechanically mixed layer on Ti-10V-2Fe-3Al is the dominant wear mechanism at higher loads. The FIB analysis shows subsurface voids and cracks at a depth of 10.3 μm from the worn surface, also known as the mechanically mixed layer (Figure 4.58-b). Subsurface voids are nucleated due to unidirectional shearing; in other words, in the

repeated one-way sliding direction, these voids extended and coalesced to form cracks underneath the worn surfaces. Further sliding allowed the subsurface cracks expanded until they are large enough for the mechanical mixed layer to be exfoliated from the bulk material.

Other than subsurface micro-cracks, surface cracks normal to the sliding direction are observed on the wear tracks of Ti-10V-2Fe-3Al samples (Figure 5.4), which indicate the damage of titanium oxides during the sliding process. Therefore, cracks initiated from the subsurface (delamination) and originated from the surface (fragmentation) are two main indicators that show that plasticity-dominated delamination wear occurred at high loads (5N).

Lower wear rates are found in ion nitrated samples because of the formation of hard compound layer. The wear rate of the 2N sample is negative, which indicates the wear of counterface and the counterface wear debris accumulated on the wear track increases the weight of the Ti-10V-2Fe-3Al sample.

5.3 Tensile properties of Ti-10V-2Fe-3Al

Observation from untreated tensile samples shows that there are microvoids in the dimple rupture region (Figure 4.68-b); these voids are initiated at the α/β interface, revealing that ductile fracture occurred at the interface between the α and β phases. Microstructural observation on the skin of tensile sample illustrated elongated α grains along the loading direction, forming a heavily deformed region, as shown in Figure 4.69-b. Elongation of α grains on the skin of the tensile surface as well as the initiation, growth and coalescence of microvoids required high plastic deformation energy, resulting from the high ductility of the Ti-10V-2Fe-3Al alloy.

The area fraction of the ductile fractured region compared to the overall fractured region for the untreated alloy and the ion nitrided alloy is 39% and 43%, respectively. Microvoids are initiated inside the dimples from the sheared region on nitrided samples (Figure 4.68-b), which differs from the void initiation sites found from the α/β interface in untreated samples. After nitriding, a compound layer ($\sim 1 \mu\text{m}$ thick) is formed on the sample surface; the brittle compound layer increased the surface hardness but reduced the ductility of the nitrided sample. The hardening effect of the nitrided surface delayed the formation of surface cracks, but the growth and coalescence of microvoids are accelerated since less plastic energy is required to form and coalesce of microvoids due to the lower ductility of the nitrided alloy.

5.4 Fatigue properties of Ti-10V-2Fe-3Al

One of the important design considerations for Ti-10V-2Fe-3Al in aerospace applications is the fatigue resistance, specifically the endurance limit [34]. For titanium alloys, fatigue life is dominated by fatigue crack initiation; an increase in high-cycle fatigue life generally results from a delay in crack initiation [132]. In most cases, an inclusion inside the material can become a crack initiation site (Figure 4.77-c). Therefore, crack initiation sites are critical when observing samples under SEM.

The fatigue strength obtained from untreated Ti-10V-2Fe-3Al is very competitive to that of other alloys, such as Ti-6Al-4V. The fatigue strength of untreated Ti-10V-2Fe-3Al might correspond to microstructural factors such as β grain size and the thickness of the boundary α phase as well. Bhattacharjee et al. [24] summarized the fracture toughness values of the Ti-10V2Fe-3Al alloy for different grain sizes, as shown in Table 2.3, which shows that the fracture toughness decreased as the grain size increased. Therefore, the

fatigue properties may vary depending on the microstructural parameters. The β grain size in the bulk area of the untreated alloy is stated in section 4.2.1, which is measured at $256 \pm 58.3 \mu\text{m}^2$ [84,85]; however, an α grain boundary is rarely observed.

For nitrided titanium alloys, the unusual crack initiation behaviour of titanium alloys is the huge difference in deformation between the bulk material and the compound layer. The titanium alloys possessed large elastic deformation, low elastic modulus and high strength. After nitriding, a thin but brittle compound layer formed; the elastic modulus of the TiN layer, however, can be two to six times higher than that of the bulk materials [70]. The elastic modulus for titanium nitrides varied between 300 and 400 GPa [91,133], while the elastic modulus for Ti-10V-2Fe-3Al in this investigation is measured at 92 GPa. The fully reversed stress amplitude generated localized fatigue deformation at the surface; the TiN layer is subjected to very high stress under severe deformation. Cracking is initiated in the TiN layer and the hardened solid solution layer since the brittle nitrided layer cannot suffer the same amount of deformation as the core material due to its brittleness. Cracks initiated from the compound layer subsequently grew rapidly into the bulk. In the meantime, traces of crack tips are found underneath the compound layer for both low cycle and high cycle fatigue life samples (Figure 4.86-b and 4.87-b), which indicate the early crack nucleation and fast crack growth at the interface of the compound layer and the diffusion zone[70].

After nitriding, the core material (500 μm below the compound layer) microstructure changed, such as grain growth. Since the fatigue strength is sensitive to the microstructure [91], enlarged β grains resulted in a drop in fatigue strength. The β grain size in the cross-sectional microstructure of the ion nitrided alloy is measured at

$332 \pm 80.6 \mu\text{m}^2$, an increase of 29.7%. The average thickness of the α grain boundary is measured at $1.68 \pm 0.53 \mu\text{m}$, which is equivalent to that of the untreated alloy. Since the Hall-Petch relationship between fatigue strength and grain size is found in nitrided titanium [134], an increase in grain size decreased the fatigue strength. Meanwhile, fatigue striations are found propagated between α grains; these α grains are confined inside enlarged β grains. Fatigue striations changed their orientation at the α grain boundary phase; therefore, the α grain boundary phases can block or delay the propagation of fatigue striations. In a unit area, enlarged β grains indicate less grain boundary, thus facilitating the fatigue propagation process and resulting in a drop of fatigue strength in nitrided fatigue samples.

Jha et al. summarized the factors affecting the fatigue behaviour of Ti-10-2Fe-3Al from a microstructure perspective [34]. There are two types of microstructure of Ti-10V-2Fe-3Al, namely Class 1 and Class 2, respectively. The Class 1 microstructure possessed uniform α grains distributed in the β matrix, which is very close to the microstructure of the as-received Ti-10V-2Fe-3Al in this research. The Class 2 microstructure possessed a nearly continuous α grain boundary and inhomogeneous α distributed in the β matrix, which is very similar to the microstructure of nitrided Ti-10V-2Fe-3Al. Jha et al. compared the fatigue limit of those two classes and stated that, in general, Class 1 microstructures show a medium to high endurance limit (800 to 1,100 MPa) over a range of strength levels. Class 2 microstructures, however, show a relatively lower fatigue limit (500 MPa to 700 MPa). Therefore, the decrease in fatigue strength in nitrided Ti-10V-2Fe-3Al is mainly due to the microstructure change from Class 1 to Class 2.

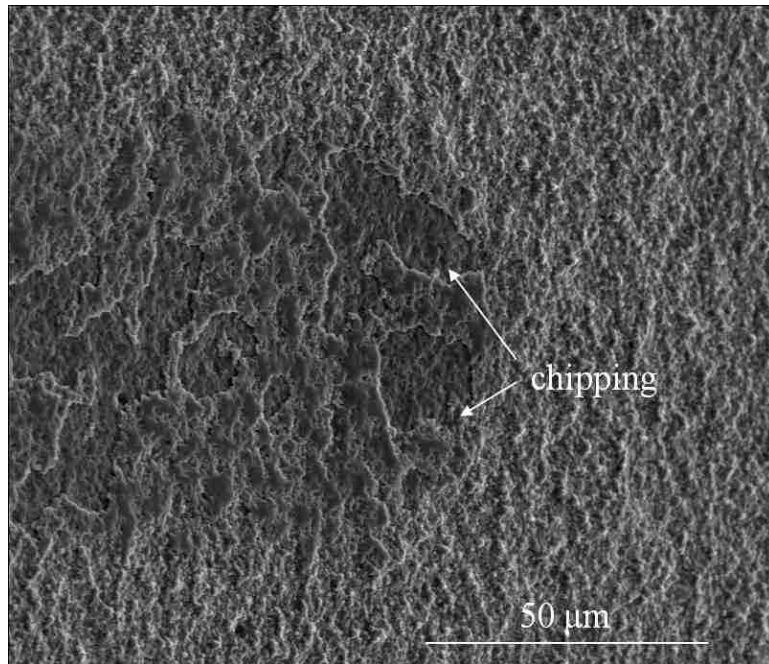


Figure 5.1 Secondary electron SEM image (SEI) showing chipping on the micro-scratch path of the sample nitrided at 600C, 24 hours, 67 Pa under constant loading of 20 N.

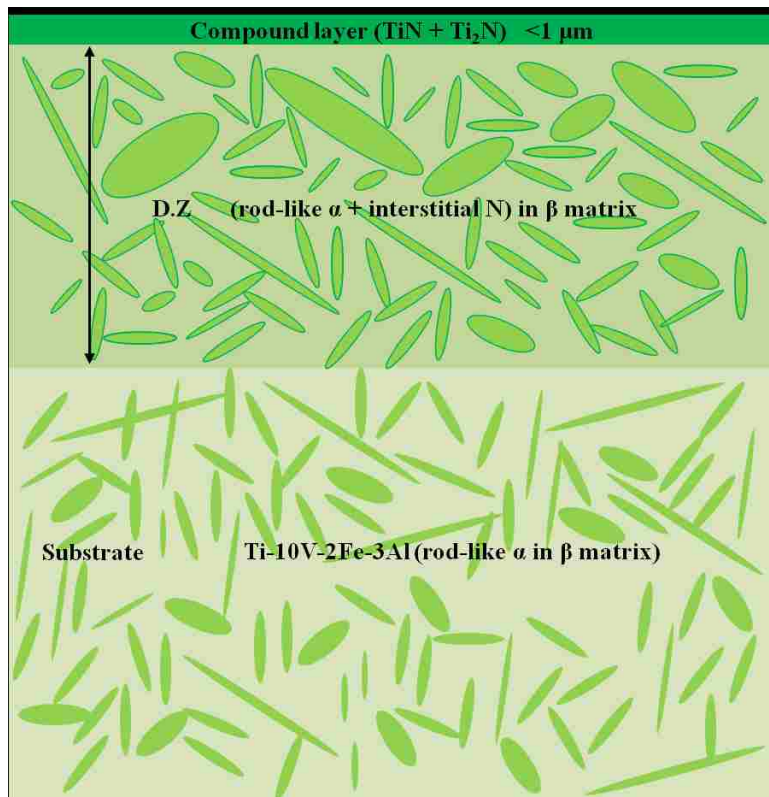


Figure 5.2 Schematic presentations of the ion nitrided Ti-10V-2Fe-3Al microstructure consisting of a thin compound layer and thick diffusion zone.

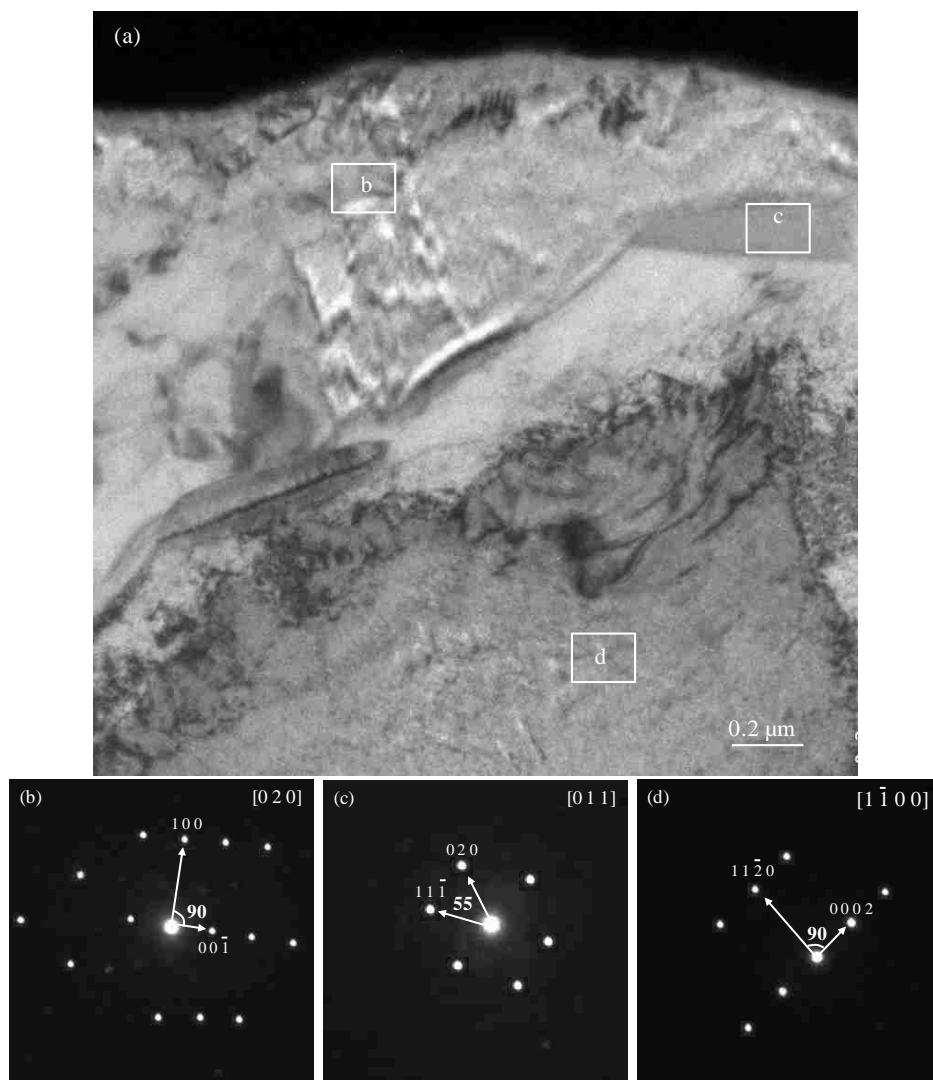


Figure 5.3 (a) A bright field TEM image (BF-TEM) showing a high magnification view of the ion nitrided Ti-10V-2Fe-3Al microstructure at location “B” in Figure 5. The locations where several convergent beam electron diffraction (CBED) patterns were taken are marked in the image. (b) A typical diffraction pattern confirming the formation of Ti_2N ($P4_2\text{-mm}$) grains in the surface vicinity. (c) A typical diffraction pattern confirming formation of V_2N ($P\text{-}31m$) grains at grain boundaries in the near surface region. (d) A typical diffraction pattern from an $\alpha\text{-Ti}$ grain underneath the compound layer.

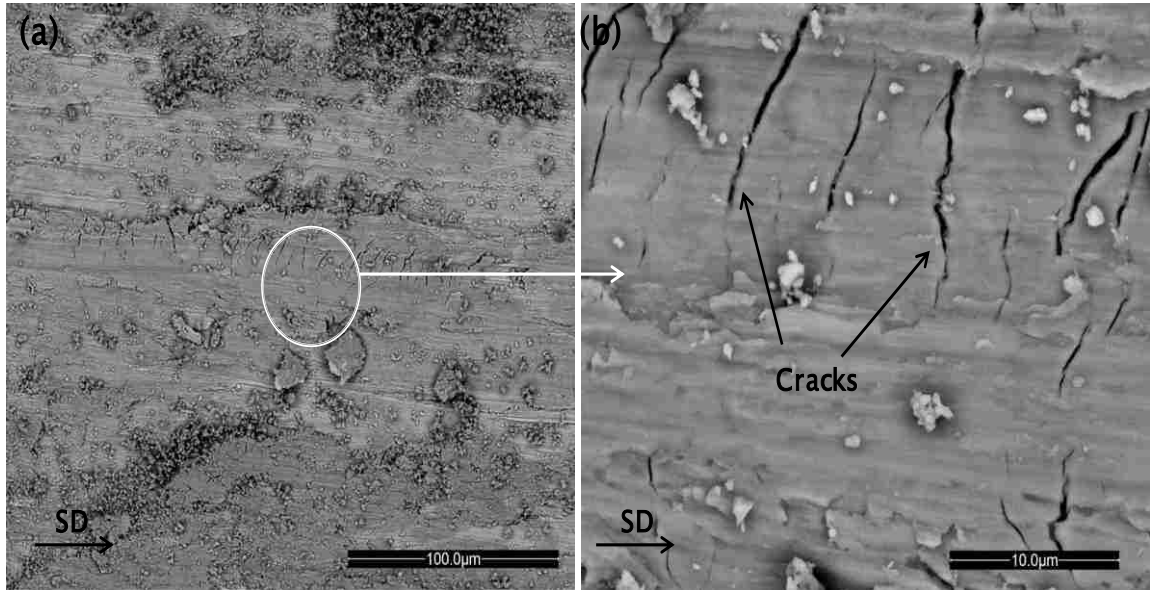


Figure 5.4 Back-scattered electron (BSE) SEM image from the flat area of wear track on Ti-10V-2Fe-3Al coupon after wear test at 5N. Magnification: (a) 500X, and (b) 4000X.

CHAPTER 6

CONCLUSIONS AND RECOMMENDATIONS

6.1 Overview

The aim of this research study is to develop an optimum surface engineering process for a near β Ti-10V-2Fe-3Al alloy to enhance its wear properties without degradation of its mechanical properties (e.g. ductility and fatigue strength).

6.1.1 Effect of ion nitriding on the microstructure

A series of ion nitriding treatments (9 trials in total) are performed at Exactatherm Ltd. The effect of the nitriding temperature (600°C vs. 800°C), nitriding duration (8 hours vs. 24 hours), nitriding pressure (67 Pa vs. 520 Pa) and pre-treatment techniques (chemical pickling vs. gas sputtering) are studied. The optimum microstructure (thin compound layer and deep diffusion zone) is achieved by the ion nitriding at a temperature of 600°C for 8 hours in a pressure (67 Pa) dilute nitriding atmosphere (2.9% N₂). Conclusions are presented below:

- Elongated gas sputtering is considered as an optimized pre-treatment method due to the fact that surface sputtering cleaning helps to improve coating adhesion.
- Higher nitriding temperature (800°C) leads to the formation of a thick compound layer ($3.1 \pm 0.64 \mu\text{m}$ versus $0.4 \pm 0.1 \mu\text{m}$ for 600°C) followed by a brittle α -stabilized layer in the diffusion zone (not observed in 600°C).
- Longer nitriding duration (24 hours) generates a thick compound layer ($1.34 \pm 0.20 \mu\text{m}$ versus $0.4 \pm 0.1 \mu\text{m}$ for 8 hours) with high residual stress, which is harmful to the coating adhesion.

- Higher nitriding pressure (520 Pa) limits the diffusion of nitrogen into the alloy results in thin diffusion zone (9 μm versus 35 μm for 67 Pa).
- The optimum microstructure consisted of a thin compound layer ($0.4 \pm 0.1 \mu\text{m}$) on the surface consisting of TiN, Ti₂N, V₂N and traces of Fe₈N and a $35 \pm 5 \mu\text{m}$ deep diffusion zone.
- By adopting the nitriding temperature of 600°C, the formation of brittle features such as the α -stabilized layer and ω precipitates (250-450°C) are avoided in the nitrided microstructure confirmed by TEM observations.
- The microhardness-depth profile obtained from Ti-10V-2Fe-3Al nitrided at optimum condition shows the highest hardness value (425 HV) is observed close to the interface and gradually decreases to reach the bulk hardness (340 HV) at approximately 35 μm .

6.1.2 Scratch resistance of ion nitrided Ti-10V-2Fe-3Al

- Microscratch tests applied to ion nitrided Ti-10V-2Fe-3Al shows a tremendous reduction in the average coefficient of friction value of Ti-10V-2Fe-3Al for all loading conditions, indicating a well-bonded compound layer that possesses considerable adhesive strength to the substrate and thus improved wear resistance.
- Formation of the compound layer increases the adhesion resistance of the Ti alloy under sliding conditions and results in a more than 72% reduction in the coefficient of friction values.
- Underneath the compound layer, a $35 \pm 5 \mu\text{m}$ diffusion zone provides mechanical support for the compound layer by minimizing the deformation mismatch between the compound layer and the Ti substrate. As a result, the nitrided

surfaces did not experience any premature failures such as buckling and delamination, and the compound layer maintains a good adhesion to its substrate up to a normal load of 17N.

6.1.3 Wear behaviour of ion nitrided Ti-10V-2Fe-3Al

Ball-on-disk wear tests are performed on treated and untreated Ti-10V-2Fe-3Al; an array of surface and subsurface techniques are used to summarize the conclusions as follows:

- The untreated Ti-10V-2Fe-3Al shows two wear mechanisms of delamination and oxidation as a function of the applied load.
- Oxidational/abrasive wear dominated at lower loads (less than 3.5N), whereas delamination wear dominated at higher loads (above 3.5N).
- Cross-sectional examinations of wear tracks using focused ion beam milling (FIB)/ scanning electron microscopy (SEM) show formation of mechanically mixed layers (MMLs) consists of pores and mixed α and β phases.
- A thicker MML ($9.3 \pm 0.6 \mu\text{m}$) is obtained in higher loading conditions (5N), indicating a more severe wear progress.
- Abrasive properties of titanium oxides result in a higher average steady-state COF value in low load conditions.
- The mechanically mixed layer at higher loads lowers the average steady-state COF value however, the delamination of this layer results in COF pattern with more fluctuations.

- The wear rates of ion nitrided Ti-10V-2Fe-3Al compare to the wear rate of untreated alloy at 5N and 3.5N test condition are 47% and 55% lower, respectively
- Average steady-state COFs are almost constant for all loading conditions with small changes inversely proportional to the load applied.

6.1.4 Tensile and fatigue properties before and after ion nitriding

Uniaxial tensile tests and rotation bending fatigue tests are performed on ion nitrided alloys to study the nitriding effect on the mechanical and fatigue behaviours of Ti-10V-2Fe-3Al. The same tests are performed on untreated alloys for comparison purposes. The highlights are summarized as follows:

- Ion nitrided Ti-10V-2Fe-3Al shows slightly higher tensile strength (increased by 6.3% and 4.7% in yield and ultimate tensile strength, respectively) compared with untreated Ti-10V-2Fe-3Al.
- Ion nitrided Ti-10V-2Fe-3Al shows loss of ductility by 15.9% when compared with the untreated alloy.
- The fatigue strength of Ti-10V-2Fe-3Al decreases to 536 MP from 800 MPa after ion nitriding treatment.
- The deterioration of the fatigue limit is subjected to the surface embrittlement that resulted from the nitriding effect. The thin but brittle compound layer enhances crack initiation in the early stage of crack growth. Furthermore, the average β grain size is increased by 29.7% in the bulk microstructure, resulting in a fast crack propagation process, thus reducing the fatigue limit.

6.2 Recommendations for future research

The current research introduces an optimum surface treatment for Ti-10V-2Fe-3Al which provides an increase in wear, tensile and yield strengths of the alloy. However, the results indicate the loss of ductility and fatigue properties as a result of the ion nitriding. Therefore, the following are suggested for future research:

- Modify the as-received microstructure of Ti-10V-2Fe-3Al to minimize the grain size in the bulk microstructure with the proper heat treatment according to standard.
- Introduce electropolishing techniques for the surface preparation of Ti-10V-2Fe-3Al prior to ion nitriding to avoid microstructural changes. A list of electropolishing parameters is given in Appendix 2.2.
- Perform ion nitriding treatments using the parameters presented in this research study followed by the same research methodology.

REFERENCES

- [1] G. Lütjering, J.C. Williams, Titanium, 1st ed., Springer, Berlin, Heidelberg, New York, 2003.
- [2] American Society for Metals, Metals Handbook, 9th ed., American Society for Metals, Metals Park, Ohio, 1985.
- [3] Wikipedia, Titanium Alloy, http://en.wikipedia.org/wiki/Titanium_alloy#cite_note-2 (2012), DOA: 2012.05.25.
- [4] L.S. Smith, P. Threadgill, M. Gittos, Titanium Information Group, 1st ed., Titanium Information Group, Granta Park, UK, 1999.
- [5] J.M. Donachie. Jr., Titanium: A Technical Guide, 2nd ed., ASM international, Ohio, 2000.
- [6] P. Schmidt, H.J. Christ, Improving the fatigue properties of meta stable beta titanium alloys by thermohydrogen processing, *Effects of Hydrogen on Materials*. (2008) 227-234.
- [7] C. Li, J.H. Chen, X. Wu, W. Wang, S. van der Zwaag, Tuning the stress induced martensitic formation in titanium alloys by alloy design, *J. Mater. Sci.* 47 (2012) 4093-4100.
- [8] H.M. Fowler, Microstructural Development in Relation to Hot Working of Titanium Alloys, *Mater. Sci. Tech.* 6 (1990) 1082-1092.
- [9] Allegheny Technologies Incorporated, Technical data sheet ATI 38-644 Beta titanium alloy, ATI (2011), DOA: 2013.05.03.
- [10] M. Jackson, R. Dashwood, L.Christodoulou, H. Flower, The microstructural evolution of near beta alloy Ti-10V-2Fe-3Al during subtransus forging, *Metall. Mater. Trans. A.* 36 (2005) 1317-1327.
- [11] D. Luquiau, X. Feaugas, M. Clavel, Cyclic softening of the Ti-10V-2Fe-3Al titanium alloy, *Mater. Sci. Eng. , A.* 224 (1997) 146-156.
- [12] G. Lütjering, J.C. Williams, Titanium, 2nd ed., Springer, Berlin, 2007.
- [13] M. Jackson, N.G. Jones, D. Dye, R.J. Dashwood, Effect of initial microstructure on plastic flow behaviour during isothermal forging of Ti-10V-2Fe-3Al, *Mater. Sci. Eng. , A.* 501 (2009) 248-254.

- [14] S. Heredia, S. Fouvry, B. Berthel, J. Panter, A non-local fatigue approach to quantify Ti10V2Fe3Al fretting cracking process: Application to grinding and shot peening, *Tribol. Int.* 44 (2011) 1518-1525.
- [15] N.G. Jones, R.J. Dashwood, M. Jackson, and D. Dye, β -Phase Decomposition in Ti-5Al-5Mo-5V-3Cr, *Acta Mater.* 57 (2009) 3830-3839.
- [16] B.S. B. Koch, Strain controlled fatigue testing of the metastable β -titanium alloy Ti-6.8Mo-4.5Fe-1.5Al (Timetal LCB), *Materials Science and Engineering A.* 528 (2011) 5999-6005.
- [17] A. Zhecheva, S. Malinov, W. Sha, Microstructure and microhardness of gas nitrided surface layers in Ti-8Al-1Mo-1V and Ti-10V-2Fe-3Al alloys, *Surf. Eng.* 21 (2005) 269-277.
- [18] C. Sauer, G. Lütjering, Influence of α layers at β grain boundaries on mechanical properties of Ti-alloys, *Mater. Sci. Eng. A.* 319-321 (2001) 393-397.
- [19] Matweb, Material Property data, <http://matweb.com/search/datasheet.aspx>. (2012), DOA: 2012.07.27.
- [20] Wikipedia, Hardness, <http://en.wikipedia.org/wiki/Hardness>, (2012), DOA: 2012.09.11.
- [21] Integrated publishing, Mechanical properties, <http://www.tpub.com/steelworker1/2> (2012), DOA: 2012.09.11.
- [22] Wikipedia, Indentation hardness, http://en.wikipedia.org/wiki/Indentation_hardness (2012), DOA: 2012.09.11.
- [23] Wikipedia, Fracture toughness, http://en.wikipedia.org/wiki/Fracture_toughness (2012), DOA: 2012.09.11.
- [24] A. Bhattacharjee, V.K. Varma, S.V. Kamat, A.K. Gogia, S. Bhaggava, Influence of β grain size on tensile behavior and ductile fracture toughness of titanium alloy Ti-10V-2Fe-3Al, *Metall. Mater. Trans. A.* 37A (2006) 1423-1433.
- [25] W. Chen, Z. Song, L. Xiao, Q. Sun, J. Sun, The influence of prior cold deformation on precipitation of alpha phase and variation of hardness in Ti-10Mo-8V-1Fe-3.5Al during aging treatment, *J. Mater. Res.* 24 (2009) 2899-2907.
- [26] K. Holmberg, A. Matthews, *Coatings Tribology, Properties, Mechanics, Techniques, and Applications in Surface Engineering*, 2nd ed., Elsevier, Amsterdam, Boston, Heidelberg, London, New York, Oxford, Paris, San Diego, San Francisco, Singapore, Sydney, Tokyo, 2009, pp. 23-67.

- [27] W. Chen, Q.Y. Sun, L. Xiao, J. Sun, P. Ge, Influence of aging process on microstructure and mechanical properties of Ti-10V-2Fe-3Al, *Rare. Met. Mater. Eng.* 40 (2011) 708-713.
- [28] W. Chen, Q.Y. Sun, L. Xiao, J. Sun, Deformation-induced microstructure refinement in primary α phase-containing Ti-10V-2Fe-3Al alloy, *Mater. Sci. Eng. A.* 527 (2010) 7225-7234.
- [29] C. Li, X. Wu, J.H. Chen, S. van der Zwagg, Influence of α morphology and volume fraction on the stress-induced martensitic transformation in Ti-10V-2Fe-3Al, *Mater. Sci. Eng. A.* 528 (2011) 5854-5860.
- [30] Q.Y. Sun, S.J. Song, R.H. Zhu, H.C. Gu, Toughening of titanium alloys by twinning and martensite transformation, *J. Mater. Sci.* 37 (2002) 2543-2547.
- [31] T. Furuhashi, S. Annaka, T. Maki, Superplasticity in beta titanium alloys with nitrogen addition, *J. Mater. Eng. Perform.* 14A (2005) 761-764.
- [32] Wikipedia, Fatigue (Material), [http://en.wikipedia.org/wiki/Fatigue_\(material\)](http://en.wikipedia.org/wiki/Fatigue_(material)) (2012), DOA: 2012.09.12.
- [33] R.I. Stephens, H.O. Fuchs, *Metal Fatigue in Engineering*, 2nd ed., John Wiley & Sons Inc., USA, 2001, pp.78-90.
- [34] S.K. Jha, K.S. Ravichandran, High-cycle fatigue resistance in beta-titanium alloys, *Adv. Mater.* (2000) 30-35.
- [35] M. Benedetti, Comparison of the fatigue crack propagation resistance of alpha + beta and beta titanium alloys, *Key Eng. Mater.* 378-379 (2008) 117-130.
- [36] S.K. Jha, K.S. Ravi Chandran, An unusual fatigue phenomenon: duality of the $S-N$ fatigue curve in the β -titanium alloy Ti-10V-2Fe-3Al, *Scripta Mater.* 48 (2003) 1207-1212.
- [37] R. Chait, T.S. DeSisto, The influence of grain size on the high cycle fatigue crack initiation of a metastable beta titanium alloy, *Mater. Trans. A.* 8A (1977) 1017-1020.
- [38] J. Takeda, M. Niinomi, T. Akahori, Gunawarman, Effect of microstructure on fretting fatigue and sliding wear of highly workable titanium alloy, Ti-4.5Al-3V-2Mo-2Fe, *Int. J. Fatigue.* 26 (2004) 1003-1015.
- [39] Y.K. Gao, Influence of shot peening on tension-tension fatigue property of two high strength Ti alloys, *Surf. Eng.* 22 (2006) 299-303.
- [40] A. Drechsler, T. Dorr, L. Wagner, Mechanical surface treatments on Ti-10V-2Fe-3Al for improved fatigue resistance, *Mater. Sci. Eng. A.* 243 (1998) 217-220.

- [41] K. Holmberg, A. Matthews, H. Ronkainen, Coatings tribology-contact mechanisms and surface design, *Tribol Int.* 31 (1998) 107-120.
- [42] E. Rabinowicz, *Friction and Wear of Materials*, 2nd ed., John Wiley & Sons Inc., New York, 1995, pp.7-56.
- [43] J.M. Thompson, M.K. Thompson, A proposal for the calculation of wear, (2006).
- [44] G.W. Stachowiak, A.W. Batchelor, *Engineering Tribology*, *Tribol News*, <http://tribologynews.wordpress.com/delamination-wear> (2012), DOA: 2012.09.24.
- [45] M. Jones, H. Scott, D. Scott, *Industrial Tribology: The Practical Aspects of Friction, Lubrication, and Wear*, Elsevier Scientific Publishing Company, New York, 1983, pp. 345-367.
- [46] A. Bloyce, Surface engineering of titanium alloys for wear protection, *Proceedings of the Institution of Mechanical Engineers.* 212 (1998) 467-476.
- [47] A. Marsui, Effect of microstructure of titanium-base materials on tribological properties, *Jpn. J. Tribol.* 40 (1995) 91-105.
- [48] S. Fayeulle, P. Blanchard, L. Vicent, Fretting Behaviour of Titanium alloys, *Tribol. Trans.* 36 (1993) 267-275.
- [49] T.W. Duerig, J. Albrecht, D. Ritcher, P. Fischer, Formation and reversion of stress induced martensite in Ti-10V-2Fe-3Al, *Acta Mater.* 30 (1982) 2161-2172.
- [50] S. Malinov, A. Zhecheva, W. Sha, Nitriding of titanium and aluminum alloys, *Met. Sci. Heat Treat.* 46 (2004) 286-293.
- [51] Y.S. Matychak, I.M. Pohrelyuk, V.M. Fedirko, Kinetic features of the process on nitriding of $\alpha+\beta$ titanium alloys, *Mater. Sci.* 46 (2011) 660-665.
- [52] H.J. Spies, Surface engineering of aluminum and titanium alloys, an overview, *Surf. Eng.* 26 (2010) 319-323.
- [53] T. Bacci, G. Pradelli, B. Tesi, C. Badini, C. Gianoglio, β transus temperature influence on α - β titanium alloys behaviour in ion-nitriding process, *Mater. Chem. Phys.* 25 (1990) 237-250.
- [54] A.A. Il'in, S.Y. Betsofen, S.V. Skvortsova, L.M. Petrov, I.O. Bannykh, Structural aspects of ion nitriding of titanium alloys, *Russ. Metall.* 2002 (2002) 209-217.
- [55] T.A. Panaioti, Effect of the pressure in the gas-discharge chamber on the depth of nitrogen diffusion in titanium alloys, *Met. Sci. Heat Treat.* 40 (1998) 381-384.

- [56] T. Bell, H. Dong, Y. Sun, Realising the potential of duplex surface engineering, *Tribol Int.* 31 (1998) 127-137.
- [57] J.H. Abbound, D.R.F. West, *J. Mater. Sci. Lett.* 13 (1994) 457.
- [58] T.N. Baker, H. Xin, C. Hu, S. Mridha, Design of surface in-situ metal, *Mater. Sci. Tech.* 10 (1994) 536.
- [59] L. Fouilland-Paille, S. Ettaqi, S. Benayoun, J.J. Hantzpergue, Structural and mechanical characterization of Ti/TiC cermet coatings synthesized by laser melting, *Surf. Coat. Technol.* 88 (1996) 204-211.
- [60] H. Xin, C. Hu, T.N. Baker, Microstructural assessment of laser nitrided Ti-6Al-4V alloy, *J. Mater. Sci.* 35 (2000) 3373-3382.
- [61] K. Euh, S. Lee, K. Shin, Microstructure of TiB₂/carbon steel surface-alloyed materials fabricated by high-energy electron beam irradiation, *Metall. Mater. Trans. A.* 30 (1999) 3143-3151.
- [62] S. Oh, D. Suh, S. Lee, N.J. Kim, *Mater. Sci. Eng. A.* 248 (1998) 245.
- [63] A.F. Vaisman, S.B. Vasserman, M.G. Golkovskii, V.D. Kedo, R.A. Salimov, About Surface Hardening by Concentrated Electron Beam at Atmosphere, Preprint, 2nd ed., Institute of Nuclear Physics, Novosibirsk, 1988, pp.5-31.
- [64] R.S. Razavi, G.R. Gordani, H.C. Man, *Anti-corrosion Methods and Materials.* 58 (2011) 140-154.
- [65] C. Muller, U. Holzwarth, J. K. Gregory, Influence of nitriding on microstructure and fatigue behaviour of a solute-rich beta titanium alloy, *Fatigue Fract Engng Mater. Struct.* 20 (1997) 1665-1676.
- [66] A. Zhecheva, S. Malinov, W. Sha, Titanium alloys after surface gas nitriding, *Surf. Coat. Technol.* 201 (2006) 2467-2474.
- [67] S.G. Lakshmi, D. Arivouli, B. Gangguli, Surface modification and characterization of Ti-Al-V alloys, *Mater. Chem. Phys.* 76 (2002) 187-190.
- [68] J.K. Gregory and U. Holzwarth, Microstructural and notch effect on fatigue of higher pressure nitrided Ti-6Al-4V, *D-E* (1995) 197-202.
- [69] J. K. Gregory, L. Wagner, Heat Treatment and Mechanical Behaviour in Beta-C, GKSS External Report, Geesthacht, Germany, 1992, pp. 7-34.
- [70] K. Tokaji, T. Ogawa, H. Shibata, The effects of gas nitriding on fatigue behavior in titanium and titanium alloys, *JMEPEG.* 8 (1999) 159-167.

- [71] P. Ekvall, E. Johansson, N. Axen, *Tribologia*. 17 (1998) 69-73.
- [72] E. Rolinski, *Politechnika Warszawska, Prace Naukowe, Mechanika*. 112 (1988) 108-118.
- [73] Buehler, *Grinding Polishing Technical Information, Refractory Metals, Beta Titanium Alloy –UNS R54610 Ti-10V-2Fe-3Al*, (2013) DOA: 2013.05.04.
- [74] CMI, Manuel pour optical profiler Veeco Wyko NT1100, introduction, http://cmi.epfl.ch/metrology/Wyko_NT1100.php. (2012), DOA: 2013.05.15.
- [75] Rigaku, MiniFlex X-ray diffraction (XRD) instrument, <http://www.rigaku.com/> (2012), DOA: 2013.08.25.
- [76] The Canadian Centre for Electron Microscopy, Focused Ion Beam, <http://ccem.mcmaster.ca/equipement-nv40.shtml> (2012), DOA: 2013.03.15.
- [77] W.C. Oliver, G.M. Pharr, An improved technique for determining hardness and elastic modulus using load and displacement sensing indentation experiments, *J. Mater. Res.* 7 (1992) 1564-1583.
- [78] ASTM E384, Standard test method for Knoop and Vickers hardness of materials, ASTM Int'l. (2012), DOA: 2013.05.03.
- [79] M3 excellence limited, www.m3tubecomponents.com (2013), DOA: 2013.08.25.
- [80] ASTM E8, Standard test methods for tensile testing of metallic materials. ASTM Int'l. 3 (1997), DOA: 2013.04.03.
- [81] ASTM E466-07, Standard practice for conducting force controlled constant amplitude axial fatigue tests of metallic materials, ASTM Int'l. (2007).
- [82] Instron, Rotating beam fatigue testing system, Instron, www.instron.com (2012), DOA: 2013.08.12.
- [83] K. Farokhzadeh, A. Edrisy, G. Pigott, P. Lidster, Scratch resistance analysis of plasma-nitrided Ti-6Al-4V alloy, *Wear*. 302 (2013) 845-853.
- [84] ASTM E1382-97, Standard test methods for determining average grain size using semiautomatic and automatic image analysis, ASTM Int'l. (2010), DOA: 2013.07.04.
- [85] J. Tiley, T. Searles, E. Lee, S. Kar, R. Banerjee, J.C. Russ, H.L. Fraser, Quantification of microstructural features in α/β titanium alloys, *Mater. Sci. Eng. A*. 372 (2004) 191-198.

- [86] A. Vadiraj, M. Kamaraj, Effect of plasma nitriding on fretting fatigue damage of surgical grade titanium alloys, *Trans. Indian Inst. Met.* 59 (2006) 503-509.
- [87] B. Peterson, P. Collins, H. Fraser, On the use of a sub-scale thermomechanical simulator to obtain the most accurate tensile properties of the $\alpha + \beta$ and β processed Ti-6Al-4V, *Mater. Sci. Eng. A.* 513-514 (2009) 357-365.
- [88] P. H. DeVries, K. T. Ruth, D. P. Dennies, Counting on fatigue: Striations and their measure, *JFAP.* 10 (2010) 120-137.
- [89] H. Schmidt, M. Soltani-Farshi, Effect of nitrogen implantation on the hydrogen depth distribution and fatigue properties of Ti-6Al-4V, *Mater. Sci. Eng. A.* 248 (1998) 73-77.
- [90] H.J. Rack, J.I. Qazi, Titanium alloys for biomedical applications, *Mater. Sci. Eng. C.* 26 (2006) 1269-1277.
- [91] H. Shibata, K. Tokaji, T. Ogawa, C. Hori, The effect of gas nitriding on fatigue behaviour in titanium alloys, *Int. J. Fatigue.* 16 (1994) 370-376.
- [92] N.P. P. Sricharoenchai, P. Visutti pitukul, P. Wangyao, Effect of substrate temperature, biasing and sputter cleaning on the structure and properties of nanostructured TiB₂ coatings on high speed steel, *Mater. Trans.* 51 (2010) 246-252.
- [93] H. Ronkainen, J. Vihersalo, S. Varjus, R. Zilliacus, U. Ehrnstén, P. Nenonen, Improvement of a-C:H film adhesion by intermediate layers and sputter cleaning procedures on stainless steel, alumina and cemented carbide, *Surf. Coat. Technol.* 90 (1997) 190-196.
- [94] G.A. Collins, R. Hutchings, K.T. Short, J. Tendys, X. Li, M. Samandi, Nitriding of austenitic stainless steel by plasma immersion ion implantation, *Surf. Coat. Technol.* 74-75 (1995) 417.
- [95] L. Wang, X. Xu, Z. Yu, Z. Hei, Low pressure plasma arc source ion nitriding of austenitic stainless steel, *Surf. Coat. Technol.* 124 (2000) 93.
- [96] M. Jackson, R. Dashwood, L. Christodoulou, H. Flower, The microstructural evolution of near beta alloy Ti-10V-2Fe-3Al during subtransus forging, *Metall. Mater. Trans. A.* 36A (2005) 1317-1327.
- [97] T. Morita, S. Fuchikawa, J. Komotori, M. Shimizu, K. Minakawa, K. Kawasaki, Fatigue strength of nitrided high-strength titanium alloy, *Transactions of the Japan Society of Mechanical Engineers, Part A.* 67 (2001) 719-725.
- [98] V. Fouquet, L. Pichon, M. Drouet, A. Straboni, Plasma assisted nitridation of Ti-6Al-4V, *Appl. Surf. Sci.* 221 (2004) 248-258.

- [99] R. Steinert, J. Lindemann, C. Leyens, Effect of nitride coatings on the wear and fatigue behavior of titanium alloy Ti-6Al-4V, 12th World Conference on Titanium, Ti 2011; Beijing; China; 19 June 2011 through 24 June 2011. 2 (2012) 858-861.
- [100] N.V. Gavrilov, A.S. Mamaev, Low-temperature nitriding of titanium in low-energy electron beam excited plasma, *Tech Phys Lett.* 35 (2009) 713-716.
- [101] T. Bell, K. Mao, Y. Sun, Surface engineering design: modelling surface engineering systems for improved tribological performance, *Surf. Coat. Technol.* 108-109 (1998) 360-368.
- [102] T.W. Duerig, G.T. Terlinde, J.C. Williams, Phase transformations and tensile properties of Ti-10V-2Fe-3Al, *Metall. Trans. A.* 11A (1980) 1987-1998.
- [103] G.T. Terlinde, T.W. Duerig, J.C. Williams, Microstructure, tensile deformation, and fracture in aged Ti-10V-2Fe-3Al, *Metall. Trans. A.* 14A (1983) 2101-2115.
- [104] T. Bacci, G. Pradelli, B. Tesi, C. Gianoglio, C. Badini, Surface engineering and chemical characterization in ion-nitrided titanium and titanium alloys, *J. Mater. Sci.* 25 (1990) 4309-4314.
- [105] A.A. Il'in, S.V. Skvortsova, L.M. Petrov, E.A. Lukina, A.A. Chernysheva, Effect of the phase composition and structure of titanium alloys on their interaction with nitrogen during low-temperature ion nitriding, *Russ. Metall.* 2006 (2006) 400-405.
- [106] S.L. Semiatin, S.L. Knisley, P.N. Fagin, F. Zhang, D.R. Barker, Microstructure evolution during alpha-beta heat treatment of Ti-6Al-4V, *Metall. Mater. Trans. A.* 34A (2003) 2377-2386.
- [107] J.F. Murdock, Diffusion of Titanium-44 and Vanadium -48 in Titanium, 29th ed., Oak ridge national laboratory, 1964.
- [108] U. Wiklund, I. M. Hutchings, Investigation of surface treatments for galling protection of titanium alloys, *Wear.* 251 (2001) 1034-1041.
- [109] T. Bell, H.W. Bergmann, J. Lanagan, P.H. Morton, A.M. Staines, Surface engineering of titanium with nitrogen, *Surf. Eng.* 2 (1986) 133-143.
- [110] M. Fallqvist, Microstructural, Mechanical and Tribological Characterization of CVD and PVD Coatings for Metal Cutting Applications, Uppsala University, 2012.
- [111] U. Wiklund, B. Cacas, N. Stavlid, Evaporated vanadium nitride as a friction material in dry sliding against stainless steel, *Wear.* 261 (2006) 2-8.
- [112] T.M. Muraleedharan, E.I. Meletis, Surface modification of pure titanium and Ti-6Al-4V by intensified plasma ion nitriding, *Thin Solid Films.* 221 (1992) 104-113.

- [113] D.F. Diao, Y. Sawaki, Fracture mechanisms of ceramic coating during the wear, *Thin Solid Films*. 270 (1995) 362-366.
- [114] A. Raveh, P.L. Hansen, R. Avni, A. Grill, Microstructure and composition of plasma-nitrided Ti-6Al-4V layers, *Surf. Coat. Technol.* 38 (1989) 339-351.
- [115] G. Cassar, J.C. Avelar-Batista Wilson, S. Banfield, J. Housden, M. Fenech, A. Matthews, A. Leyland, Evaluating the effects of plasma diffusion processing and duplex diffusion/PVD coating on the fatigue performance of Ti-6Al-4V alloy, *Int. J. Fatigue*. 33 (2011) 1313-1323.
- [116] D. Nolan, S.W. Huang, V. Leskovsek, S. Braun, Sliding wear of titanium nitride thin films deposited on Ti-6Al-4V alloy by PVD and plasma nitriding processes, *Surf. Coat. Technol.* 200 (2006) 5698-5705.
- [117] J. Meneve, K. Vercammen, E. Dekempeneer, J. Smeets, Thin tribological coatings: magic or design? *Surf. Coat. Technol.* 94-95 (1997) 476-482.
- [118] M. Mubarak Ali, S. Ganesh Sundara Raman, S.D. Pathak, R. Gnanamoorthy, Influence of plasma nitriding on fretting wear behaviour of Ti-6Al-4V, *Tribol Int.* 43 (2010) 152-160.
- [119] Y. Liu, E.I. Meletis, Tribological behavior of DLC coatings with functionally gradient interfaces, *Surf. Coat. Technol.* 153 (2002) 178-183.
- [120] A.D. Wilson, A. Leyland, A. Matthews, A comparative study of the influence of plasma treatments, PVD coatings and ion implantation on the tribological performance of Ti-6Al-4V, *Surf. Coat. Technol.* 114 (1999) 70-80.
- [121] G. Cassar, S. Banfield, J.C. Avelar-Batista Wilson, J. Housden, A. Matthews, A. Leyland, Tribological properties of duplex plasma oxidized, nitrided and PVD coated Ti-6Al-4V, *Surf. Coat. Technol.* 206 (2011) 395-404.
- [122] G. Abrasonis, W. Möller, X.X. Ma, Anomalous ion accelerated bulk diffusion by interstitial nitrogen, *Phys. Rev. Lett.* 96 (2006) 065901-1-065901-4.
- [123] F. Cemin, F.G. Echeverrigaray, A.C. Rovani, C.L.G. Amorim, R.L.O. Basso, I.J.R. Baumvol, C.A. Figueroa, Influence of atomic and mechanical attrition on low temperature plasma nitriding of ferrous alloys, *Mater. Sci. Eng. A*. 527 (2010) 3206-3209.
- [124] S. Korres, T. Feser, M. Dienwiebel, In situ observation of wear particle formation on lubricated sliding surfaces, *Acta Mater.* 60 (2012) 420-429.
- [125] S.C. Lim, M.F. Ashby, Overview No.55, wear-mechanism maps, *Acta Metall.* 35 (1987) 1-24.

- [126] M.J. Neale, T.A. Polak, M. Priest, M. Cartier, Handbook of Surface Treatments and Coatings, John Wiley and Sons Ltd, Dublin, Ireland, 2003.
- [127] Q. Xue, M.A. Meyers, V.F. Nesterenko, Self-organization of shear bands in titanium and Ti-6Al-4V alloy, *Acta Mater.* 50 (2002) 575-596.
- [128] D.A. Rigney, Comments on the sliding wear of metals, *Tribology Int.* 30 (1997) 361-367.
- [129] S.C. Liao, J. Duffy, Adiabatic shear bands in a Ti-6Al-4V titanium alloy, *J Mech. Phys. Solids.* 46 (1998) 2201-2231.
- [130] Y.S. Zhang, Z. Han, K. Wang, K. Lu, Friction and wear behaviors of nanocrystalline surface layer of pure copper, *Wear.* 260 (2006) 942-948.
- [131] D.A. Rigney, L.H. Chen, M.G.S. Naylor, A.R. Rosenfield, Wear processes in sliding systems, *Wear.* 100 (1984) 195-219.
- [132] M. Peters, A. Gysler, G. Lutjering, Influence of texture on fatigue properties of Ti-6Al-4V, *Metall. Trans. A.* 15A (1984) 1597-1605.
- [133] D. Rodriguez, J.M. Manero, F.J. Gil, J.A. Planell, Low cycle fatigue behaviour of Ti-6Al-4V thermochemically nitrated for its use in hip prostheses, *J. Mater. Sci. Mater. Med.* 12 (2001) 935-937.
- [134] T. Morita, H. Takahashi, M. Shimizu, K. Kawasaki, Factors controlling the fatigue strength of nitrated titanium, *Fatigue Fract. Engng Mater. Struct.* 20 (1997) 85-92.
- [135] J. Zhang, A.T. Alpas, Transition between mild and severe wear in aluminum alloys, *Acta Mater.* 45 (1997) 513-528.
- [136] V. Voort, Materials Science and Engineering Series, in: I. McGraw-Hill (Ed.), *Metallography Principles and Practice*, 1st ed., McGraw-Hill, Inc., New York, St. Louis, San Francisco; Auckland; Bogota; Caracas; Lisbon; London; Madrid; Mexico; Milan; Montreal; New Delhi; Paris; San Juan; Singapore; Sydney; Tokyo; Toronto, 1984, pp. 599-612.
- [137] M. Yu, J. Yi, J. Liu, S. Li, G. Wu, L. Wu, Effect of electropolishing on electrochemical behaviours of Ti-10V-2Fe-3Al, *J. Wuhan. Univ. Tech. Mater. Sci. Ed.* 26 (2011) 469-477.
- [138] ASTM E1558-09, Standard guide for electrolytic polishing of metallographic specimens, ASTM Int'l. (2013), DOA: 2013.05.05.

[139] C.C. Chen, J.H. Chen, C.G. Chao, W.C. Say, Electrochemical characteristics of surface of titanium formed by electrolytic polishing and anodizing, *J. Mater. Sci.* 40 (2005) 4053-4059.

[140] R. W. Gardiner, P. G. Partridge, Preparation of thin foils of titanium and titanium alloys for transmission electron microscopy, *J. Sci. Instrum.* 44 (1967) 63-65.

[141] G.T. Terlinde, T.W. Duerig, J.C. Williams, The effect of heat treatment on microstructure and tensile properties of Ti-10V-2Fe-3Al, *Titanium '80 Science and Technology - Proceedings of the 4th Int'l Conference on Titanium.* 2 (1980) 1571-1581.

APPENDICES

Appendix 1: List of parameters for calculation of flash and bulk temperature during wear tests [125,135]

		0.8N	5N	
SYMBOLS	UNIT			COMMENTS
μ		0.7041	0.6033	
F	N	0.8	5	APPLIED FORCE
RN	M	0.000279	0.0005	NOMINAL RADIUS
RO	M	0.0003	0.0005	RADIUS OF BALL WEAR MARK
LB	M	0.001	0.001	EQUIVALENT LINEAR DIFFUSION DISTANCE FOR BULK HEATING
LR	M	0.001	0.003	LINEAR DIFFUSION DIST. FOR FLASH H
B		0.616010687	0.560013462	LB(STEEL)/RO
V	M/S	0.1	0.1	SLIDING VELOCITY
AN	M ²	2.82743E-07	7.85398E-07	NOMINAL AREA OF CONTACT
HO	N/M ²	4750000000	4750000000	ROOM T HARDNESS OF METAL
K(Ti)	W/M-K	7.8	7.8	THERMAL CONDUCTIVITY OF METAL
K(STEEL)	W/M-K	45	45	THERMAL COND. OF 52100 STEEL BALL
K(Ti)/L(Ti)		2600	2600	
LF(Ti)	M	4.28337E-06	6.27356E-06	
LF(STEEL)	M	4.30795E-06	6.31729E-06	
K(Ti)/LF(Ti)		1820997.454	1243312.789	
K(STEEL)/LF(STEEL)		10445791.78	7123303.743	
LB(STEEL)	M	0.000184803	0.000280007	
T*	K	1644.230769	1644.230769	
TO	K	293	293	SINK TEMPERATURE FOR BULK HEATING
F BAR		0.000595668	0.001340252	
A(Ti)	M ² /S	0.0000027	0.0000027	THERMAL DIFFUSIVITY OF METAL (Ti)
A(STEEL)	M ² /S	0.000012	0.000012	THERMAL DIFF. OF COUNTERFACE STEEL
V BAR		11.11111111	18.51851852	
T*	K	1644.230769	1644.230769	EFFECTIVE EQUIVALENT TEMPERATURE FOR METAL
RA	M	0.00001	0.00001	RADIUS OF ISOLATED UNIT CONTACT 10 ⁻⁵ M

TE*	K	1986.525645	2129.145266	EFFECTIVE EQUIVALENT. TEMPERATURE FOR METAL
N		1.535781532	4.346139748	NORMAL LOAD
TB	K	294.4360816	296.9278666	BULK TEMP
TB	°C	21.28608156	23.77786658	BULK TEMPERATURE
(F BAR/N)^0.5		0.019694152	0.017560684	
Tf (LIM AND ASHBY)	K	388.6795435	413.8235733	FLASH TEMP
KOX	W/M-K	6.531	6.531	RUTILE AT 373K
Z	M	0.0000066	0.0000085	THICKNESS OF OXIDE FILM
KE	W/M-K	6.455995185	6.023543908	EQUATION A6 IN APPENDIX 4
Tf (LIM AND ASHY)	°C	115.5295435	140.6735733	FLASH TEMPERATURE

Appendix 2: List of electropolishing parameters from Literatures [136]

ELECTROLYTE COMPOSITION	CONDITIONS				COMMENTS
	CURRENT DENSITY	VOLTAGE DC	TEMP., °C	TIME, MIN	
1. 90 mL ETHANOL 10 mL N-BUTYL ALCOHOL 6 G ANHYDROUS ALUMINUM CHLORIDE 28 G ANHYDROUS ZINC CHLORIDE	0.16-0.8 A/CM2	30-60 (EXT.) 20-25	ROOM TEMP.	1-6 MIN	STIR GENTLY. VERY CORROSIVE SOLUTION BUT NOT EXPLOSIVE. STABLE FOR ABOUT 1 WEEK. PRODUCES SOME SURFACE RELIEF. [REM-CRU TITANIUM, INC].
2. 764 mL ACETIC ANHYDRIDE 184 mL PERCHLORIC ACID 48 mL WATER	20-25 A/DM2	40-60 (EXT.)	ROOM TEMP.	45-60 S	USE SAMPLE A FEW SQUARE CENTIMETERS IN AREA. PLACE SAMPLE HORIZONTAL, FACE DOWN, JUST BELOW THE BATH SURFACE. CATHODE VERTICAL OR HORIZONTAL, SEVERAL CENTIMETERS FROM SAMPLE. MOVE ANODE RAPIDLY DURING POLISH. [JACQUET]
3. 200ML PERCHLORIC ACID 350 mL ETHANOL 100 mL BUTYL CELLOSOLVE	2-4 A/DM2	30	ROOM TEMP.	30 S	ELECTROLYTE CAN BE PUMPED. REMOVE GAS BUBBLES ADHERING TO SURFACE [KNUTH-WINTERFELDT].
4. 36 mL PERCHLORIC ACID 390 METHANOL 350 mL ETHYLENE GLYCOL 24 mL WATER		30-50	5-10°C	10-40 S	EXCELLENT RESULTS REPORTED. SAFE SOLUTION. PUMP ELECTROLYTE [P.R. MALLORY & Co.].
5. 5 G ZnCl2 15 G AlCl3·6H2O 200 mL METHANOL 10 mL H2SO4	1-2 A		ROOM TEMP.	2 MIN	USE 10 BY 10 MM SAMPLE SIZE. GRIND TO 600-GRIT SiC. USE PLATINUM CATHODE AND ANODE LEAD WIRES. AGITATE CATHODE. DISSOLVE SALTS IN METHANOL, ADD SULFURIC ACID SLOWLY [COONS AND IOSTY].
6. 1 PART PERCHLORIC ACID 20 PARTS ACETIC ANHYDRIDE	1 A/CM2		<4°C	4 MIN	PREGRIND TO 600-GRIT SiC. ETCH PROMPTLY AFTER ELECTROPOLISHING [LEIGHLY].
7. SOLUTION A: 90 mL ETHANOL 10 mL N-BUTYL ALCOHOL 6 G ALUMINUM CHLORIDE 25 G ZINC CHLORIDE	1-5 A/CM2	30-60 80 (EXT.) 20-40 (EXT.)	23-30°C	1-6 5 S 30-60 S	FOR ALPHA-BETA ALLOYS. CAN BE SINGLE-STEP PROCESS USING ONLY SOLUTION A OR TWO-STEP PROCESS (SECOND SET

SOLUTION B: 175 mL METHANOL 25 mL H ₂ SO ₄					CONDITIONS). SAMPLE PREGROUND TO 3/0 PAPER. ELECTROPOLISH IN SOLUTION A, THEN TRANSFER TO SOLUTION B WITHOUT WASHING OR DRYING. PUMP ELECTROLYTE [SOLUTION A DEVELOPED BY REM- CRU TITANIUM, INC.] [COONS].
8. 1000 mL ACETIC ACID 60 mL PERCHLORIC ACID	30-40 A/DM ²	30	20°C	2 MIN	FOR TI WITHOUT CARBIDES. USE TI CATHODE, 3-CM ANODE- TO-CATHODE SPACING. STIR SOLUTION. PREGRIND SAMPLE TO 3/0 GRADE EMERY [SUTCLIFFE AND COWORKERS].
9. 60-65 mL H ₂ SO ₄ 20-25 mL HF 10-20 mL GLYCERIN	0.7 -2.0 A/CM ²	14-20	25- 35°C	2-5 MIN	USE TI CATHODE WITH AREA 10 TIMES THE ANODE AREA. REMOVE SAMPLE FROM SOLUTION WITH THE CURRENT ON [PEKSHEVA AND VORONTSOV]
10. 390 mL METHANOL 350 mL ETHYLENE GLYCOL 60 mL PERCHLORIC ACID	9 A	35	< 30°C	15 s	USED A 6-MM DIAMETER AREA, GRIND THROUGH 0 GRADE EMERY PAPER. KEEP COOL [MALLORY- SHARON METALS CORP.]
11. 11.1 mL HF 59.0 mL LACTIC ACID 24.6 mL H ₂ SO ₄ 3.6 mL DIMETHYL SULFOXIDE 1.7 mL GLYCERIN	0.1 A/CM ²	24-35			FOR PURE TI. PREGRIND SAMPLE. USE GRAPHITE CATHODE, 0.8-CM SPACING. EFFECTS OF COLD WORK REMOVED AFTER 1H ELECTROPOLISH. COOL WITH ICE BATH [PELLEG]
12. 600 mL /L CONCENTRATION OF ETHANOL 160 mL /L CONCENTRATION OF LACTIC ACID 5% CONCENTRATION OF PERCHLORIC ACID 3G /L CONCENTRATION OF SODIUM PERCHLORATE	0.2 A/CM ²		20 ± 2°C	6 MIN	ANODE: GROUND TITANIUM SPECIMEN; CATHODE: A LEAD PLATE [137][EFFECT OF ELECTROPOLISHING ON ELECTROCHEMICAL BEHAVIOURS OF Ti-10V- 2Fe-3Al]
13. 700 mL ETHANOL (95%) 100 mL 2-BUTOXY ETHANOL 200 mL PERCHLORIC ACID (30%)		30 TO 65		15 TO 60 s	[138][ASTM E1558-09]
14. 590 mL METHANOL (ABSOLUTE) 350 mL 2-BUTOXY ETHANOL 60 mL PERCHLORIC ACID		58 TO 66		45 s	POLISH ONLY [138][ASTM E1558-09]

(65%)					
15. 700 mL ETHANOL (95%) 100 mL BUTYLCELLOSOLVE 137 mL WATER		20		20 s	MIX ETHANOL AND WATER, ADD PERCHLORIC ACID CAREFULLY. THEN, ADD BUTYLCELLOSOLVE BEFORE USE. [138][ASTM E1558-09]
16. 940 mL ACETIC ACID (GLACIAL) 60 mL PERCHLORIC ACID (60%)		20 TO 60		1 TO 5 MIN	[138][ASTM E1558-09]
17. 900 mL ACETIC ACID (GLACIAL) 100 mL PERCHLORIC ACID (60%)		12 TO 70		0.5 TO 2 MIN	[138][ASTM E1558-09]
18. 800 mL ACETIC ACID (GLACIAL) 200 mL PERCHLORIC ACID (60%)		40 TO 100		1 TO 15 MIN	[138][ASTM E1558-09]
19. 5% PERCHLORIC ACID 53% ETHYLENE GLUCOL MONOBUTYLEETHER 42% METHANOL		52	15°C	1MIN	GRIND TO 1500-GRIT SIC CATHODE: PLATINUM SHEET ANODE: TITANIUM PLATE FOLLOWED BY 28 V FOR 13 MINS, AT A CONSTANT STIRRING RATE OF 200 RPM [139][ELECTROCHEMICAL CHARACTERISTICS]
20. 60 mL PERCHLORIC ACID (70%) 590 mL METHANOL 350 mL 2-BUTOXYETHANOL (BUTYL CELLOSOLVE)	0.8 A/cm ²	30	0 TO - 30 °C		[140][PREPARATION OF THIN FOIL OF TITANIUM]
21. 5 PCT H ₂ SO ₄ 1 PCT HF BALANCE METHANOL		21	ROOM TEMP		ETCHANT: EQUAL PART OF 10 PCT OXALIC ACID AND 1 PCT HF IN WATER CLOSED CIRCUIT [102][PHASE TRANSFORMATIONS AND]
22. 5 PCT H ₂ SO ₄ BALANCE METHANOL		21	ROOM TEMP		ETCHANT: EQUAL PART OF 10 PCT OXALIC ACID AND 1 PCT HF IN WATER [103,141][MICROSTRUCTU RE, TENSILE; THE EFFECT OF HEAT]
23. 94 PCT METHANOL 5 PCT H ₂ SO ₄ 1 PCT HF			ROOM TEMP		[24][INFLUENCE OF B GRAIN]
23. 3.2 mL PERCHLORIC ACID (60-62%) 40.3 mL BUTAN-1-OL 56.5 mL METHANOL		24	-30 °C		[13][EFFECT OF INITIAL]
24. 36 mL PERCHLORIC ACID 390 mL METHANOL 350 mL ETHYLENE GLYCOL					ETCHANT: 5 mL HF + 10 mL HNO ₃ + 30 mL H ₂ O [7][TUNING THE STRESS]

24 mL WATER					
-------------	--	--	--	--	--

VITA AUCTORIS

NAME: Jin Qian

PLACE OF BIRTH: Nanjing, China

DATE OF BIRTH: 1989

EDUCATION: Secondary School Diploma

Grand Canadian Academy, Nanjing Foreign Language School

Nanjing, China

2004-2007

Bachelor of Applied Science,

Honours Mechanical Engineering Co-op

University of Windsor

Windsor, ON, Canada

2007-2011

Master of Applied Science

Engineering Materials

University of Windsor

Windsor, ON, Canada

2011-2013